SEISMIC STRUCTURE ABOVE AND BELOW THE CORE-MANTLE BOUNDARY

Thesis by

Edward James Garnero

In Partial Fulfillment of the Requirements

for the Degree of

Doctor of Philosophy

California Institute of Technology

Pasadena, California

1994

(Submitted May 2, 1994)

Acknowledgements

I would first like to express my deep gratitude to my research advisor, Don Helmberger. He has consistently displayed encouragement and enthusiasm over the years towards this research, as well as great patience in allowing me independence to conduct my studies. It is through my interaction with Don that I have gained a great appreciation for raw seismic data, and any skill and enthusiams I may have acquired as an observational seismologist are certainly due to being exposed to him. In addition to the scientific and financial support, Don has also been a friend to me – which made my years as a graduate student a lot of fun (especially at conferences.)

At various stages of this work, I benefited from discussions with Don Anderson and Dave Stevenson. Hiroo Kanamori is a constant inspiration in his scientific approach to problems of all types. I thank Steve Grand for his continual reiterating of the importance of careful seismology, our various collaborations, useful computer programs, and for the many discussions on my work. Much of my work involved the reflectivity method for generating synthetic seismograms. The code I use was supplied by Harley Benz, who has answered my numerous questions, for which I am grateful. I will certainly miss the Seismo Lab coffee hours, especially the wisdom and enthusiasm of the regulars, such as Hiroo, both Dons, Tom Heaton, and others. I also

thank Don Anderson for extended loan of the little known "core-mantle boundary binders" (ten of them!), which continue to be a source of ideas and inspiration.

My life as a grad student in the Seismo Lab was made easier (as well as much more interesting) by the friendship and/or help of various students, staff, post docs, and faculty. Help with Caltech logistics was kindly provided by Cheryl Contopulous and Janet Fernandez. Helpful computer codes and computer system information was supplied by Xiao-dong Song, Richard Stead, Hong Kie Thio, Dave Wald, Brad Woods, and Lian-she Zhao. I thank the above and give special thanks to Shawn Larsen for his MPLOT code, which generated most of the figures in this thesis, as well as in my publications.

Last and definitely not least, I thank Pam for her continual support and love, and my parents for their support all along the way.

To *My Parents*

Abstract

Edward James Garnero, Ph.D.

California Institute of Technology 1994

Seismic structure above and below the core-mantle boundary (CMB) has been studied through use of travel time and waveform analyses of several different seismic wave groups. Anomalous systematic trends in observables document mantle heterogeneity on both large and small scales. Analog and digital data has been utilized, and in many cases the analog data has been optically scanned and digitized prior to analysis.

Differential travel times of $S - SKS$ are shown to be an excellent diagnostic of anomalous lower mantle shear velocity (V_S) structure. Wavepath geometries beneath the central Pacific exhibit large $S - SKS$ travel time residuals (up to 10 sec), and are consistent with a large scale 0(1000 km) slower than average V_S region ($\geq$3%). $S - SKS$ times for paths traversing this region exhibit smaller scale patterns and trends 0(100 km) indicating V_S perturbations on many scale lengths. These times are compared to predictions of three tomographically derived aspherical models: MDLSH of Tanimoto [1990], model SH12_WM13 of Su et al. [1992], and model SH.10c.17 of Masters et al. [1992]. Qualitative agreement between the tomographic model

predictions and observations is encouraging, varying from fair to good. However, inconsistencies are present and suggest anomalies in the lower mantle of scale length smaller than the present 2000+ km scale resolution of tomographic models. 2-D wave propagation experiments show the importance of inhomogeneous raypaths when considering lateral heterogeneities in the lowermost mantle.

A dataset of waveforms and differential travel times of S, ScS, and the arrival from the D" layer, Scd, provides evidence for a laterally varying V_S velocity discontinuity at the base of the mantle. Two different localized D" regions beneath the central Pacific have been investigated. Predictions from a model having a V_S discontinuity 180 km above the CMB agree well with observations for an eastern mid-Pacific CMB region. This thickness differs from V_S discontinuity thicknesses found in other regions, such as a localized region beneath the western Pacific, which average near 280 km. The "sharpness" of the V_S jump at the top of D", i.e., the depth range over which the V_S increase occurs, is not resolved by our data, and our data can in fact may be modeled equally well by a lower mantle with the increase in V_S at the top of D" occurring over a 100 km depth range. It is difficult at present to correlate D" thicknesses from this study to overall lower mantle heterogeneity, due to uncertainties in the 3-D models, as well as poor coverage in maps of D" discontinuity thicknesses.

P-wave velocity structure (V_P) at the base of the mantle is explored using the seismic phases SKS and SP_dKS. SP_dKS is formed when SKS waves at distances around 107^o are incident upon the CMB with a slowness that allows for coupling with diffracted P-waves at the base of the mantle. The P-wave diffraction occurs at both

the SKS entrance and exit locations of the outer core. SP_dKS arrives slightly later in time than SKS, having a wave path through the mantle and core very close to SKS. The difference time between SKS and SP_dKS strongly depends on V_P at the base of the mantle near SKS core entrance and exit points. Observations from deep focus Fiji-Tonga events recorded by North American stations, and South American events recorded by European and Eurasian stations exhibit anomalously large $SP_dKS - SKS$ difference times. SKS and the later arriving SP_dKS phase are separated by several seconds more than predictions made by 1-D reference models, such as the global average PREM [Dziewonski and Anderson, 1981] model. Models having a pronounced low-velocity zone (5%) in V_P in the bottom 50-100 km of the mantle predict the size of the observed $SP_dKS - SKS$ anomalies. Raypath perturbations from lower mantle V_S structure may also be contributing to the observed anomalies.

Outer core structure is investigated using the family of $SmKS$ (m=2,3,4) seismic waves. $SmKS$ are waves that travel as S-waves in the mantle, P-waves in the core, and reflect (m-1) times on the underside of the CMB, and are well-suited for constraining outermost core V_P structure. This is due to closeness of the mantle paths and also the shallow depth range these waves travel in the outermost core. $S3KS - S2KS$ and $S4KS - S3KS$ differential travel times were measured using the cross-correlation method and compared to those from reflectivity synthetics created from core models of past studies. High quality recordings from a deep focus Java Sea event which sample the outer core beneath the northern Pacific, the Arctic, and northwestern North America (spanning 1/8th of the core's surface area), have $SmKS$ wavepaths that traverse regions where lower mantle heterogeneity is pre-

dicted small, and are well-modeled by the PREM core model, with possibly a small V_P decrease (1.5%) in the outermost 50 km of the core. Such a reduction implies chemical stratification in this 50 km zone, though this model feature is not uniquely resolved. Data having wave paths through areas of known D" heterogeneity ($\pm$2% and greater), such as the source-side of $SmKS$ lower mantle paths from Fiji-Tonga to Eurasia and Africa, exhibit systematic $SmKS$ differential time anomalies of up to several seconds. 2-D wave propagation experiments demonstrate how large scale lower mantle velocity perturbations can explain long wavelength behavior of such anomalous $SmKS$ times. When improperly accounted for, lower mantle heterogeneity maps directly into core structure. Raypaths departing from homogeneity play an important role in producing $SmKS$ anomalies. The existence of outermost core heterogeneity is difficult to resolve at present due to uncertainties in global lower mantle structure. Resolving a one-dimensional chemically stratified outermost core also remains difficult due to the same uncertainties. Restricting study to higher multiples of $SmKS$ (m=2,3,4) can help reduce the affect of mantle heterogeneity due to the closeness of the mantle legs of the wavepaths. $SmKS$ waves are ideal in providing additional information on the details of lower mantle heterogeneity.

Table of Contents

List of Tables

List of Figures

Chapter 1

General Introduction

1.1 The Core-Mantle Boundary Region

The core-mantle boundary (CMB) marks Earth's largest step increase in density, where it nearly doubles in magnitude. This boundary exists some 2890 km beneath the surface, and is the interface between the solid rock mantle and the underlying liquid iron alloy outer core. The contrast in chemistry, dynamics, and physical states across the CMB is large (see Table 1.1) and comparable to that at the Earth's surface. The thermal, chemical, and compositional environments where the mantle meets the core are all of great interest to geoscientists. Data elucidating this area will have applications to theories of the Earth's evolution, thermal history, and mantle and core dynamics.

Thermal and gravitational energy released from the slow growth of the freezing of the inner core drives rapid outer core convection in a low viscosity regime. Such core motions power the geodynamo responsible for Earth's magnetic field. The heat flow from the core is coupled to convective motions in the more viscous overlying mantle, as well as deformations of the CMB. Lower mantle density variations drive viscous mantle flow, and resulting CMB topography contributes to geoid anomalies

Property	Lower Mantle	Outer Core
Composition	$Mg_{0.9}Fe_{0.1}SiO_3$ (perovskite structure) + (Mg,Fe)O + $CaSiO_3$	Fe + 10% (O,S,Si,C)
State	subsolidus	molten alloy
Temperature	2600 K - 3100 K	3800 K - 4700 K
Flow velocity	$O(10^{-4})$ km/a	$O(10^{1})$ km/a
Viscosity	$10^{21} - 10^{22}$ Pa s	$O(10^{-2} - 10^{3})$ Pa s
Density	5.57×10^3 kg/m^3	9.90×10^3
Rigidity	2.911×10^{11} Pa	$O(0?)$ Pa

Table 1.1: Core and mantle properties at the core-mantle boundary [modified from Lay, 1989].

observed at the Earth's surface [e.g., Hager et al., 1985; and Forte et al., 1992]. Coupling between such CMB topography and fluid core motions can ultimately cause fluctuations in the Earth's rotation [e.g., Hide et al., 1993].

Laboratory studies indicate that the CMB also serves as a zone of chemical reactions between the crystalline silicates of the lower mantle and iron alloy of the outermost core [Knittle and Jeanloz, 1986, 1989, 1991; Gourant et al., 1992; and Jeanloz, 1993]. Reaction products may produce orders of magnitude variations in resulting electrical conductivity [Jeanloz, 1990]. Metal-rich "dregs" can accrue on the mantle side of the CMB from these reactions, but how thick a layer can be dynamically stable in the environment of overlying mantle convection is not presently known.

The density contrast at the CMB (4.3 g/cc) is greater even than that at the

surface of the Earth. This makes it an essentially impermeable barrier to denser silicate material sinking through the mantle and light material exolving from the core. We therefore expect both sides of the CMB to collect the dregs of terrestrial differentiation just as the surface of the Earth is the repository for buoyant crustal material.

The base of the mantle, termed the D″ region by Bullen [1949], is expected to act as a thermal boundary layer between the mantle and hot outer core [e.g., Jeanloz and Richter, 1979; and Doornbos et al., 1986]. The steep thermal gradient between the mantle and core is thought to be directly related to the decrease in seismic velocity gradients 150-200 km above the CMB in globally averaged seismic Earth models. D″ also contains a first-order step increase in seismic properties between 130-350 km above the CMB [e.g., Lay and Helmberger, 1983a]. Whether this layer is a global feature is currently not resolved.

The thermal, chemical, and dynamical regimes above and below the CMB are quite different (Table 1.1), and can interact in complex processes. For example, Wysession et al. [1992, 1993] note that the fluid flow patterns in the outer core flow model of Voorhies [1986] correlate with a region of pronounced low seismic velocities at the base of the mantle beneath Indonesia. They note that slow D″ velocities overlay a vigorous rising core plume. Such core-mantle interactions have been discussed by many, and may be related to long-term behavior of Earth's geomagnetic field [e.g., Hide, 1967; Jones, 1977, Bloxham and Gubbins, 1987; Loper, 1991;, and Jault and Le Mouël, 1991a].

Investigating such phenomena is only possible through remote sensing methods, such as seismic, magnetic, gravitational, and even geochemical techniques. Much of our knowledge of the detailed structure of the deep Earth comes from seismological studies. Seismic phases sensitive to specific depth ranges have been used historically, in both forward and inverse approaches in order to provide regionally and

globally averaged vertical profiles of, for example, compressional and shear velocities, and density [for example, Jeffreys and Bullen, 1948; Dziewonski and Anderson, 1981; and Kennett and Engdahl, 1991]. In the past decade, using a variety of techniques and data, 3-D images of mantle heterogeneity have been provided through tomographic inversions of body waves, surface waves, and normal modes [see, for example, Dziewonski, 1984; Hager et al., 1985; Grand, 1987, 1994; Dziewonski and Woodhouse, 1987; Giardini et al., 1987; Tanimoto, 1990; Woodward and Masters, 1991; Li et al., 1991; and Su et al., 1992, 1994].

The minimum scale length of lower mantle resolution in the tomographic studies is usually $\geq$3000 km. One exception is the study of Grand [1994], which has lateral features with scale $\geq$ 500 km. Many areas of the globe are not resolved at all due to limitations in wavepath path coverage, and limited source-receiver geometries. Nonetheless, these studies provide information on long-wavelength variations in lower mantle properties, which can be compared to studies of mantle dynamics [e.g., Jordan et al., 1993].

To gain information on smaller lateral and vertical scale lengths, many studies of confined geographical and vertical regions have been conducted. Since the work in this thesis focuses on the seismic approach for investigating the deep Earth, past seismic studies of the lower mantle, outer core, and the CMB are discussed in the following three sections. This is followed by a section concerning some of the problems and uncertainties related to seismic studies of the Earth's deep interior, then finally the motivation, objective and overview of the thesis.

1.1.1 The D″ Region

The D″ region was originally defined by Bullen [1949] as the lowermost 200 km or so of the mantle, due to a lower gradient in seismic velocities than that of the overlying lower mantle, the D′ region according to Bullen's nomenclature. Since then, its

definition has expanded to include a 2-3% increase in seismic properties 130-350 km above the CMB. Hereafter, the term D″ refers to the bottom few hundred km of the mantle, with the exact thickness depending on the geographic region, since lateral variations in D″ properties are present.

Over the past decade, abundant evidence for a step discontinuity at the top of the D″ layer has been presented for both *S*-waves [Lay and Helmberger, 1983a; Zhang and Lay, 1984; Lay, 1986; Young and Lay, 1987a, 1990; Weber and Davis, 1990; Revenaugh and Jordan, 1991; Gaherty and Lay, 1992; Weber, 1993; Garnero et al., 1993a; and Kendall and Shearer, 1994] and *P*-waves [Wright and Lyons, 1981; Wright et al., 1985; Baumgardt, 1988; Davis and Weber, 1990; Weber and Davis, 1990; Weber, 1993; Houard and Nataf, 1992, 1993; and Vidale and Benz, 1993]. D″ layer thicknesses vary from region to region, and it is not yet clear whether or not this layer is a global feature [Nataf and Houard, 1993]. The different regions where D″ discontinuities have been proposed have been modeled with a range of D″ layer thicknesses, velocity increases across the discontinuity, sharpness of discontinuity, and velocity gradients above and below the discontinuity, suggesting strong lateral heterogeneity in going from region to region.

Even more studies than listed above present evidence for heterogeneity and lateral variations in the D″ region. Such studies, while not focusing on detecting a distinct D″ discontinuity, suggest lateral variations in the D″ region having a variety of scale lengths of the order of O(100-1000 km), as well as document that D″ heterogeneity is significantly stronger than the overlying lower mantle. Waves having near vertical incidence to the CMB, such as *ScS* and *PcP*, exhibit both travel time and amplitude variations, and are attributed to lowermost mantle heterogeneity [e.g., Mitchell and Helmberger, 1973; Chowdhury and Frasier, 1973; Sipkin and Jordan, 1976, 1980; Müller et al., 1977; Lay, 1983; Snoke and Sacks, 1986; Lavely et al., 1986; Schlittenhardt, 1986; Niazi and McLaughlin, 1987; Weber and Kornig, 1990, 1992;

Neuberg and Wahr, 1991; Woodward and Masters, 1991; Revenaugh and Jordan, 1991; Krüger et al., 1993; and Wysession et al., 1994].

Observations of waves that diffract around the Earth's core are sensitive to D″ velocities and velocity gradients [e.g., Phinney and Alexander, 1966, 1969; Alexander and Phinney, 1966; Bolt et al., 1970; Mondt, 1977; Doornbos and Mondt, 1979ab; Mula and Müller, 1980; Mula, 1981; Ruff and Helmberger, 1982; Bolt and Niazi, 1984; Garnero et al., 1988; Young and Lay, 1989; Wysession and Okal, 1988, 1989, 1992; and Garnero and Helmberger, 1993]. Both positive and negative D″ velocity gradients have been proposed in past studies, which has significant implications on the temperature profile at the base of the mantle.

It has been shown that small scale lower mantle heterogeneity of the order $< O(100$ km), particularly in the D″ region, can scatter seismic energy and complicate waveforms [Haddon and Cleary, 1972; Doornbos and Vlaar, 1973; Haddon and Buchbinder, 1986, 1987; and Menke, 1986ab]. Small scale scatterers, as well as roughness of the CMB interface and the surface of the D″ discontinuity, may be responsible for observations of PKP precursors, and is discussed in a later next section.

D″ is thought to be a region of high attenuation [e.g., Anderson and Hart, 1978; Mula, 1981; and Schlittenhardt, 1986]. Also, attenuation in D″ has been argued to be frequency dependent such that it is an increasing function of frequency [Alexander and Phinney, 1966]. More recently, however, a analysis of D″ using free oscillations found no strong decrease of Q [Kumagai et al., 1992]. More data is needed, however, to map out the details and any lateral variations in the Q structure in D″ . Complicated behavior of diffracted SV waves has been used to suggest anisotropy in D″ [Vinnik et al., 1989; and Lay and Young, 1991]. Better resolving this issue remains a task for future studies, and relates to chemistry and fabric flow in the region.

Indeed seismic studies present a wealth of information concerning details of D″

structure. However, the cause or evolution of local or global stratification of D$''$ is not known. There are many possible explanations, such as mantle differentiation early in Earth's history, a repository for deep subducting slabs, a lower mantle phase change, or a zone of reaction products from core-mantle chemical interactions.

1.1.2 The Outer Core

Seismic evidence for a core in the Earth was first presented by Oldham [1906], and the first accurate determination of the depth to the CMB, 2900 km, was provided by Gutenberg [1912]. Jeffreys [1926] pointed out that the outer core is a fluid. The outer core has extremely high Q, transmitting P waves with very low attenuation, and is generally thought to be homogeneous in composition [Stevenson, 1987].

Many different seismic phases have been used to investigate the P-wave velocity structure of the outer core. The seismic phases $SmKS$ (m=1,2,3, etc.) are most sensitive to the outermost core structure, while $PmKP$ (m=1,2,3, etc., up to 7), along with associated triplications, are sensitive to deeper outer core structure. Our focus will be the outermost core; for deeper core structure, see, for example, Masters and Shearer [1990] for a review of previous work [and more recently, Song and Helmberger, 1992]. Analyses of travel time and amplitude information from $SmKS$ phases have resulted in various outermost core structures [e.g., Gutenberg, 1938; Randall 1970; Hales and Roberts, 1970, 1971; Kind and Müller, 1977; Schweitzer and Müller, 1986; Lay and Young, 1990; Souriau and Poupinet, 1991; Tanaka and Hamaguchi, 1993a; and Garnero et al., 1993b]. These phases have been used in addition to normal modes information in core construction for various reference Earth models [e.g., Dziewonski and Anderson, 1981; Kennett and Engdahl, 1991; and Morelli and Dziewonski, 1993]. There is poor agreement in the outermost 300 km or so of the above core models.

Core waves typically exhibit much smaller scatter in travel time than do mantle

waves, suggesting small or nonexistent outer core lateral heterogeneity. There are, however, several studies suggesting the existence of outermost core heterogeneity [Souriau and Poupinet, 1990; Kohler and Tanimoto, 1992; and Tanaka and Hamaguchi, 1993b]. This issue is explored in detail in the latter part of this thesis, along with explanations for the wide range of variance between the different models.

There is some evidence for a reduction in the V_P gradient in the outermost 50-100 km of the core [Lay and Young, 1990; Tanaka and Hamaguchi, 1993a; and Garnero et al. 1993b]. Such a decrease in V_P values may relate to chemical or thermal stratification just beneath the CMB. However, more research in this area is necessary to access the resolution of these structures [Garnero and Helmberger, 1994].

1.1.3 The CMB

The nature of the interface between the mantle and the core has been a subject of great interest the Earth scientists. Related topics, such as the sharpness of the transition, possible layering between the mantle and core, CMB bumps, degree of smoothness, and mechanisms of heat transfer across the boundary, all have impact on our understanding of the composition and evolution of the Earth.

Since the CMB is a chemical boundary (silicate/metal) as well as a phase boundary (solid/melt), we expect it to be sharp. Also, we expect the boundary to be relatively smooth because of the large density contrast. In fact, it has been proposed that the transition region from the mantle and core is sharp, less than 10 km (from Sacks [1966], using P and P_{diff} waves), and less than 1 km (from Kanamori [1967], using P and PcP waves; and Vidale and Benz [1992], using P, PcP, and ScP waves).

PKP waves are know to have precursors [e.g., Haddon and Cleary, 1972; Doornbos and Husebye, 1972; and Doornbos and Vlaar, 1973]. These precursors have been attributed to PKP wave scattering in the lowermost mantle and also roughness of

the CMB [e.g., Doornbos, 1978; Bataille and Flatte, 1988; and Rekdal and Doornbos, 1992]. Other core phases with the same D'' wavepath geometry, such as $PKKP$, SKP, and $SKKP$, also have precursors due to the same phenomena [Doornbos, 1974]. Chang and Cleary [1978, 1981] interpret $PKKP$ precursors as occurring at the underside reflection point at the CMB, caused by topographic irregularities on the boundary itself. As pointed out by, for example, Doornbos [1978] and Bataille et al. [1990], in many cases there is a trade off between lower mantle heterogeneity and a rough CMB as a cause of the precursors. It is also possible that such precursors may be related to roughness and heterogeneities at the top of a discontinuous D'' layer, though this has not been explored since most studies on this subject occurred before the discovery of a distinct D'' layer by Lay and Helmberger [1983a].

In a convecting mantle, the CMB is expected to have topography, with CMB highs under mantle upwellings and CMB depressions under colder downwelling portions of the mantle. Several maps of CMB topography have been produced [Hide and Horai, 1968; Gudmundsson et al., 1986; Morelli and Dziewonski, 1987; Doornbos and Hilton, 1989; and Morelli, 1993], though lack of agreement between amplitude and placement of CMB bumps exists between these models. The seismically derived maps use travel time picks from the International Seismic Centre (ISC) catalog, giving long wavelength topography ranging from ± 3 km to ± 7 km, depending on the model. Some uncertainties and problems with methods and data used to obtain CMB topography have been recently discussed [e.g., Gudmundsson, 1989; Pullium and Stark, 1993; Stark and Hengartner, 1993; and Rodgers and Wahr, 1993]. Azimuthal variations of $PKP(AB) - PKIKP$ differential times have been used to suggest that models with larger scale topography (± 7 km) are incompatible with waveform observations [Poupinet et al., 1993]. More research is required in this area to reconcile the varied CMB maps.

1.2 Some Problems and Uncertainties in Seismic Studies of the CMB Region

Many issues in seismic studies of the Earth's deep interior remain unresolved. The seismological behavior of the D″ layer has been presented for localized regions, but important questions remain unanswered, such as: Is the D″ discontinuity a global feature? Is the top of the layer sharp? Does it represent a chemical or phase change from overlying mantle properties? If a distinct D″ layer can be shown to be an intermittent feature, then how does the pattern of regional D″ layer patches relate to overall mantle dynamics? Evidence for two separate step increases in V_S (150 and 300 km above the CMB) was presented by Gaherty and Lay [1992]. If such a feature is resolved, how wide-spread is it? And how might anisotropy in the D″ region affect the above issues?

Better resolution in tomographically derived images of mantle heterogeneity plays an important role as well. With better resolved 3-D mantle heterogeneity images, and more detailed and resolved D″ structure maps, a correlation between D″ stratification thickness (and existence), velocity gradient, and lower mantle heterogeneity can be pursued with greater confidence. Variations in D″ structure and lower mantle heterogeneity can be related to core-mantle interactions and overall mantle dynamics only if such an increase in resolution is obtained. Improved CMB topography maps will facilitate integrating structural, thermal, and dynamical behavior of the lower mantle, D″ , the CMB, and the outermost core in a coherent picture of the core-mantle system applicable and relevant to the Earth.

Many factors can complicate seismic determination of D″ structure. Small and large scale heterogeneity can scatter seismic energy, producing spurious arrivals that interfere with the S, Scd, and ScS phases used to determine D″ discontinuity structure [Haddon and Buchbinder, 1987], and similarly with P-waves. Large and small

scale topography at the top of the D″ layer, along with smearing the depth interval over which the D″ velocity increase occurs, can obscure the *Scd* arrival. In fact, some regions for which a discontinuity structure has been derived exhibit intermittently present *Scd* arrivals [e.g., Young and Lay, 1990; and Gaherty and Lay, 1992]. Such intermittency argues for either small scale lower mantle (and D″) heterogeneity and/or small scale undulations in the surface of the D″ layer.

As pointed out by Cormier [1985], other complicating factors exist. D″ anisotropy, heterogeneity, and strong lateral velocity gradients can complicate *S* and *ScS* waveforms. Also, if slab structure extends into the lower mantle, as suggested by Creager and Jordan [1986], then waveform broadening and distortions can occur [Vidale, 1987; and Cormier, 1985] which can obscure *Scd* arrivals.

Schlittenhardt et al. [1985] argued against the existence of a discontinuity at the top of D″ based on comparison of observed and predicted waveforms in the distance range 90°-115°. At such distances, the discontinuity model tested by Schlittenhardt et al. [1985] (model SLHO of Lay and Helmberger, 1983a) predicts waveform complexities at these larger distances, which are not clearly seen in the data. In a subsequent effort, Young and Lay [1990] reduced the positive V_S gradient in D″ of SLHO to become slightly negative. This modification in turn diminished the predicted waveform complications used by Schlittenhardt et al. [1985] to argue against a D″ discontinuity, and suggests the difficulty in using the above distance range to preclude discontinuity structures. This example is discussed to illustrate how different model features have varied implications depending on the seismic phase and distance range, and can ultimately result in structural trade-offs.

A presently unresolved issue in seismic studies of the lower mantle is the degree to which *P*- and *S*-wave structures correlate. Wysession et al. [1992] analyzed long-period diffracted *P*- and *S*-waves, and conclude that V_P and V_S structures do not vary in parallel, resulting in variations in Poisson's ratio of up to 6%. While

the degree of horizontal averaging in D" is not well understood in such diffraction studies, the result emphasizes the need to pursue more detailed images of both V_P and V_S behavior in the lower mantle. In another example, Vidale and Benz [1993] present evidence for a 130 km thick P-wave D'' discontinuity for a region beneath Alaska using short-period array data. Young and Lay [1990] analyze the same region for V_S structure, and resolve a 243 km thick D'' layer using long-period shear wave data. It is indeed a challenge to interpret over 110 km difference in V_P and V_S D'' discontinuity depths. Better understanding uncertainties and assumptions in these studies, along with inclusion of broadband data for the study area, may help in this regard.

There has been recent evidence for the predominance of long-wavelength heterogeneity in the mantle [Su and Dziewonski, 1991]. They argue that heterogeneity occurs mainly on length scales greater than about 6000 km. This statement has been supported by observations of long-period $ScS - S$ times [Woodward and Masters, 1991]. Nevertheless, evidence for the importance of heterogeneity at smaller scales of order $O(100$ km) contributing to observed travel time and waveform perturbations is prevalant in the literature [e.g., Mitchell and Helmberger, 1973; Müller et al., 1977; Lay, 1983; Schlittenhardt, 1986; Lavely et al. 1986; Garnero et al., 1988; Weber and Davis, 1990; Weber and Kornig, 1990; Gaherty and Lay, 1992; Weber, 1993; Bokelmann and Silver, 1993; Krüger et al., 1993; Grand, 1994; and Wysession et al., 1994]. More data elucidating this issue is important, as it may relate to patterns of mantle convection.

The velocity gradient at the base of the mantle, within a distinctly stratified D'' layer, or at the base of the mantle in absence of a distinct D'' layer, may relate to the nature of the thermal boundary layer, and thus the temperature drop across the CMB. Estimates of dV_P/dz and dV_S/dz have typically come from older studies that averaged data from regions with widely varying velocities, and thus may be contam-

inated by path effects. Also, many studies were conducted before knowledge of a velocity increase at the top of D'' was discovered, and therefore may not be applicable. There is presently abundant evidence for both positive and negative velocity gradients at the base of the mantle [for a review, see Young and Lay, 1987b]. If lateral variations in dV/dz are resolvable, then their relationship to lower mantle heterogeneity, dynamics and thermal structure can be pursued. Future studies will need to access trade-off between velocity gradient and heterogeneity, while incorporating D'' discontinuity structure, if present.

Studies of the structure of the outer core use seismic waves that traverse the lower mantle before penetrating the core. Lower mantle heterogeneity can perturb these waves to yield biased core models, if not properly accounted for. Therefore great care must be taken when constructing a core model. The above uncertainties are discussed to emphasize the need for a continued effort in documenting the detailed behavior of seismic data sensitive to deep Earth structure.

1.3 Overview of the Thesis

1.3.1 Motivation

CMB research is highly multidisciplinary. Advances in the separate disciplines will pave the way for more comprehensive and accurate descriptions of the core-mantle system. As the previous section discussed, many uncertainties, problems, and ambiguities relating to seismic studies of the CMB region exist. The work in this thesis has been motivated by the need to provide additional information concerning seismic velocities and trends in their variations, lateral and vertical, in order to increase our understanding and resolution of deep Earth structure. We are also motivated by the need to bridge the gap between long-wavelength tomographic studies and smaller wavelength detailed regional studies. Many seismic phases exist that can

provide additional detailed information on the nature of deep mantle heterogeneity, and outer core structure. To make progress towards integrating seismically resolved structures and studies of the thermal, chemical and dynamic behavior or the deep earth, particularly the core-mantle system, documenting detailed behavior of seismic phases sensitive to the region is necessary.

1.3.2 Objective

The objective of this work is to provide detailed measurements and subsequent analysis on seismic data sets sensitive to deep Earth structure. Particular emphasis is on seismic phases that have not been utilized for documenting mantle heterogeneity, as well as phases previously used, but using data from new regions of study. It is the goal of this work to: provide information on the scale lengths of heterogeneity prevalent in the lower mantle, present data supporting large lateral variations in V_S discontinuity thickness, show evidence for a low-velocity zone for P-waves at the base of the mantle, and provide a detailed analysis of outermost core structure along with resolution issues. It is also an objective to present evidence for the potential improvement in future tomographic studies if some of the seismic phases presented here, particularly core phases, are utilized.

1.3.3 Outline

The body of the thesis that follows has been divided up into six chapters. Each of the subsequent chapters has been individually published, or submitted for publication. Each chapter is thus self contained, with its own abstract, introduction, and conclusion. This has resulted in some overlap in material in some of the introduction sections. For reference, Chapter 2 was published as "Lateral variations near the core-mantle boundary," in *Geophys. Res. Lett.*, **15**, 609-612, 1988. More recent broadband data and analysis from "Detailed imaging of laterally varying lower man-

tle structure," *Eos Trans. AGU*, **74**, no. 43, 557, 1993, has also been included in Chapter 2. Chapter 3 embodies "Travel times of S and SKS: Implications for 3-D lower mantle structure," *J. Geophys. Res.*, **98**, 8225-8241, 1993. Chapter 4 contains the work of "Preliminary evidence for a lower mantle shear wave velocity discontinuity beneath the central Pacific," *Phys. Earth Planet. Inter.*, **79**, 335-347, 1993, and also recent findings from "Detailed imaging of laterally varying lower mantle structure," *Eos Trans. AGU*, **74**, no. 43, 557, 1993. Chapter 5 can be found as "Low P-velocity at the base of the mantle," *Geophys. Res. Lett.*, **20**, 1843-1846, 1993, and contains a few additional figures from "Anomalously low P-wave velocity at the base of D$''$ ", *Eos Trans. AGU*, **74**, no. 16, 50, 1993. Chapter 6 is taken from "Constraining outermost core velocity with $SmKS$ waves," *Geophys. Res. Lett.*, **20**, 2463-2466, 1993. Chapter 7 has been submitted for publication to *Phys. Earth Planet. Inter.*, and is presently in review. Additional analysis and figures from "Constraining D$''$ and outermost core structure using $SmKS$ (m=2,3,4) waves," *Eos Trans. AGU*, **74**, no. 43, 415-416, 1993, has been added to Chapters 6 and 7.

Chapter 2

Lateral Variations in Lower Mantle V_S Structure

2.1 Abstract

Differential travel times between S and SKS (T_{S-SKS}) are ideal for mapping out lateral variations in lower mantle structure. Differential times between $SKKS$ and SKS ($T_{SKKS-SKS}$) along with their amplitude ratios are also sensitive to lower mantle variations. These seismic phases have been used to study lateral variations in lower mantle S-wave (V_S) structure beneath the mid-Pacific region. Analog and digital data are utilized to document variations in lower mantle properties. The lowermost mantle beneath the Pacific exhibits both large and small scale structures on the order of 1000 km and 100 km, respectively (hereafter denoted as O(1000 km) and O(100 km)), with a noted large scale slower than average feature. A region traversed by SKS and S from Fiji-Tonga sources recorded by North American stations shows the most anomalous behavior in T_{S-SKS} times in that SKS and S are separated by up to 8 sec greater than 1-D reference model predictions. In addition to the T_{S-SKS} anomalies, SKS and $SKKS$ are anomalously separated by 2 to 3 sec greater than

predicted values for this source region and azimuth [Schweitzer and Müller, 1986]. Modeling these anomalous observations requires preferentially slowing down S and $SKKS$ relative to SKS, or speeding up SKS relative to S and $SKKS$. Our preferred explanation is lateral variations in D'' V_S velocities of up to 3% or greater. 2-D wave propagation experiments show the data are consistent with a model having normal D'' velocities where SKS enters and exits the core, which reduce to up to 3% slower than average in the D'' region beneath the central Pacific near wavepath mid-points. Other models that can explain the data are discussed, such as a laterally varying core with P-wave velocities up to 3% greater than the PREM model [Dziewonski and Anderson, 1981], but are argued to be unlikely scenarios.

2.2 Introduction and Data Set

Understanding the core-mantle boundary (CMB) region is of fundamental importance to Earth sciences because of its impact on many other geophysical disciplines. Seismic studies effectively provide an indirect probe of this region. As mentioned in Chapter 1, past studies have used the seismic phases S, ScS (core-reflected S-wave), and S-waves diffracted around the Earth's core (S_{diff}) to study S-wave velocity structure (V_S) in the lowermost mantle, and the core phases SKS and $SKKS$ have been used to study V_P in the outer core. SKS travels through the mantle as an S-wave, converting to a P-wave in the core, and converts back to an S-wave for the final mantle leg. $SKKS$ is similar to SKS, with the addition of a CMB underside reflection. This study attempts to tie together information from S, S_{diff}, SKS, and $SKKS$, to forward model a region beneath the mid-Pacific exhibiting anomalous amplitude and differential travel time behavior for S, SKS and $SKKS$. The geometric ray paths for these phases are shown in Figure 2.1. In what follows, the symbol S may represent both S and S_{diff}.

Analog data from various archives, along with modern digital broadband data have been studied. Long- and short-period paper analog records from the World Wide Seismographic Station Network (WWSSN), the Canadian Seismic Network (CSN), and short-period Long Range Seismic Monitoring (LRSM) stations were utilized. Broadband digital recordings from the California Institute of Technology Terrascope array and the University of California at Berkeley UCBnet array were also studied. Deep focus earthquakes from the southwest and northwest Pacific, and South America have been used and are listed in Table 2.1. Most of the analog data have been digitized and rotated into radial and transverse components of motion. An example showing quality of analog data before and after digitization is presented in Figure 2.2. All data used in this study have very good signal-to-noise ratios (SNR) as that in Figure 2.2.

2.3 Travel Times and Waveform Observations

Differential travel times between SKS and S (T_{S-SKS}) were measured from the data by differencing the onset times of the S and SKS waveforms. The advantage of using differential times is that effects of source mislocation and unknown upper mantle structure are minimized, since SKS and S paths are close in the upper mantle (Figure 2.1) and assumed to be affected similarly by such unknowns. Epicentral distances used for T_{S-SKS} measurements were from the $S-SKS$ crossover distance (beyond 82^o) out to near 100^o. T_{S-SKS} residuals (observed T_{S-SKS} minus predicted T_{S-SKS}, denoted δT_{S-SKS}) with respect to predictions from 1-D reference models of the Earth, such as the Jeffrey-Bullens (JB) tables [Jeffreys and Bullens, 1948], PREM [Dziewonski and Anderson, 1981], and *iasp91* [Kennett and Engdahl, 1991], are found to vary systematically for the lower mantle beneath the Pacific. For a region beneath the central Pacific, SKS and S are anomalously separated by up to 8

Date	Latitude	Longitude	Depth (km)	M_b	Region	Source
08/25/63	17.50S	178.80E	565	6.1	Fiji-Tonga	ISC
10/09/67	21.10S	179.18W	633	6.2	Fiji-Tonga	ISC
02/10/69	22.70S	178.61E	673	6.9	Fiji-Tonga	ISC
04/28/81	23.72S	179.98E	540	6.0	Fiji	ISC
08/05/64	32.22S	179.80W	210	5.7	Kermadec Is.	ISC
08/07/93	26.80N	125.60E	160	6.0	NE of Taiwan	NEIS
01/18/93	18.40N	145.90E	170	5.9	Marianas Is.	NEIS
08/23/68	21.95S	63.64W	513	5.6	S. Bolivia	ISC
10/25/73	21.96S	63.65W	517	6.1	S. Bolivia	ISC
04/01/81	27.31S	63.32W	554	5.9	Argentina	ISC
06/08/93	31.70S	68.90W	110	6.5	Argentina	NEIS

Table 2.1: Source parameters for events in this study.

Figure 2.1: Cross-section of the Earth showing geometric raypaths for S, SKS, and $SKKS$, for 95° epicentral distance and a 500 km source depth. A 300 km thick zone at the base of the mantle is denoted a D″ and dotted.

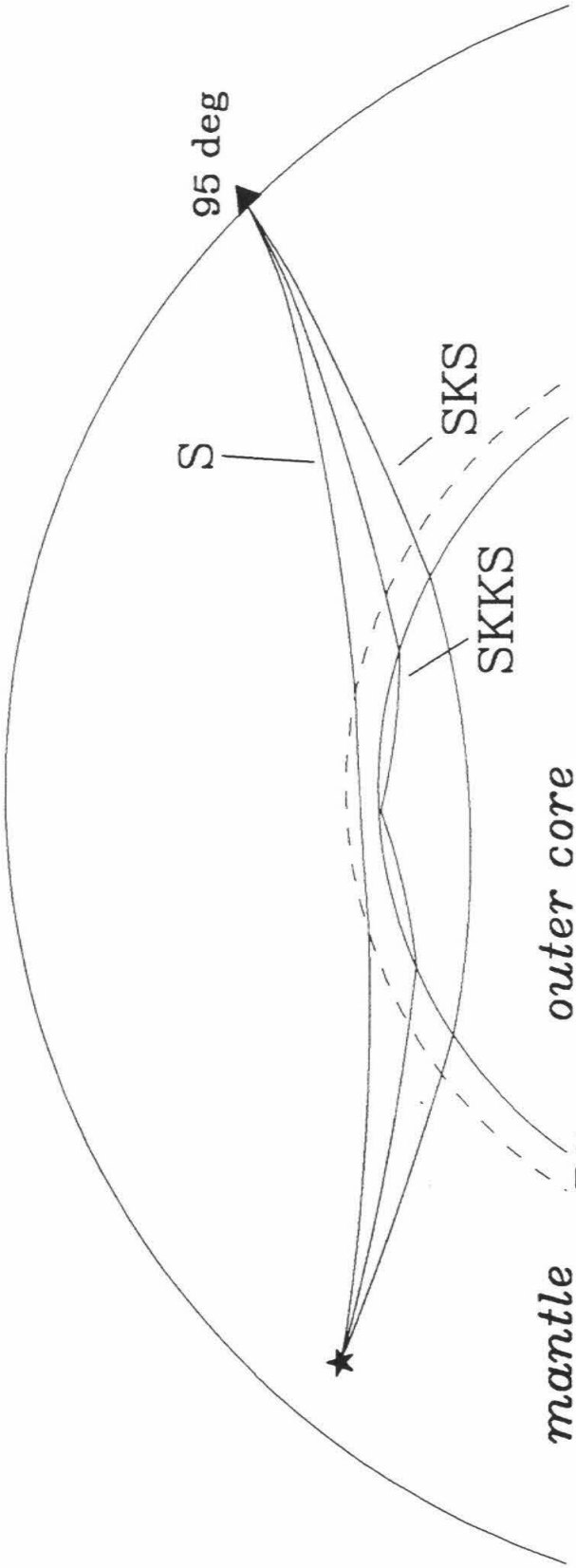
95 deg
S
SKS
SKKS
mantle
D''
outer core

Figure 2.2: A long-period WWSSN seismogram before (left) and after (right) digitization. The digitized record accurately reproduces the original.

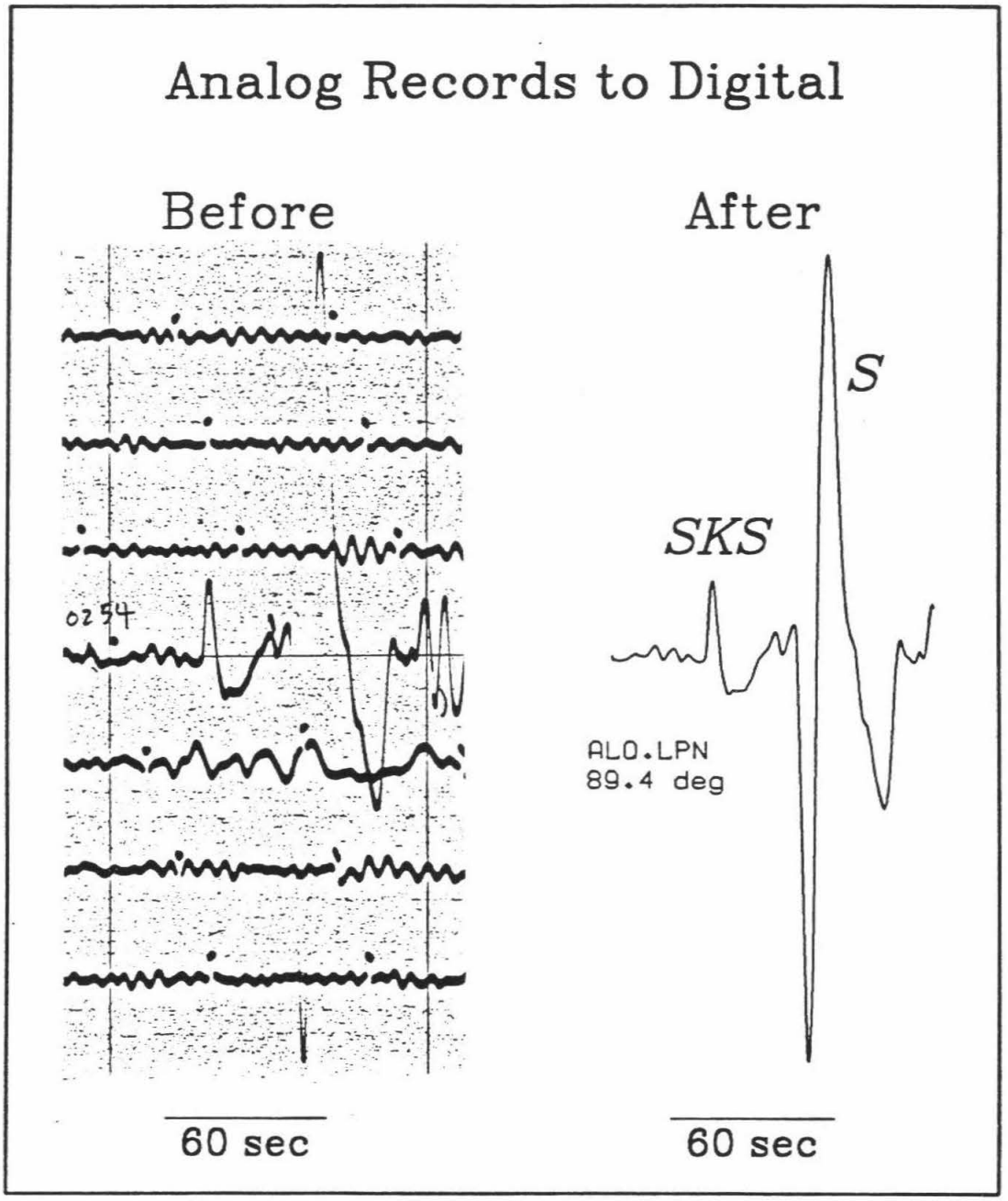
Analog Records to Digital
Before
After
0254
S
SKS
ALO.LPN
89.4 deg
60 sec
60 sec

sec and display a systematic azimuthal trend between Fiji-Tonga sources and North American receivers. These times are studied in what follows.

Figure 2.3 and Figure 2.4 present radial component profiles of SKS and S data, and surface projections of their great circle paths, respectively. The three panels in Figure 2.3 correspond to three different events and data types, all recorded in North America. SKS phases have been lined up and maximum amplitudes of the traces are normalized to unity. When the traces are plotted absolutely in time, there is scatter in arrival times of up to 10 sec that is due to source, receiver, and path differences for the different path geometries. This scatter prevents a confident estimate of the apparent velocity at the base of the mantle from $\frac{dT}{d\Delta}$ measurements. Since SKS and S paths for a given source-receiver pair are close to each other, except in the lowermost mantle where the SKS goes into the core and the S passes through the bottom of the mantle, the differential travel time can be interpreted as being mostly dependent on V_S in D'' and V_P in the outer core for the distance range used in this study. The dotted lines in Figure 2.3 represent predictions from the *iasp91* model for SKS and S for the appropriate source depth of each event. The left, center, and right panels contain long-period WWSSN, short-period LRSM, and broadband Terrascope plus UCBnet data, respectively. For all three data types, SKS and S exhibit good SNR and easy to measure $S - SKS$ times. A striking feature in Figure 2.3 is the size and variations of T_{S-SKS} anomalies for the different paths. For example, the Fiji event profile (left panel) exhibits 2 to 7 sec anomalies in S delays with respect to SKS; the Kermadec event profile (center panel) displays 5 to 9 sec anomalies; and the northeast of Taiwan event (right panel) has $S - SKS$ times well predicted by *iasp91*, except beyond 93°, where S arrives earlier than *iasp91* predictions.

The data of Figure 2.3 exhibit large anomalies associated with the different source-receiver geometries. In addition to the first-order feature of anomalously large $S - SKS$ times for paths traversing the central Pacific lower mantle, smaller scale

Figure 2.3: Radial component recordings of SKS and S for deep focus events. Shown are long-period WWSSN recordings of a Fiji event (left panel), short-period LRSM recordings of a Kermadec Islands event (center panel), and broadband Terrascope and UCBnet recordings of an event northeast of Taiwan. SKS phases have been lined up in time, and maximum amplitude of traces have been normalized to unity. Dashed lines correspond to predictions from the *iasp91* model. The different regions display different $S - SKS$ differential time behavior.

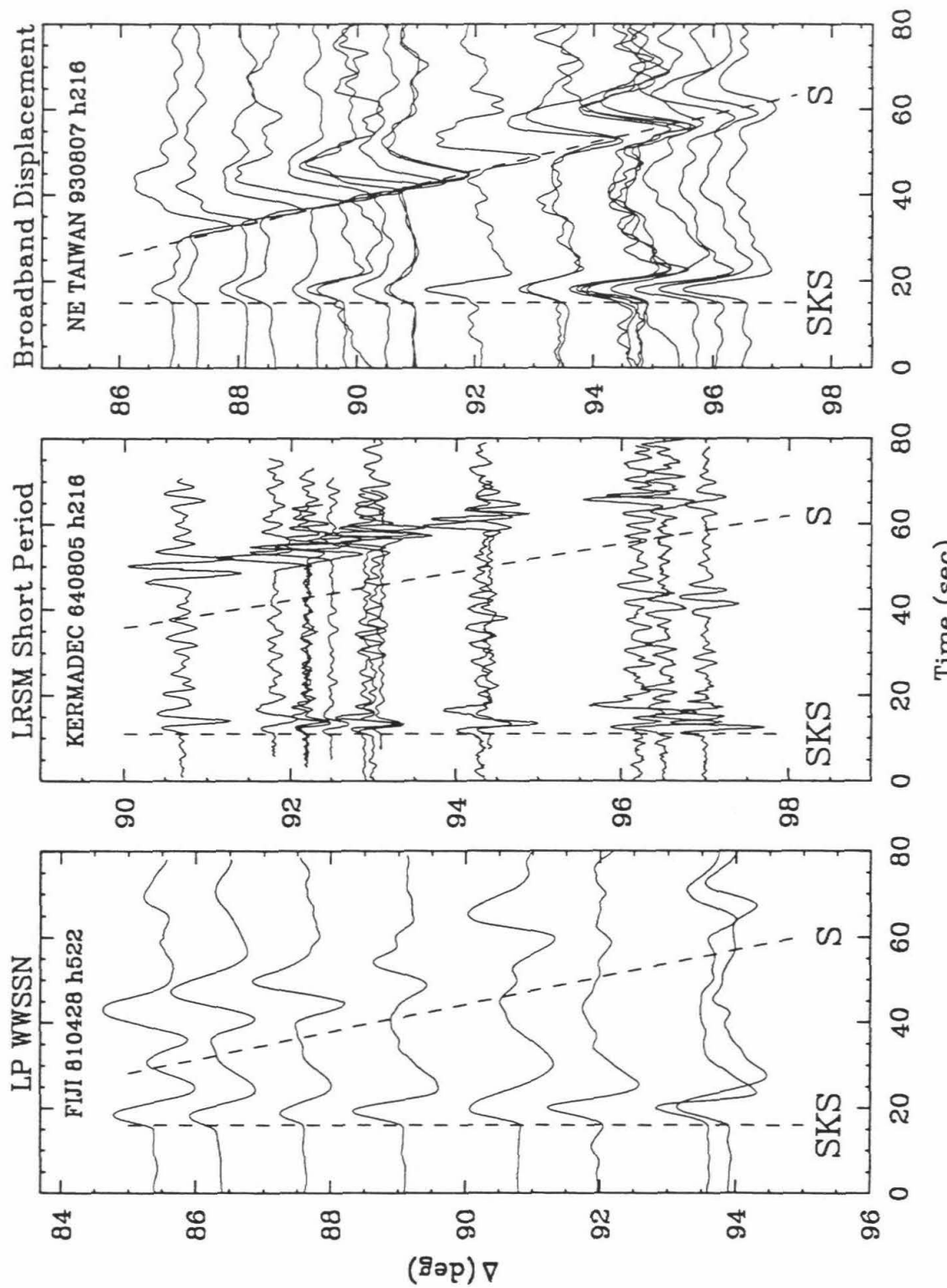
LP WWSN
FIJI 810428 h522
LRSM Short Period
KERMADEC 640805 h216
Broadband Displacement
NE TAIWAN 930807 h216
SKS
S
Δ (deg)
Time (sec)

Figure 2.4: Surface projections of wavepaths between sources (stars) and receivers (triangles) for the three events of Figure 2.3.

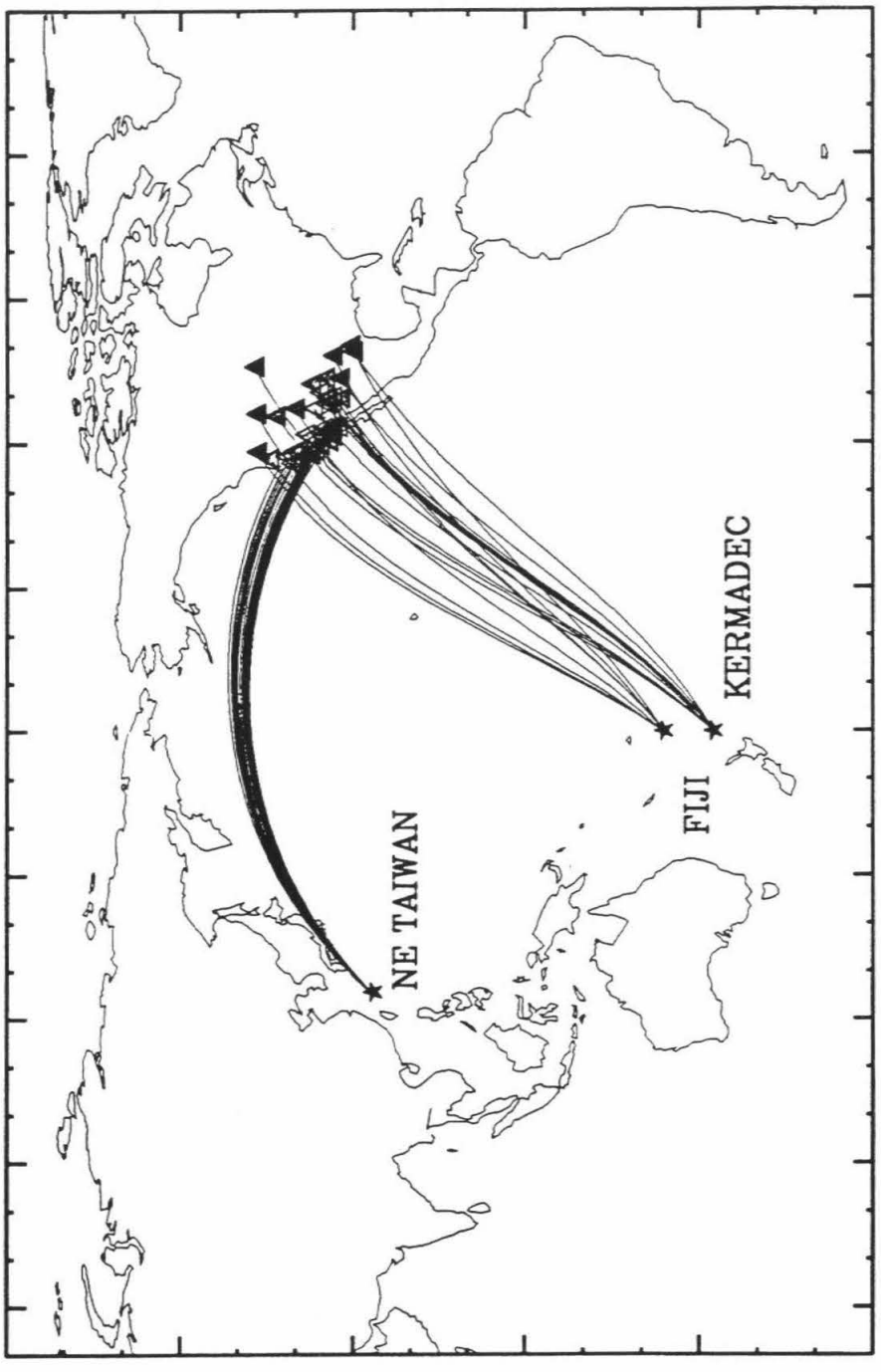
NE TAIWAN
FIJI
KERMADEC

variations within each of the profiles are present. These variations for the central Pacific region are further explored below. δT_{S-SKS} residual times for the 4 Fiji-Tonga events of Table 2.1 are plotted at the surface projection of wavepath mid-points in Figure 2.5. There is an azimuthal trend in the residuals plotted such that δT_{S-SKS} increases to the southeast beneath the Hawaiian volcanic chain. The scale length of the sampled mid-Pacific core-mantle boundary patch is about 2700 km in width (from northwest to southeast.) The size of the residuals vary from around 1 to 8 sec. The size of the residuals do not change significantly with the use of different reference models, and in particular, the azimuthal trend is a robust feature independent of reference model. How these times compare to predictions from 3-D mantle models is discussed in Garnero and Helmberger [1993]. They conclude a qualitative agreement between the azimuthal trend of the $S-SKS$ observations and 3-D model predictions, though the size of the observed anomalies are underpredicted by the aspherical structures.

A similar map for South American events of Table 2.1 is shown in Figure 2.6. In contrast to the central Pacific region, the lower mantle beneath Central America produces δT_{S-SKS} residuals less than zero. This region has previously been noted having faster than average lower mantle velocities by, for example, Grand [1987]. Bokelmann and Silver [1993] also present evidence for a fast anomaly beneath the Caribbean, suggesting short-wavelength variations in the structure. The negative residuals in Figure 2.6 are compatible with this, since faster than average lower mantle V_S structure will speed up S more than SKS, thus decreasing δT_{S-SKS} times. The lower mantle beneath the Caribbean has also been depicted as having a first-order discontinuous 2.7% increase in V_S nearly 300 km above the CMB [Lay and Helmberger, 1983a]. This model (SLHA) resulted from detailed waveform and travel time analysis of S phases and associated triplications. Model SLHA nicely predicts the $S-SKS$ behavior for the Argentina source region. Figure 2.7 (a) shows

Figure 2.5: δT_{S-SKS} residuals plotted at turning points of S and SKS projected to the surface for Fiji-Tonga events (open triangles) of Table 2.1. Each point represents a residual from one source-receiver pair. Solid triangles, squares, and circles correspond to different events.

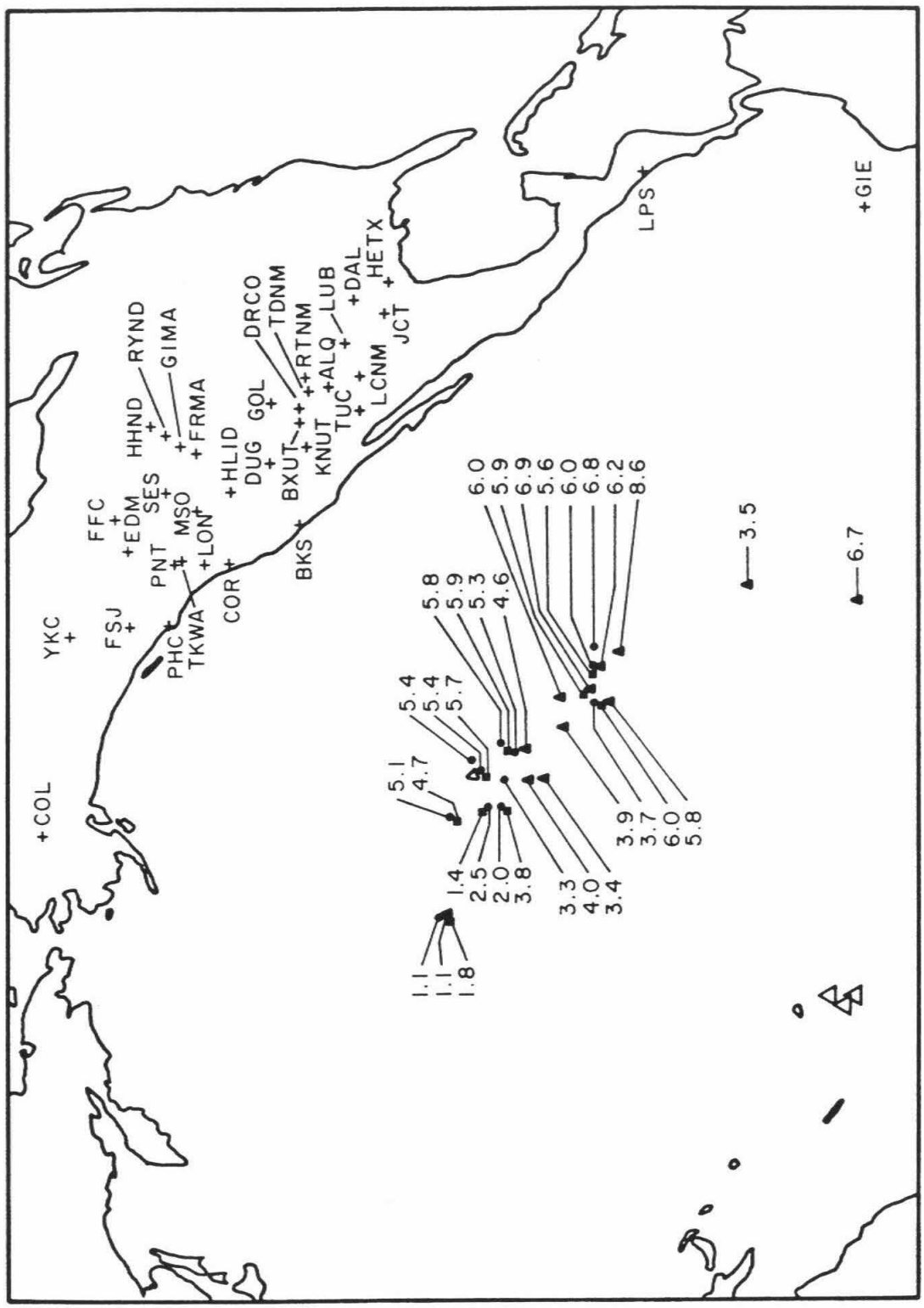
+COL
YKC
FSJ
PHC
TKWA
PNT
+EDM
FFC
SES
MSO
+LON
COR
+HLID
HHND
RYND
GIMA
+FRMA
DUG
GOL
DRCO
TDNM
BXUT
+RTNM
KNUT
+ALQ
LUB
TUC
+DAL
LCNM
JCT
HETX
BKS
LPS
+GIE
1.1
1.1
1.8
1.4
2.5
2.0
3.8
5.1
4.7
5.4
5.4
5.7
5.8
5.9
5.3
4.6
3.3
4.0
3.4
6.0
5.9
6.9
5.6
6.0
6.8
6.2
8.6
3.9
3.7
6.0
5.8
3.5
6.7

a sample Argentina event long-period WWSSN seismogram and the corresponding SLHA synthetic generated by the Cagniard de Hoop technique [Helmberger, 1983] as filtered by a long period WWSSN instrument. Figure 2.7 (b) illustrates that SLHA does poorly in modeling the Fiji event shown in Figure 2.3; the $S - SKS$ time separation in the record shown (station TUC) is 6 sec larger than that of the synthetic. This anomaly is further illustrated by comparing the South American data directly to the Fiji-Tonga data, as seen in Figure 2.7 (c). To match $S - SKS$ separations of the two data sets, one must pick seismograms from the South American data set with Δ up to 2 degrees larger than that of the Fiji-Tonga data. Both events used in Figure 2.7 are deep focus, differing only by 14 km in source depth (as reported by the ISC catalogues.) Note that a 50 km difference in source depth for a given Δ will only produce about a half second difference in δT_{S-SKS}.

As apparent in Figure 2.7, differences in T_{S-SKS} times for different regions are easily seen when comparing data directly to data. Figure 2.8 displays some broadband data on data comparisons for $S - SKS$ waveforms and Figure 2.9 presents a map showing wavepath geometries. The top panel of Figure 2.8 displays broadband data for events in Argentina and Marianas. The peaks of the SKS arrivals have been lined up in time, and the records display comparable $S - SKS$ times. The lower panel, however, demonstrates that the Argentina event (and thus the Marianas event) have T_{S-SKS} times less than that of the NE Taiwan event of Figure 2.3. All records in Figure 2.8 were plotted at distances such that event source depths are normalized.

δT_{S-SKS} times for wavepaths beneath different regions of the Pacific have been presented. These times vary over both large and small scales. Paths from the southwest Pacific to North America display large δT_{S-SKS} residuals (up to 9 sec), those from South America and Marianas to North America are small (around -2 sec), and those from NE of Taiwan to North America are average (near zero). In sweeping

Figure 2.6: δT_{S-SKS} residuals plotted at turning points of S and SKS projected to the surface for three South American events (crosses) of Table 2.1. Each point represents a residual from one source-receiver pair. Solid triangles, squares, and circles correspond to different events.

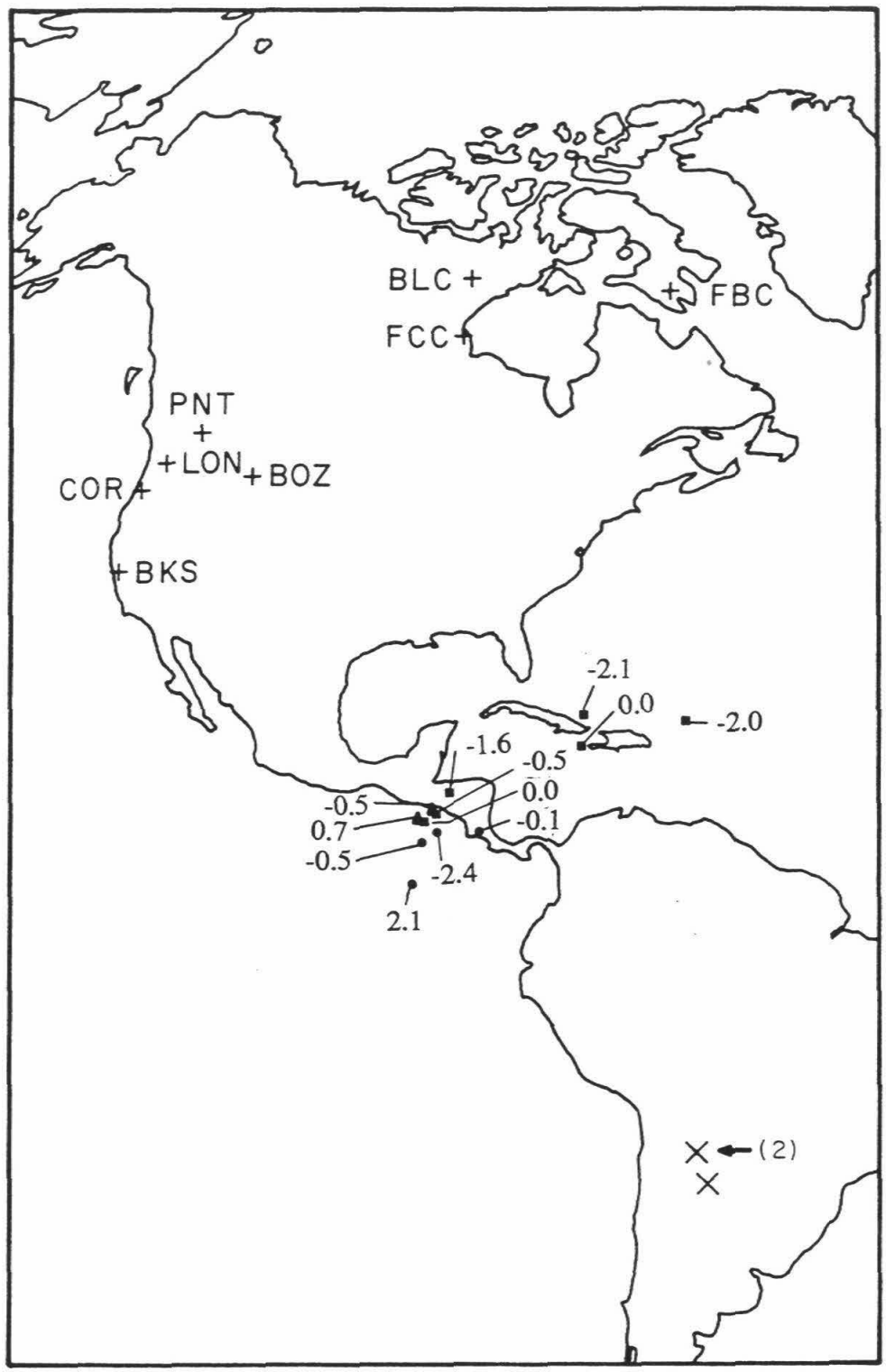
BLC
FBC
FCC
PNT
LON
BOZ
COR
BKS
-2.1
0.0
-2.0
-1.6
-0.5
0.0
-0.5
-0.1
0.7
-0.5
-2.4
2.1
(2)

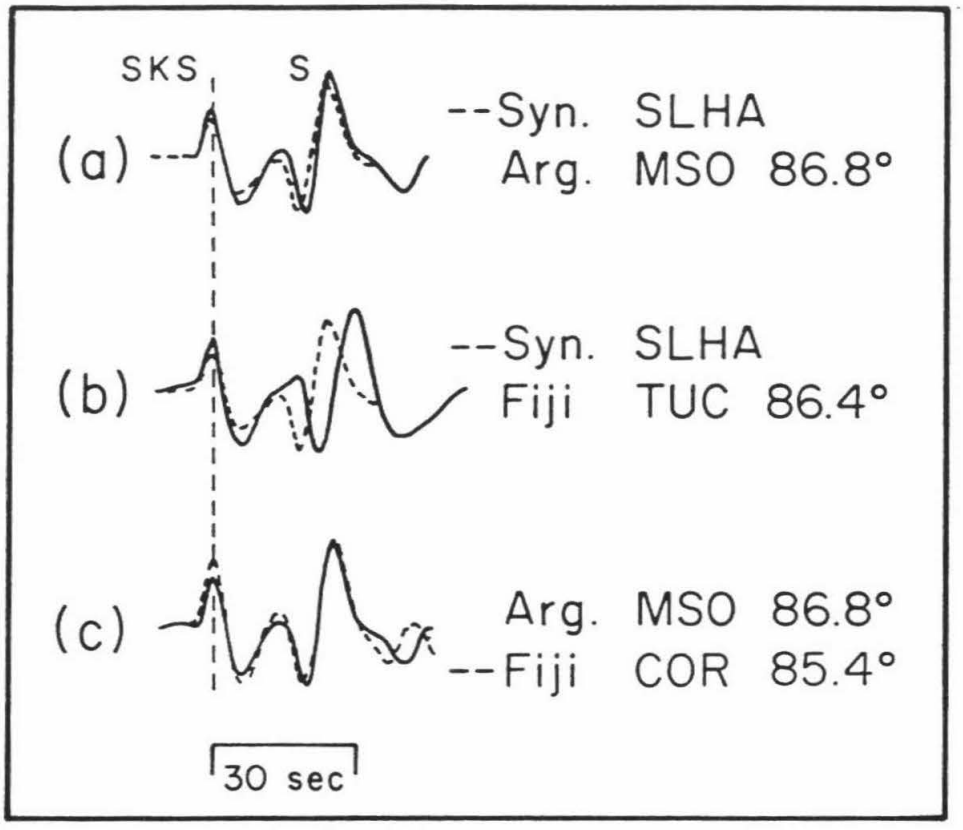

Figure 2.7: Long-period WWSSN radial component seismogram comparisons: (a) a recording of an Argentina event compared to an SLHA synthetic; (b) a Fiji event record and SLHA synthetic; (c) records from the Fiji and Argentina events.

Figure 2.8: Distance profiles of $S - SKS$ for broadband radial component displacement seismograms of and Argentina and Marianas event (top panel), and the same Argentina event and an event northeast of Taiwan. The peaks of SKS are aligned to demonstrate differences in T_{S-SKS} times. Thin solid lines denote approximate SKS and S arrival times.

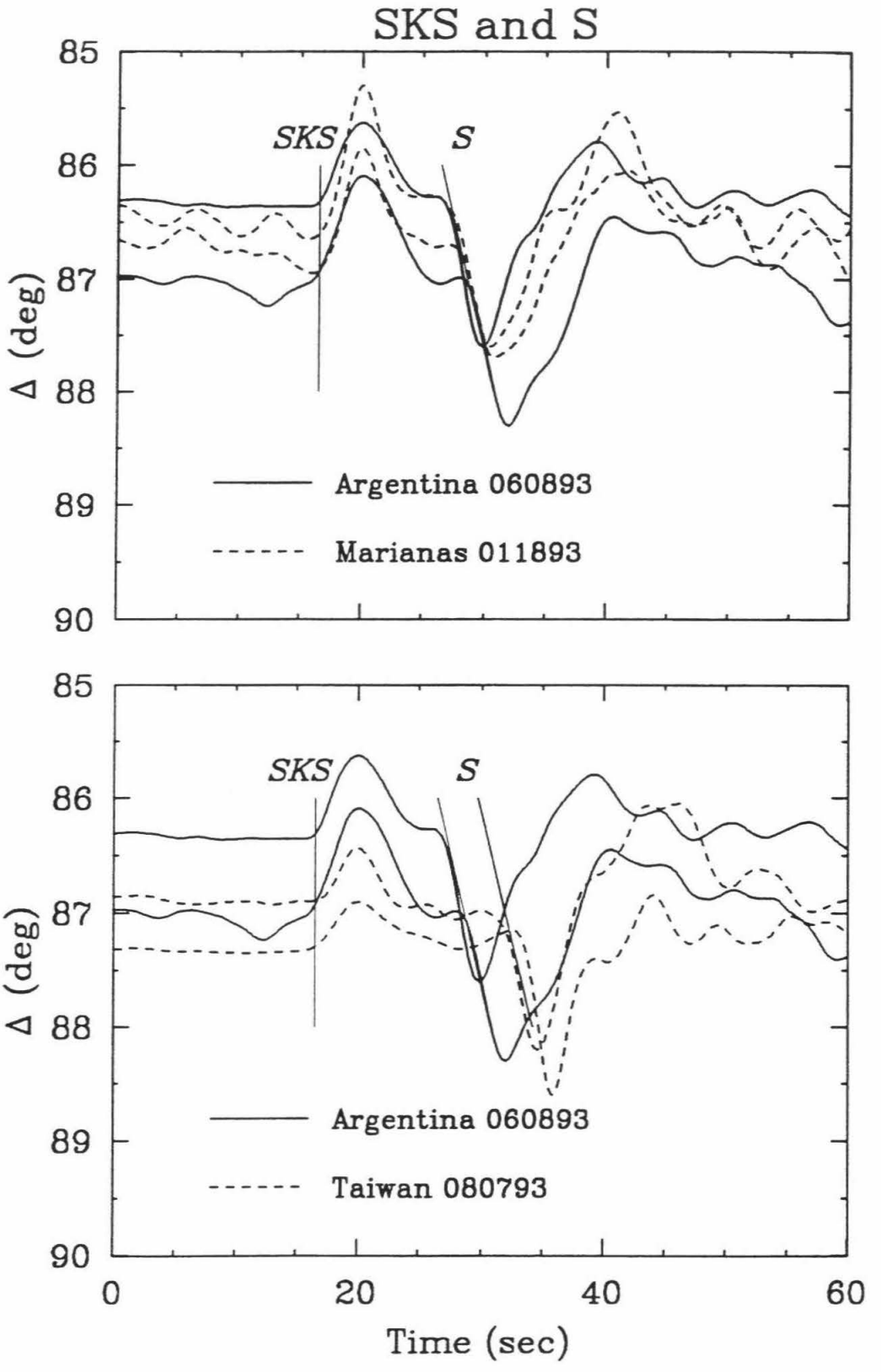
SKS and S
85
86
87
88
89
90
Δ (deg)
SKS
S
Argentina 060893
Marianas 011893
85
86
87
88
89
90
Δ (deg)
SKS
S
Argentina 060893
Taiwan 080793
0
20
40
60
Time (sec)

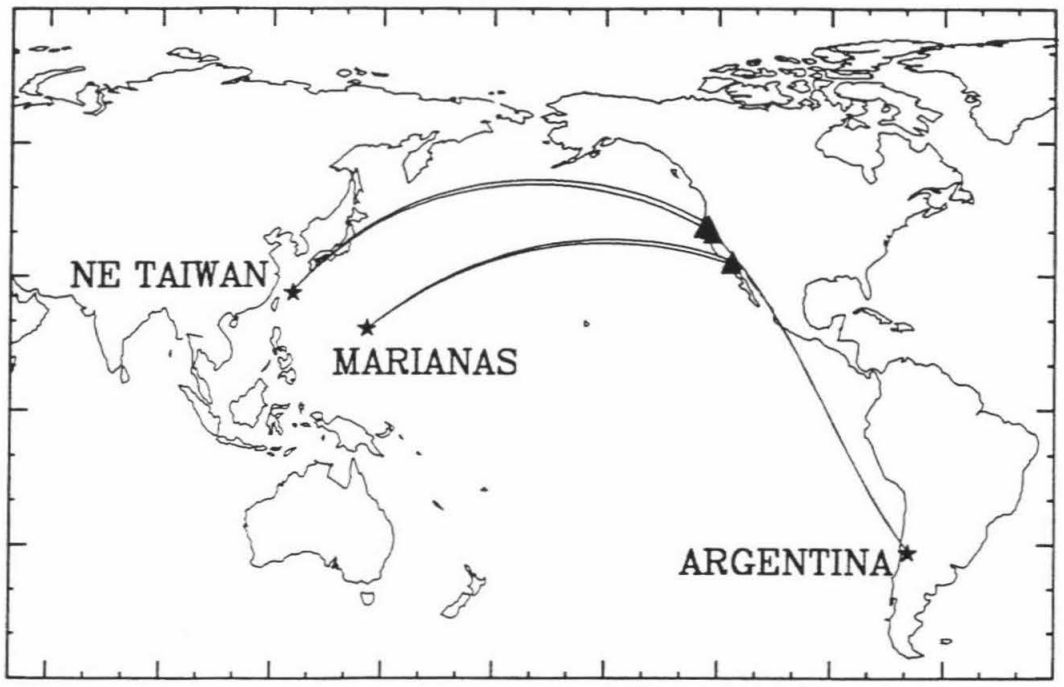

Figure 2.9: Surface projections of wavepaths between sources (stars) and receivers (triangles) for the three events of Figure 2.8.

south from Taiwan to Marianas to Fiji-Tonga/Kermadec wavepath mid-points, i.e., from the lower mantle region beneath the north Pacific down to the central Pacific, δT_{S-SKS} residuals alternate from near zero to less than zero to much greater than zero. These anomalies can be interpreted as either SKS or S (or both) traversing anomalous lower mantle structure. In the next section, it is argued that the S-waves turning in the lower mantle and D$''$ region contribute the most to the anomalies in T_{S-SKS} times. The above variations from north to south are not explored further in this study, though a scenario of lower mantle V_S variations from average to fast to very slow (in sweeping from the Taiwan to Fiji and Kermadec events) can explain the observations.

2.4 Modeling the Data

In this section we focus on possible mechanisms to explain the most anomalous $S-SKS$ times. The observed δT_{S-SKS} differential travel times from Fiji-Tonga and Kermadec deep focus source regions recorded at North and South American stations are up to around 9 sec greater than those predicted by the *iasp91* reference model. This implies SKS is anomalously fast, S is anomalously slow, or a combination of both. Thus, to model δT_{S-SKS} one can explore different structural possibilities that speed up SKS and/or slow down S. In doing so, scenarios containing different D$''$ discontinuity structures must also be explored, since several regions bordering and within the Pacific have been modeled with such structures [see for example, Garnero et al., 1993a; and Nataf and Houard, 1993].

Lower mantle V_S discontinuity models for regions bordering the Pacific contain a D$''$ layer averaging around 280 km thick. Such models predict waveform distortions in transversely polarized SH waves visible from around 90^o to 94^o [Lay and Helmberger, 1983a; and Young and Lay, 1987a], due to an interference effect of the

direct S and the S traversing the higher velocity discontinuity lid. For this distance range, the Fiji-Tonga data do not show evidence for such complexites as seen in other regions. SH data of the Fiji event in Figure 2.3 are compared to predictions of model SYL1 of Young and Lay [1987a] in Figure 2.10. Model SYL1 was used instead of SLHA because it has a negative velocity gradient within the D$''$ layer. This is preferred because non-negative gradient discontinuity models produce pulse distortion anomalies at $\Delta > 95^o$ [see Young and Lay, 1987a, for a discussion on this issue]. The SH pulse triplication predicted by SYL1 are not evident in the Fiji profile. The other Fiji-Tonga region events used in this study (Table 2.1) also possess simple SH waveforms. Schlittenhardt et al. [1985] also report no evidence for a D$''$ discontinuity for such events. Garnero et al. [1993a] argue that a much thinner D$''$ layer (150-180 km), which moves the pulse distortions out to larger distances (such as 98^o-100^o), is appropriate for this source-receiver geometry. Scenarios where a D$''$ layer varies laterally, becoming thinner in the central Pacific, are discussed after the following 1-D modeling investigations.

2.4.1 1-Dimensional Modeling Considerations

Attempts to model δT_{S-SKS} were made by assuming different input V_S profiles, then creating generalized ray synthetics for these profiles to compare with data. 1-D Spherically symmetric modeling attempts included: (i) decreases in V_S from the upper mantle (670 km) down to the CMB; (ii) exploring different V_S gradients in the bottom 300 to 600 km of the lower mantle; and (iii) different D$''$ models allowing for a discontinuity up to 3% and exploring different V_S gradients in these discontinuities. None of these attempts increase T_{S-SKS} predictions enough to match the large Fiji-Tonga and Kermadec times. Attempts to increase T_{S-SKS} with different spherically symmetric mantle models have the drawback that both SKS and S are somewhat similarly affected by the model changes.

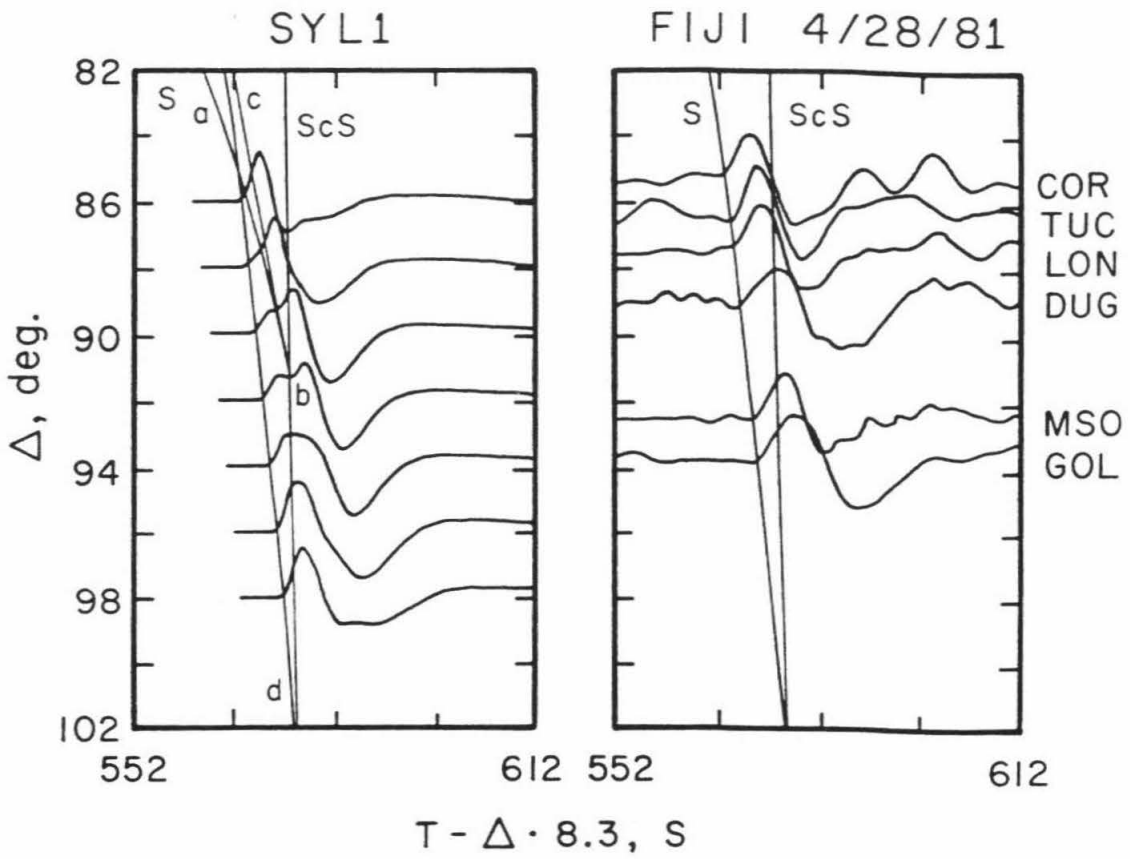

Figure 2.10: Comparison of SH synthetics for model SYL1 and the 042881 Fiji event. The amplitudes have been normalized and the data have been shifted to line up with the S arrival of the travel time curve.

Since SKS travels through the core, a modeling attempt to speed up SKS was made by increasing V_P in the top 300 km of the outer core, thus increasing δT_{S-SKS}. Increasing V_P at the top of the outer core can produce T_{S-SKS} times that match the anomalous data. The outermost core velocity model of Randall [1970], where $V_P = 8.26$ km/s at the top of the core, a 2.4% increase from that of the PREM model [Dziewonski and Anderson, 1981], can produce δT_{S-SKS} residuals of up to 6 sec. Increasing V_P even further produces T_{S-SKS} times the size of the observations. The azimuthal trend in the δT_{S-SKS} residuals seen in Figure 2.5 can thus be modeled by varying outer core velocities as necessary with azimuth (amounting to V_P variations of 5%). However, fluid dynamic arguments imply that lateral variations in velocity and density in the outer core are negligible [Stevenson, 1987], suggesting such a model is unlikely. Garnero and Helmberger [1994] discuss this issue further, and attribute such large anomalies to lower mantle structure.

Increasing the velocity at the top of the outer core, and thus decreasing the outer core velocity gradient, also is incompatible with $SKKS - SKS$ times ($T_{SKKS-SKS}$) observed for the same region and source-receiver geometry. Schweitzer and Müller [1986] and Schweitzer [1990] have observed these differential times to be anomalously large by up to 6 sec (for deep focus Fiji-Tonga events recorded at North American stations) which agrees with $\delta T_{SKKS-SKS}$ measurements made from the Fiji-Tonga events in this study. The observations indicate the later arriving $SKKS$ phase is delayed relative to SKS, or that SKS arrives early, both of which increase the $SKKS - SKS$ time. Increasing the outermost core velocity as that in Randall [1970], however, increases the outer core V_P gradient. This in turn speeds $SKKS$ up relative to the more deeply penetrating SKS, thus decreasing $T_{SKKS-SKS}$ times instead of increasing them. This argues that increasing outer core velocity (such that the outer core velocity gradient decreases) is not a plausible explanation for the anomalous δT_{S-SKS} differential travel times. Therefore, further investigation

of mantle possibilities to explain the anomalous δT_{S-SKS} data and possibly the $\delta T_{SKKS-SKS}$ anomalies as well is necessary.

2.4.2 2-Dimensional Modeling Experiments

Tomographic inversions have resulted in maps of 3-D mantle structure showing a large scale (> 3000 km) anomalously slow region in the lower mantle beneath the central and southwest Pacific, surrounded by circum-Pacific faster than average velocities [e.g., Tanimoto, 1990; Masters et al., 1992; and Su et al., 1992, 1994]. Body wave studies of ScS waves [Sipkin and Jordan, 1976, 1980; and Woodward and Masters, 1991] have illustrated large lateral variations in the central and southwest Pacific on smaller scales of around 1000 km. Studies of S_{diff} also suggest strong heterogeneity in the region [e.g., Wysession, 1992]. These studies, along with evidence for lateral variations in thickness of the D″ discontinuity [Garnero et al., 1993a; Weber, 1993; and Kendall and Shearer, 1994] emphasize the importance in pursuing 2- and 3-D models to explain the anomalous δT_{S-SKS} and $\delta T_{SKKS-SKS}$ residuals.

It is possible to have such lateral variations in the lower mantle that affect S (or $SKKS$) times more than SKS, or visa-versa. Using a modified WKBJ technique, [see Chapman, 1978; and Helmberger et al., 1985a, 1994] and a modified Cagniard de Hoop Method [Helmberger et al., 1994], tests were conducted using models containing various 2-D structures. Since aspherical mantle models have slow velocities in the lowermost mantle beneath the central Pacific region surrounded by faster than average velocities, our tests concentrated on models with laterally varying D″ structure. Figure 2.11 shows such a model along with resulting radial component synthetics passed through a long-period WWSSN instrument. In this model, the discontinuity structure (model B) "fades" out (to model A) and in (back to model B.) More specifically, a 2-D model was used where SKS encounters a D″ discontinuity before entering and after exiting from the core, while S traverses the bottom of the mantle

where the discontinuity is nonexistent (i.e., the D″ discontinuity fades out in the mid-Pacific thus slowing down S relative to SKS while not distorting the waveform of SH, and increasing δT_{S-SKS}). The model A in the figure is the extreme that S encounters in the mid-Pacific, and model B is bordering the Pacific such that only SKS passes through it. Different combinations of synthetics are given for SKS and S going through model A or B. It is found that δT_{S-SKS} is 6 sec when SKS passes through model B and S passes through model A. With a 2-D laterally varying D″ , the variation in δT_{S-SKS} residuals shown in Figure 2.5 can be modeled by varying the degree to which a D″ discontinuity fades out. This 2-D model also increases $\delta T_{SKKS-SKS}$ by up to 1.5 sec.

The model in Figure 2.11, while able to explain the large δT_{S-SKS} observations (by varying the extremes of models A and B), is poorly constrained and thus cannot be interpreted physically. Also, the manner in which the D″ might "fade out" is not clear. As mentioned above, past studies present evidence for a thick D″ discontinuity in regions surrounding the Pacific (280-320 km) and a thin discontinuity beneath the central Pacific (180 km.) Figure 2.12 presents a second model, where the D″ discontinuity becomes thin in one direction, without completely diminishing. The left and right sides of the figure display the end member models, and the center panel shows S, ScS and SKS raypaths through the stack of 2-D layers. The layers are presented as iso-velocity lines. For this model, synthetics were generated for different source placements relative to the dipping D″ structure. Many S and ScS raypaths in the figure are unsymmetric about their midpoints, which demonstrates how 2-D structures can distort wavepaths and thus affect travel times. Figure 2.13 shows radial component displacement synthetic seismograms for two different source placements through this model. T_{S-SKS} times differ by 6 sec for these two different runs.

Such 2-D experiments as above show how observed T_{S-SKS} times can be modeled

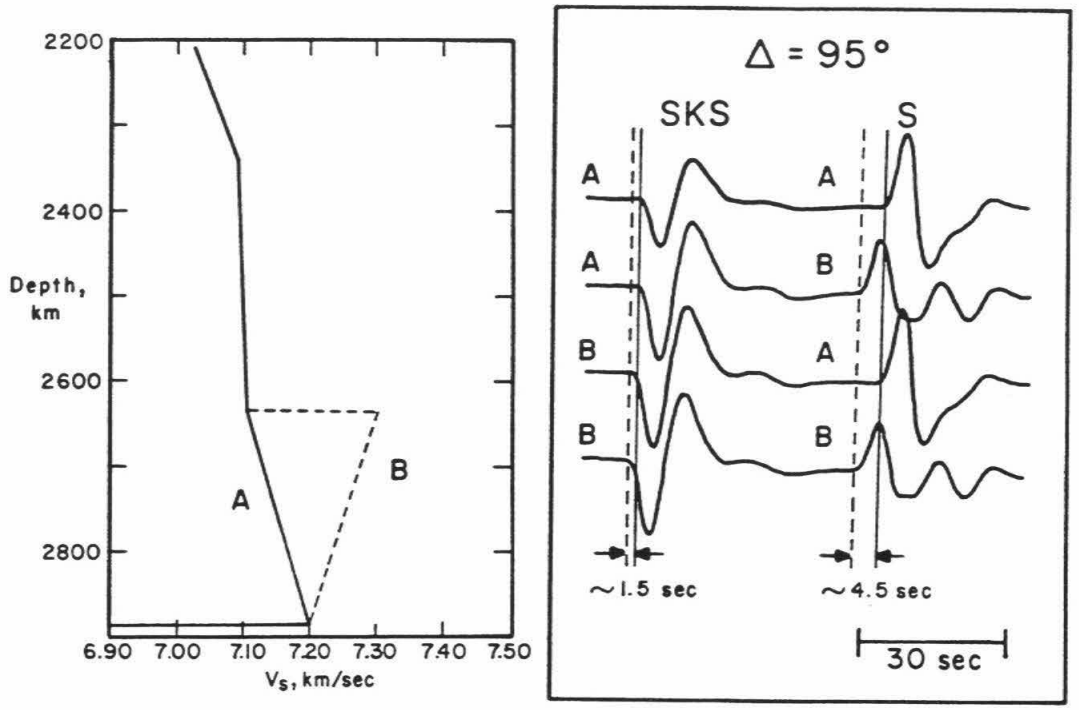

Figure 2.11: Two model extremes used in a 2-D varying D″ model (left) and results of different runs in which SKS ans S traversed through either model A or B (right.) The largest δT_{S-SKS} occurs for SKS passing through model B with S traveling through model A.

Figure 2.12: 2-D model with changing D″ thickness. Panels on left and right display end member models having D″ layer thicknesses of 300 and 80 km, respectively. The center panel shows Earth-flattened isovelocity contour lines connecting the two models, along with geometric raypaths for S, ScS, and SKS, for 90°. For this particular lateral placement of the source, the 2-D structure distorts the wavepaths of ScS and S, which results in both travel time and waveform perturbations.

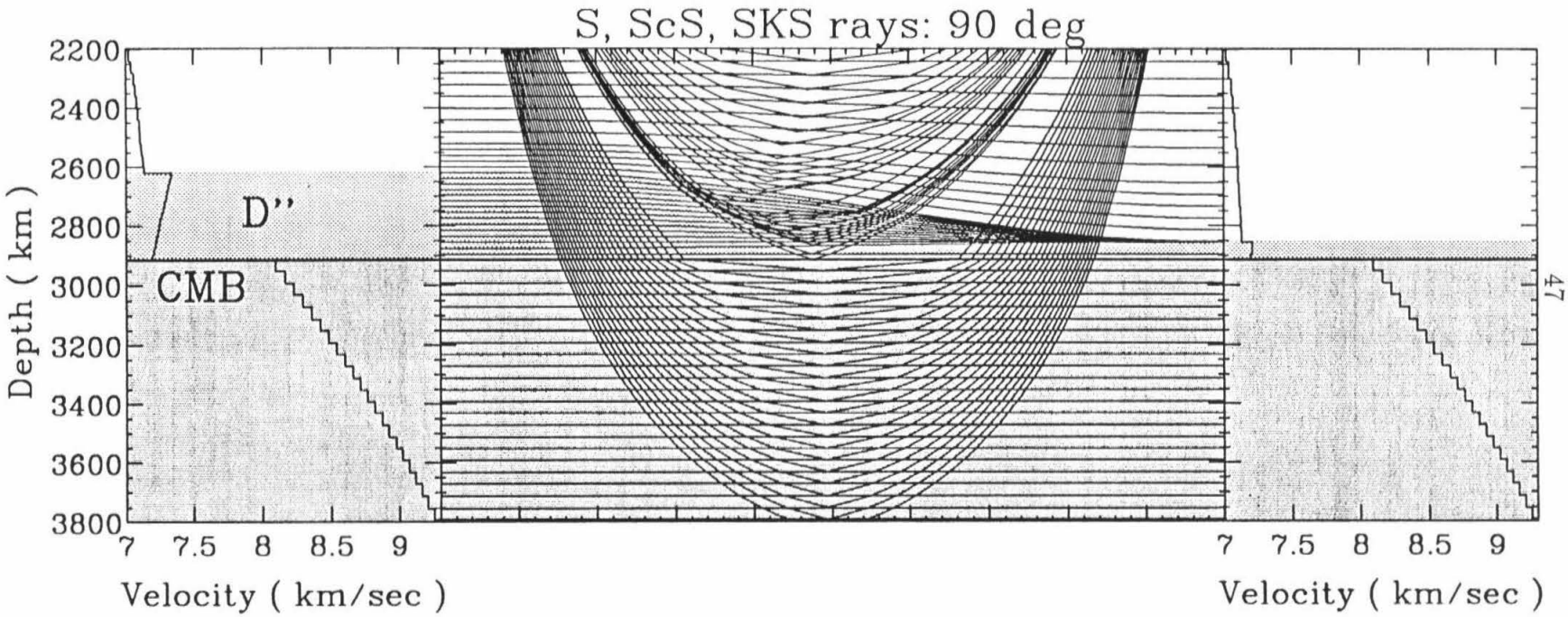
S, ScS, SKS rays: 90 deg
Depth (km)
2200
2400
2600
2800
3000
3200
3400
3600
3800
D''
CMB
7
7.5
8
8.5
9
Velocity (km/sec)
7
7.5
8
8.5
9
Velocity (km/sec)

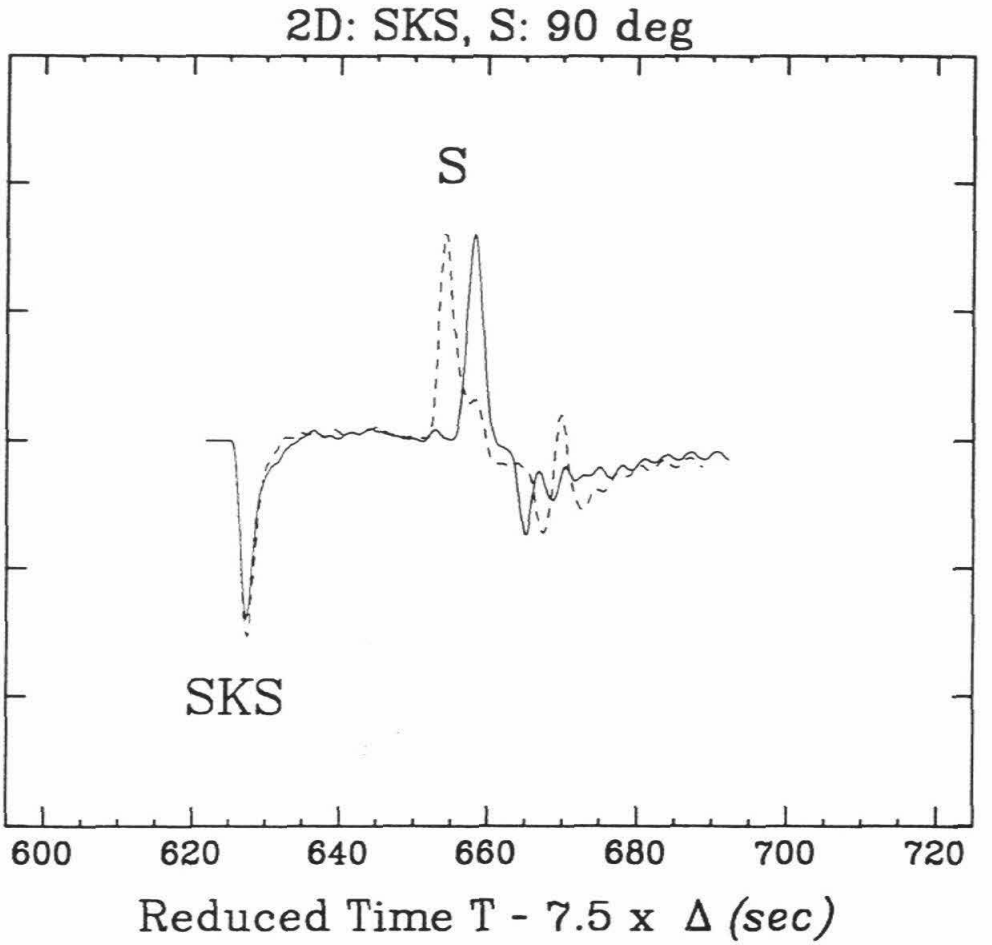

Figure 2.13: Radial component displacement synthetic seismograms for two different lateral placements of the source for a 2-D model having D″ of variable thickness, resulting in T_{S-SKS} times differing by 6 sec.

by a laterally varying D'' region. The above 2-D models are, however, not well-constrained. Nevertheless, they present evidence for how the scenario of a thinner D'' layer beneath the central Pacific, accompanied by slower than average lower mantle velocities, along with faster than average circum-Pacific velocities, as suggested by tomographic studies, may explain the observations.

2.5 Discussion

The size of the δT_{S-SKS} anomalies seen from SKS and S bottoming under the mid-Pacific are very large. There may be other factors contributing to these anomalies. For instance, CMB topography could affect this differential time. Synthetic tests show that a 10 km increase in CMB radius for a down and up going SKS will increase δT_{S-SKS} by about 1 sec. From close inspection of the transverse and radial components of the data, no splitting in arrival times was noticeable for the long-period data, suggesting that upper mantle anisotropy [as presented by Silver and Chan, 1988] is not playing any significant part in the measurements. The broadband data, however, do show cases where SKS is present on the tangential component. The δT_{S-SKS} anomalies observed for the Fiji-Tonga and Kermadec regions recorded in North and South America, are as large as 9 sec, and $\delta T_{SKKS-SKS}$ times up to 6 sec, which are much larger than maximum expected SV splitting effects on these arrivals (near 1 sec). Therefore our conclusions are unaffected by such unmodeled phenomena. Source mislocation can contribute to small scatter in the observations, though such affects will also be very small compared to the large observed anomalies.

If anisotropy is present in the D'' region, as suggested by Vinnik et al. [1989] and Lay and Young [1991], T_{S-SKS} times can be affected. Waveforms of the data set presented here were carefully inspected for S-wave splitting between the tangential and radial components. A small percentage of our data ($\sim$ 5 %) display slight offsets

($\sim$ 1 sec) between the peaks or onsets of the S waveforms. T_{S-SKS} times from these waveforms have not been used in our analysis. Nevertheless, some evidence for D'' anisotropy is evident in our data, and possibly up to 1 sec of uncertainty may be incurred from such. Analyzing the anomalous records is left for future study.

In seismic studies of D'' and CMB phenomena, travel-time information is often averaged to infer a velocity structure. Averaging can be misleading when lateral variations exist within the region being averaged. Figure 2.5 shows an azimuthal trend for δT_{S-SKS} residuals, which increase to the southwest. But when these residuals are put on a δT_{S-SKS} vs. Δ plot, the 3-D variations in δT_{S-SKS} are mapped into 1-D, resulting in a plot appearing to have large scatter. If one were to average these apparently scattered δT_{S-SKS} residuals on this plot, interpretation would be in error. More data traversing this mid-Pacific anomaly from other azimuths will help constrain the size and magnitude of the anomaly as well as the degree to which δT_{S-SKS} residuals vary systematically.

Many studies have investigated V_S velocity gradients in the lowermost mantle (for example, Phinney and Alexander, 1969; Mitchell and Helmberger, 1973; Mondt, 1977; Doornbos and Mondt, 1979a, 1979b; Mula and Müller, 1980; Lay, 1983; Bolt and Niazi, 1984; and Weber, 1993). Both positive and negative D'' velocity gradients have been proposed. This issue is not addressed in this study, and it is noted that changes in the V_S gradient at the base of the mantle only slightly affect δT_{S-SKS} in the distance range presented. The nature of the velocity gradient at the base of the mantle, along with how lower mantle lateral variations responsible for the anomalous T_{S-SKS} times might affect time and amplitude behavior of diffracted P- and S-waves is of great importance. This topic, along with how such lower mantle variations may correlate geographically to PKP precursors, D'' thickness, overall lower and mid-mantle 3-D structure, CMB topography, possible lower mantle thermal and dynamical flow patterns, and possible D'' anisotropy remains for future

study.

2.6 Conclusion

Differential travel time residuals between the phases SKS and S are a powerful diagnostic for detecting anomalous lower mantle structure. Previously noted slow and fast lower mantle regions correlate with anomalously large and small $S - SKS$ separations, respectively. SKS and S data presented here suggest lower mantle lateral variations having a variety of scale lengths, from O(100 km) to O(1000 km). Large scale differences in δT_{S-SKS} residuals appear for differing source-receiver geometries, such as the central Pacific compared to the Carribean. And for a given geometry, such as Fiji-Tonga to North America, systematic small scale to large scale variations are present. δT_{S-SKS} residuals for this geometry show a trend varying from 0 to 8 sec when sweeping clockwise in azimuth from the source region. This trend implies the D$''$ region beneath the central Pacific has a systematic trend in V_S from average to anomalously slower than average velocities in sweeping to the southeast from beneath the Hawaiian islands.

Synthetic tests demonstrate that 1-D structures are incapable of predicting the size of both the δT_{S-SKS} and $\delta T_{SKKS-SKS}$ residuals. 2-D modeling experiments, however, show how the lower mantle scenario of a D$''$ discontinuity (around 300 km) in circum-Pacific regions thinning to 180 km beneath the central Pacific, accompanied by faster than average circum-Pacific velocities surrounding a slower than average central Pacific (as suggested tomographic studies), can explain the observations. Such a model, while being our preferred explanation of the data, is not fully constrained by the data. More data along with absolute travel times will help in this regard. Explaining the observations with laterally varying outer core structure requires lateral changes in V_P of up to 5%, which is assumed to be dynamically in-

feasible [as argued by Stevenson, 1987], therefore this study has assumed a laterally homogeneous outer core. In the following chapter, a larger data set of $S - SKS$ times are analyzed and compared to predictions from 3-D mantle models, to further assess the issue of scale length of heterogeneity in the lowermost mantle.

Chapter 3

Travel Times of S and SKS: Implications for 3-D Lower Mantle Structure Beneath the Central Pacific

3.1 Abstract

The travel-times of S and SKS phases from deep focus Fiji-Tonga events recorded in North America by Canadian Station Network and World Wide Seismographic Station Network stations exhibit a strong azimuthal dependence from the source region. The differential times of $S - SKS$ exhibit relatively little scatter, and are used to investigate 3-D mantle models for the central Pacific region. $S - SKS$ times are corrected for the Earth's ellipticity and residuals are computed with respect to the *iasp91* [Kennett and Engdahl, 1991] reference model. Anomalously large $S - SKS$ times, ranging up to 9 sec larger than *iasp91* predictions for $\Delta > 100^o$, suggest a slow lower mantle beneath the central Pacific. These results are compared to the predictions of three tomographic models: MDLSH of Tanimoto [1990], model SH12_WM13 of Su et al. [1992], and model SH.10c.17 of Masters et al. [1992].

The 3-D whole mantle models have been parameterized into 11 spherical shells. Qualitative agreement between the tomographic model predictions and observations is encouraging, varying from fair to good. However, inconsistencies are present and suggest anomalies in the lower mantle of scale length smaller than the present 2000+ km scale resolution of tomographic models. Laterally varying outer core structure is not necessary to explain the anomalies in this data set, although such a scenario cannot be resolved with this data.

3.2 Introduction

In the past few years, the lowermost mantle beneath the Pacific ocean has been characterized as having anomalously slow seismic velocities with a circum-Pacific fringe of high velocities. This large-scale structure has been inferred by seismic tomography using body waves [e.g., Dziewonski and Woodhouse, 1987], surface waves [e.g., Tanimoto, 1990], as well as normal modes [e.g., Li et al., 1991]. This slow V_S region has been observed by non-tomographic body wave studies as well. For example, using $ScS - S$ differential travel times, Woodward and Masters [1991] identify a very slow lower mantle region beneath the southwest Pacific, with residuals up to 8 sec. This same anomaly was noted previously by Sipkin and Jordan [1980] using multiple ScS travel times. This region corresponds to the southwest part of the slow central-Pacific anomaly seen in the tomography models. Also, Garnero et al. [1988] analyzed differential travel times of $SmKS$ waves to infer a laterally varying slow lower mantle beneath the central Pacific, with S-SKS times up to 9 sec larger than predictions. Any seismic information on this region has particular relevance to models of mantle dynamics and geochemistry, as well as models of heat flow from the core. Such issues relate directly to the nature of mantle convection and possible plume formation [e.g., Stacey and Loper, 1983; and Olsen et al., 1987]. Whether

the central Pacific lower mantle is the site of mantle upwelling may eventually be addressed by the seismic tomography models, but information concerning the details of such features exists primarily in the smaller wavelengths.

Tomographic models of the lower mantle beneath the central Pacific often correlate at longer periods (such as degree 2), while differing the most at smaller wavelengths. The purpose of this paper is to compare direct travel time measurements with predictions of the 3-D mantle models as a first step towards understanding the 3-D lower mantle S-wave anomalies beneath the Pacific.

S-SKS differential travel times are ideal for comparison to time predictions of 3-D mantle models to assess lower mantle S-wave velocity structure (V_S) beneath the central Pacific. Differential times have the advantage over absolute times in that source and receiver complexities are suppressed. For the lower mantle beneath the central Pacific, deep-focus Fiji-Tonga earthquakes recorded in North and South America are well suited for such an investigation. The dense station arrays of the World Wide Seismographic Station Network (WWSSN) and the Canadian Seismic Network (CSN) make possible a detailed sampling of the mid-Pacific lower mantle region.

3.3 Data Set

Long- and short-period seismograms have been used from 13 Fiji-Tonga earthquakes recorded in North and South America by WWSSN and CSN stations. The hypocentral information as reported by the ISC is given in Table 3.1. All events used were deep-focus except one mid-focus event (no. 3, Table 3.1.) The path coverage from the Fiji-Tonga events recorded on the North and South American stations is shown in Figure 3.1. The great-circle paths show the dense ray coverage where the S-wave passes through the bottom of the mantle beneath the central and eastern Pacific.

EV	Date mmddyy	Origin time hhmm sec	Latitude	Longitude	Depth km	M_b
01	12-28-64	1616 8.7	-22.13	-176.62	577	5.2
02	3-17-66	1550 32.3	-21.08	-179.15	627	5.9
03	8-12-67	0939 45.7	-24.79	-177.38	144	6.0
04	10-09-67	1721 46.2	-21.10	-179.18	605	6.2
05	1-24-69	0233 3.4	-21.87	-179.54	587	5.9
06	6-28-70	1109 51.3	-21.66	-179.42	587	5.8
07	11-20-71	0727 59.5	-23.45	-179.88	533	6.0
08	3-30-72	0534 50.4	-25.69	179.58	479	6.1
09	12-28-73	0531 3.8	-23.88	-179.99	517	6.2
10	3-23-74	1428 33.0	-23.93	179.88	504	6.0
11	10-21-74	0412 28.7	-17.97	-178.49	596	5.9
12	7-20-80	2120 3.6	-17.88	-178.61	588	6.0
13	4-28-81	2114 47.1	-23.70	-179.99	522	6.0

Table 3.1: Hypocentral information of Fiji-Tonga events. EV denotes the event number.

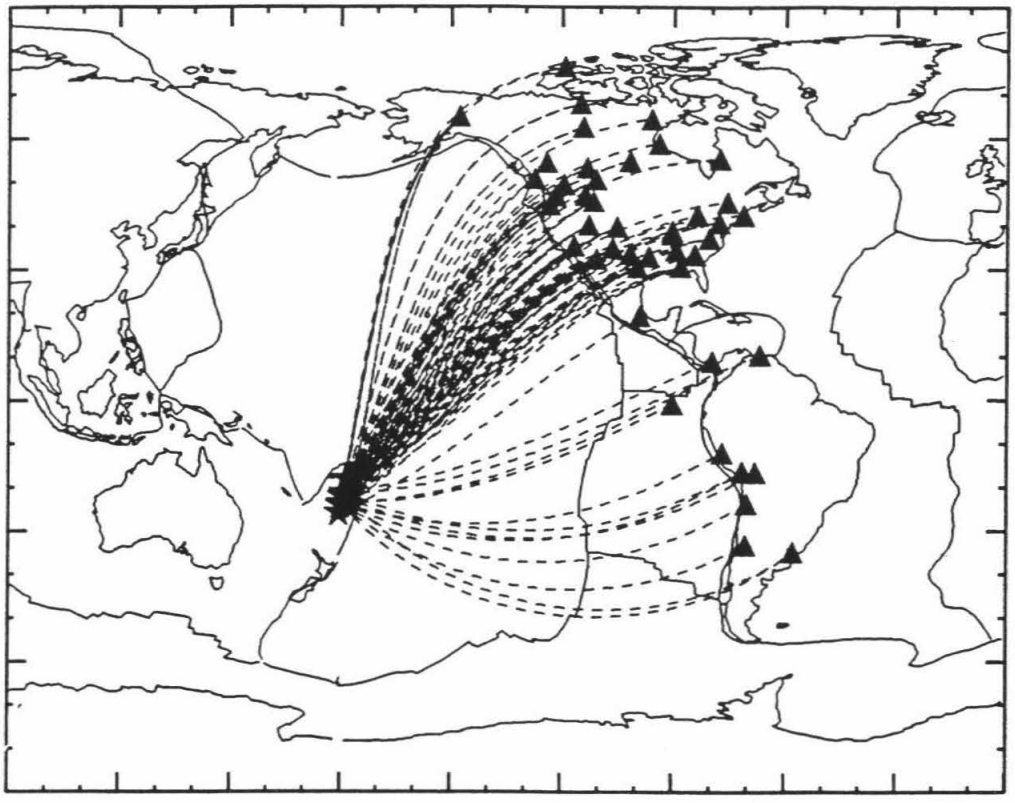

Figure 3.1: Map of the world showing great circle ray paths from Fiji-Tonga events (stars) to North and South American stations (triangles).

A sample profile of long-period recordings of SKS and S is shown in Figure 3.2. The longitudinal SV components shown have been obtained by rotating the digitized horizontal records into their great-circle longitudinal and transverse components. In the left panel of Figure 3.2, the SV traces have been plotted with absolute time, along with predictions of the reference Earth model *iasp91* of Kennett and Engdahl [1991] as dotted lines. The travel time delays for SKS and S with respect to *iasp91* are indicated by the numbers in the figure. For example, at station DUG (Dugway, Utah), SKS and S are late by 6.6 and 8.0 sec, respectively. Large delays for this station have been noted in previous studies [e.g., Graves and Helmberger, 1988]. However, shifting the SKS arrivals to line up with the *iasp91* prediction for SKS, as seen in the right panel of Figure 3.2, illustrates the stability in the differential travel time of S and SKS (T_{S-SKS}) in the data. The $S - SKS$ anomalies with respect to *iasp91* are indicated by the numbers, and show that T_{S-SKS} in the data is up to around 7 sec larger than that predicted by *iasp91* for this profile. The large absolute time anomalies in the left panel of Figure 3.2 may be due to upper mantle structure. The $S - SKS$ differential time anomalies (as in Figure 3.2 on the right), however, are more related to the deep Earth where SKS and S travel very different paths. The will be explored in further detail in a later section. A mislocation in source depth by 50 km will only produce a 0.7 sec change in T_{S-SKS}. In these profiles, all amplitudes have been normalized to the maximum amplitude of the trace.

3.4 Travel Time Observations

The times of S and SKS (T_S and T_{SKS}, respectively) were measured by picking the onset time of the phase using synthetic seismograms as a guide [as in Grand and Helmberger, 1985]. This measurement was only made in cases where the phase of

Figure 3.2: Sample data from Event 13. Radial components are shown for SKS and S along with predictions of *iasp91* as dotted lines. (left panel) Traces plotted absolutely in time. Numbers are SKS and S anomalies with respect to *iasp91*; (right panel) SKS phase is lined up with *iasp91* prediction. Numbers are $S - SKS$ anomalies with respect to *iasp91*.

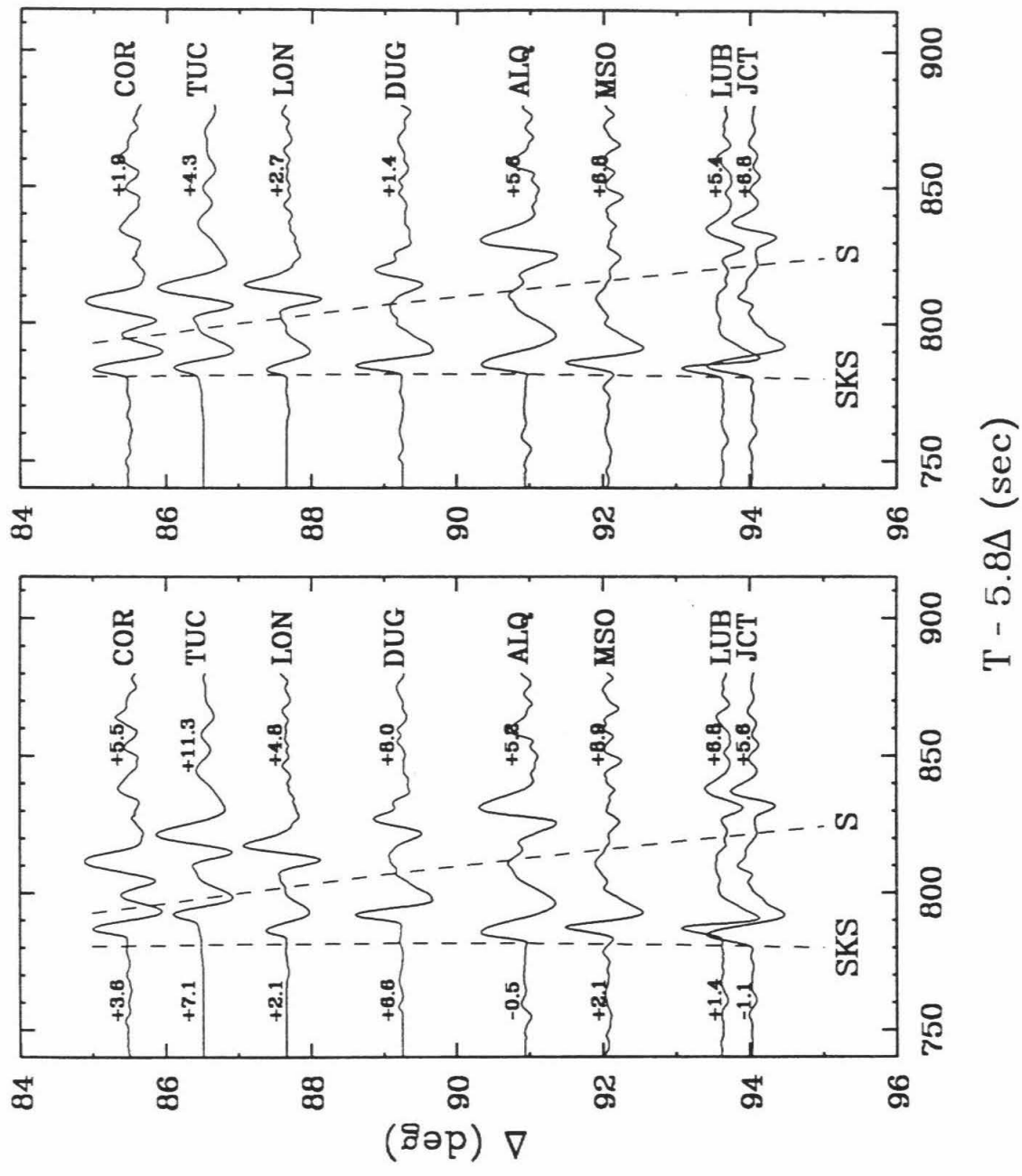
COR
TUC
LON
DUG
ALQ
MSO
LUB
JCT
SKS
S
+3.6
+7.1
+2.1
+6.6
-0.5
+2.1
+1.4
-1.1
+5.5
+11.3
+4.8
+8.0
+5.8
+8.9
+6.8
+5.6
+1.9
+4.3
+2.7
+1.4
+5.4
+8.8
+5.4
+8.8
Δ (deg)
T - 5.8Δ (sec)

interest was well above the noise level. For digitized data, these picks were made on a computer graphics screen using a mouse and cross-hairs. T_S was measured on the SV component for the digitized data. For this data set, no discrepancy could be seen between T_S(SH) and T_S(SV). At distances beyond the core shadow, the SH component was used for S_{diff} times, yielding the time $S(SH)$-$SKS(SV)$. For records that weren't digitized, measurements were made on the paper records on the north-south and east-west components, and cross checked for accuracy. If the short-period recordings had good signal to noise ratio, they were also measured as a check of the long-period times. For a given event-station pair, if any measurements from the different components of the non-rotated paper records gave discrepant times by more than 0.3 sec, they were discarded from the data set. Of all the data gathered for the 13 events in Table 3.1, 110 measurements of each of T_S and T_{SKS} were kept. These times were then differenced to obtain the T_{S-SKS} differential time. This greatly increases the size of our previous $S - SKS$ data set of 33 measurements for the same region [Garnero et al., 1988].

The observed T_S and T_{SKS} times were corrected for the Earth's ellipticity [Dziewonski and Gilbert, 1976], then used to construct the T_{S-SKS} differential time. Residual times with respect to the *iasp91* model (for the appropriate depths and distances) were then computed. We define these residual times as the observed minus predicted,

$$\delta T_S = (T_S)_{obs} - (T_S)_{iasp91}$$
$$\delta T_{SKS} = (T_{SKS})_{obs} - (T_{SKS})_{iasp91}$$
$$\delta T_{S-SKS} = (T_{S-SKS})_{obs} - (T_{S-SKS})_{iasp91}$$

All travel time anomalies were rounded off to the nearest 10th of a second. These times were tabulated in Garnero and Helmberger [1993] and are plotted in Figure 3.3 as a function of distance. No station corrections have been applied. Figure 3.3a shows that δT_S times are anomalously large, by as much as 10 sec in many cases, and at

first glance appear very scattered. δT_{SKS} times are less scattered than δT_S, and between 82^o and 95^o show a slight trend of decreasing with distance. δT_{S-SKS} times are given in Figure 3.3c. Differencing the S and SKS times helps to suppress some of the scatter seen in Figure 3.3a and b, and reveals an apparent trend with δT_{S-SKS} increasing with distance. This suggests that much of the scatter in the absolute travel times of Figure 3.3 a is due to near source or near receiver regions. Variations in upper mantle shear structure under North America is expected to cause at least 5-6 sec variations [Lay and Helmberger, 1983b; Grand and Helmberger, 1987]. The same residual travel times are plotted as a function of azimuth in Figure 3.4. In all three panels Figure 3.4abc, a tendency for residuals to increase between the azimuths of 10^o and 65^o (from NNE to ENE from Fiji-Tonga) is apparent. With pronounced distance and azimuthal trends in the observations, a closer look at the S and SKS times is necessary.

In Figure 3.5, the densely sampled azimuth range from 10^o to 65^o is divided up into three "pie slices." The boundaries of these slices are great circle paths. Data with paths to Central and South America are not included in the rest of the analysis due to their sparser core-mantle boundary (CMB) sampling for our data set (see Figure 3.1.) Figure 3.6 displays the residual times with respect to distance, where the symbols are shaded to correspond to the azimuth slices of Figure 3.5. The white circles correspond to the most northerly azimuth slice from Fiji-Tonga to North America; the gray circles are for the intermediate azimuth slice; and the black circles are measurements from the most easterly azimuth slice. In Figure 3.6a, the δT_S times are seen to systematically increase with increasing azimuth. The black circles are systematically the most anomalously large δT_S, the white circles are systematically the smallest δT_S, while the gray circles are intermediate between the white and black circles, with some overlap of the black circles. This trend indicates that increasingly slow velocities are encountered by the paths as the azimuth from the source region

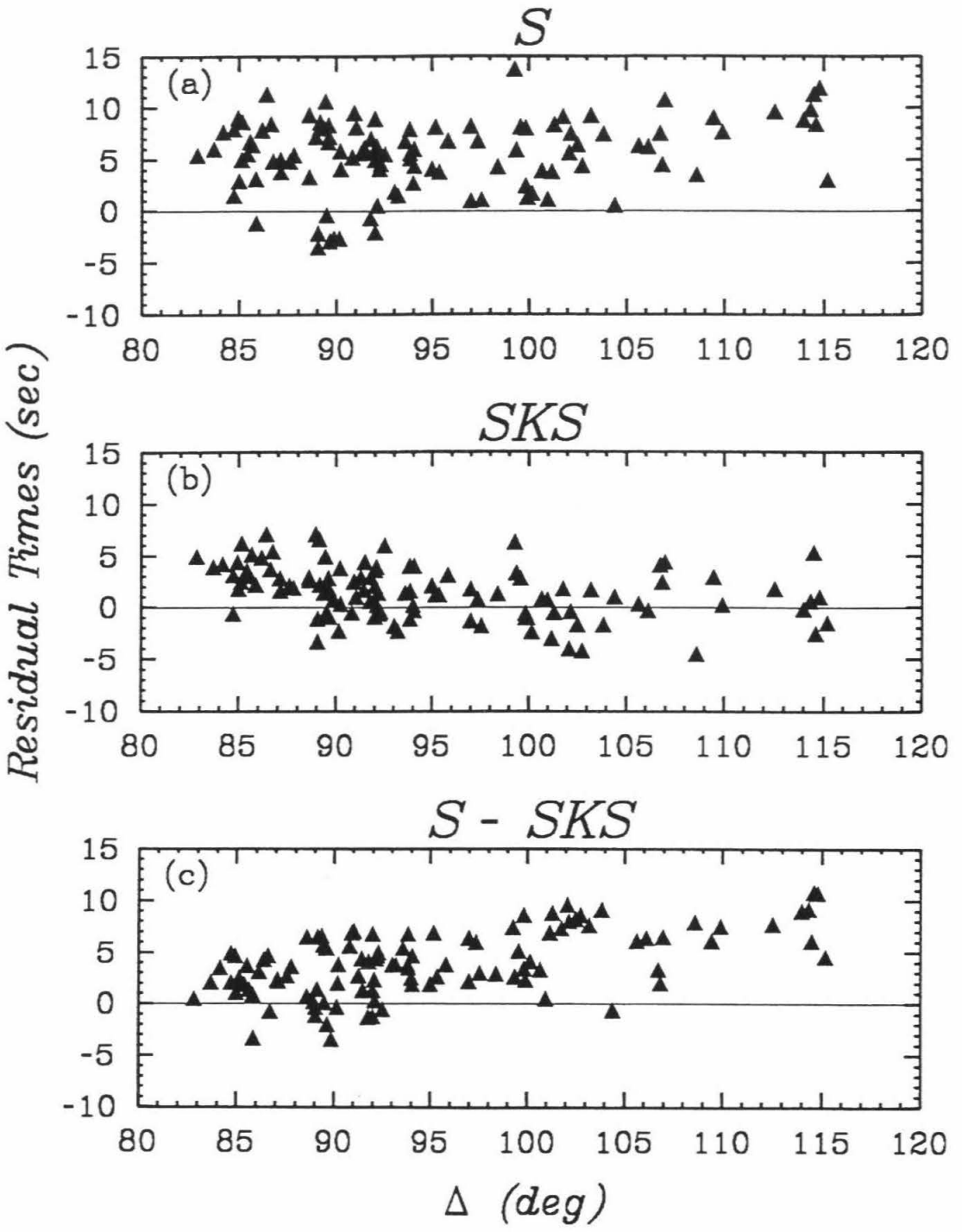

Figure 3.3: Residual travel times (with respect to *iasp91*) of (a) S, (b) SKS, and (c) $S - SKS$ are plotted as a function of distance for Fiji-Tonga events recorded in North and South America.

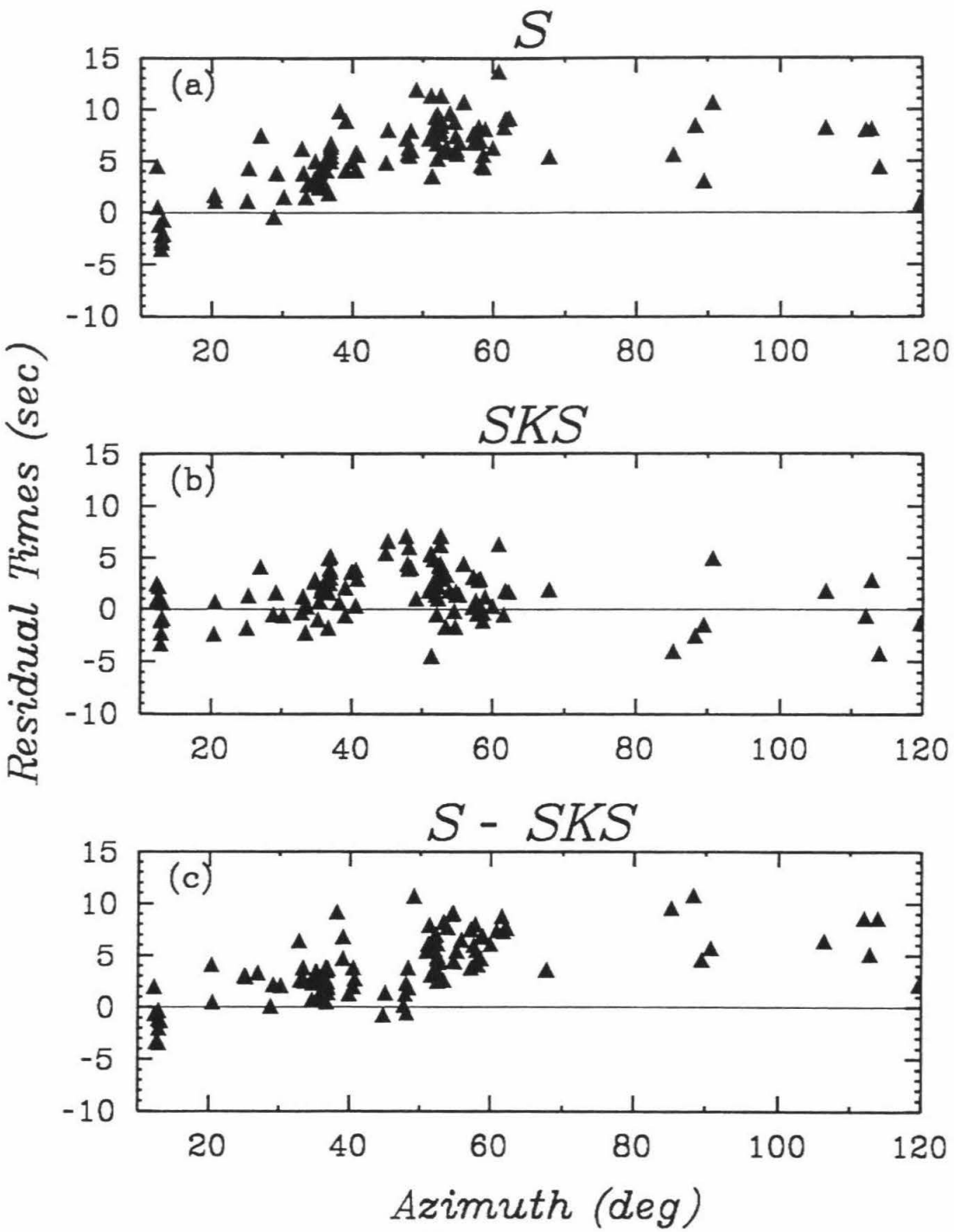

Figure 3.4: Residual travel times (with respect to *iasp91*) of (a) S, (b) SKS, and (c) $S - SKS$ are plotted as a function of azimuth from the Fiji-Tonga source region events recorded in North and South America.

is increased clockwise from the north. This pattern also varies with azimuth from the strike of the slab, though slab effects on the S and SKS times for paths to the North American stations from the Tonga trench are expected to be minimal. S and SKS spend very little time in the slab, since the slab dips towards the west, striking around N15°E, and raypaths depart NNE from the underside of the slab. The azimuth range (relative to slab strike) of stations used here is such that slab effects are predicted to be absent (or small) [Cormier, 1989].

The δT_{SKS} times are displayed in Figure 3.6b. For distances greater than 95°, the data are scattered with a mean near 1 sec. From about 83° to 90°, however, the mean of the measurements is greater than this with a slight negative trend. This may be due to 3-D lower mantle structure in the central Pacific or outermost core structure and will be addressed in the following section. Figure 3.6c shows the residual times δT_{S-SKS}. The trends for the different azimuth slices are clearly present, with the easterly azimuth (black circles) measurements on average the most anomalous. The scatter for this 50° - 65° azimuth slice is reduced for δT_{S-SKS} in comparison to that of δT_S or δT_{SKS} in Figures 3.6a and b. The scatter for the 25° - 50° slice is also reduced. For each azimuth bin, the residuals increase at larger delta in Figure 3.6c. To further illustrate that the δT_{S-SKS} times from the 3 different azimuth sectors behave differently, Figure 3.7 shows a simple least squares fit of a line to the data from different azimuth slices. It is possible that the error in such a fit may be decreased by fitting a polynomial to the data, though the purpose of Figure 3.7 is merely to show that the data on average behave distinctly differently for the different azimuth binnings of Figure 3.5.

Since the δT_S residual times in Figure 3.6a increase with distance at large delta, the trend whereby δT_{S-SKS} increases with distance can be explained by a slow lower mantle beneath the central Pacific that preferentially slows down S relative to SKS. Such a slow anomaly may also explain the anomalously slow δT_{SKS} seen

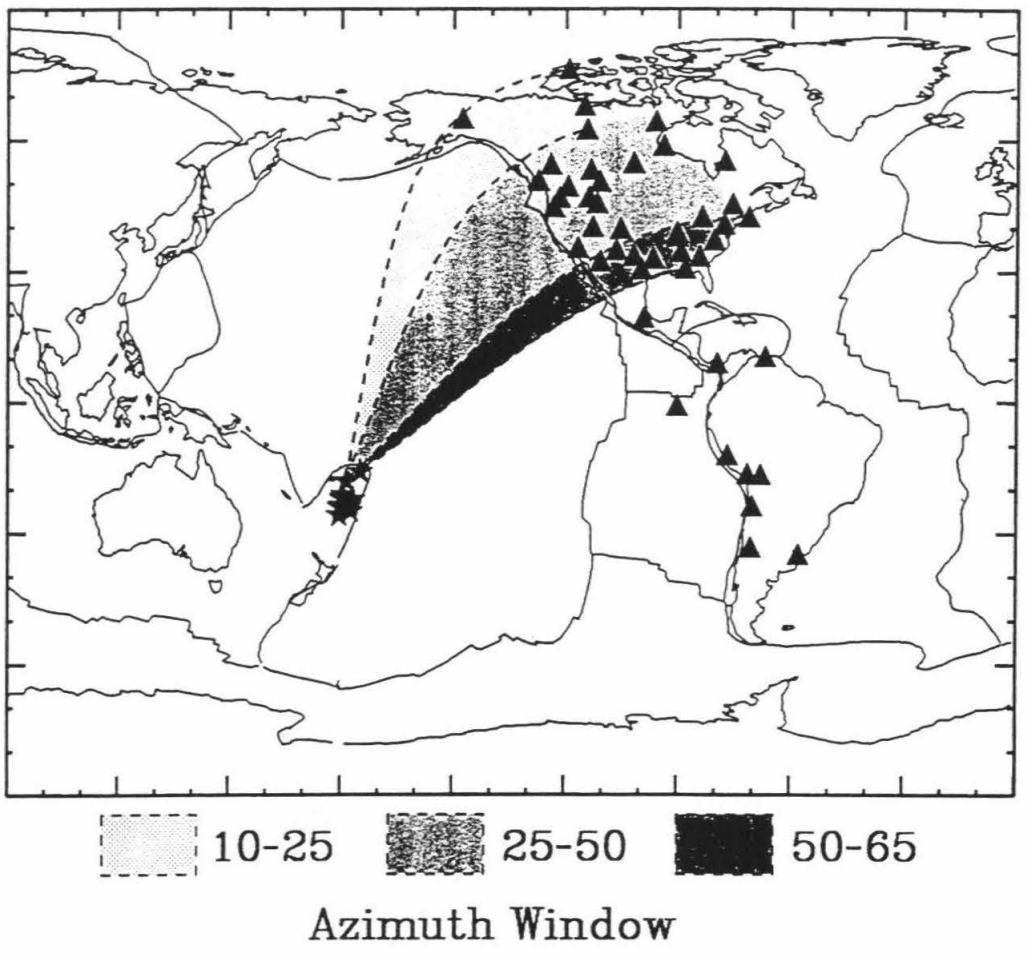

Figure 3.5: Fiji-Tonga events (stars) to North American stations (triangles). The divisions between the shaded regions (dotted lines) are great circle paths.

Figure 3.6: Residual travel times (with respect to *iasp91*) of (a) S, (b) SKS, and (c) $S-SKS$ are plotted as a function of distance for Fiji-Tonga events recorded in North America. The times are shaded to correspond to the azimuth slices of Figure 3.5.

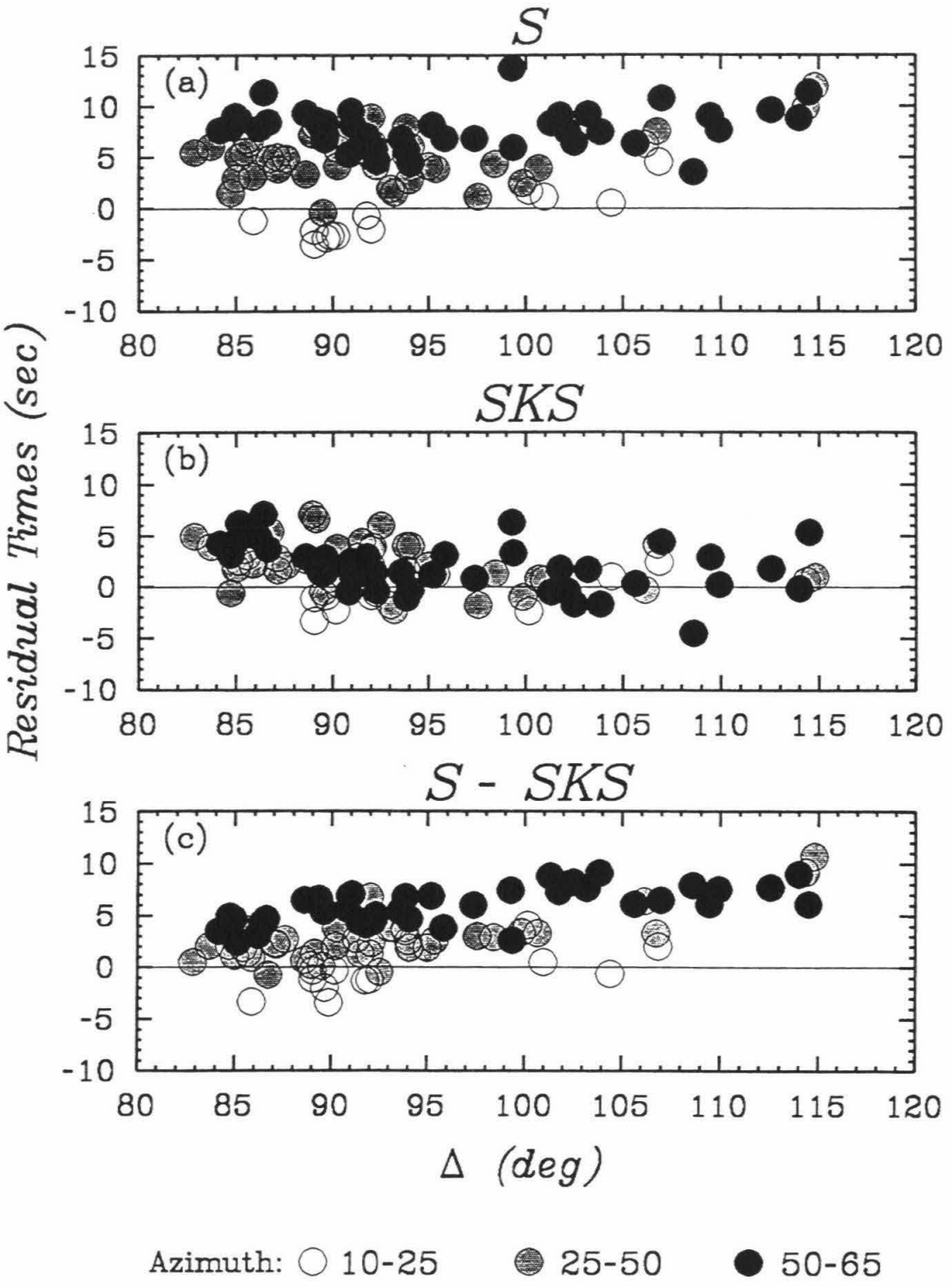
S
(a)
SKS
(b)
S - SKS
(c)
Residual Times (sec)
15
10
5
0
-5
-10
80
85
90
95
100
105
110
115
120
Δ (deg)
Azimuth: 10-25
25-50
50-65

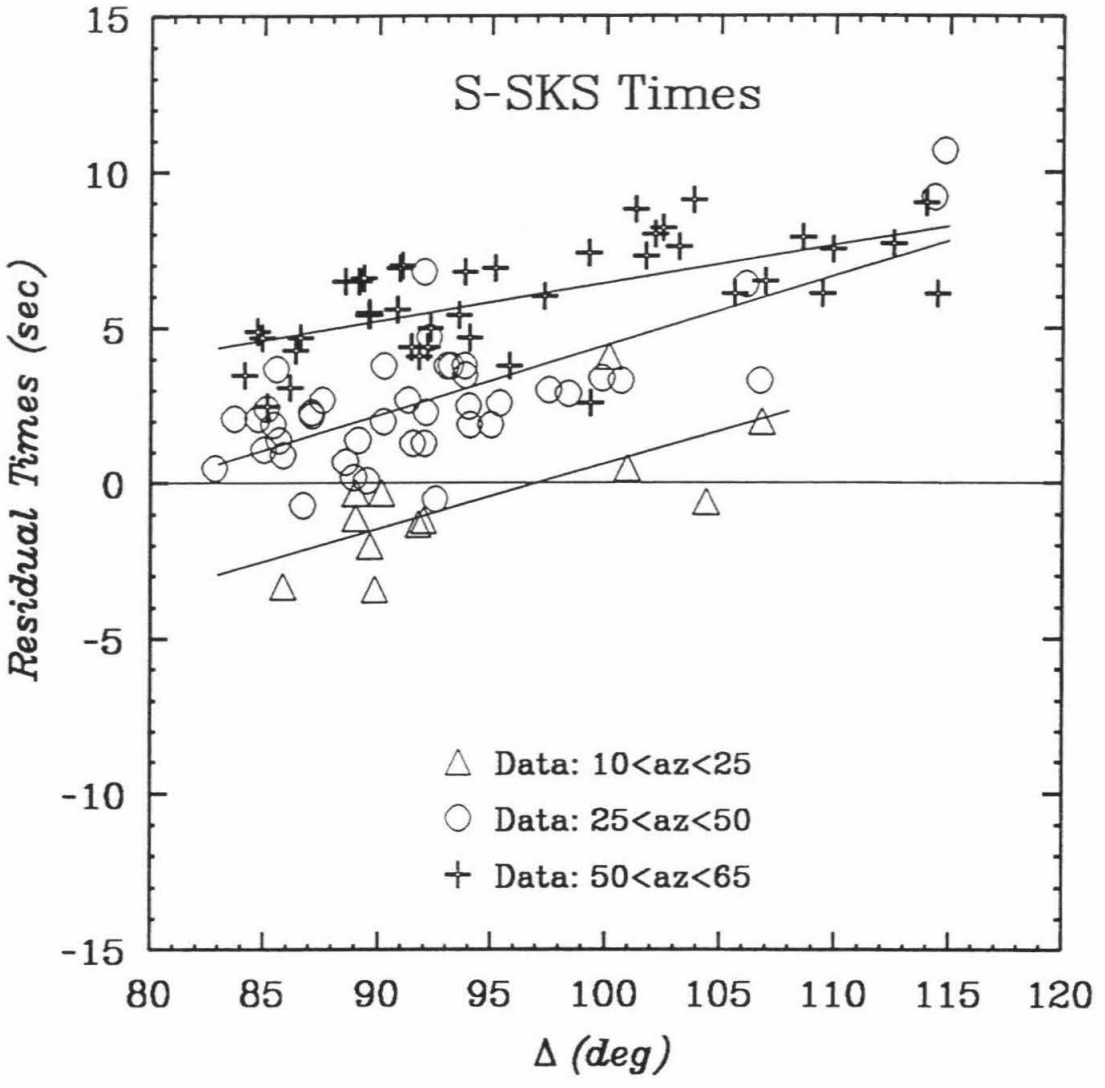

Figure 3.7: Residual travel times (with respect to *iasp91*) of $S-SKS$ are plotted as a function of distance with different symbols indicating the azimuth slice of Figure 3.5. The solid lines represent linear least square fits to the data for each of the three data groups.

in Figure 3.6b at $\Delta < 95^o$, because SKS at smaller distances spends more time in the lower mantle than do larger distance SKS arrivals. Such 2-D scenarios will be investigated more quantitatively in the following sections. First we will address implications of different 1-D models on the travel times of SKS and S.

3.5 1-D Model Implications

As reported in Garnero et al. [1988], 1-D lower mantle shear wave (V_S) structures fail to model the anomalously large central Pacific S-SKS observations. In principle, an approach can be taken whereby three different 1-D models are sought to individually explain observations from each azimuth window. However, any 1-D model having an anomalously slow lower mantle in effort to match the slow Fiji-Tonga S-wave observations predicts SKS times that are much too slow for the whole distance range of observations. Such 1-D models also underpredict the T_{S-SKS} anomaly, since both S and SKS are predicted slow, thus the predicted difference time is less anomalous than observed. While more emphasis is put on the differential times of S and SKS, the absolute times contain important information that can be used as constraints on different travel time experiments. However, since we do not make an effort to include source or receiver effects, only the general trends in the absolute times will be considered here.

SKS arrival times are highly sensitive to outer core velocity structure. In fact, $SmKS$ (SKS, $SKKS$, etc.) times have been used in many studies to infer outer core velocity structure [for example, Randall, 1970; Hales and Roberts, 1971; Kind and Müller, 1977; Lay and Young 1990; Souriau and Poupinet, 1991; and Kohler and Tanimoto, 1992]. In principle, the magnitude of the anomalous δT_{S-SKS} times in Figure 3.6c can be modeled by using a much faster outer core model, such as that of Randall [1971], to speed up SKS relative to S, thus increasing T_{S-SKS},

along with a slow lower mantle model to delay S times. Our $S - SKS$ observations indicate that such a model would have to vary laterally over extended depth ranges in the outer core in order to model the data. Such large outer core P-wave velocities (V_P) variations are routinely assumed highly unlikely due to the low viscosity in the outer core. Bounds on lateral velocity changes in the outer core are expected to be orders of magnitude smaller [Stevenson, 1987] than necessary to explain the $S - SKS$ anomalies.

This issue of outer core heterogeneity is discussed in greater detail in Chapter 7 of the thesis. Nevertheless, an attempt can be made to account for mantle side heterogeneity. In the recent study of Kohler and Tanimoto [1992], the 3-D mantle model of Tanimoto [1990] is subtracted off of long-period (33-100 s) $SmKS$ data to infer a $\pm$ 5% variation in V_P in the outermost 200 km of the core [see also Souriau and Poupinet, 1990; and Tanaka and Hamaguchi, 1993b]. Such anomalies can produce $\pm$ 5-6 sec T_{SKS} anomalies for the extreme cases where SKS enters the outer core in a $\pm$ 5% V_P anomaly, and exits the core through a 5% V_P anomaly of the same sign. For such a scenario to explain the δT_{S-SKS} residuals plotted in Figure 3.6c, SKS times would have to be anomalously fast to produce a larger T_{S-SKS} time, since SKS arrives before S for our distance range. Therefore attributing the anomalously large difference times of S and SKS to solely the outer core would require a faster outer core for our anomalous azimuths $25^o - 50^o$ and $50^o - 65^o$. There is qualitative agreement between this requirement and the outer core V_P map of Kohler and Tanimoto [1992]. Unfortunately, the trade off in outer core P velocity with lower mantle S velocity is an inherent feature of any $SmKS$ data set. In this study we choose to explore various 3-D lower mantle models, while keeping the outer core fixed as a laterally homogeneous model. This is motivated in part by the suggestion of Figure 3.6 that larger travel-time anomalies exist for S and diffracted S than for SKS, and also by our limitations of using only one phase of the $SmKS$ group, namely SKS.

The residual times of SKS in Figure 3.6b have a mean near 1 sec in the distance range of $\Delta > 95^o$, with scatter on the order of several seconds. To extract any deep earth information from only SKS, source information and receiver structure must be assessed. However, differential travel times of $SmKS$ (e.g., $T_{SKKS-SKS}$, etc.) are useful for such modeling [Schweitzer, 1986; Schweitzer and Müller, 1986; Lay and Young, 1990; Souriau and Poupinet, 1991; and Kohler and Tanimoto; 1992]. No effort is made here to resolve such differences, as we will concentrate mainly on the difference times of S and SKS. It is noted however that the δT_{SKS} times in Figure 3.6b are anomalously slow between 83^o and 95^o degrees, tapering to near 1 sec at larger distances. For this trend to be solely attributed to outer core V_P structure, an outer core model with a very slow outermost core would be necessary, along with an anomalously fast deeper core to produce the small mean in δT_{SKS} at larger distances ($\Delta > 95^o$.) Figure 3.8a displays the outer core models of *iasp91*, Hales and Roberts [1971], Lay and Young [1990], Randall [1970], Souriau and Poupinet [1991], and Dziewonski and Anderson [1981]. The predictions of T_{SKS} residuals (with respect to *iasp91*) for these five outer core models are presented in Figure 3.8b along with the observations. The Randall [1970] model predicts the fastest SKS times, while the Hales and Roberts [1971] model predicts the slowest. The models of Lay and Young [1990], Souriau and Poupinet [1991] and Dziewonski and Anderson [1981] are intermediate between the latter two models, and provide the best overall fit of the five models in Figure 3.8a to the data. However, effects of the mantle must be addressed before choosing an appropriate outer core model. For example, a very slow central Pacific D$''$ anomaly will slow down SKS at the smaller distances, whose raypaths spend more time in the lower mantle than do large delta SKS paths. Such a scenario would be compatible with the δT_{SKS} observations at small delta (Figure 3.8b).

Figure 3.8: (a) P-wave velocity models of the Earth's outer core. (b) Residual travel times (with respect to *iasp91*) of SKS observations (circles shaded to indicate azimuth) plotted with predictions of the outer core models of (a). The *iasp91* mantle has been used for the calculations in (b).

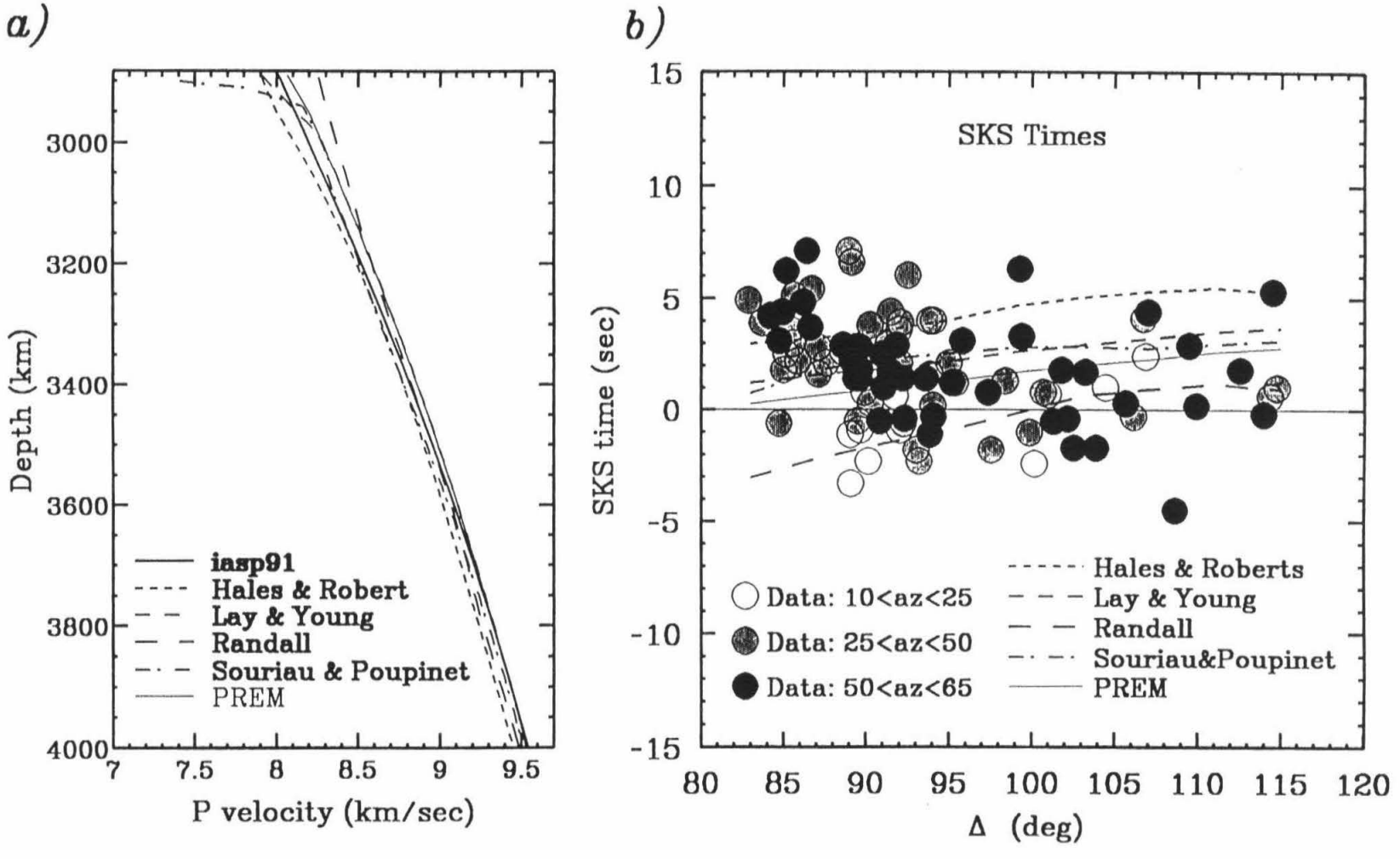
a)
b)
Depth (km)
P velocity (km/sec)
iasp91
Hales & Robert
Lay & Young
Randall
Souriau & Poupinet
PREM
SKS Times
SKS time (sec)
Δ (deg)
Data: 10<az<25
Data: 25<az<50
Data: 50<az<65
Hales & Roberts
Lay & Young
Randall
Souriau&Poupinet
PREM

3.6 S-SKS Time Predictions from 3-D Models

In this section predictions for $S - SKS$ times are made for three different 3-D tomographic V_S models of the mantle. The models used for comparison are MDLSH of Tanimoto [1990], SH.10c.17 of Masters et al. [1992], and SH12_WM13 of Su et al. [1992]. Basic information about these models is listed in Table 3.2. Models MDLSH and SH.10c.17 are parameterized with depth into 11 spherical shells for the whole mantle [see Tanimoto, 1990]. The thickness of the shells varies from around 180 km to 350 km thick. Model SH12_WM13, however, is parameterized vertically with Chebyshev polynomials. A conversion subroutine [Su, personal communication; 1992] was used to convert this model into a series of layered shells to be in the same format as the other two models. Model SH12_WM13 of Su et al. [1992] has been updated in Su et al. [1994], but displays nearly identical features in the lower mantle beneath the central Pacific.

Three great circle paths from the Fiji-Tonga source region to North America are chosen to represent the mean of the paths for each specific azimuth window of Figure 3.5. These three representative paths, termed AZ1, AZ2, and AZ3, are for azimuths of around 13^o, 39^o, and 60^o, respectively, and are shown in Figure 3.9 with the map view of the D'' layer anomalies for the 3 models. As the figure indicates, the degree 2 component of the models is similar, but some of the details widely differ. Also shown in the figure are solid black triangles representing distances of 85^o, 95^o, 105^o, and 115^o along each path from a hypothetical Fiji-Tonga source at 500 km depth, latitude -20.0^o, and longitude -179.0^o. Here the assumption is made that the average of the δT_{S-SKS} times for each azimuth window in Figure 3.6c can be modeled by a single great circle path 2-D cross-section (one cross-section for each azimuth window), based on the small scatter for each azimuth sector. δT_{S-SKS} predictions of the tomographic models are made for these representative cross-sections and the above hypothetical source, and then compared to observations.

Model	Researcher	Deg	CMB scale	Data
MDLSH	Tanimoto [1990]	6	3400	Waveform inversion of long-period (40-100 sec) SH body waves S, SS, SSS, etc., and long-period (100-500 sec) Love-waves.
SH.10c.17	Masters et al. [1992]	10	2100	Inversion of travel-times of long period body waves S, SS, SSS, differential times of $SS-S$, $ScS-S$, $sS-S$, and free oscillation structure coefficients.
SH12_WM13	Su et al. [1992]	12	1800	Joint inversion of travel times of S, ScS, differential times of $SS-S$, $ScS-S$, and the waveforms of body and mantle waves.

Table 3.2: Tomographic models used for T_{S-SKS} predictions in this study. CMB scale denoted minimum CMB scale length in km.

Figure 3.9: Map views of the D″ layer of models MDLSH, SH.10c.17, and SH12_WM13 are shown in (a), (b), and (c), respectively. Also shown for each are the three representative azimuths AZ1, AZ2, and AZ3 corresponding to the azimuth slices of Figure 3.5. The triangles indicate epicentral distances along the great circle paths of 85°, 95°, 105°, and 115°. Dark regions represent slower than average velocities, while light regions represent faster than average velocities.

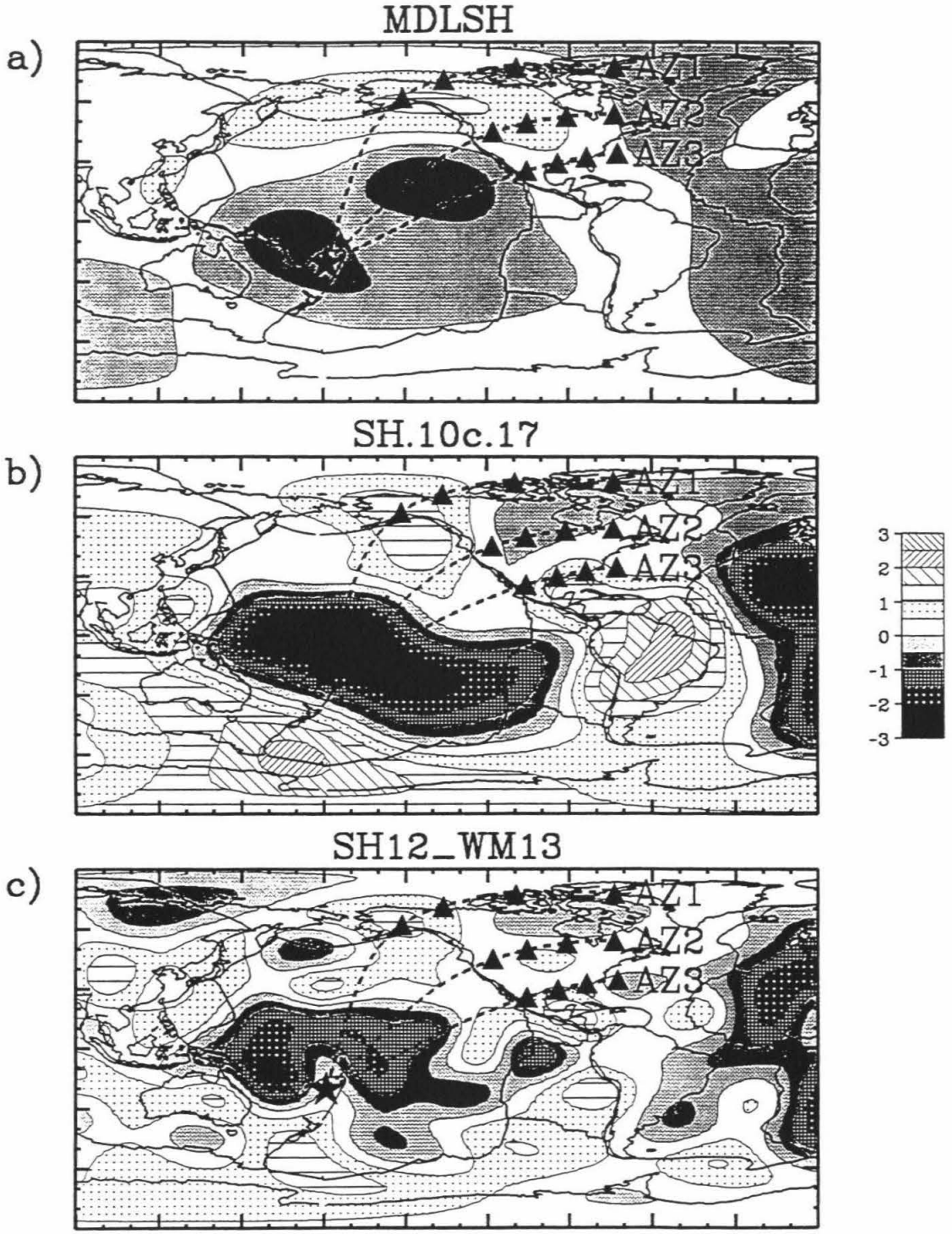
MDLSH
a)
AZ1
AZ2
AZ3
SH.10c.17
b)
AZ1
AZ2
AZ3
3
2
1
0
-1
-2
-3
SH12_WM13
c)
AZ1
AZ2
AZ3

The technique employed to calculate δT_{S-SKS} predictions for the tomography models assumes the ray paths of S and SKS from source to receiver are those of a laterally homogeneous Earth, and then the residuals for the specific paths and 3-D model are added up along each ray path. The predicted δT_{S-SKS} residuals were obtained using the PREM reference model [Dziewonski and Anderson, 1981] since the residuals were originally derived with respect to PREM. Each of the 11 spherical shells where divided into a grid of blocks. Each block measures about 250 km square laterally, having the vertical dimension of the thickness of the spherical shell. V_S residuals for a specific model were then assigned to the 3-D network of blocks. This parameterization is convenient to calculate residuals for specific ray paths, though it is an approximation, see Grand [1989]. However, with the horizontal length scales of features in the tomographic models being on the order of 3000 km and greater, such an approximation is justified.

For the following predictions of the residual times of S and SKS, the *iasp91* core model has been used. Since we first wish to assess mantle affects on these travel-times, the choice of a core model is arbitrary due to the trade-off mentioned above. The offset of any favored core model from the zero line of *iasp91* in Figure 3.8b may be added to any of the 3-D predictions that follow. This will in affect adjust the δT_{S-SKS} measurement to be that which includes the favored core model.

3.6.1 Model MDLSH Predictions

Whole mantle cross-sections for the shear wave velocity model MDLSH of Tanimoto [1990] are presented in Figure 3.10 for the great circle paths in Figure 3.9 (Figure 3.10a, b, and c corresponds to AZ1, AZ2, and AZ3, respectively). The contour plots are rectangular mappings of the mantle heterogeneities, where the vertical dimension of the box is the thickness of the mantle, and the horizontal dimension is 115^o in arc. The actual horizontal dimension at the Earth's surface (top of the box)

is about 12800 km, while at the CMB (bottom of the box) it is $\approx$ 7000 km. Mapping of ray paths of SKS and S (and S_{diff}) for the laterally homogeneous model *iasp91* [Kennett and Engdahl, 1991] are also shown for the distances 85°, 95°, 105°, and 115°. The V_S heterogeneities are plotted by percent, where dark regions indicate slower than average velocities, and white and hatched regions represent faster than average velocities. Model MDLSH predicts a slow anomaly growing out of D″ beneath the central Pacific region in sweeping from AZ1 to AZ3. All of the S ray paths traverse this slow anomaly in the more easterly azimuths, but SKS paths miss it. This is in qualitative agreement with what might be needed to slow down S relative to SKS in order to model anomalously large $S-SKS$ times. The actual T_{S-SKS} residual time predictions of the cross-sections in Figure 3.10 are presented in Figure 3.11 (plotted with respect to *iasp91*) along with the data from Figure 3.6c. As in Figure 3.6c, the different symbols correspond to data from the three different azimuth slices of Figure 3.5. The lines represent the δT_{S-SKS} time predictions of MDLSH. The line with long dashes is for AZ1, and poorly fits data from that azimuth (white circles). The line with short dashes is for AZ2 and fits the data for that azimuth (gray circles) within the scatter for distances $< 100^o$ though is too small by several seconds at larger Δ (though data sampling are sparser for this azimuth at larger ranges.) The solid line is the prediction for AZ3 and is too small by 2-3 sec, though the predictions has the approximate shape of the trend of the data. Also, the MDLSH predictions for AZ1, AZ2, and AZ3 are all nearly the same near 85°, where the data visibly group separately for the different azimuths. At distances larger than 105°, the MDLSH predictions have the relative trend of δT_{S-SKS}(AZ3) > δT_{S-SKS}(AZ2) > δT_{S-SKS}(AZ1), which qualitatively agrees with the observations.

As an alternative attempt at modeling the observations with MDLSH, the residuals in the bottom four layers of the mantle (the bottom 1075 km of the lower mantle) were doubled in value to produce model "MDLSH+" (Figure 3.12abc). Such an ex-

Figure 3.10: Whole mantle cross-sections from model MDLSH of Tanimoto [1990] for azimuths AZ1, AZ2, and AZ3 of Figure 3.5 in (a), (b), and (c), respectively. The vertical dimension of each plot is 2891 km, and the horizontal dimension is 115° in epicentral distance. V_S perturbations in percent are shown, where dark regions are slower than average, white and hatched regions are faster than average. The star and triangles for each cross-section represent a 500 km deep source at (-20,-179) and stations at 85°, 95°, 105°, and 115°, respectively. Also plotted are the mantle raypaths of S and SKS for the above distances.

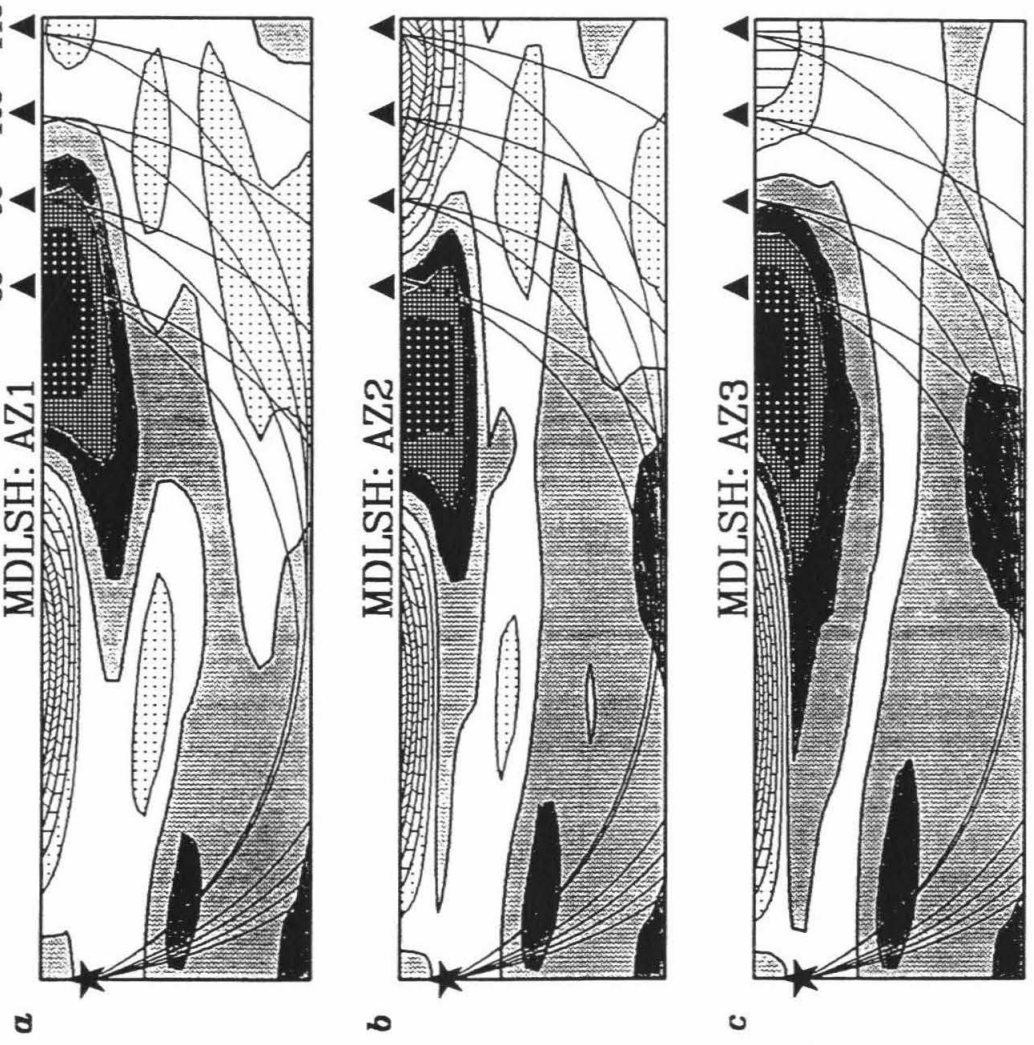
MDLSH: AZ1
MDLSH: AZ2
MDLSH: AZ3
85
95
105
115
%
3
2
1
0
-1
-2
-3
a
b
c

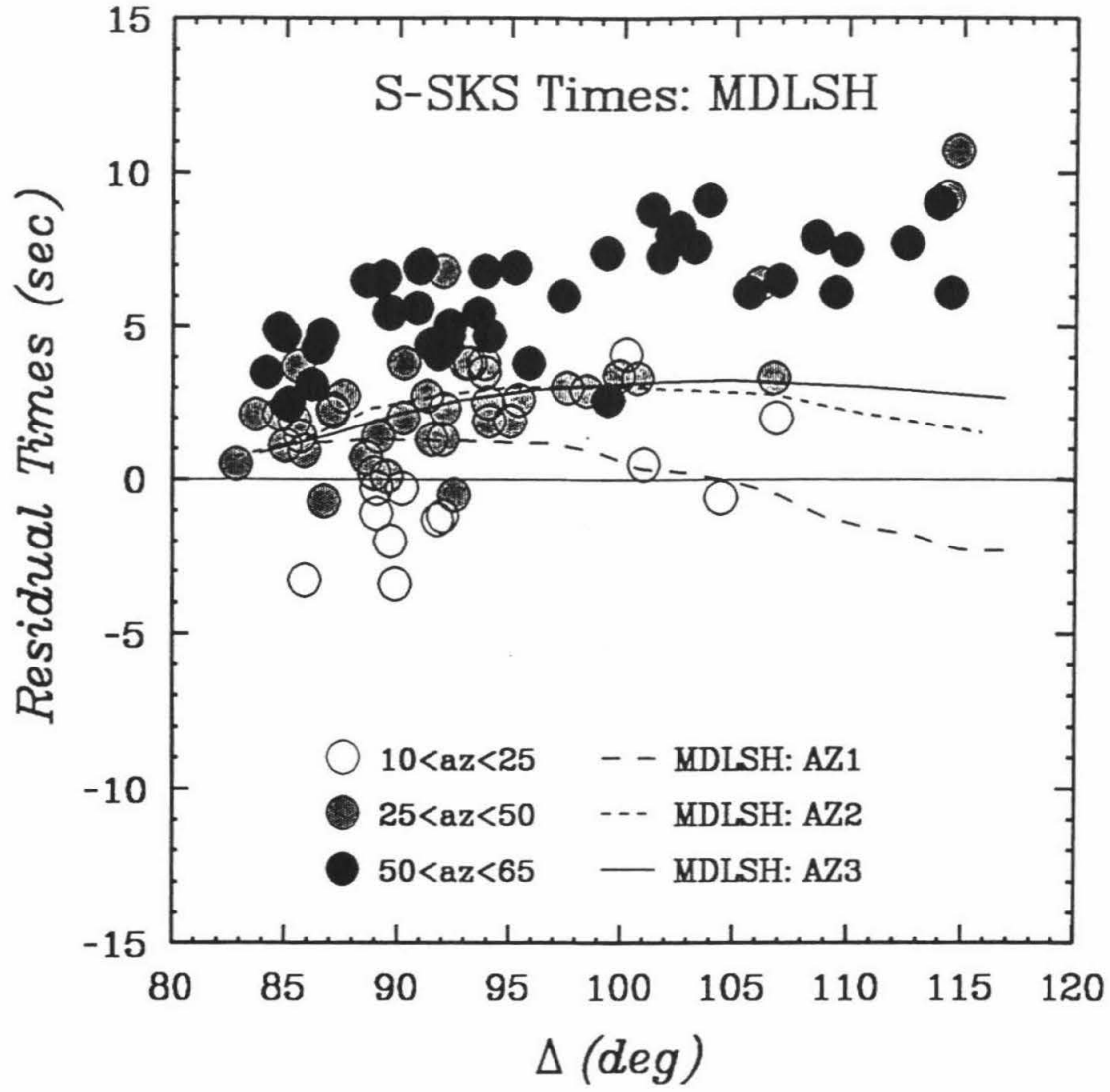

Figure 3.11: Residual travel times (with respect to *iasp91*) of $S-SKS$ (circles shaded to correspond to azimuth slice) are plotted as a function of distance along with the predictions from model MDLSH (lines) for the three cross-sections AZ1, AZ2, and AZ3 shown in Figure 3.10.

ercise is arbitrary, but may be justified due to an ambiguity in the choice of damping parameters used in originally constructing MDLSH [Tanimoto, personal communication, 1992]. As Figure 3.12 shows, this emphasizes the growth of the lower mantle slow anomaly from Figure 3.12 (a) to (c). It also accentuates the fast lower mantle anomaly underneath the receivers in Figure 3.12a. The δT_{S-SKS} residuals predicted for MDLSH+ are compared to observations in Figure 3.13. All plotting conventions are the same as Figure 3.11. A first-order affect of doubling δV_S in the bottom four layers is to enlarge the positive δT_{S-SKS} predictions and decrease the negative δT_{S-SKS} predictions (from those in Figure 3.11.) Doing this predicts $S-SKS$ difference times for AZ1 and AZ2 that are incompatible with the data. However, the increased size of the mid-Pacific lower mantle slow anomaly in Figure 3.12c increases the predicted δT_{S-SKS} for that cross-section, and the fit to the data for that azimuth (black circles) is greatly improved. Given the scatter in the data of $\approx \pm 2$ sec for that azimuth, we consider this a good fit. In doubling the size of the δV_S residuals in the bottom four layers of the mantle, the resulting $S-SKS$ travel time residuals are roughly doubled (compare Figure 3.11 and Figure 3.13). This is expected since δT_{S-SKS} times are very sensitive to the lowermost mantle.

In summarizing the predictions of MDLSH, the following may be stated: (i) δT_{S-SKS} predictions for the most northerly azimuth cross-section AZ1 from Fiji-Tonga to North America differ from observations; (ii) at distances $< 100^{\circ}$, δT_{S-SKS} predictions for AZ2 are fair to good, and within the scatter of the data; (iii) when δV_S in the bottom four layers (bottom 1075 km of mantle) of MDLSH is doubled, the δT_{S-SKS} predictions for AZ3 are greatly improved, resulting in a fit for the whole distance range within the scatter of the data, though this causes predictions for AZ1 and AZ2 to increasingly differ from the observations. A combination of the two models MDLSH and MDLSH+ may in turn provide good fits to data from both of the azimuths AZ2 and AZ3, however predictions from AZ1 disagree with our

Figure 3.12: Whole mantle cross-sections from model MDLSH+, which is MDLSH of Tanimoto [1990] with residuals in bottom four layers doubled. Cross-sections for AZ1, AZ2, and AZ3 are presented in (a), (b), and (c), respectively. V_S perturbations in percent are shown, where dark regions are slower than average, white and hatched regions are faster than average. See Figure 3.10 caption and text for more information.

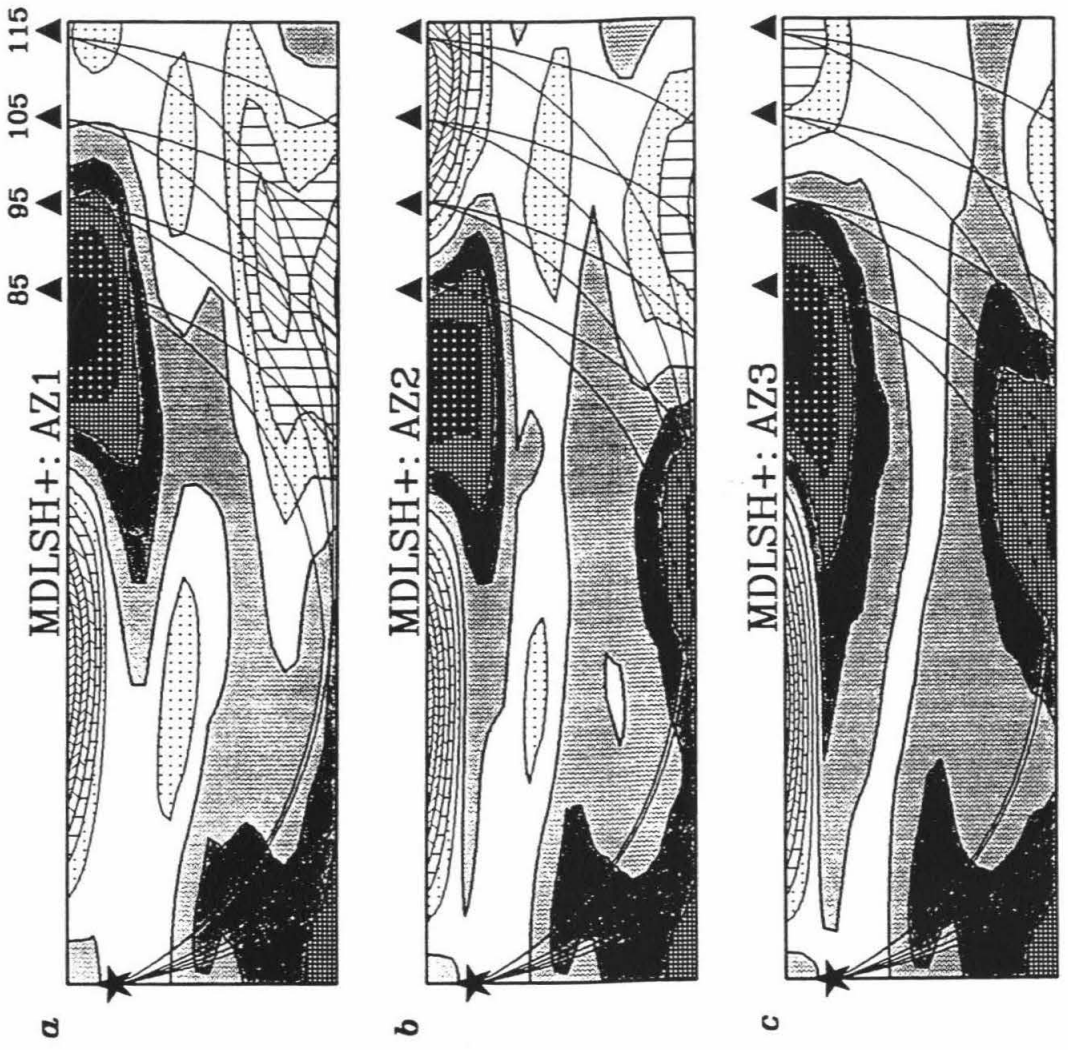
MDLSH+: AZ1
85
95
105
115
a
MDLSH+: AZ2
b
MDLSH+: AZ3
c
%
3
2
1
0
-1
-2
-3

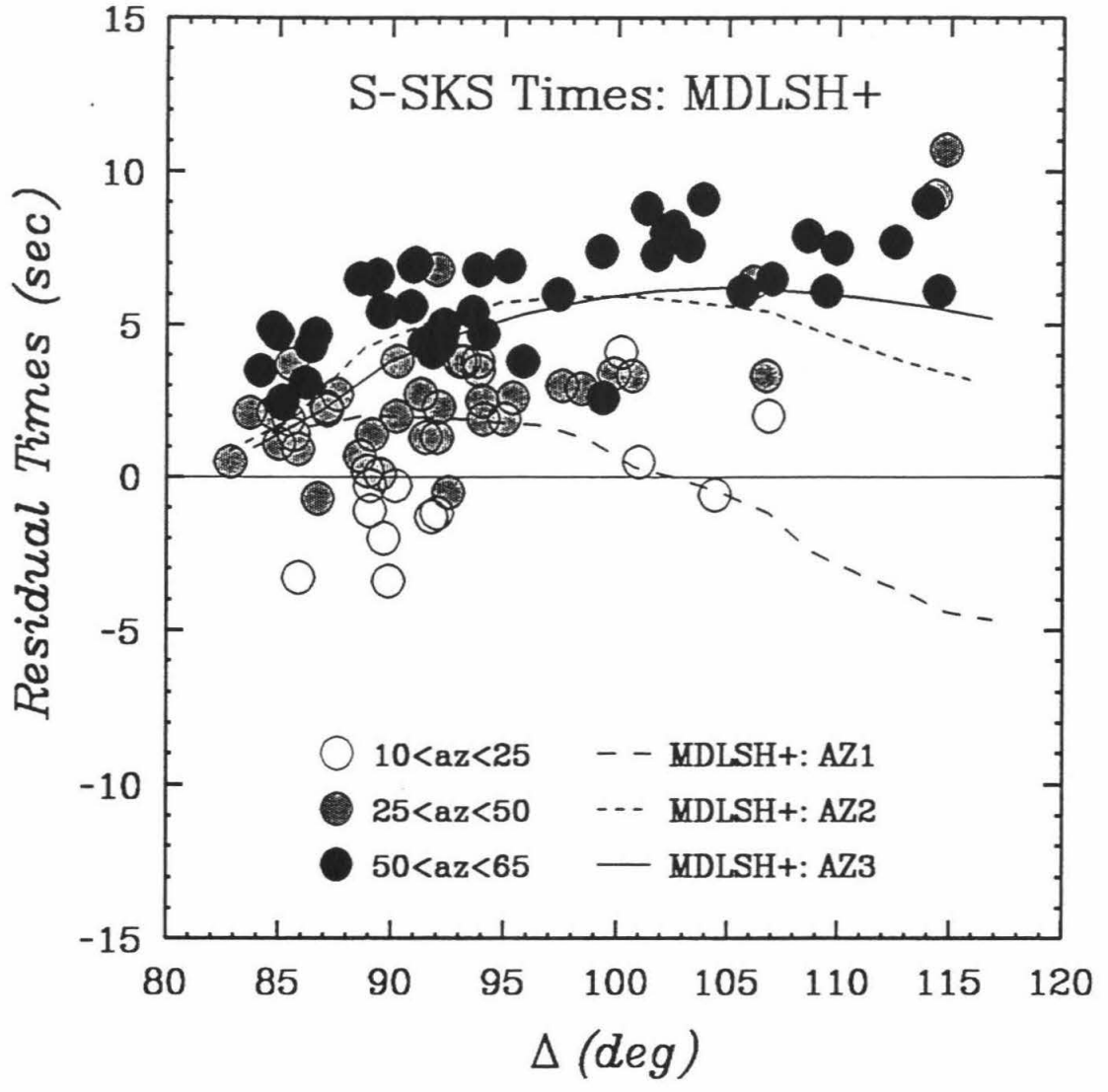

Figure 3.13: Residual travel times (with respect to *iasp91*) of $S-SKS$ (circles shaded to correspond to azimuth slice) are plotted as a function of distance along with the predictions from model MDLSH+ (lines) for the three cross-sections AZ1, AZ2, and AZ3 shown in Figure 3.12.

observations.

3.6.2 Model SH.10c.17 Predictions

Whole mantle cross-sections for the shear wave velocity model SH.10c.17 of Masters et al. [1992] are presented in Figure 3.14 for the great circle paths in Figure 3.9 (again, Figure 3.13a, b, and c corresponds to AZ1, AZ2, and AZ3, respectively). A first-order difference between this model and MDLSH (or MDLSH+) is the location of the lower mantle slow anomaly: in SH.10c.17, the slow anomaly is roughly 2000 km closer to the source-side of the ray paths (compare Figure 3.12c and Figure 3.14c). Other features, such as upper mantle structure, also differ. The δT_{S-SKS} predictions of SH.10c.17 are presented along with the observations in Figure 3.15. For this model, the δT_{S-SKS} predictions for all three azimuths are within a $\pm$ 3 sec range with respect to *iasp91*. This is much smaller than the range of the data, where the anomalies are as large as 8-9 sec. However, the SH.10c.17 predictions for AZ1 (line with long dashes) are within the scatter of the data for that azimuth (white circles) for the distance range of the observations. Also, the SH.10c.17 predictions for AZ2 (line with short dashes) provide a fit to the data for that azimuth (gray circles) within the scatter up to near 95°. For distances greater than 95°, SH.10c.17 under-predicts the observations. For AZ3 (solid line), the SH.10c.17 predictions of δT_{S-SKS} are several seconds smaller than the observations. The reason that the δT_{S-SKS} predictions for this azimuth are not larger than 1-2 sec is due to the large lower mantle, slightly fast anomaly in Figure 3.14c. From Figure 3.14a to Figure 3.14c, this anomaly becomes less fast, though in 14c there is still a large enough negative contribution from this anomaly to counter the slow lower mantle anomaly on the source-side of the path.

Summarizing the predictions of SH.10c.17: (i) δT_{S-SKS} predictions for the most northerly azimuth cross-section AZ1 from Fiji-Tonga to North America provide a fair fit to the data within the scatter; (ii) at distances $< 95°$, δT_{S-SKS} predictions for

Figure 3.14: Whole mantle cross-sections from model SH.10c.17 of Masters et al. [1992] with Cross-sections for AZ1, AZ2, and AZ3 are presented in (a), (b), and (c), respectively. V_S perturbations in percent are shown, where dark regions are slower than average, white and hatched regions are faster than average. See Figure 3.10 caption and text for more information.

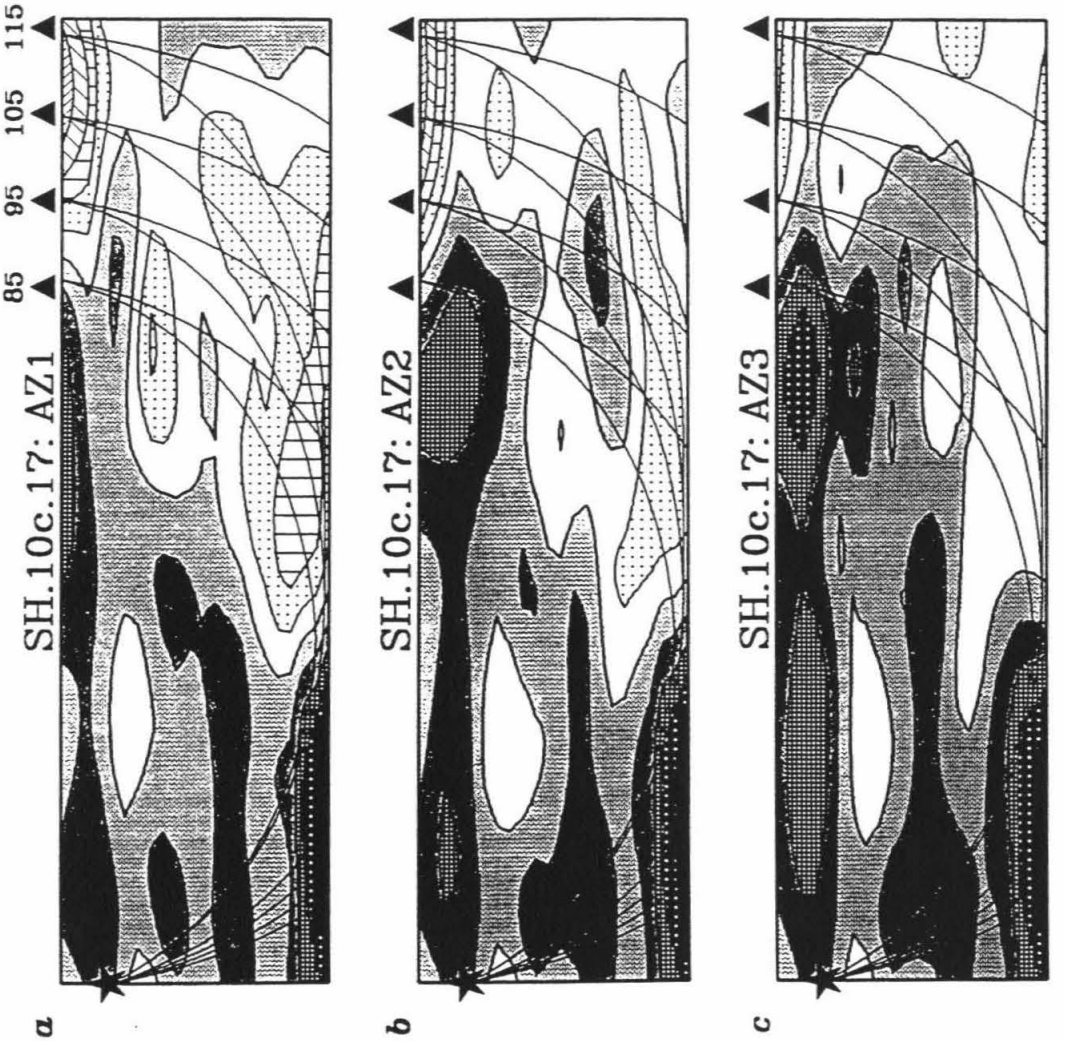
SH.10c.17: AZ1
SH.10c.17: AZ2
SH.10c.17: AZ3
85
95
105
115
%
3
2
1
0
-1
-2
-3
a
b
c

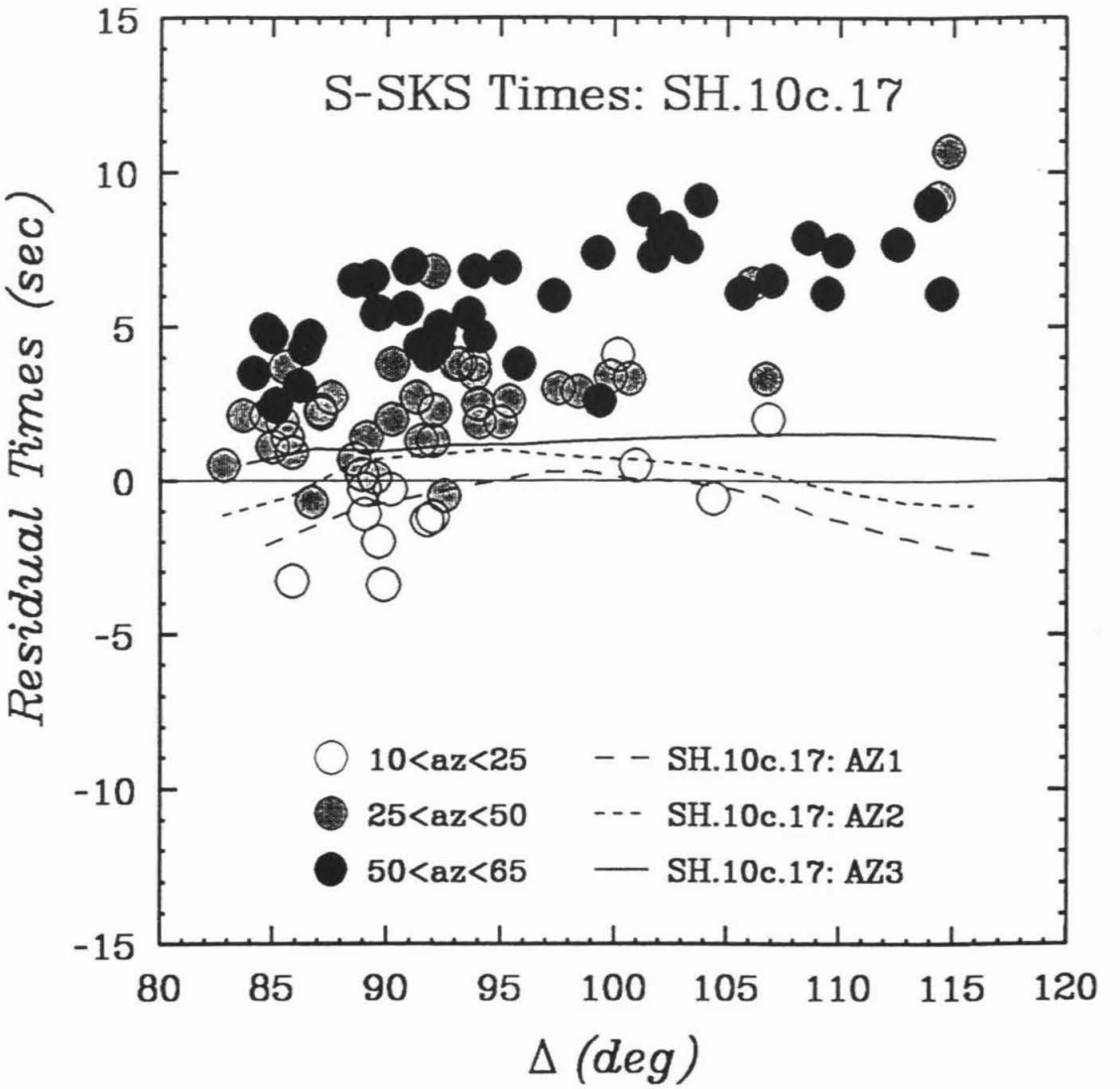

Figure 3.15: Residual travel times (with respect to *iasp91*) of $S-SKS$ (circles shaded to correspond to azimuth slice) are plotted as a function of distance along with the predictions from model SH.10c.17 (lines) for the three cross-sections AZ1, AZ2, and AZ3 shown in Figure 3.14.

AZ2 are fair to good, and within the scatter of the data; (iii) the δT_{S-SKS} predictions for AZ3 are several seconds smaller than the average of the data for that azimuth; (iv) for the entire distance range, predictions of δT_{S-SKS}(AZ3) > δT_{S-SKS}(AZ2) > δT_{S-SKS}(AZ1), which qualitatively agrees with the observations; and (v) there is not substantial "growth" of the the low velocity D'' anomaly as seen in the other models.

3.6.3 Model SH12_WM13 Predictions

Whole mantle cross-sections for the shear wave velocity model SH12_WM13 of Su et al. [1992] are presented in Figure 3.16abc for the great circle paths AZ1, AZ2, and AZ3, respectively. For these cross-sections, model SH12_WM13 is very similar to SH.10c.17 in Figure 3.14abc. The main difference is that the sizes of the SH12_WM13 anomalies are larger, and there is a more pronounced increase in the low velocity region toward AZ3. Of significance is the increased size of the lower mantle slow anomaly in Figure 3.16c on the source-side of the path. This serves to further slow down S relative to SKS, which in principle will give a better fit to the observations. This slow anomaly, as in SH.10c.17, is $\approx$ 2000 km closer to the source-side of the path than that of MDLSH (and MDLSH+, see Figures 3.16c and Figure 3.12c). The δT_{S-SKS} predictions of SH12_WM13 are compared to the data in Figure 3.17. The predictions for AZ1 (long dashes) are 1-2 sec larger than observations (white circles) for distances < 95°, though at larger distances they fit the mean of the remaining AZ1 data points. SH12_WM13 predictions for AZ2 (short dashes) are within the scatter of the data (gray circles) for nearly the entire distance range (excluding only two anomalous points at 114°). For the azimuth AZ3, the predictions (solid line) are within the scatter of the observations (black circles) for up to around 100°. For larger ranges, SH12_WM13 predicts δT_{S-SKS} 2-3 s smaller than observations. The size of the relative differences in the SH12_WM13 predictions for the three different

azimuths is very close to that of the observations.

For model SH12_WM13, we summarize: (i) the first-order fit to the data for all three azimuths is fair to good within the scatter of the data, and more specifically: (ii) δT_{S-SKS} predictions for AZ1 provide a fair fit to the data within the scatter for distances $> 95^o$; (iii) predictions for AZ2 are within the scatter of the data for the entire distance range (except for two data at 114^o); (iv) the δT_{S-SKS} predictions for AZ3 are also with the scatter of the observations for distances $< 100^o$. (v) the relative differences of the predictions for the three different azimuths roughly matches relative differences of the observations from the different azimuth slices.

3.7 Discussion

In comparing direct measurements of the observed differential travel times of S and SKS phases with those predicted by tomographic models of the mantle, an understanding may be gained concerning what part of the Earth's structure plays the most important role in affecting these difference times. Such comparisons, as presented in the previous section, suggest that 3-D mantle models may ultimately account for all of the T_{S-SKS} anomalies. To test the sensitivity of the δT_{S-SKS} predictions to the depth of 3-D mantle structure, predictions of δT_{S-SKS} were made for the tomographic models with various thicknesses of the upper mantle made laterally homogeneous. Specifically, calculations of δT_{S-SKS} were made for cases where contributions from the tomographic models were limited to the depth ranges 0-2891 km, 670-2891km, 1022-2891 km, 1555-2891 km, and 1816-2891 km (which correspond to depths of boundaries between various model layers.) In these runs, no contribution to δT_{S-SKS} is made from the mantle above the boundary between the 1-D and 3-D sections. The results for model SH12_WM13 of Su et al. [1992] are presented in Figure 3.18. Predictions for the three azimuth cross-sections AZ1, AZ2, and AZ3 of

Figure 3.16: Whole mantle cross-sections from model SH12_WM13 of Su et al. [1992] with Cross-sections for AZ1, AZ2, and AZ3 are presented in (a), (b), and (c), respectively. V_S perturbations in percent are shown, where dark regions are slower than average, white and hatched regions are faster than average. See Figure 3.10 caption and text for more information.

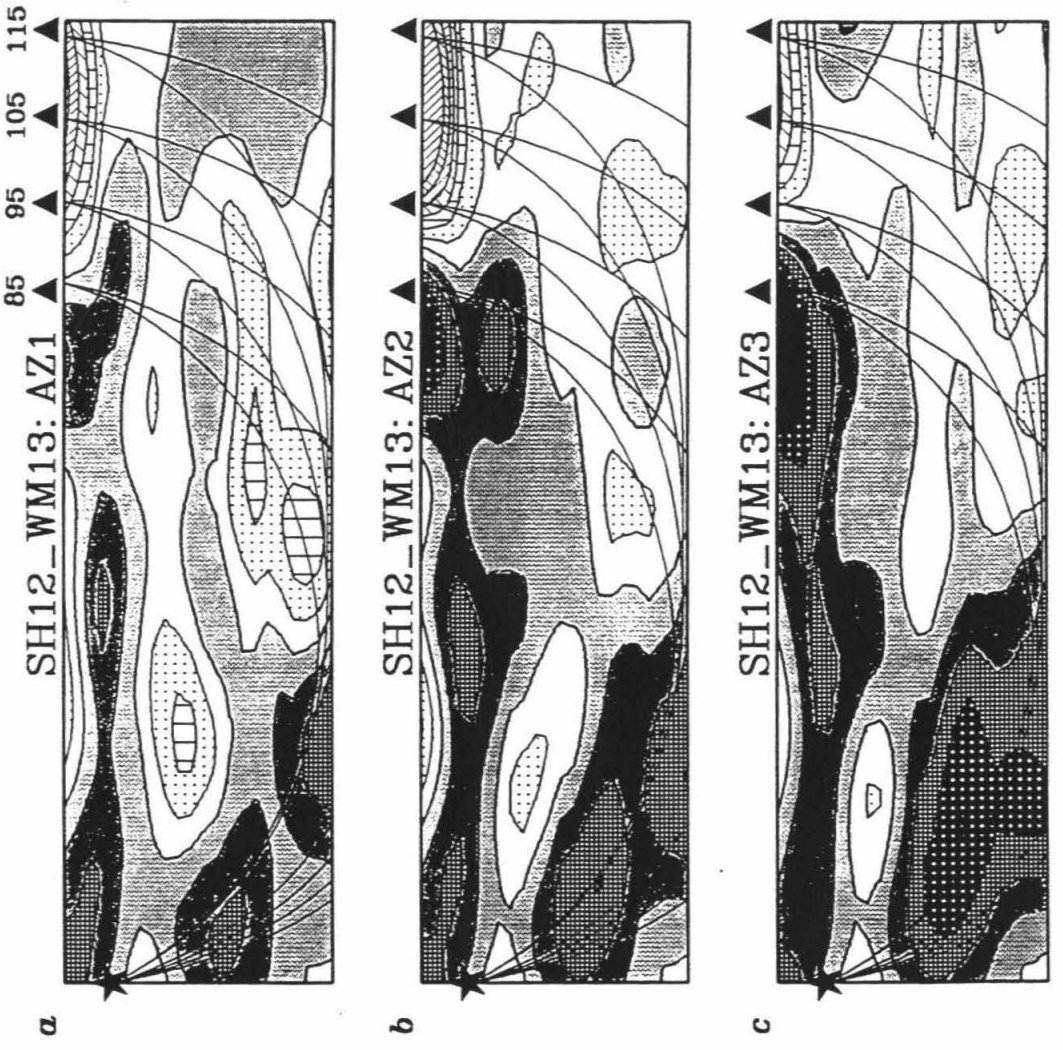
SH12_WM13: AZ1
85
95
105
115
a
%
3
2
1
0
-1
-2
-3
SH12_WM13: AZ2
b
SH12_WM13: AZ3
c

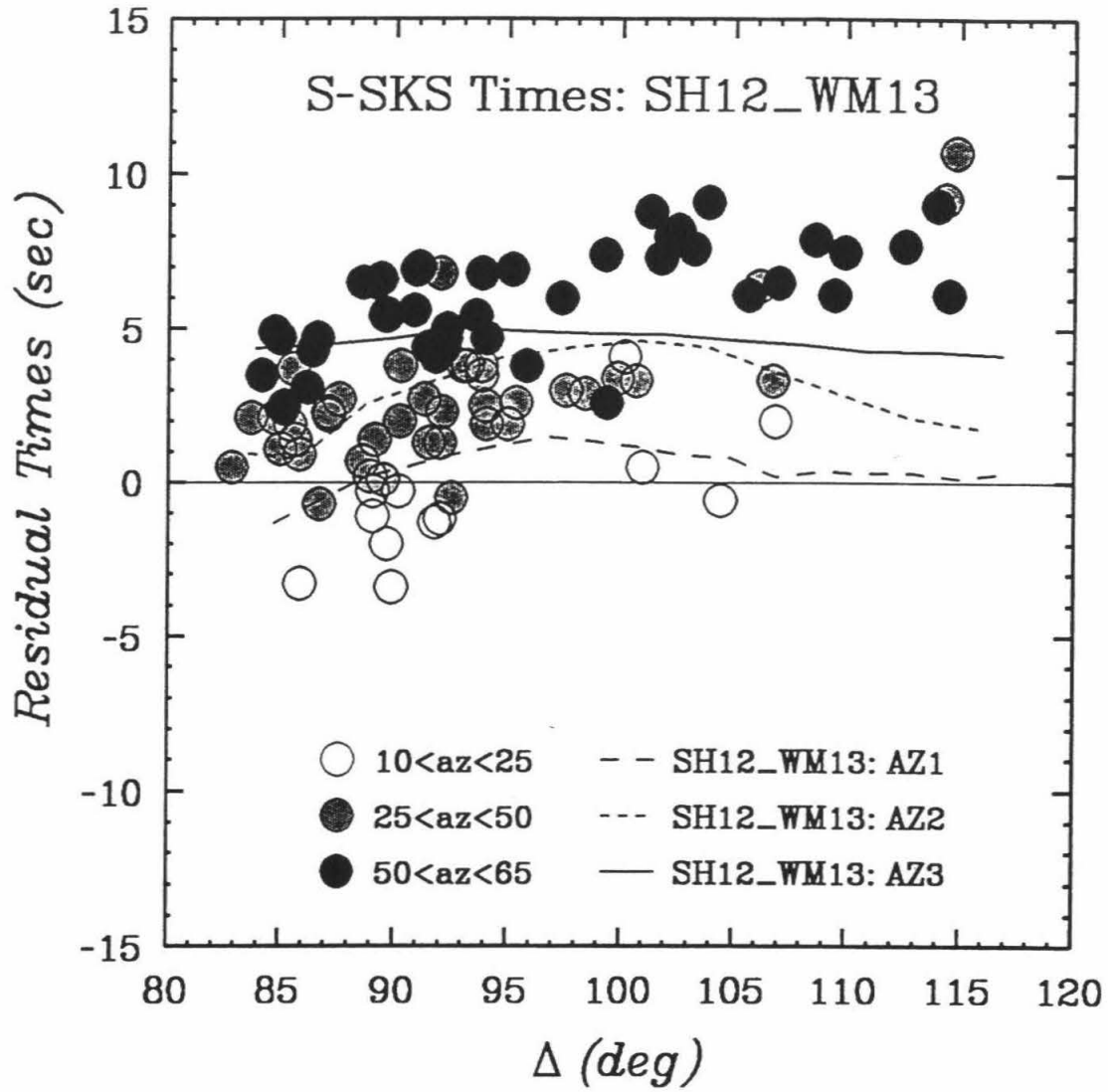

Figure 3.17: Residual travel times (with respect to *iasp91*) of $S-SKS$ (circles shaded to correspond to azimuth slice) are plotted as a function of distance along with the predictions from model SH12_WM13 (lines) for the three cross-sections AZ1, AZ2, and AZ3 shown in Figure 3.16.

Figure 3.9 are shown. The upper 670 km of the mantle contributes very little to the predicted $S - SKS$ differential travel time. This is seen from the nearly complete overlap of the solid curves for the whole mantle, and the short dashed curve for the 670-2891 km region. (Also, the predictions are made with the source at 500 km depth, so the uppermost mantle is traversed only on the receiver side of the paths.) In fact, ignoring the upper 1500 km or so of the mantle only produces deviations of less than one second from the whole mantle 3-D model predictions. Even with the 3-D mantle contributions limited to the bottom 1000 km of the mantle, the shapes of the curves for the different azimuths are basically the same, and the predictions are early on average by only $\approx$ 1 sec.

It makes intuitive sense that the anomalies in $S - SKS$ times can be produced synthetically (for this region) solely from the bottom 1500 km of a 3-D mantle, with lateral homogeneity above 1500 km depth, because it is in the deeper portion of the mantle that the paths of S and SKS diverge the most. The upper mantle of the tomography models would affect the $S-SKS$ times more if the lateral scale lengths of the anomalies were smaller. However, at present, with imaging of features with scale lengths on the order of 3000 km and greater, upper mantle affects on these predicted times are negligible. This is probably not the case in the real Earth, however. The difference in take-off angle between S and SKS for a 500 km deep source is around 10^o at 85 degrees in epicentral distance, and increases to about 15^o at 115 degrees in distance. For such take-off angle differences, small scale-length heterogeneities surely play an important role. An example of such would be near-source slab diffraction as proposed by Cormier [1989], though using deep focus events should help to minimize such effects.

In making δT_{S-SKS} predictions for the tomography models, the assumption was made that the raypaths are for a laterally homogeneous Earth structure (the same assumption made in the construction of all models tested). We are presently unable to

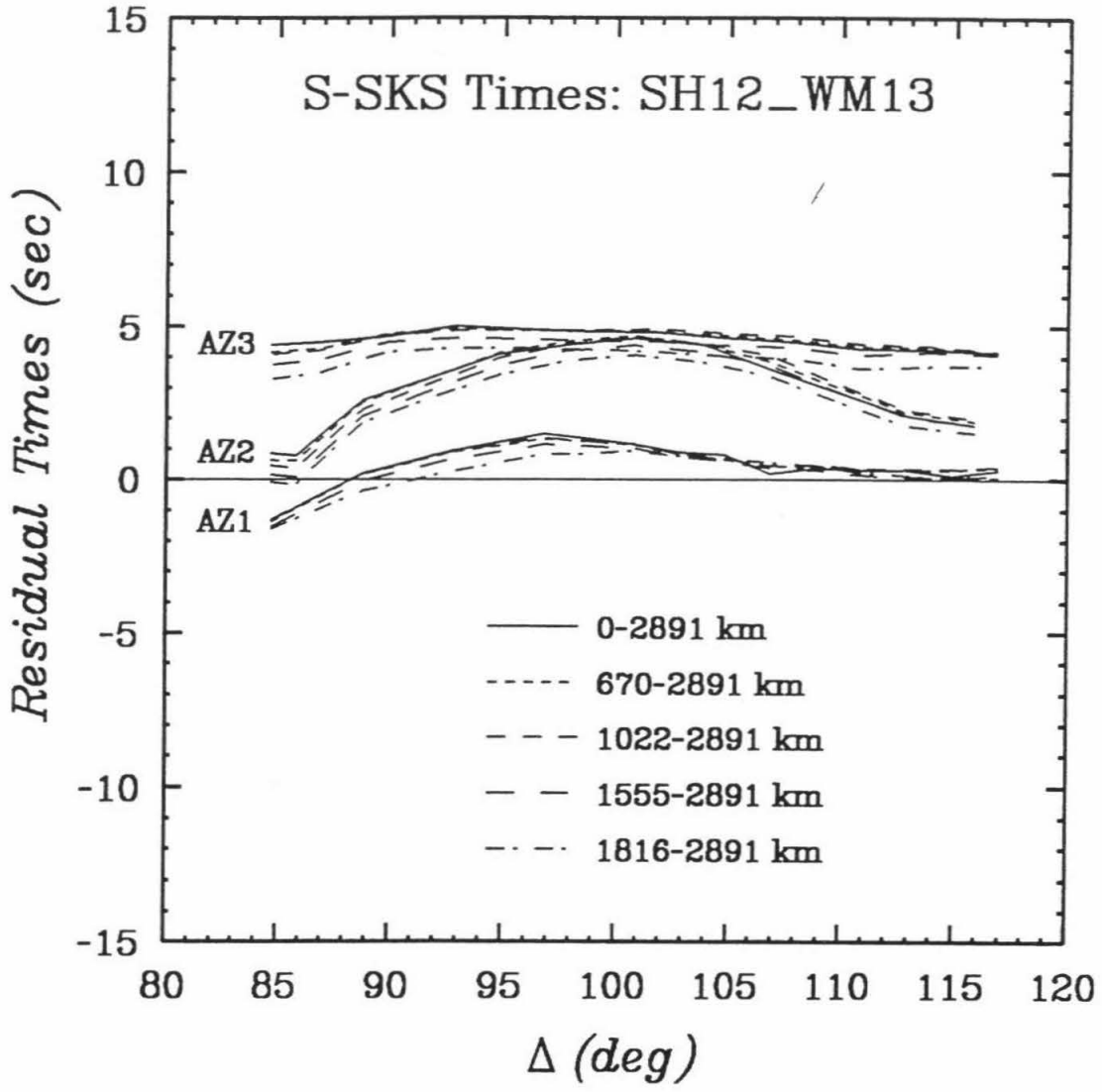

Figure 3.18: The predicted residual travel times (with respect to *iasp91*) of $S-SKS$ of model SH12_WM13 (of Figure 3.17) for AZ1, AZ2, and AZ3 (solid lines). Also plotted are predictions of residuals for various vertical thicknesses of 3-D cross-sections of SH12_WM13 where mantle above these 3-D sections is laterally homogeneous (dotted lines). The depths above correspond to depth ranges of the 3-D sections.

assess the validity of this assumption, though the features of the tomographic models are much larger than the wavelengths of the seismic waves analyzed, and presumably contribute negligibly to bending of the raypaths as to significantly affect the difference times. However, 2-D wave propagation experiments presented in Chapters 1, 4, and 6 suggest the significance of inhomogeneous wavepaths for dipping structures and strong heterogeneity in the D'' region. Future studies must pursue this issue further in order to obtain more detailed images of lower mantle heterogeneity.

Also assumed was that the outer core does not vary laterally, and the outer core from the *iasp91* reference model was used [Kennett and Engdahl, 1991]. As mentioned earlier, the δT_{S-SKS} time predictions of Figures 3.11, 3.13, 3.15, and 3.17 may be adjusted to accommodate the predictions of the other core models in Figure 3.8 by simply adding to the δT_{S-SKS} prediction the subtraction (from Figure 3.8b): T_{SKS}(*iasp91*) - T_{SKS}(preferred core model). The T_{SKS} times alone cannot be used to determine outer core structure without first accounting for the affects of mantle heterogeneity, which at present are not adequately resolved for such a purpose.

Figure 3.19 shows the observed δT_{SKS} times of Figures 3.6b, along with predictions for δT_{SKS} where SKS has traversed the whole mantle model SH12_WM13 of Su et al. [1992]. Of particular significance is the δT_{SKS} prediction for AZ3 (the cross-section in Figure 3.16c). The source-side lower mantle anomaly significantly slows down SKS at smaller distances, as Figure 3.19 displays. However, the scatter in the absolute travel times is easily observed as addressed earlier in Figure 3.2, and not explained by present global tomographic models, which must be damped and smoothed for stability in the inversion process. Thus, we have chosen to concentrate on the differential times of S and SKS with respect to the 3-D models instead of either phase individually because of the reduction in scatter seen in Figure 3.6 in going from δT_S and δT_{SKS} times to the δT_{S-SKS} times. Though it is important

to note from the different curves in the Figure 3.19 how 3-D mantle structure can strongly affect the SKS times.

Two other possible structural features that may affect $S - SKS$ difference times are CMB topography and anisotropy. A CMB undulation of ± 5 km at the entering and exiting points for SKS would only change the SKS time, and hence T_{S-SKS}, by about ± 0.2 sec. This is a negligible contribution given the size of the $S - SKS$ anomalies. Upper mantle anisotropy [e.g., Silver and Chan, 1988] is not expected to strongly affect our measurements, since SKS was rarely observed on the tangential components of motion for this data set. This affect is more significant for broad-band data. In examining S and S_{diff} on the radial and tangential components of the rotated seismograms (at distances where SV_{diff} is still observable), shear wave splitting was not apparent, hence D'' anisotropy is assumed not to play a role in the T_{S-SKS} times. Though as mentioned in Chapter 2, a very small percentage of data traversing the lower mantle beneath the Pacific display some splitting. This may be evidence for D'' anisotropy, and should be pursued with a more comprehensive data set.

While the above affects are assumed negligible, the azimuth binning of Figure 3.5 still results in scatter on the order of seconds, as seen in Figure 3.6c. This can be a result of deep mantle structure varying on scale lengths smaller than the azimuth binning chosen, as well as errors in the T_{S-SKS} times due to source mislocation or picking errors. A mislocation in a 500 km deep event by 50 km will produce an error in T_{S-SKS} of 0.7 sec for the distance range of data used in this study. A 50 km mislocation in depth may be extreme, though smaller mislocation errors are likely, and probably contribute up to $\pm$ 0.5 sec to the scatter in our observations. Relocating the events would help in this regard, though the scatter is larger than $\pm$ 0.5 sec for the different azimuth slices (Figure 3.7) and must be attributed to additional sources, such as strong near-source anomalies (e.g., slab complexities).

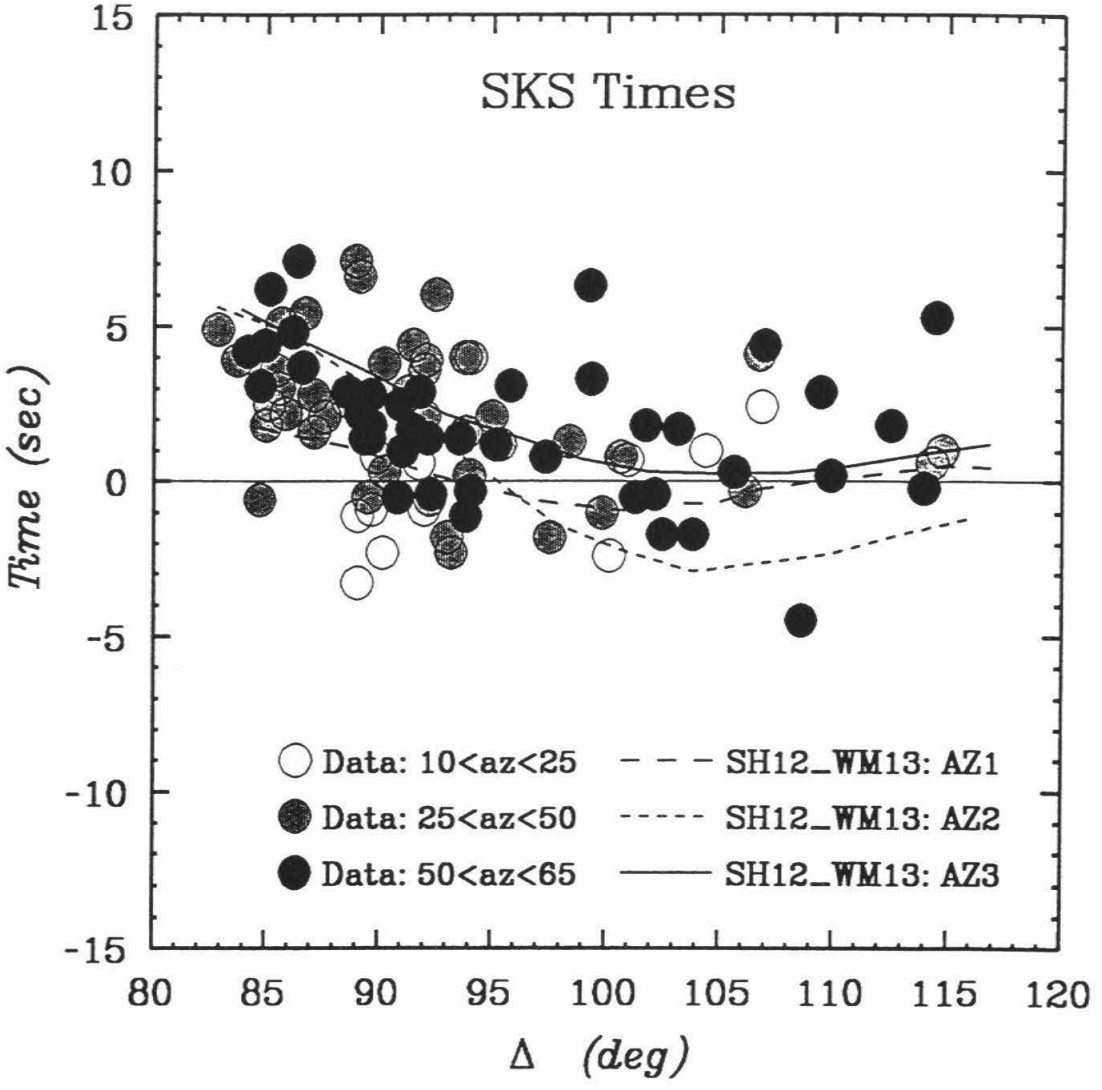

Figure 3.19: Residual times of SKS (with respect to *iasp91*, circles shaded to correspond to azimuth slice) along with predictions of model SH12_WM13 [Su et al., 1992] for AZ1, AZ2, and AZ3 cross-sections of Figure 3.16 (lines).

All travel times were picked from records with good SNR, and accuracy can usually be made to within a few 10ths of a second, depending on the record. Placing a ± 0.5 sec error bound on measurements of T_S or T_{SKS} results in a ± 1.0 sec error for T_{S-SKS} times. This is comparable to results obtained from T_{SS-S} as reported by Grand and Helmberger [1985]. These error bounds may be larger than warranted by the careful measurements. However, since we make no effort at a more rigorous error analysis, this $\pm$ bound is chosen for discussion purposes. If all of the above errors were to constructively add, e.g., 0.2 sec (5km CMB topography) + 0.7 sec (50 km depth mislocation) + 1.0 sec (picking error), a ≈ 2 sec error would result. This is on the order of the scatter seen in Figure 3.7, though it is unlikely that all of the scatter is due to such extremes.

It is very likely that the scatter is also due to smaller scale heterogeneities than the scale length of the azimuth slices of Figure 3.5. For the same source-receiver geometry, Schweitzer [1988] concluded that tomography models are too smooth to explain anomalies seen in the $SKS - SKKS$ data set. Realistically, the δT_{S-SKS} times do not smoothly change from the smallest to largest azimuth for the source-receiver geometry of this data set. Rather, the azimuth binning was chosen as to represent the dominant trend in the data, which is readily seen in Figure 3.7. Unexplained scatter about the general trends of Figure 3.7 may be an indication of small scale deep Earth anomalies of wavelength 10-100 km encountered by S and SKS. Such anomalies are presently assumed to be the cause of precursors to PKP waves [e.g., Doornbos and Husebye, 1972; Haddon and Cleary, 1974]. Further studies on scattering phenomena associated with particularly anomalous regions and its affect on diffracted P- and S-waves may help resolve such issues. Errors in estimation of the hypocentral locations may also be an important contributor to the scatter.

All three models tested in this study have lower mantle velocities beneath the central Pacific that are slower than average (Figure 3.9). The S-SKS observations are

also best explained by an anomalously slow lower mantle beneath the mid-Pacific. These slower velocities may indicate a hotter than average lower mantle. The lowermost mantle surrounding the Pacific contains faster than average velocities in the models of Figure 3.9, which may indicate colder than average regions. These patterns may be related to large scale convection in the lower mantle beneath the Pacific: the surrounding cold regions representing downward mantle flow; the central hot region relating to mantle upwelling, possibly relating to a plume source.

The details of the D″ anomalies of the different models in Figure 3.9 differ, which precludes further mantle dynamics interpretation. $S-SKS$ times, however, may be used as an added constraint in future tomographic inversions to help resolve such differences. These times provide a powerful constraint between the deep mantle regions of SKS entrance and exit points into the core, and the deep mantle region traversed by S (or S_{diff}) near the mid-point of the source-receiver raypath. Abundant $S-SKS$ data is available for such a study due to the frequent and numerous circum-Pacific events. Such results may be used to subtract off mantle contributions to SKS-SKKS times in effort to address the question of core-side heterogeneity [as in Kohler and Tanimoto, 1992; Tanaka and Hamaguchi, 1993b; and Souriau and Poupinet, 1990].

3.8 Conclusions

The travel-times of S and SKS from long- and short-period recordings of deep focus Fiji-Tonga events recorded in North America by CSN and WWSSN stations exhibit a strong azimuthal dependence from the event source region. The differential time T_{S-SKS} proves to be an effective measure of lower mantle structure. Azimuths to the north from the source region are generally accompanied by small to average δT_{S-SKS} residual times (with respect to the *iasp91* model), suggesting on average a normal

lower mantle structure; while δT_{S-SKS} times from azimuths trending towards the northeast are anomalously large (by up to 9 s), implying a slower than average lower mantle beneath the central Pacific. This finding is also seen in tomographically derived models of the region. T_{S-SKS} time predictions from the three different tomography models studied illustrate how a large lower mantle V_S anomaly of around -2% or more (slow V_S) can produce T_{S-SKS} anomalies of the size of the observations from the slow azimuth AZ3. However, anomalies of scale lengths smaller O(100 km) than those in the tomographic models O(1000 km) may be responsible for some of the inconsistencies in the predictions of the 3-D models when compared to observations.

Predictions of SH12_WM13 [Su et al., 1992] provide a reasonable overall fit to the observations, though the most northerly azimuth AZ1 observations suggest a slightly faster path than that predicted, and observations at the largest distances for AZ3 suggest a slightly slower path than predicted (Figure 3.17). Model SH.10c.17 [Masters et al., 1992] under-predicts the size of the δT_{S-SKS} anomalies to the slowest azimuth AZ3 (Figure 3.15), though provides a reasonable prediction for the faster northerly azimuth AZ1, due to a large lower mantle fast anomaly on the receiver side of the structure (Figure 3.14a). Predictions from model MDLSH [Tanimoto, 1990] with residuals in the bottom four layers doubled (model MDLSH+) provide a good fit to the data for the AZ3 path (Figure 3.13), though the other two paths AZ1 and AZ2 differ from observations. The slow anomaly in MDLSH+ responsible for producing large δT_{S-SKS} predictions for AZ3 is about 2000 km to the northeast from the location of the slow feature in SH12_WM13 (as well as in SH.10c.17) responsible for the same affect. This suggests a problem of non-uniqueness in the finer details of deep Earth modeling from the phases S and SKS alone. However, the strong azimuthal dependence of the difference times for this region may provide a powerful constraint for future 3-D lower mantle modeling. Finally, the use of a laterally varying outer core is not necessary to explain the anomalies of this data set, though

such a scenario cannot be resolved with this data. The following chapter further investigates seismic structure near the base of the mantle beneath the central Pacific in an investigation of D″ discontinuity structure from waveform analysis.

Chapter 4

Evidence for a Lower Mantle Shear Wave Velocity Discontinuity Beneath the Central Pacific

4.1 Abstract

In a dataset consisting of long-period waveforms (5-20 sec) and differential travel times of S, ScS, and the arrival from the D$''$ layer, Scd, evidence is found for a laterally varying shear wave velocity (V_S) discontinuity at the base of the mantle. Two different localized D$''$ regions beneath the central Pacific have been investigated. Predictions from a model having a V_S discontinuity 180 km above the core-mantle boundary (CMB) agree well with observations for an eastern mid-Pacific CMB region. This thickness differs from V_S discontinuity thicknesses found in other regions, which average near 280 km. The data presented here from a western mid-Pacific CMB region are more complicated, and are difficult to fit with a 1-D structure. Some of the data from the western region show evidence for a thicker D$''$ layer ($\approx$ 280 km, or greater), though this finding is poorly constrained. Our data do not resolve the

"sharpness" of the Vs jump at the top of D'' , i.e., the depth range over which the V_S increase occurs, and in fact may be modeled equally well by a lower mantle with the increase in V_S at the top of D'' occurring over a 100 km depth range. The $Scd - S$ and $ScS - S$ differential travel times were corrected for the 3-D mantle model of Su et al. [1992], to study possible upper and middle mantle heterogeneity affects on these times, as well as possible correlation between the 3-D structure and discontinuity thickness. Uncertainties in both the D'' discontinuity structure and 3-D images prevents confidence in such correlations.

4.2 Introduction

Direct forward modeling as well as tomographic inversion results have indicated that the velocity structure of the lowermost 100 - 300 km of the mantle (the D'' region) beneath the central Pacific is very anomalous in comparison to global Earth averages [see, for example, Dziewonski, 1984; Hager et al., 1985; Dziewonski and Woodhouse, 1987; Giardini et al., 1987; Tanimoto, 1990; Woodward and Masters, 1991; Li et al., 1991; Garnero and Helmberger, 1993; and Su et al., 1992, 1994]. In these studies, the central Pacific D'' region is characterized by having slower than average seismic velocities with bordering regions that are faster than average. Such patterns have important implications for the temperature distribution, and therefore, convection patterns in the lower mantle. Constraining the details of the D'' structure in these regions, such as the possible existence of a shear wave V_S discontinuity, will have relevance to any mid-Pacific convection model [e.g., Sleep, 1988; Olsen and Kincaid, 1991].

We utilize waveforms of direct S and core reflected ScS seismic phases, along with observations of an arrival intermediate in time to S and ScS, termed Scd by Lay and Helmberger [1983a]. The raypath of Scd is very similar to ScS except that it bottoms

above the core-mantle boundary (CMB) within the D″ layer (see Figure 4.1.) The timing and amplitude of the *Scd* arrival have been used in detailed modeling studies of V_S structure for many different D″ regions [e.g., Lay and Helmberger, 1983ac; Zhang and Lay, 1984; Lay, 1986; Young and Lay, 1987a; Young and Lay, 1990; Weber and Davis, 1990; Lay and Young, 1991; Gaherty and Lay, 1992; and Kendall and Shearer, 1994]. Figure 4.2 shows regions where D″ discontinuities in V_S have been proposed in past studies, along with the proposed V_S structures. Also presented in Figure 4.2 are the two localized central Pacific regions investigated in this study. The details of the models differ, such as depth of discontinuity and velocity gradients, indicating the degree of lateral heterogeneity encountered in the lower mantle. The study of Kendall and Shearer [1994] presents a map of lateral variations in height of D″ discontinuity above the CMB. In that study, a D″ discontinuity is proposed for nearly all of the shaded regions in Figure 4.2, and comparisons are made to the models of previous studies.

The primary purpose of this paper is to present evidence for a V_S discontinuity in D″ for two localized regions beneath the central Pacific. The data for the more easterly patch in Figure 4.2 are interpreted to suggest an average V_S structure having a discontinuity around 180 km above the CMB. This D″ layer is much thinner than structures presented in other areas (e.g., 250 to 320 km thick, averaging around 280 km thick, see Figure 4.2). The data for the more westerly CMB region behave less uniformly, but give tentative evidence for a thicker D″ layer ($\approx$ 280 km.) These observations are discussed in more detail in following sections.

In a previous study, Garnero et al. [1988] proposed a lower mantle model beneath the Pacific whereby a V_S discontinuity in regions bordering the Pacific "fades away" to no discontinuity in the mid-Pacific (model SGHE, Figure 4.2). This was based on anomalously large $S-SKS$ times which were interpreted as being due to anomalously slow S waves, along with a lack of waveform evidence at 92^o for a discontinuity

Figure 4.1: Earth cross-section displaying S, ScS, Scd, and SKS geometric raypaths for a 500 km deep source and 85° epicentral distance. The top of the D″ layer is denoted by the dashed line, and is drawn 300 km above the CMB.

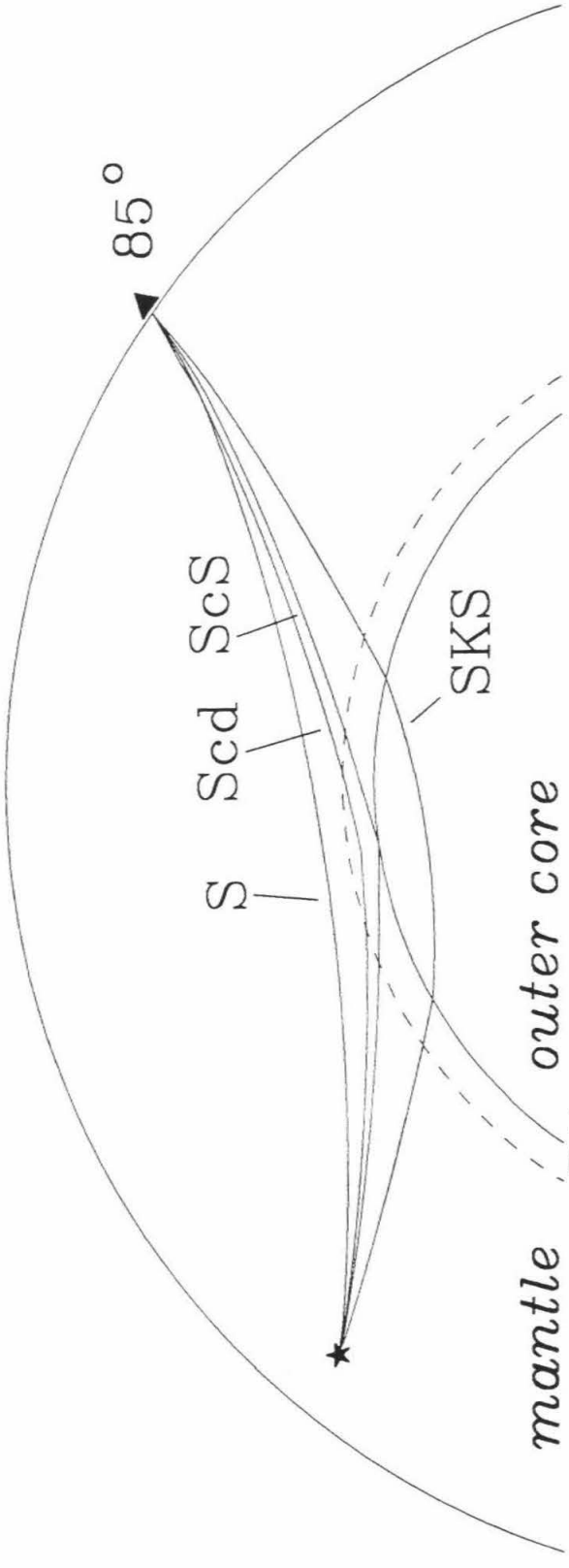
85°
S
Scd
ScS
SKS
mantle
D''
outer core

Figure 4.2: Map of the world showing regions of D″ where V_S discontinuities have been proposed. The two small regions in the central Pacific are investigated here. The hatched regions are labeled with the name of the model derived for that region. The V_S profiles for these models are plotted on the right, and authors are as follows: SLHA, SLHE [Lay and Helmberger, 1983a]; SYL1 [Young and Lay, 1987a]; SGHE [Garnero et al., 1988]; SYLO [Young and Lay, 1990], SWDK [Weber and Davis, 1990]; and SGLE [Gaherty and Lay, 1992].

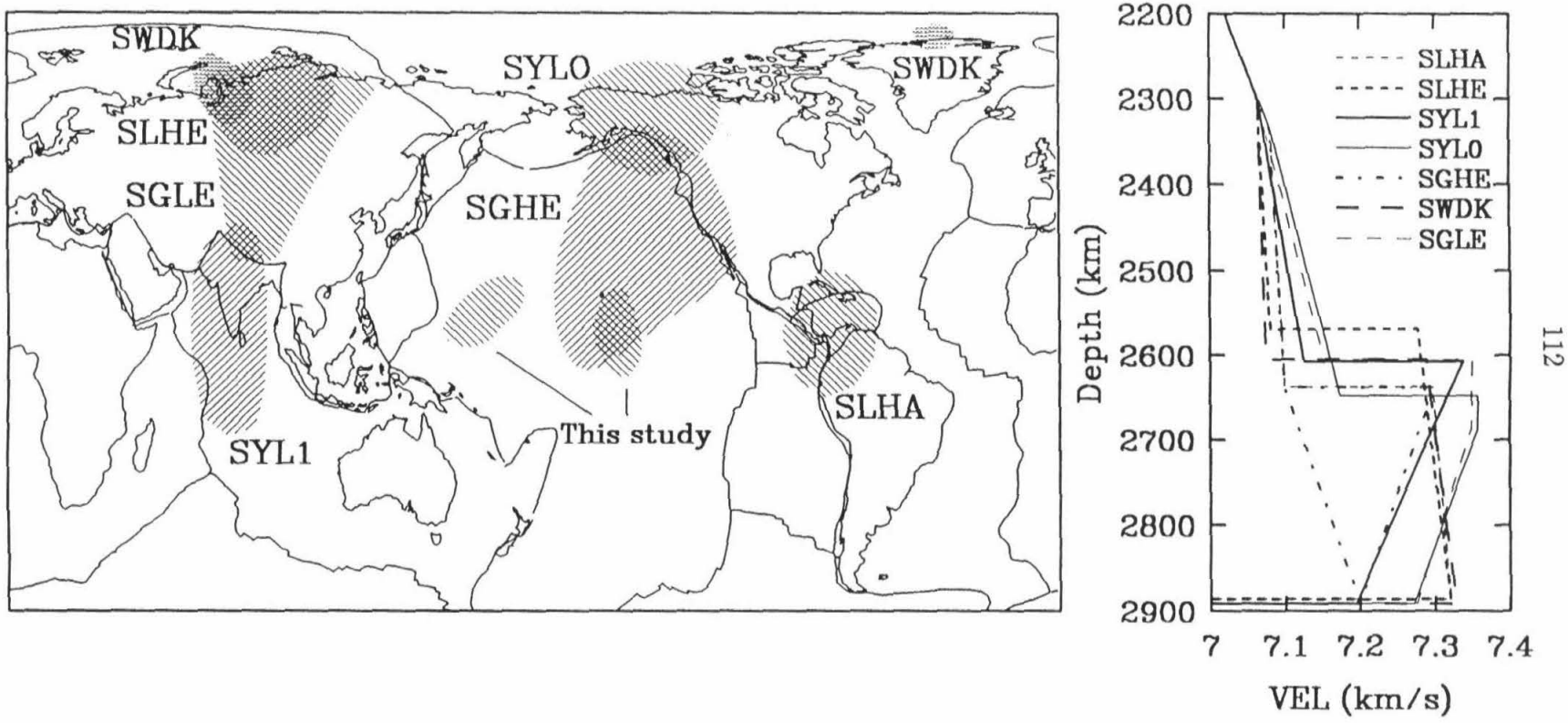
SWDK
SYLO
SWDK
SLHE
SGLE
SGHE
SLHA
SYL1
This study
2200
2300
2400
2500
2600
2700
2800
2900
Depth (km)
SLHA
SLHE
SYL1
SYLO
SGHE
SWDK
SGLE
7
7.1
7.2
7.3
7.4
VEL (km/s)

arrival that has been observed in other D″ discontinuity studies [such as Lay and Helmberger, 1983a; Young and Lay, 1987a; and Gaherty and Lay, 1992]. For these reasons, Garnero et al. [1988] favored a central Pacific D″ region not having a V_S discontinuity. The large $S - SKS$ times of Garnero et al. [1988], however, can be explained even if a D″ discontinuity exists. The large travel time anomalies may be due to lateral changes in mantle velocity such as those derived from tomographic studies. Also, the absence of a double arrival at 92° can be produced by a model with a thin D″ discontinuity, which in turn delays the triplication normally seen at 92° to a larger distance, such as 98° for a D″ discontinuity 180 km above the CMB. (Such affects were explored by Lay and Young [1991] for the SYLO region beneath Alaska, Figure 4.2.) This 98° double arrival can be further affected, and reduced to a single arrival, by smearing the step increase in V_S at the top of the D″ fast layer over a 50-100 km depth range. Observations of anomalously slow mid-Pacific S times and the non-existence of the Scd arrival at 92° can thus be reconciled with a model containing a much thinner D″ discontinuity.

4.3 1-D Synthetics

The approach taken here is to compare synthetic seismograms to observations in a forward modeling process. Particular attention is given to SH motions, since reflection coefficients for ScS and Scd are the largest for this type of motion, making it ideal to investigate deep mantle discontinuities. Some SV records were analyzed, though our data selection has been biased to gather SH rich events for our source-receiver geometries in an effort to facilitate investigating V_S discontinuity structure in D″ .

Figure 4.3 shows the SH predictions of four models for a source depth of 500 km: models PREM [Dziewonski and Anderson, 1981], SYL1 [Young and Lay, 1987a], and

two new models having a thinner D″ layer, SGHP and SGRD. PREM was chosen to represent structures not having a V_S discontinuity in D″ . SYL1 is utilized to represent a D″ having a commonly found thickness of around 280 km. Model SGHP is similar to SYL1 with the notable exception being the reduced thickness of the D″ layer (180 km). The fourth model SGRD is similar to SGHP except the increase in V_S at the top of D″ in SGRD is distributed over a 100 km gradient transition zone. The generalized ray method was used [see Helmberger, 1983] to produce the synthetics, which were then convolved with the long-period World Wide Seismographic Station Network (WWSSN) instrument response. Most of the data analyzed in this study are long-period WWSSN, so particular attention will be focused on the long-period synthetics. As originally pointed out by Lay and Helmberger [1983a] (and subsequent studies as well), a 2.7 % V_S increase approximately 270 km above the CMB produces an arrival between S and ScS in the $70^o - 84^o$ distance range, as well as an observable double arrival near 92^o. These affects can be seen in the SYL1 predictions of Figure 4.3. The SGHP predictions differ from the SYL1 predictions most notably in the timing of the Scd phase. Due to a thinner D″ fast layer, SGHP produces a Scd arrival later in time than that of SYL1 in the $70^o - 84^o$ distance range, and moves the double arrival affect seen at 92^o in the SYL1 synthetics, to around 98^o. By smearing the V_S increase at the top of D″ into a 100 km thick gradient as in model SGRD, the amplitude of the Scd arrival is slightly reduced, especially at the tips of the Scd triplication branches, as seen at 74^o and 98^o (Figure 4.3). However, the S, ScS, and Scd SH waveforms and travel times for model SGRD are almost identical to that of model SGHP in the distance range $76^o - 96^o$. In the following section, synthetics calculated for the appropriate distances and source depths are compared to the observations for the three source-receivers geometries.

Figure 4.3: *SH* component long-period WWSSN generalized ray synthetics for PREM [Dziewonski and Anderson, 1981], SYL1 [Young and Lay, 1987a], and SGHP (this study). The presence of a thinner D″ discontinuity delays the arrival time of *Scd* as seen in the SGHP synthetics compared to SYL1. Smearing the D″ discontinuity V_S increase over 100 km (as in model SGRD) has added effect of reducing *Scd* amplitude at the smaller and largest distances (near the ends of the triplication), but still produces an *Scd* arrival in the 78° to 82° distance range.

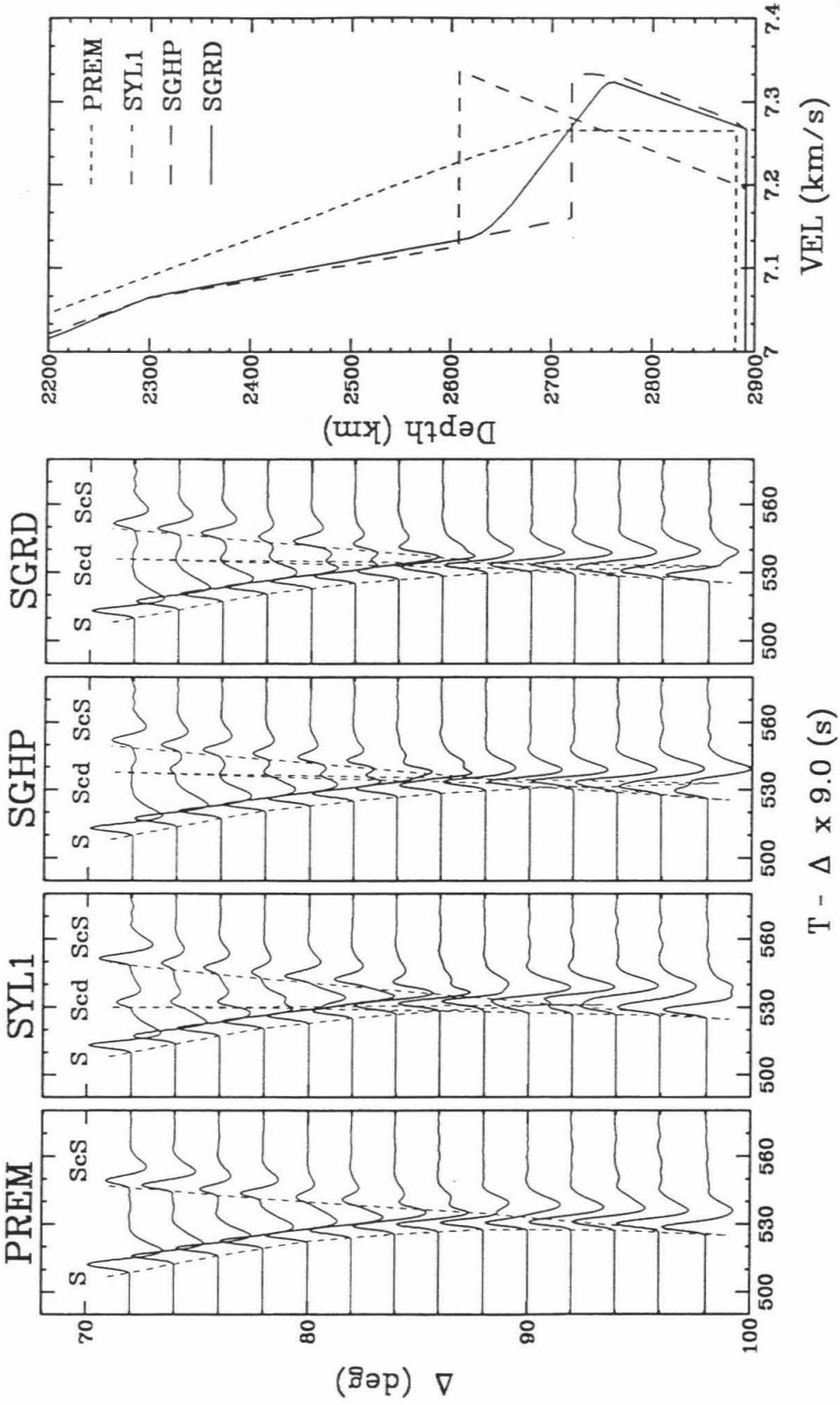
PREM
SYL1
SGHP
SGRD
S
ScS
Scd
Δ (deg)
T - Δ x 9.0 (s)
Depth (km)
VEL (km/s)

4.4 Data Set

Data samples are presented here from three source-receiver geometries having raypaths that traverse the lower mantle beneath the Pacific: (1) records from Fiji-Tonga events recorded at west coast North American stations; (2) Java Sea, Banda Sea, and Phillipines Islands events recorded at the central Pacific station KIP (Kipapa, Hawaii); and (3) Sea of Okhotsk and Sea of Japan events recorded at the SW Pacific station AFI (Afiamalu, Samoa). The event and station information for data presented in this section is given in Table 4.1. All events used are deep focus except for two intermediate depth events. The data used were recorded by long-period WWSSN and long-period Benioff 1-90 seismometers of the Caltech Network, which are both ideal in frequency response for detecting the *Scd* seismic phase. The traces were optically scanned from paper records, digitized, then rotated to the source-receiver azimuth to obtain the natural radial and transverse components.

The different source-receiver geometries and raypaths of data are presented in Figure 4.4. The great circle raypaths are indicated by the dotted lines, with the mid-points of the raypaths indicated by a shaded ellipse. The dimension of the ellipse minor and major axes on the Earth's surface are approximately 200 and 1000 km, respectively, and roughly 100 by 500 km at the depth of the CMB. As the figure indicates, there are two primary CMB regions of study: a western central Pacific region sampled by the KIP and AFI data; and an eastern central Pacific region sampled by the North American data. In gathering AFI and KIP analog long-period WWSSN records for studying the western CMB region, a limiting factor is the low gain of the instruments at both stations. This in turn requires gathering events as large as M_b=6.8 to insure proper signal to noise ratio for these two stations. With records from the larger deep focus events often being more complex in waveshape, the data presented for this region are sparse. In investigating the eastern central Pacific D″ region of Figure 4.4, the limiting factor in the data selection process is that data at

EV Code	STA	Δ (deg)	Az (deg)	Inst *code*[a]	Date mmddyy	Z (km)	Lat	Lon	Mb
F1	LON	78.4	34.2	LPWW	061584	247	-15.82	-174.83	6.1
F2	COR	78.8	36.1	LPWW	042584	415	-17.31	-177.23	5.7
F3	BKS	78.8	42.3	LPWW	100781	620	-20.75	-178.63	6.1
F4	BKS	79.2	42.4	LPWW	082885	625	-21.01	-178.98	6.2
F5	BKS	79.9	42.6	LPWW	062870	587	-21.66	-179.42	5.8
F6	PAS	79.9	47.5	B190	100967	605	-21.10	-179.18	6.2
F7	RVR	80.4	48.0	B190	100967	605	-21.10	-179.18	6.2
F8	LON	80.9	35.0	LPWW	042584	415	-17.31	-177.23	5.7
F9	BAR	81.3	48.2	B190	081267	144	-24.79	-177.38	6.0
F10	DAL	93.1[b]	56.7	LPWW	085263	557	-17.58	-178.73	6.1
F11	DAL	95.9[b]	57.2	LPWW	022275	333	-23.98	-178.88	6.1
F12	DAL	96.1[b]	57.2	LPWW	012469	587	-21.87	-179.54	5.9
F13	DAL	97.4[b]	57.6	LPWW	032374	504	-23.93	179.88	6.0
K1	KIP	75.8	70.1	LPWW	092073	560	9.05	123.79	6.0
K2	KIP	76.2	69.9	LPWW	030584	649	8.15	123.76	6.5
K3	KIP	79.7	66.8	LPWW	062282	450	-7.34	126.04	6.8
A1	AFI	73.1	142.5	LPWW	090570	580	52.23	151.43	6.2
A2	AFI	72.9	142.6	LPWW	122175	554	51.94	151.58	6.4
A3	AFI	75.5	121.3	LPWW	062975	560	38.76	129.99	6.5

Table 4.1: Event and station information of analog data used in this study. [a]LPWW = long-period WWSSN seismometer, B190 = Benioff 1-90 seismometer, [b]adjusted to 500 km source depth.

less than 78^o in distance are unavailable. Distance profiles of data are thus limited for this source-receiver azimuth to distances greater than this minimum distance. Because of these limitations, waveform modeling results for this path geometry are less unique than those having an epicentral distance range available that also spans the smaller distances, such as path geometries of the other study areas in Figure 4.2. Nevertheless, first-order model features may be addressed for this geometry.

Data are first presented for the more abundantly sampled eastern central Pacific D$''$ region. Figure 4.5 displays the North American SH observations of Fiji-Tonga events (top bold traces). The traces are labeled with a letter-number code that corresponds to Table 4.1 and Figure 4.4 (F1 through F9), and the epicentral distance and event source depth are printed above each panel of traces. Plotted along with the data are generalized ray synthetics using models SGHP, SYL1, and PREM. Synthetics from model SGRD are not included in the figure because the SGHP and SGRD synthetics fit the observations equally well. The data and synthetics have been lined up on the first arrival S-wave, and maximum amplitudes have been normalized to unity. The data show evidence for an arrival between S and ScS (denoted by a black dot), which is not predicted by the smooth D$''$ structure in model PREM. Black dots also denote the Scd arrivals in the SGHP and SYL1 synthetics. The observed differential times of $Scd - S$ are better modeled by the thinner D$''$ discontinuity in SGHP than that in SYL1 for this path geometry. However, timing and amplitude anomalies are present in Scd, as well as ScS, indicating the shortcomings of trying to fit the observations with a 1-D model for a region known to be anomalous. For example, for the record F4, the amplitude ratio of Scd/S is larger than the synthetic for model SGHP, which best predicts the differential time of $Scd - S$. But for record F5, the Scd/S ratio is larger in the SGHP synthetics. Such amplitude variations may be an indication of the scale length over which lower mantle lateral variations occur. Also, records F8 and F9 display an anomalously large differential travel time

Figure 4.4: Events, stations, and great circle ray paths (dotted lines) are plotted along with ellipses depicting the CMB mid-point regions of the paths. The ellipses are accompanied with a letter-number code that corresponds to event and station information in Table 4.1.

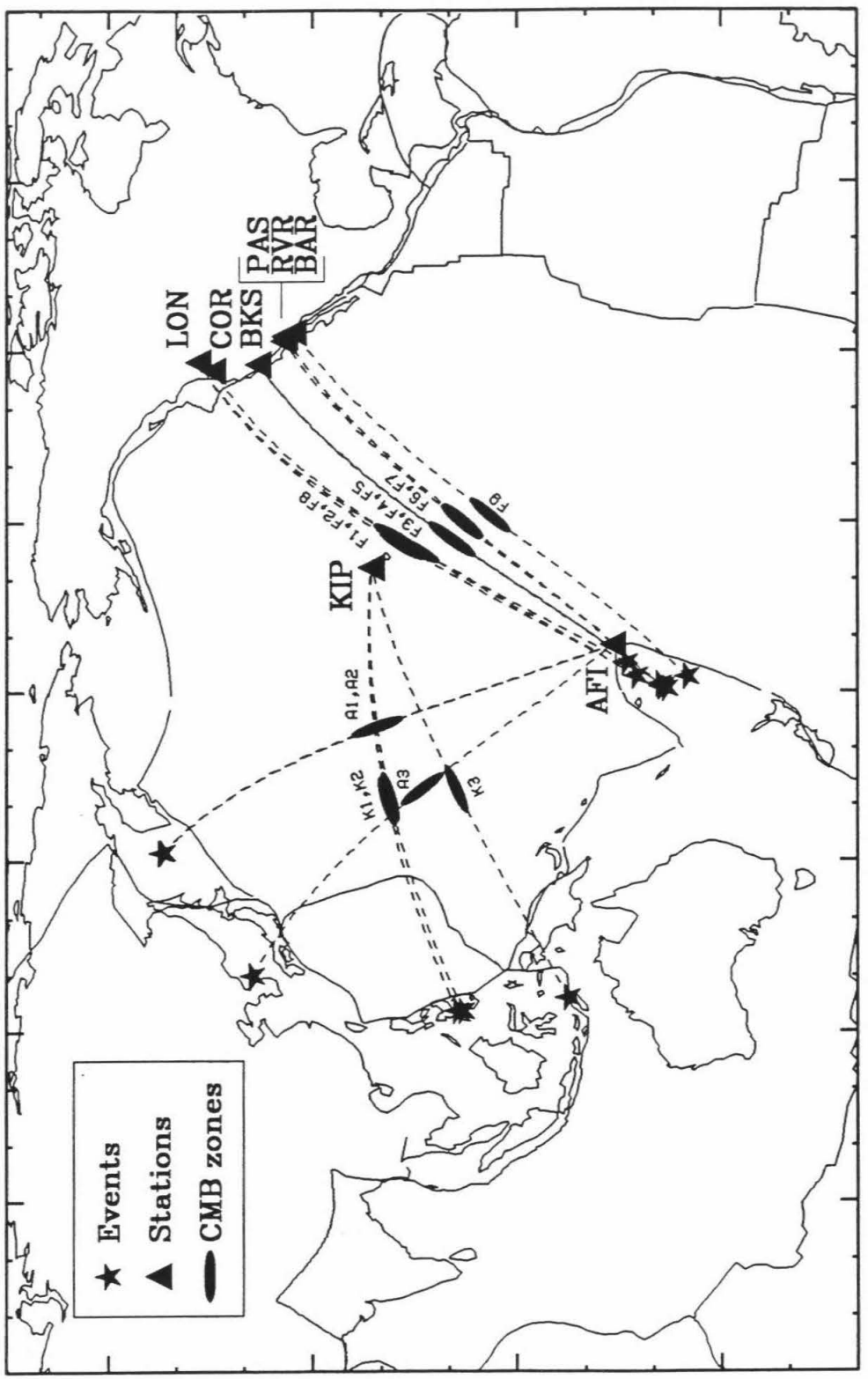
LON
COR
BKS
PAS
RVR
BAR
KIP
AFT
A1,A2
A3
K1,K2
K3
F1,F2,F8
F3,F4,F5
F6,F7
F8
Events
Stations
CMB zones

of $ScS - S$ in comparison to the synthetics. This may be due to an anomalously slow central Pacific lower mantle [as in Garnero and Helmberger, 1993] and will be further discussed in the travel times section of this paper. Nevertheless, the relative timing of S, Scd, and ScS in the observations presented in Figure 4.5 are fit in an average sense by model SGHP. The details of model SGHP, however, are not well constrained. The gradients above and below the D'' discontinuity can affect the relative amplitude ratios. And as Figure 4.3 indicates, we are unable to resolve such gradients with the long-period data in the intermediate distance range.

We have investigated Fiji-Tonga data at larger distances to look for the double arrival seen at 98° in the SGHP SH synthetics of Figure 4.3. The SH data we reviewed do not show conclusive evidence for a double arrival. However, there does appear to be a broadening of the SH waveform relative to SKS. Figure 4.6 shows a sample of the data at the North American station DAL (Dallas, Texas). Radial and tangential profiles are shown for 4 events recorded at DAL (top row), and for synthetics from models SGHP, SGRD, and PREM (the following 3 rows). The data has been adjusted in distance to correspond to a 500 km source depth to compare to synthetics. All maximum amplitudes have been normalized to unity, and traces are lined up on the SKS arrival. The radial traces have been included because the discontinuity models predict a double arrival in SV at distances greater than 94°. The period of the synthetics has been adjusted to roughly fit the SKS observations except for F10 which appears anomalous. Note that simple models such as PREM predict SH waveforms nearly identical to the SKS observations except inverted in polarity. The SH observations, however, clearly display some broadening relative to SKS. If this were due to diffraction alone, the PREM SH synthetics should predict this broadening affect. For a 500 km source depth and the distance range presented in Figure 4.6, the contribution to S-wave broadening in the PREM SH synthetics from diffraction is predicted to be negligible or non-existent. The SH record F13 is

Figure 4.5: SH data (top bold traces) and synthetics (models SGHP, SYL1, and PREM) comparison for the Fiji-Tonga data recorded at North American stations. The data are labeled to correspond to information in Table 4.1. The epicentral distance and source depth are printed above each panel. Black dots indicate the Scd arrival, which in all cases better agrees with predictions from the thinner D$''$ layer model, SGHP.

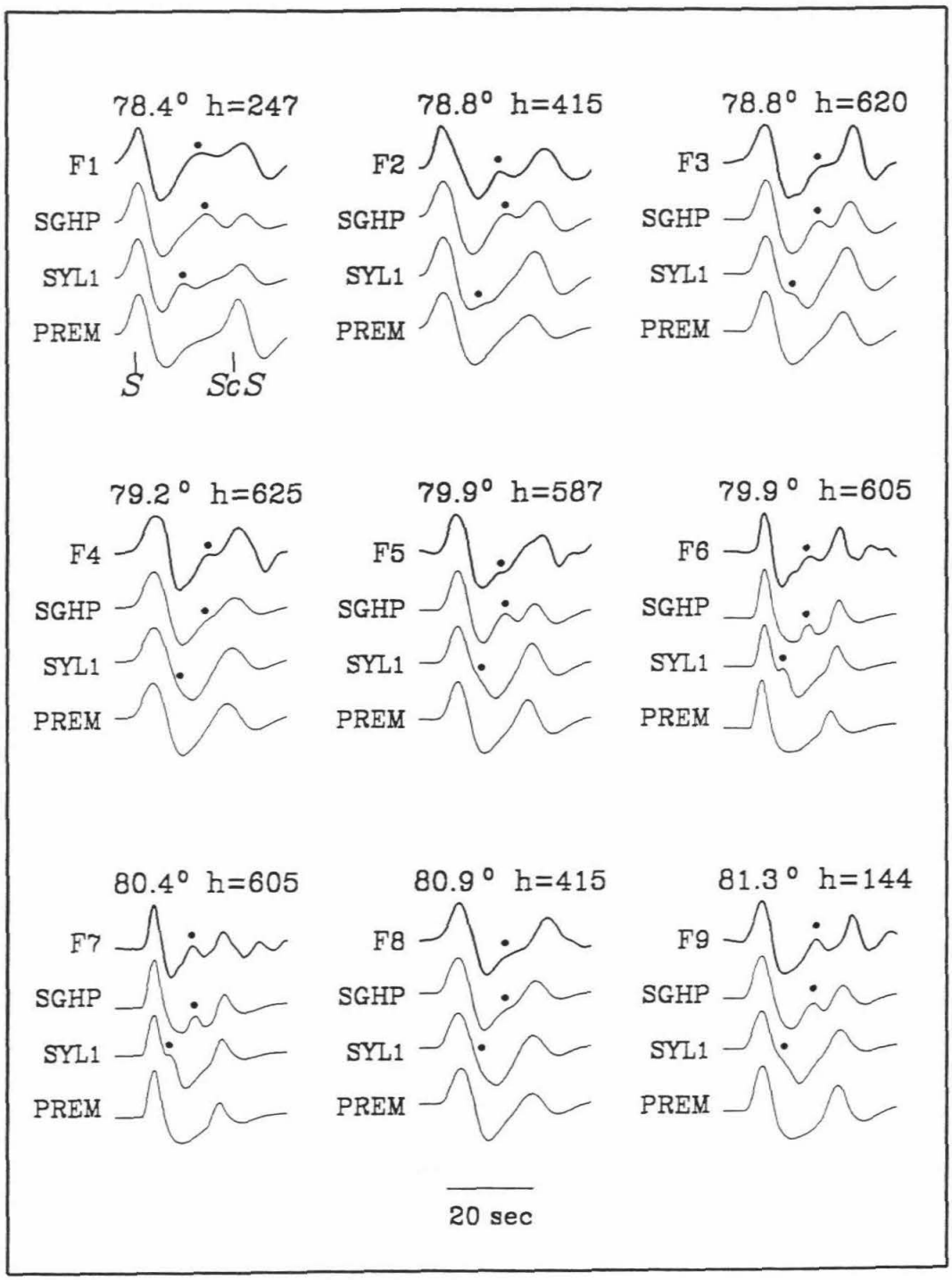
78.4° h=247
F1
SGHP
SYL1
PREM
S
Sc
S
78.8° h=415
F2
SGHP
SYL1
PREM
78.8° h=620
F3
SGHP
SYL1
PREM
79.2° h=625
F4
SGHP
SYL1
PREM
79.9° h=587
F5
SGHP
SYL1
PREM
79.9° h=605
F6
SGHP
SYL1
PREM
80.4° h=605
F7
SGHP
SYL1
PREM
80.9° h=415
F8
SGHP
SYL1
PREM
81.3° h=144
F9
SGHP
SYL1
PREM
20 sec

best fit by SGHP. The DAL SV data shows complexities in the direct S wave that are not seen in the PREM synthetics. The SGHP and SGRD SV predictions are very similar, and perhaps fit the data better than PREM. However, the complicated SV observations may indicate the difficulty encountered when attempting to model this data with 1-D synthetics in a region where the lower mantle is thought to be very anomalous, as discussed in Chapters 2 and 3. There are other difficulties in the interpretation of S-wave broadening being due to the presence of an Scd phase. The broadening of S relative to SKS is common due to greater attenuation affects on the longer path of S in the mantle. Also, the spectrum of waves diffracted along the CMB is modified differently depending on the velocity gradient in D$''$ [see, for example, Doornbos and Mondt, 1979].

The $S - SKS$ times for the mid-Pacific lower mantle region are anomalously large [Garnero et al., 1988; Garnero and Helmberger, 1993], as can be seen in the DAL data when compared to the synthetics in Figure 4.6. Correcting the DAL $S - SKS$ time observations for the 3-D mantle model of Su et al., [1992] produces $S - SKS$ times similar to the synthetic predictions. The 3-D model $S - SKS$ time corrections are indicated in the DAL data panels of Figure 4.6 by arrows denoting the adjusted S times with respect to SKS. As indicated by Garnero and Helmberger [1993], this particular 3-D model predicts $S - SKS$ time anomalies in agreement with observations for this source-receiver geometry for distances less than around 100^o (within the scatter of the data.) At larger distances, this model underpredicts the observed anomalies, possibly due to an underprediction of the size of the mid-Pacific large scale low velocity D$''$ region.

Data from the two source-receiver geometries used to study the western CMB region are presented in Figure 4.7. The labeling and plotting convention are the same as in Figure 4.5. The 2 KIP SH records K1 and K2 are at ideal distances for studying the Scd arrival. For these two records, the timing of Scd is closest to

Figure 4.6: Radial and transverse recordings from Fiji-Tonga events recorded at station DAL (top row), and synthetics for the models SGHP, SGRD, and PREM (bottom 3 rows) are displayed in the $92^o - 98^o$ distance range. Arrows indicate the $S - SKS$ time correction of model SH12_WM13 by Su et al. [1992]: the arrow points to the predicted S time relative to SKS after correction, which better agrees with synthetics. The complicated waveshape of the SV component of observed S-waves along with the broadened SH pulse of observed S-waves is more compatible with predictions from the discontinuity models.

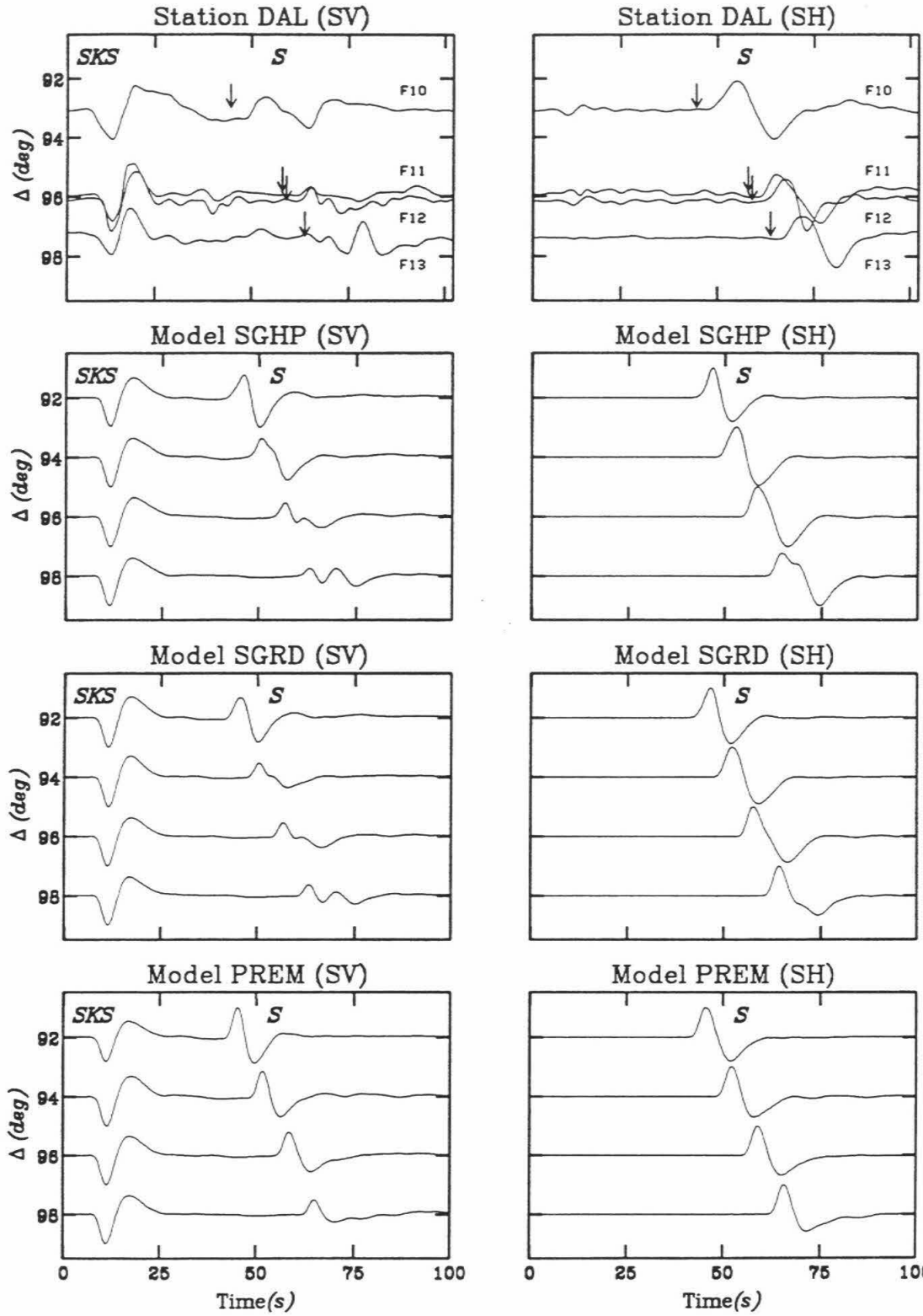
Station DAL (SV)
Station DAL (SH)
Model SGHP (SV)
Model SGHP (SH)
Model SGRD (SV)
Model SGRD (SH)
Model PREM (SV)
Model PREM (SH)
SKS
S
F10
F11
F12
F13
Δ (deg)
92
94
96
98
0
25
50
75
100
Time(s)

the predictions of SYL1. The timing of *Scd* for record K3 appears closer to that of SGHP, but is ambiguous due to the complex *Scd* waveshape, which may be related to the size of the source (M_b6.8). Since record K3 has a D″ bounce point for *Scd* that is around 800 km to the south of records K1 and K2, lateral variations in D″ thickness may be contributing to the anomalous observation. Observations at station AFI from NW Pacific events are presented in Figure 4.7 as A1 *SV*, A1 *SH*, A2, and A3. For A1 *SV* and *SH*, model SYL1 produces the best fit of the three models, with the $Scd - S$ time for that model most closely matching the observations. The *SH* records A2 and A3 are more complicated in waveshape but still show strong evidence for an *Scd* arrival. The A2 $Scd - S$ time is closer to that of SYL1, though A3 has a time intermediate to predictions of SYL1 and SGHP. The recordings A1, A2, and A3 are from relatively large events (M_b 6.2, 6.4, and 6.5, respectively), which may be related to the waveform complexities. More data is needed to better model the western CMB region. The data presented in Figure 4.7 may ultimately be better modeled by a D″ layer with a thickness closer to that of SYL1 (280 km). But the travel time and waveform variations in our small number of samples for this western region precludes any confident determination of D″ layer thickness.

4.5 Travel Times and 3-D Structure

The data in Figure 4.5 suggest that the eastern CMB region in this study (see Figure 4.2) may be better modeled by a D″ layer about 180 km thick. The data in Figure 4.7 however, are less uniform indicating that the western CMB region may be too complicated to model with a 1-D structure. In this section we present raw differential travel times with respect to the 1-D structures SYL1 and SGHP, then correct the travel times for the 3-D mantle structure of Su et al. [1992].

The travel times of *S*, *Scd*, and *ScS* were measured by a procedure similar to

Figure 4.7: SH data (top bold traces) and synthetics (models SGHP, SYL1, and PREM) comparison for the southwest Pacific events recorded at station KIP, and northwest Pacific events recorded at stations AFI. The data are labeled to correspond to information in Table 4.1. As in Figure 4.5, the black dots indicate the Scd arrival.

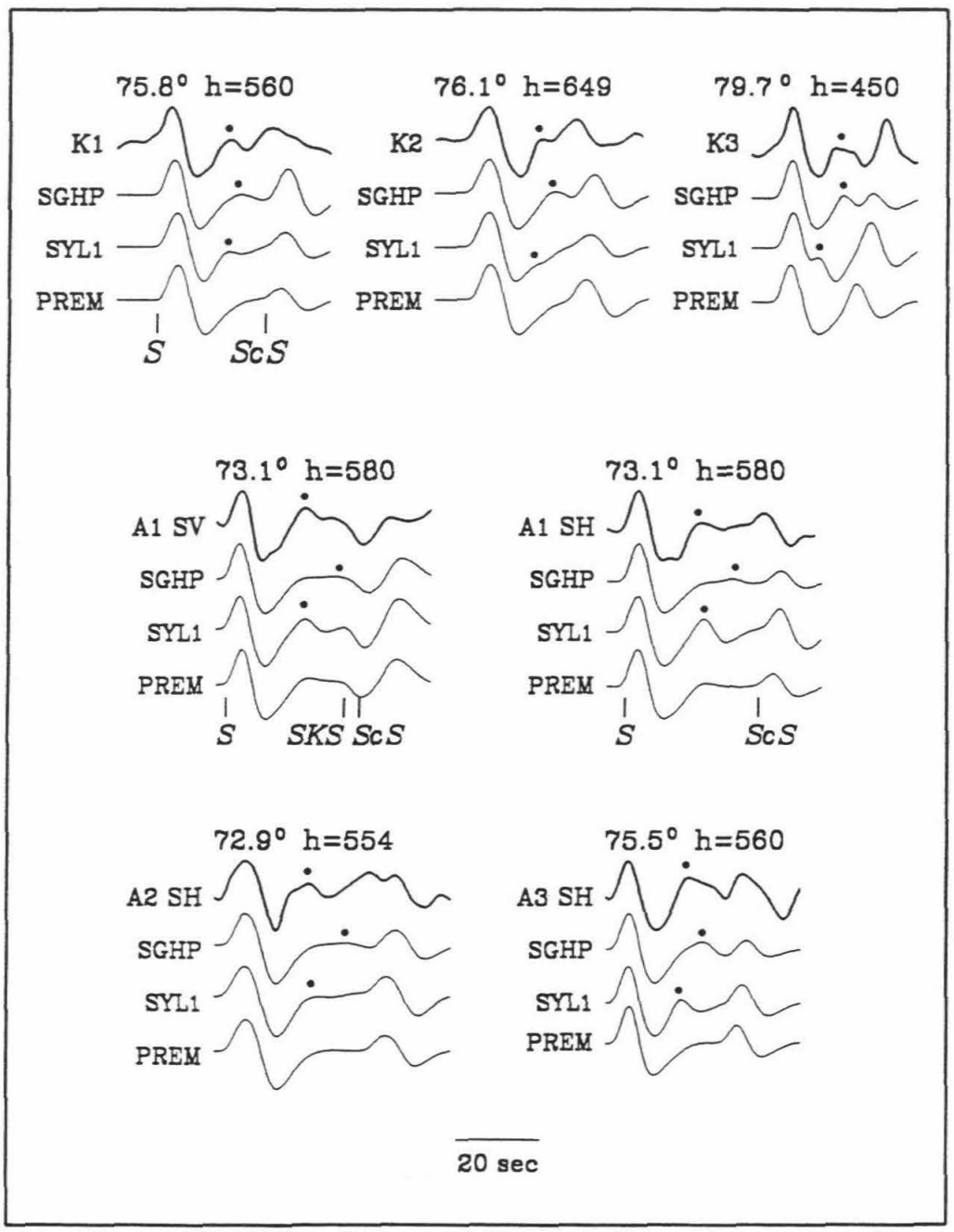
75.8° h=560
K1
SGHP
SYL1
PREM
S
ScS
76.1° h=649
K2
SGHP
SYL1
PREM
79.7° h=450
K3
SGHP
SYL1
PREM
73.1° h=580
A1 SV
SGHP
SYL1
PREM
S
SKS
ScS
73.1° h=580
A1 SH
SGHP
SYL1
PREM
S
ScS
72.9° h=554
A2 SH
SGHP
SYL1
PREM
75.5° h=560
A3 SH
SGHP
SYL1
PREM
20 sec

Grand and Helmberger [1985] by: (i) line up the first arrival S-wave of the observation and the appropriate synthetic seismogram; (ii) pick the peak times of the Scd and ScS phases for each of the observations and synthetics; and (iii) take the differences $T_{OBS}(Scd)$ - $T_{SYNTH}(Scd)$ and $T_{OBS}(ScS)$ - $T_{SYNTH}(ScS)$. Figure 4.8 presents the travel times of the data with respect to SYL1 and SGHP predictions (solid and dotted lines, respectively). All S times have been lined up with that of SYL1 to study the differential times. The observed times have all been adjusted to correspond to a source depth of 500 km. Different symbols are used corresponding to the different paths of Figure 4.4: crosses for the Fiji-Tonga data recorded in North America; diamonds for the SW Pacific events recorded at KIP; and circles for the NW Pacific events recorded at AFI. No corrections for 3-D structure have been included in this figure. As seen in Figure 4.5, the $Scd - S$ times of the Fiji-Tonga data are more compatible with SGHP. The $Scd - S$ times of the KIP and AFI data are better predicted by SYL1. The $ScS - S$ times of the observations, however, are anomalous with respect to the predictions and will be explored below.

The 3-D mantle model of Su et al. [1992] (SH12_WM13) was used to make differential travel time predictions for $Scd - S$ and $ScS - S$. SH12_WM13 was shown to account for the general long-wavelength behavior of anomalous $S - SKS$ times in the mid-Pacific [Garnero and Helmberger, 1993], and hence is utilized here in an effort to subtract out 3-D mantle contributions to the $Scd - S$ and $ScS - S$ differential travel times. The model was parameterized into 116 spherical shells vertically (25 km thick each), and laterally by blocks of dimension 2.5^o x 2.5^o. This grid is then used to calculate travel time anomalies for laterally homogeneous raypaths of S, Scd, and ScS. The resulting residuals were subtracted from the observations and are presented in Figure 4.9.

For the Fiji-Tonga data, model SH12_WM13 reduces the scatter in the $Scd - S$ times and shifts the $ScS - S$ times to better agree with predictions. Large travel

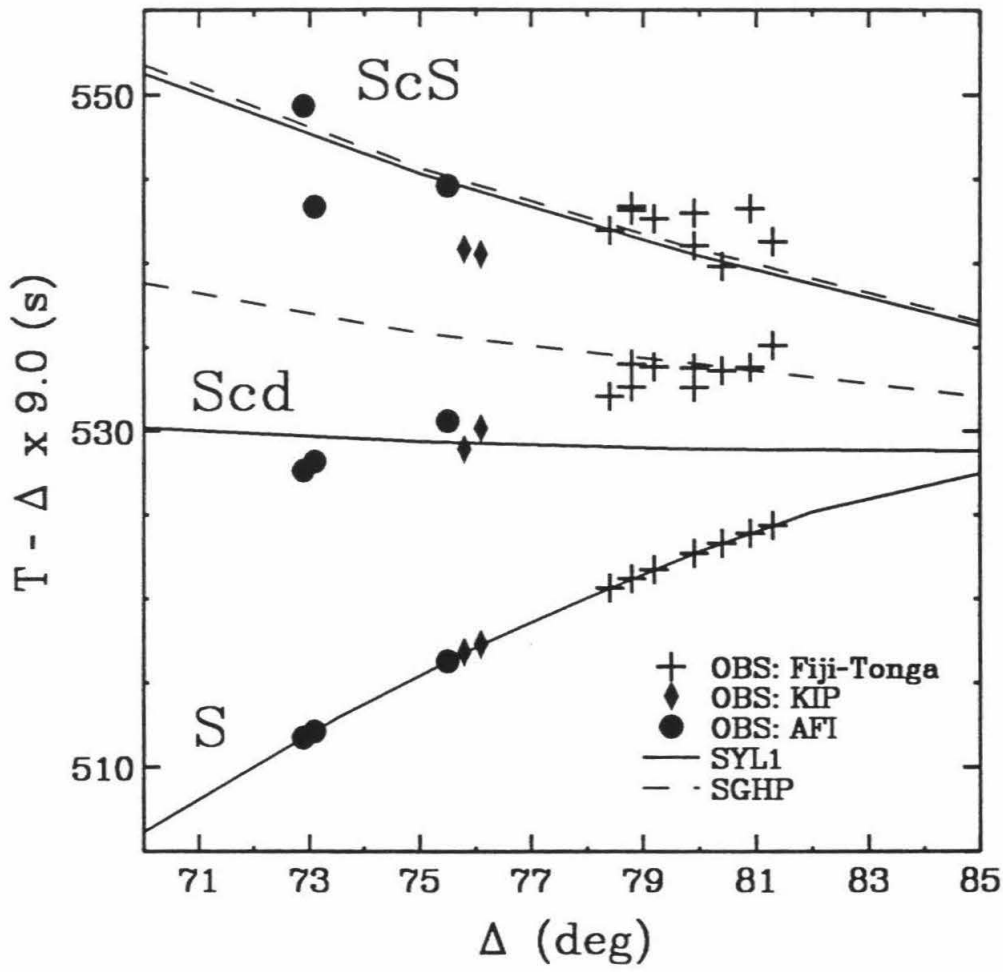

Figure 4.8: Raw differential travel times of S, Scd, and ScS, for the data of Figures 4.5 and 4.7, compared to predictions of SYL1 (solid lines) and SGHP (dotted lines). All S times have been aligned with those of SYL1.

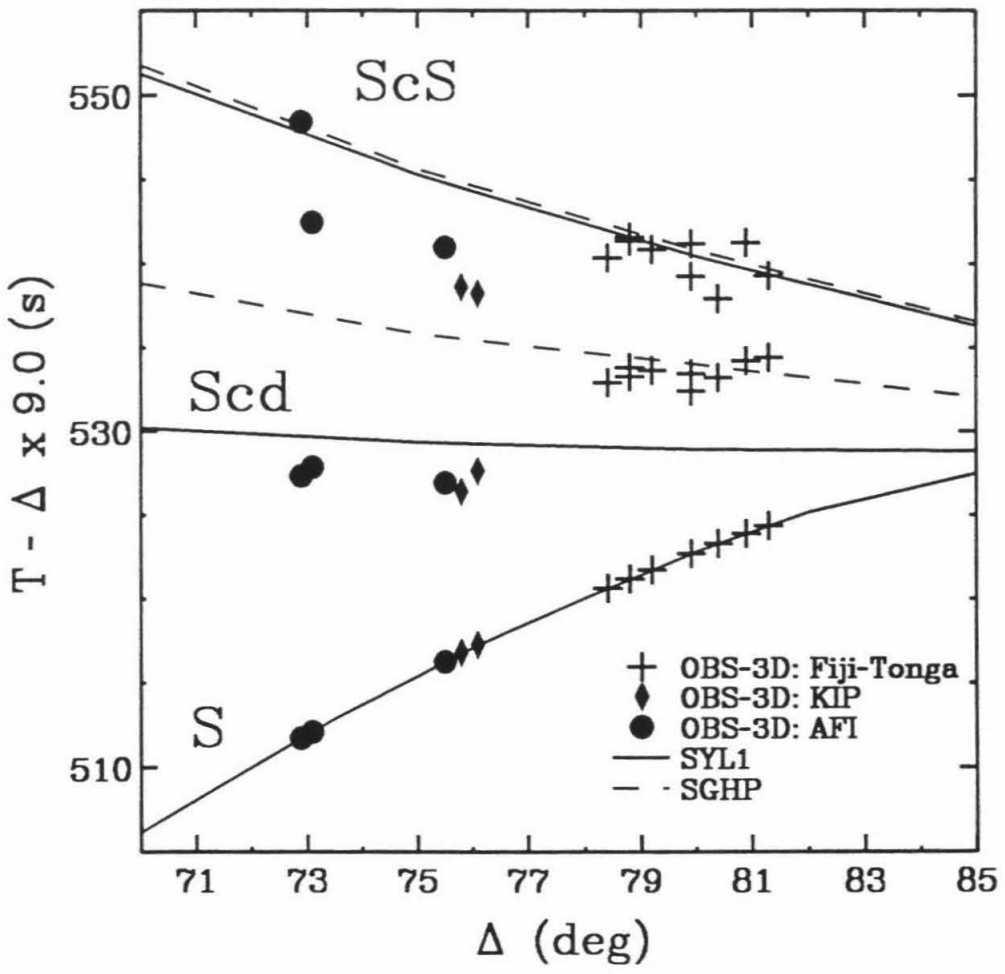

Figure 4.9: Differential travel times of S, Scd, and ScS, for the data of Figures 4.5 and 4.7, corrected for the 3-D mantle model of Su et al., [1991], compared to predictions of SYL1 (solid lines) and SGHP (dotted lines). All S times have been aligned with those of SYL1.

time anomalies are still present after correction, which may indicate the presence of anomalies of wavelength smaller than those presently resolvable by tomographic models. For the AFI and KIP data, after SH12_WM13 corrections, the $Scd-S$ times reduce to about 2.5 sec less than that of SYL1, and the $ScS-S$ times on average are about 5.5 sec less than SYL1 predictions. With such few data, these times will not be used to infer a structure. However, it is interesting to note that a D″ layer thicker than that of SYL1 will reduce both the $Scd-S$ and $ScS-S$ times. And also a change in the V_S gradient in D″ of SYL1 from its present negative value to zero will cause a reduction in the $ScS-S$ time by 2.6 sec (at 80°). Therefore a faster and thicker D″ layer would do better at predicting these times. Alternatively, an upper mantle that is slower than SH12_WM13 will slow down S-waves relative to Scd and ScS, reducing $Scd-S$ and $ScS-S$ times, thus better predicting the observations. More data (analog and digital) for this region is necessary to help identify the travel time trends. Absolute timing information can then be used to help resolve the anomalies.

4.6 Broadband Data: Preliminary Observations

Some preliminary observations of digital broadband data from the TERRAscope and UCBnet arrays are presented in this section. Data from four deep focus Fiji-Tonga events (Table 4.2) have been studied. Three of the events have epicentral distances ideal for studying Scd pulses and the tangential component displacement seismograms for these are presented in Figure 4.10. The dominant arrivals in the time window shown in the figure are S and ScS, as denoted by the dashed lines. These lines correspond to the observed arrival times and not a reference model. Also shown in the figure are shaded regions that represent the time window Scd is predicted to be present according to the range of models in Figure 4.3. In each of the three profiles of Figure 4.10 the shaded time window displays complicated waveform

DATE	OT			Z		
ddmmyy	hhmmss	LAT	LON	(km)	M_b	Region
080492	065835	-21.5	-177.3	269	5.8	FIJI IS.
083092	200907	-17.5	-179.0	570	5.8	FIJI IS.
041693	140840	-17.4	-178.9	570	5.9	FIJI IS.
080793	175328	-23.6	179.1	580	5.9	S. OF FIJI IS.

Table 4.2: Event information for Fiji Islands region events recorded by TERRAscope and UCBnet broadband stations (as reported by NEIS.)

behavior, and a single systematic *Scd* pulse is difficult to identify. For example, the panel on the left of the figure has some records appearing to have two pulses in the shaded region, with other records showing little energy at all. The center panel predominantly displays one pulse with highly variable arrival time. The panel on the right has complicated waveforms displaying both single and double arrivals in the shaded time window, and in general has a lower signal-to-noise ratio making *Scd* identification difficult.

Broadband data contain more source and receiver structure information than the long-period data of the previous sections. Interpreting the seismograms of Figure 4.10 in terms of *Scd* arrivals can thus be complicated by source and receiver complexities. Unless a clear arrival displays moveout in time as predicted by D″ discontinuity models, *Scd* identification (and modeling) can be obscured by such complications.

For most of the records of Figure 4.10, however, distinct *S* and *ScS* arrivals are present. These difference times were measured, and display anomalies as with the Fiji-Tonga data of Figure 4.8, varying from 0 to 5 sec more separated than PREM predictions. After correcting for the SH12_WM13 model, these times display the

Figure 4.10: Broadband tangential component displacement recordings from 3 deep focus Fiji events recorded by TERRAscope and UCBnet stations. Dotted lines denote observed S and ScS arrivals, and shaded region indicates the predicted time window of Scd arrivals for the different D$''$ discontinuity models of Figure 4.3. Event information is listed in Table 4.2.

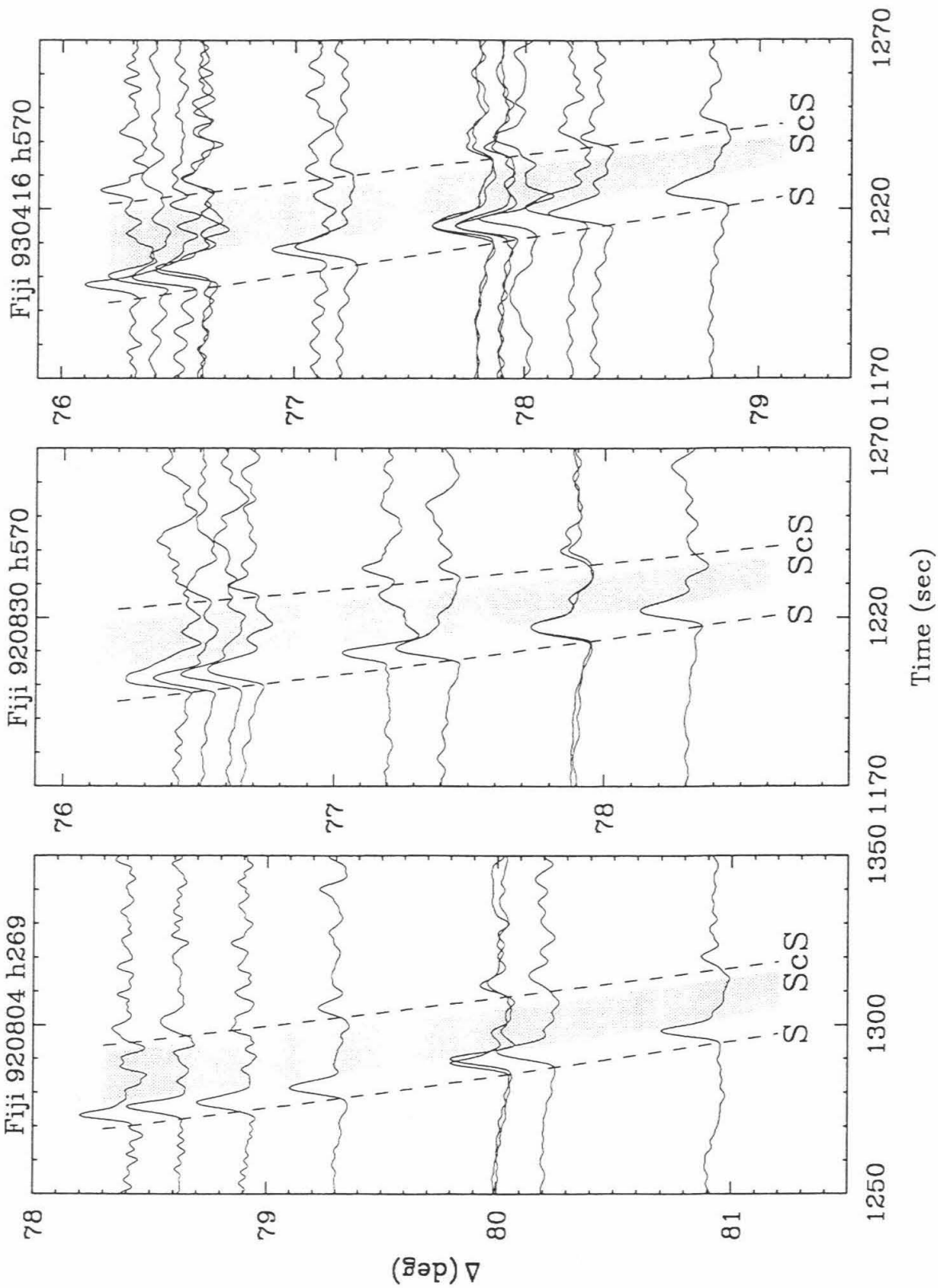
Fiji 920804 h269
Fiji 920830 h570
Fiji 930416 h570
S
ScS
Δ (deg)
Time (sec)

same type of small scale variations as shown in Figure 4.9, again indicating that heterogeneity at wavelengths smaller than that in SH12_WM13 must be present in the mantle.

An event slightly greater epicentral distances than those in Figure 4.10 for the same region shows such small scale $ScS - S$ time variations, as well as with ScS/S amplitude ratios. Figure 4.11 displays the tangential component displacement traces for this event (solid traces) along with predictions from PREM (dashed traces) for the appropriate source depth. To highlight $ScS - S$ time deviations, a thin dashed line is drawn vertically through the ScS peaks of all five of the PREM traces, and bold vertical short lines indicate peaks of ScS arrivals in the observations. As the figure displays, differential travel time perturbations from around -2 to +5 sec are present, indicating small scale O(100 km) perturbations in the lower mantle. Using high quality broadband data such as this in future tomographic inversions can greatly increase the resolution for lower mantle structure. The long-period data typically used in past inversions (including SH12_WM13) is too long-period to detect separate S and ScS phases at this distance range as displayed in the broadband data, which gives resolution in the bottom of the mantle of several hundred kilometers vertically and even less horizontally.

4.7 Discussion

As summarized by Gaherty and Lay [1992], many seismic structure scenarios can produce arrivals between S and ScS in the distance range $75^o - 82^o$ which may be misinterpreted as Scd arrivals. One case is that of slab diffraction discussed by Cormier [1989]. Slab diffraction produces a double arrival from multipathing effects. Paths to the North American stations from the Tonga trench spend very little time in the slab, since the slab dips towards the west, striking around N15°E,

Figure 4.11: Broadband tangential component displacement recordings from a deep focus Fiji event recorded by TERRAscope and UCBnet stations. The large first arrival is S, which is followed by a smaller amplitude ScS arrival. Waveform predictions from the PREM model are dotted, with ScS peaks of the PREM traces connected by a dashed line. ScS peaks in the data are denoted by short vertical lines, and display deviations from PREM predictions by -2 to +5 sec, as well as amplitude fluctuations.

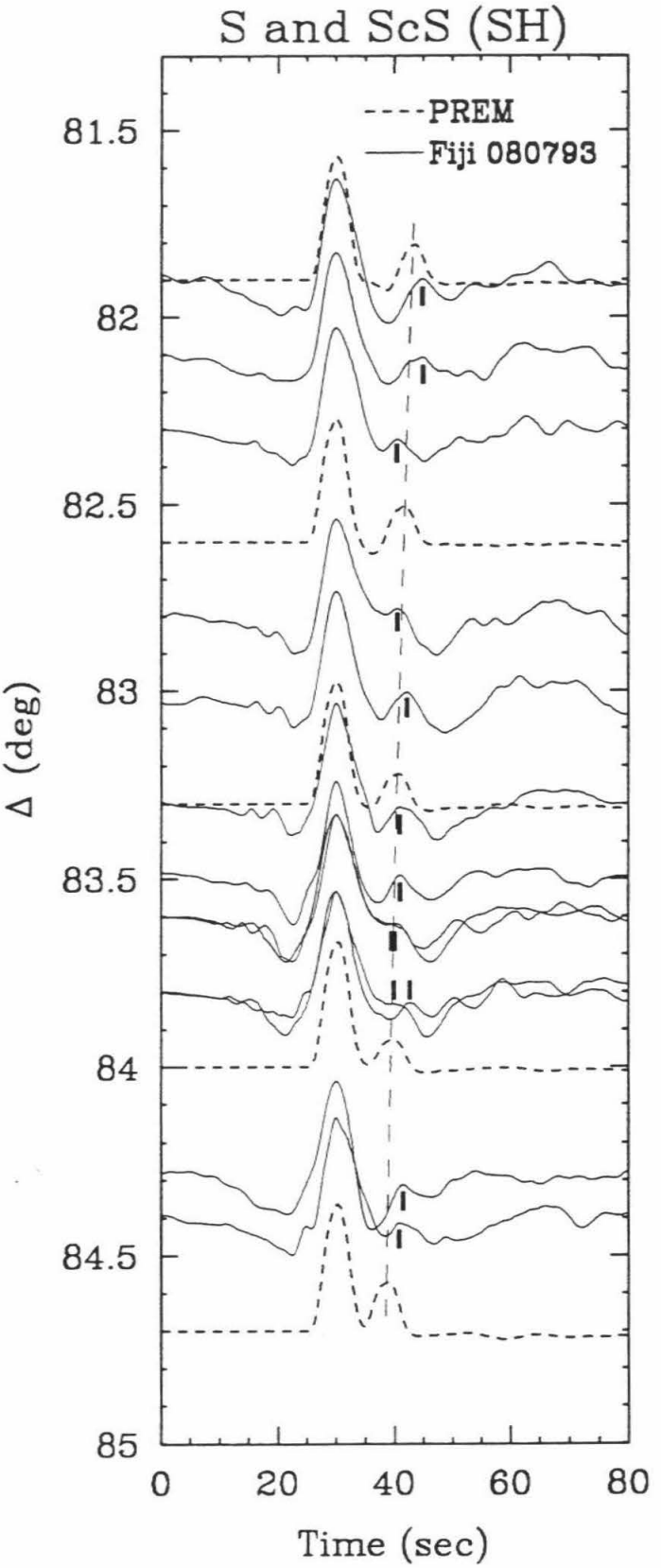
S and ScS (SH)
PREM
Fiji 080793
81.5
82
82.5
83
83.5
84
84.5
85
Δ (deg)
0
20
40
60
80
Time (sec)

and raypaths depart easterly from the underside of the slab. The azimuth range (relative to slab strike) of stations used here is such that slab effects are predicted to be absent (or small) [Cormier, 1989]. The same path geometry in relationship to the slab orientation should be true for the 3 NW Pacific events recorded at station AFI, and recordings K1 and K2 recorded at KIP. Record K3, however, has a path geometry that may be affected by slab multipathing. It has a complex *Scd* waveform and therefore was not used in the travel time analysis.

Another scenario is that proposed by Haddon and Buchbinder [1986, 1987], whereby *S*-waves are scattered by 3-D heterogeneities at the base of the mantle, producing another arrival. Such phenomena may exist for this central-Pacific D″ region. However, for our dataset, the arrival we interpret as *Scd* has moveout as expected for a triplication arrival, and is observed with some regularity at the west coast U.S. stations for the Fiji-Tonga events. Deep mantle heterogeneities may be responsible for the variabilities seen in the observations from station to station, as well as small scale scatter for this study area [see Garnero and Helmberger, 1993]. It is our interpretation that the seismic arrival observed between *S* and *ScS* in the 78° to 82° distance range is most easily explained by a discontinuity in V_S at the top of D″ .

A possible scenario for a D″ cross-section starting from the region from beneath India and the Indian Ocean (SYL1) trending across the Pacific to the region beneath Central and South America (SLHA) is presented in Figure 4.12, along with SH12_WM13 model predictions from the 670 km discontinuity down to the CMB. The top panel displays a map with D″ study regions and cross-section line. The bottom panel shows the cross-section spherical layer which has been flattened out and vertically exaggerated. The cartoon illustrates how D″ might be a continuous layer, though the thickness would vary laterally, as indicated by the thick line above the CMB. The velocities would not be constant through this layer, as the profiles

in Figure 4.2 indicate. Many smaller wavelength features may exist in addition to the long wavelength structure depicted. The slowest V_S perturbations predicted by SH12_WM13 roughly coincide with the thickest D″ section. Whether slower than average velocities are actually resolved for that region, and whether D″ thickness correlates to the overall lower mantle velocity perturbation remains for future study. Determining how thinner and thicker than average D″ thicknesses relate to global lower mantle velocity structure, and lower mantle dynamics is of fundamental importance in understanding the overall core-mantle system. As mentioned above, higher resolution tomographic inversions of lower mantle velocity structure will greatly help in this regard.

The region slightly to the west, northwest, and southwest of our western CMB region was investigated by Revenaugh and Jordan [1991], where they report that only 5 of their 18 source-receiver geometries support a lower mantle V_S discontinuity from a reverberation analysis of close-distance, SH polarized multiple ScS waves. Their finding can be compatible with an ubiquitous D″ discontinuity in the region if the vertical dimension over which the jump in V_S occurs at the top of D″ is smeared over 50-100 km. This dimension would obscure evidence of the Scd arrival at near vertical incidence, as well as at the smallest ($70^o - 75^o$) and largest (near 92^o for a 280 km thick D″) distances where Scd is routinely identified in studies that involve wide angles of incidence to D″ . This feature, however, will still produce an Scd arrival in the $75^o - 80^o$ distance range. Revenaugh and Jordan [1991] report that the 5 paths showing evidence for a D″ discontinuity are accompanied by different D″ thicknesses, from 270 km to 340 km (± 25 km). Their region would correspond to the slight bulge in Figure 4.12 between SYL1 and SGHP, which has been assigned a thickness of 310 km. This bulge also corresponds to the western CMB region of this study, where a thicker D″ would better model the KIP and AFI travel time data. Such speculation is poorly constrained by the data presented here, though future study may help resolve

Figure 4.12: Schematic cartoon depicting a possible D″ cross-section from beneath India and the Indian Ocean (model SYL1) westward to the two regions studied here (see Figure 4.2) to beneath Central and South America (model SLHA). The cross-section extends from the 670 km discontinuity down to the CMB, with the vertical dimension exaggerated. D″ thicknesses are around 280 km (SYL1), 180 km (SGHP), and 250 km (SLHA). The pronounced area between SYL1 and *SH*GP corresponds to the poorly constrained western CMB region of this study, and is assigned a thickness of 300 km. V_S perturbations of model SH12_WM13 [Su et al., 1992] are super-imposed on the cross-section, where dark regions are slower than average velocities and light regions are faster than average. The slowest feature in model SH12_WM13 for this cross-section corresponds to the thicker D″ zone.

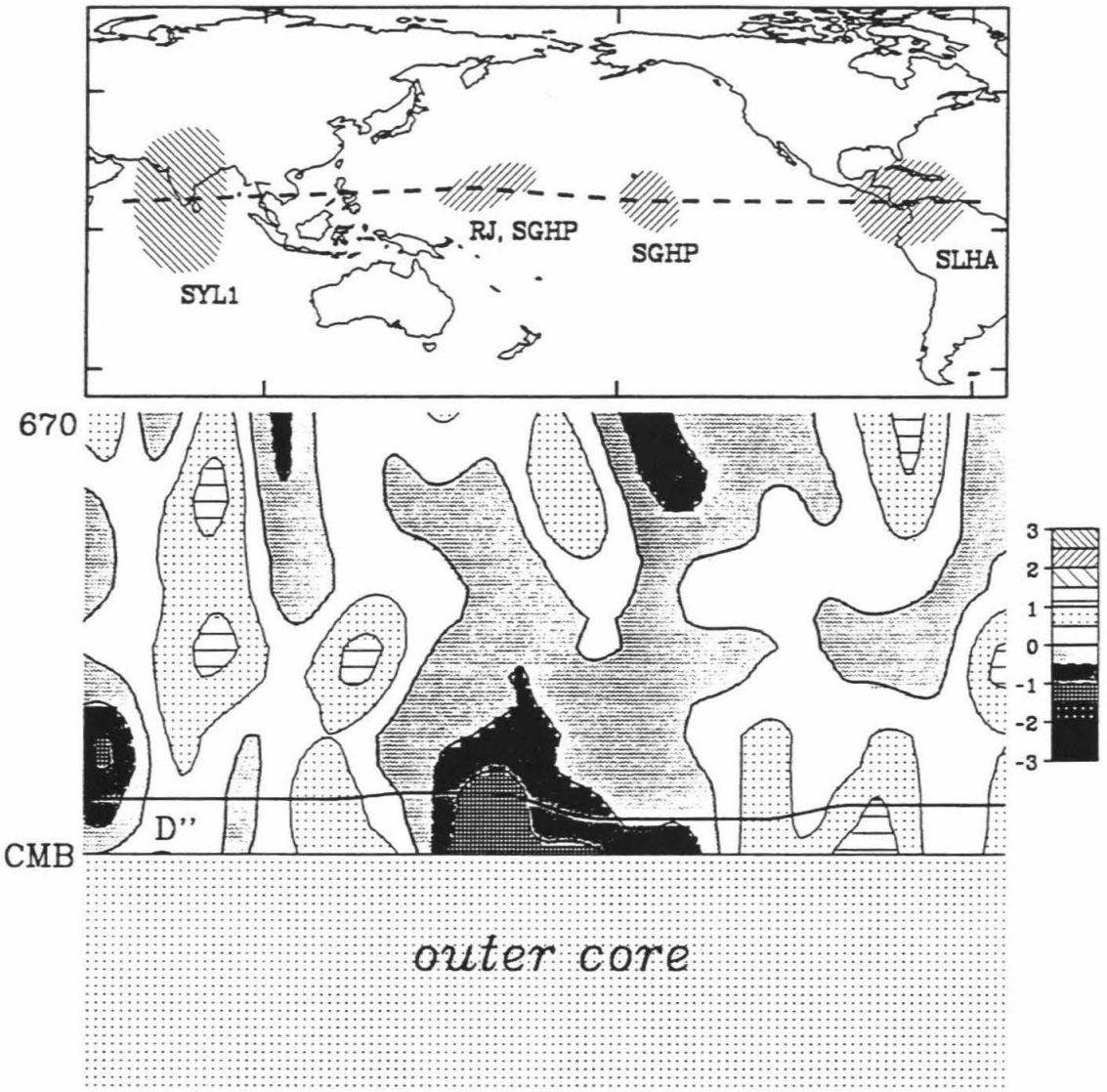
SYL1
RJ, SGHP
SGHP
SLHA
670
D''
CMB
outer core
3
2
1
0
-1
-2
-3

such structure using the North American array of broadband and analog stations, as well as digital data from KIP, AFI, and other stations. Perhaps the complexities in the data of Figure 4.7 are related to such a variable D″ layer. Lateral variation in D″ thickness relates to many other disciplines of deep Earth study, and directly relates to studies concerned with D″ as a "reservoir" for old slabs, and has even been discussed in relation to reaction products from chemical reactions between the liquid outer core and the crystalline silicates of the lowermost mantle [for a review, see Jeanloz, 1993]. The preliminary finding here is that D″ thickness may vary by as much as 150 km between two distinctly different regions (e.g., see models SLHE and SGHP).

The scenario of having a continuous D″ layer as in Figure 4.12 bears upon the issue of D″ discontinuity as a global feature [as discussed by Nataf and Houard, 1993]. Since our data is localized to two CMB patches, we are unable to help resolve this issue. The study of Kendall and Shearer [1994] utilizes long-period GDSN data to infer lateral variations in height above the CMB of the D″ discontinuity. Their study presents the most comprehensive D″ thickness map for any one investigation, and a D″ discontinuity was found for all regions sampled by their data, which amounts to nearly 20% of the surface area of the CMB. Incomplete sampling of the D″ region, along with evidence proposed against the existence of a D″ discontinuity [Schlittenhardt et al., 1985], makes difficult at present conclusions of whether or not the D″ discontinuity is a global feature.

The study of Schlittenhardt et al. [1985] argues against D″ stratification based on predictions of model SLHO of Lay and Helmberger [1983a] compared to observations. Model SLHO predicts a small but detectable second arrival in the tail of diffracted $S-$ and P-waves. This model, however, has been updated in Young and Lay [1990]; a slightly positive V_S gradient beneath the D″ discontinuity has been changed to a slightly negative one. The model modification results in an absence of the second

arrival over the distance range used by Schlittenhardt et al. [1985] to argue against the discontinuity's existence. Therefore the approach of Schlittenhardt et al. [1985] must be applied to other more current models before such conclusions can be drawn.

We have interpreted observations of *Scd* arrivals between *S* and *ScS* in terms of 1-D discontinuity structures of differing thicknesses. It is important, however, to point out that lateral variations in D″ structure as presented above can add complexities to *Scd* and *ScS* travel times and waveforms. Synthetic tests were conducted for a 2-D model with a thin D″ structure (Figure 4.13). In Figure 4.13 the *S*, *Scd*, and *ScS* raypaths are shown along with iso-velocity contours for an Earth-flattened whole mantle cross-section, depicting a D″ layer that becomes thin in the center (SGHP) from a thicker D″ layer (SYL1) in the bordering regions. As in Figure 4.12, this structure is by no means unique, and is used to aid in understanding 2-D wavepath effects. Wavepaths distort and become non-uniform as a result of the dipping structure. The example shown is for a 500 km deep source depth and 82°. Three source placements for this structure were run for epicentral distances of 78°, 80°, and 82°. Resulting long-period synthetics are presented in Figure 4.14. The 2-D Cagniard de Hoop technique used to generate the synthetic seismograms is discussed in Helmberger et al. [1985a] and Helmberger et al. [1994]. In each trace, *S* and *ScS* are the first and last positive polarity arrival, respectively, and the arrival with the dot above it is *Scd*. For each distance, the Scd-S time increases for increasing source placement number, due to *Scd* encountering an even slower D″ structure. This 2-D run differs from the 1-D runs having different D″ thicknesses in that the *ScS* arrival is also delayed relative to *S*, and that the amplitude ratio of *Scd* to *ScS* is highly variable, with some cases showing *Scd* larger than *ScS*. Ultimately, through constructing a more comprehensive data set along with studying *S*, *Scd*, and *ScS* behavior from synthetic tests, it may be possible to more uniquely model such D″ variations.

Several different factors may contribute to uncertainties in the travel time mea-

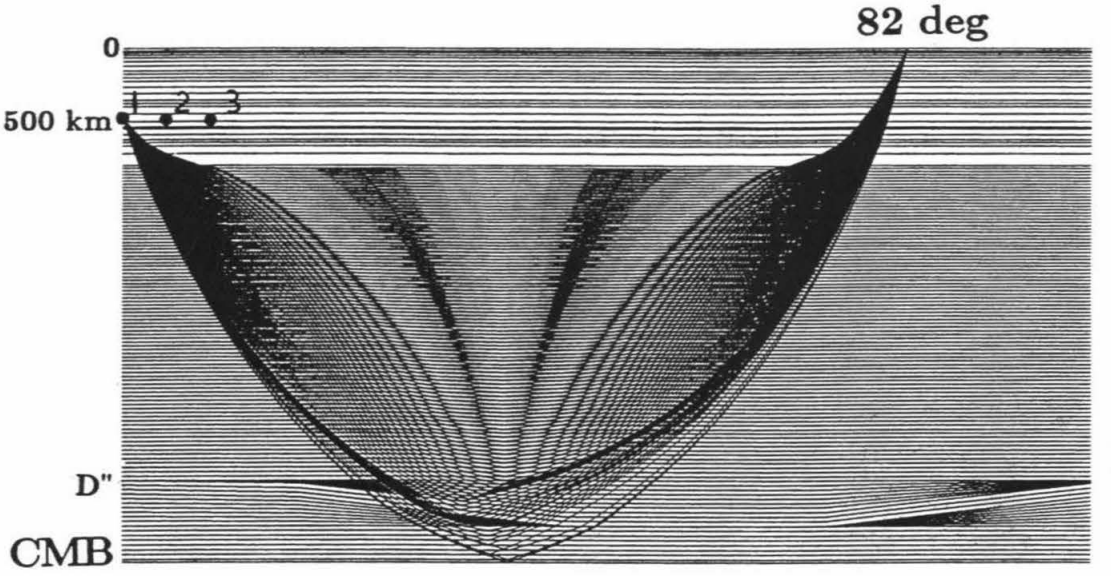

Figure 4.13: Iso-velocity contours representing a whole mantle cross-section of a laterally varying D″ region. In this test, a 280 km thick D″ discontinuity thins towards the center of the model to a thickness of 180 km. Geometric raypaths reflecting from each layer interface of this structure are displayed, and are perturbed due to the 2-D structure. Three source locations were tested, and are indicated at the left end of the model.

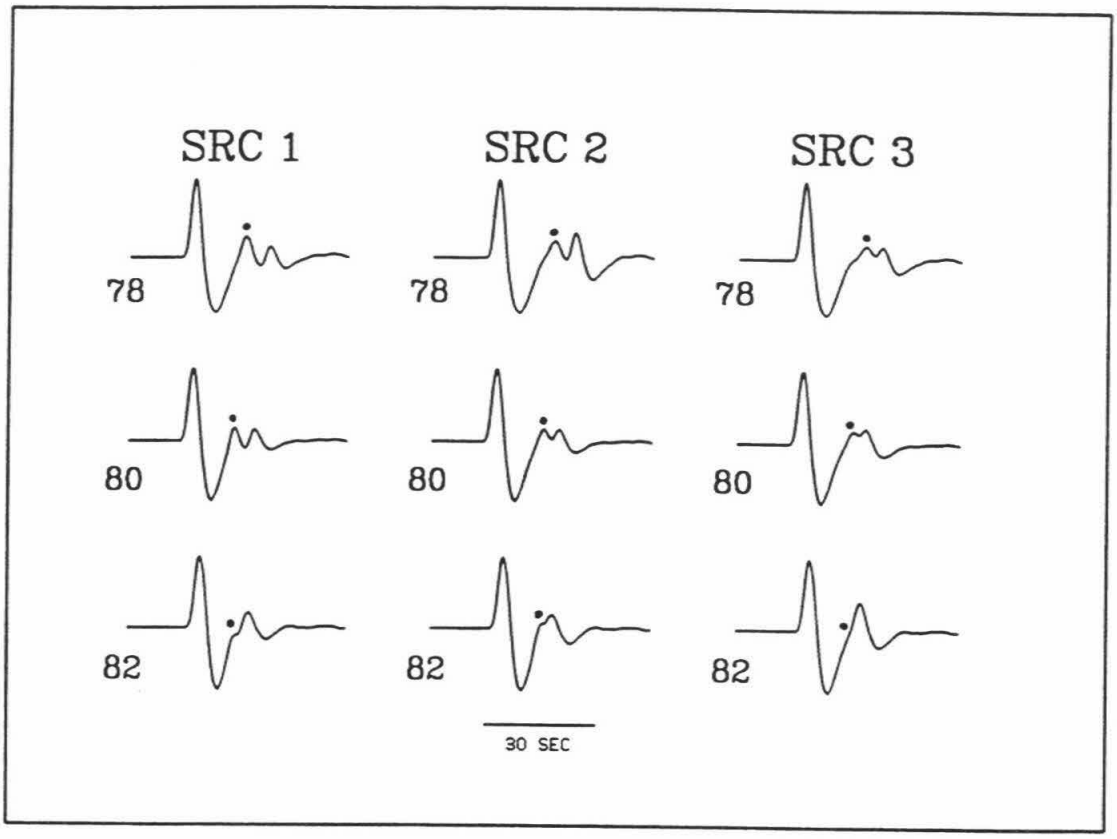

Figure 4.14: Tangential component synthetics from the 2-D model of Figure 4.13 as filtered through a long-period WWSSN instrument. The 3 columns correspond to the 3 different lateral source placements, and 3 epicentral distances are shown for each source (78^o, 80^o, and 82^o.) The first, second and third arrivals in each case are S, Scd, and ScS, respectively, except in one case where Scd is obscured at 82^o for SRC 3.

surements. For example, a 50 km error in source depth will result in approximately a 0.5 sec error in both $Scd-S$ and $ScS-S$. Travel time picking errors may be as large as $\pm$ 1.5 sec for complicated records. Compounding these errors to obtain a ± 2 sec error bound on the differential travel time measurements does not change our basic conclusions about lateral variations in D$''$ thickness beneath the mid-Pacific. CMB topography will affect the ScS times, which are not used here to infer D$''$ thickness.

4.8 Conclusions

In this study, we present evidence for a D$''$ discontinuity in V_S for two different regions beneath the central Pacific from an analysis of S, Scd, and ScS waves. The 3-D mantle model of Su et al. [1992] was used to correct the $Scd - S$ and $ScS - S$ differential travel times in an effort to isolate contributions to these times from D$''$ structure. Data traversing the CMB region to the east are best modeled by a D$''$ discontinuity around 180 km above the CMB. The data from the western region have significant scatter, precluding a confident estimate of a D$''$ layer thickness, though may ultimately be better modeled by a D$''$ layer having thickness closer to that of SYL1, or larger, as suggested by travel times. The gradients above and below the D$''$ discontinuity, as well as the depth range over which the V_S increase at the top of D$''$ discontinuity occurs, are not well resolved with the long-period data. Preliminary analysis of broadband data displays complex waveform behavior in the vicinity of the Scd arrival, and makes necessary better understanding of source and receiver structure than for the long-period data.

A possible D$''$ scenario is presented where the D$''$ layer may be a continuous feature in large portions of the lower mantle, with its thickness varying from region to region, by more than 100 km, possibly having velocities within and above the layer varying as well. The V_S jump at the top of this layer may be sharp in some

places, and distributed in other regions. 2-D synthetic tests, along with larger more comprehensive data sets, may help to eventually constrain such features.

These results add to the accruing body of evidence that D″ is stratified in many different locations. Path geometry limitations prevent rapid progress in determining if this distinct layer is a ubiquitous feature on Earth. Nonetheless, the locations studied here are in completely different regions from those of previous studies using this technique. Upon better resolution of D″ structures and their lateral variations, it will be of great importance to understand their relationship to the dynamics of the lower mantle.

Chapter 5

Low P-wave velocity at the Base of the Mantle

5.1 Abstract

A tool for investigating P-wave (V_P) structure at the base of the mantle is presented. SKS waves at distances around 107^o are incident upon the core-mantle boundary (CMB) with a slowness that allows for coupling with diffracted P-waves (P_{diff}) at the base of the mantle. The P-wave diffraction occurs at both the SKS entrance and exit locations of the outer core. The resulting phase, SP_dKS, arrives slightly later in time than SKS, having a wave path through the mantle and core very close to SKS. The difference time between SKS and SP_dKS strongly depends on V_P at the base of the mantle near SKS core entrance and exit points. Digitized long-period (5-15 sec) observations from deep focus Fiji-Tonga events recorded by North American World Wide Seismographic Station Network (WWSSN) and Canadian Seismographic Network stations, and South American events recorded by European and Eurasian WWSSN stations exhibit anomalously large SP_dKS-SKS difference times. SKS and the later arriving SP_dKS phase are separated by several seconds

more than predictions made by 1-D reference models, such as the global average PREM model [Dziewonski and Anderson, 1981]. Models having a pronounced low-velocity zone in V_P at the base of the mantle predict the size of the SP_dKS-SKS anomalies seen in the observations. These models are perturbations of the PREM model, whereby the lowermost 50-100 km of the D'' layer has a negative V_P gradient, with the mantle-side CMB V_P reduced from PREM by 5% (to 13.0 km/s) at the base of the mantle. Raypath perturbations from lower mantle V_S structure may also be contributing to the observed anomalies.

5.2 Introduction

Knowledge of the core-mantle boundary (CMB) region is based entirely on data gathered near the Earth's surface. Our probes of the interior include seismic waves and free oscillations, tides, gravity, heat flow, rotation of the Earth, electric and magnetic field measurements, and information from rocks transported to the surface by dynamic geological processes. Interpreting these data often requires assuming an initial Earth model constructed using previously determined knowledge of the region. In most CMB studies, this knowledge comes mostly from past seismic investigations. A more detailed understanding of the seismic structure of the CMB region will have a strong influence on many other geophysical disciplines.

In this study, an important seismic constraint on the P-wave velocity (V_P) structure at the base of the mantle is presented. SKS waves near 107^o in epicentral distance have an angle of incidence to the CMB that is the critical angle of incidence for ScP waves. At such a ray parameter, SKS couples with diffracted P-waves (P_{diff}) along the mantle side of the CMB at the SKS core entrance and exit locations, to make a later arriving phase named SP_dKS. This phase was theoretically discussed by Kind and Müller [1975] and Choy [1977], and shown to have a travel-

time curve with the same slope as that for P_{diff}, and tangential to the travel-time curve of SKS at around 107° (Figure 5.1.) This distance is a model dependent feature. Observations of SP_dKS were noted by Schweitzer [1984] and Schweitzer and Müller [1986] in studies of SKS and $SKKS$, but travel time and waveshape of SP_dKS have not been explored for modeling purposes. An interrelated phenomena, however, is the drop in SKS amplitudes as seen in $SKKS/SKS$ ratios due to losing SKS energy to the SP_dKS phase [Silver and Bina, 1993].

SP_dKS becomes visibly separate from SKS near 109°-110°, with the SP_dKS-SKS difference time increasing with distance. Figure 5.2a shows a ray-path representation of SKS and SP_dKS waves at 118° distance (for a 500 km deep source). The figure shows two different paths (SP_dKS + SKP_dS) contributing to the composite diffraction arrival. However, as pointed out by Choy [1977], there are an infinite number of such paths between the two end-members shown in the figure that connect the source and station (i.e., $SP_{diff}KP_{diff}S$ waves). These paths travel partly as a P-wave in the core (K) and partly as P_{diff} in the mantle, all having in common the same total angular distance traveled by P_{diff}+K. Figure 5.2b presents the separation of SKS and SP_dKS wave paths as they approach the CMB. The dotted line gives the distance between the S leg of SKS and SP_dKS raypaths at the CMB, which at 125°, is only around 220 km. This suggests that if lower mantle S-wave velocity (V_S) structure is contributing to the observed SP_dKS-SKS time anomalies, D'' V_S heterogeneity must exist at wavelengths smaller than 220 km, or that strong lateral gradients capable of perturbing SKS and SP_dKS wavepaths (and thus travel times) are present. The solid line in Figure 5.2b represents the total length (source-receiver-side) of the P_{diff} arc for any of the infinite paths comprising SP_dKS, which shows that at the large distances, the P_{diff} arc on can be greater than 1000 km.

Figure 5.3 shows the same raypath representation for SP_dKS as in Figure 5.2 along with radial component long-period synthetics for 3 different distances. The

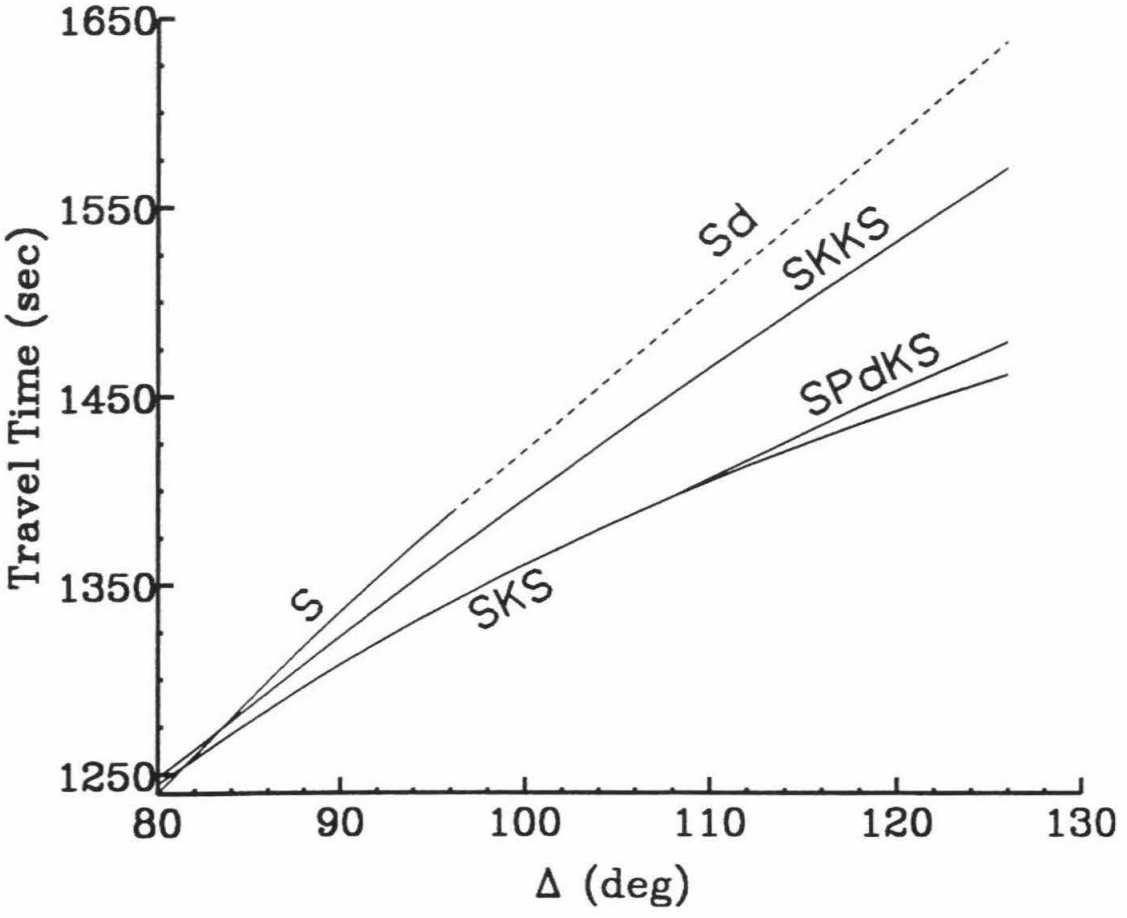

Figure 5.1: Travel time-distance curve showing SP_dKS behavior in relation to that of SKS, $SKKS$, and S. The SP_dKS curve is tangent to that of SKS, with the same slope as that of P_{diff}.

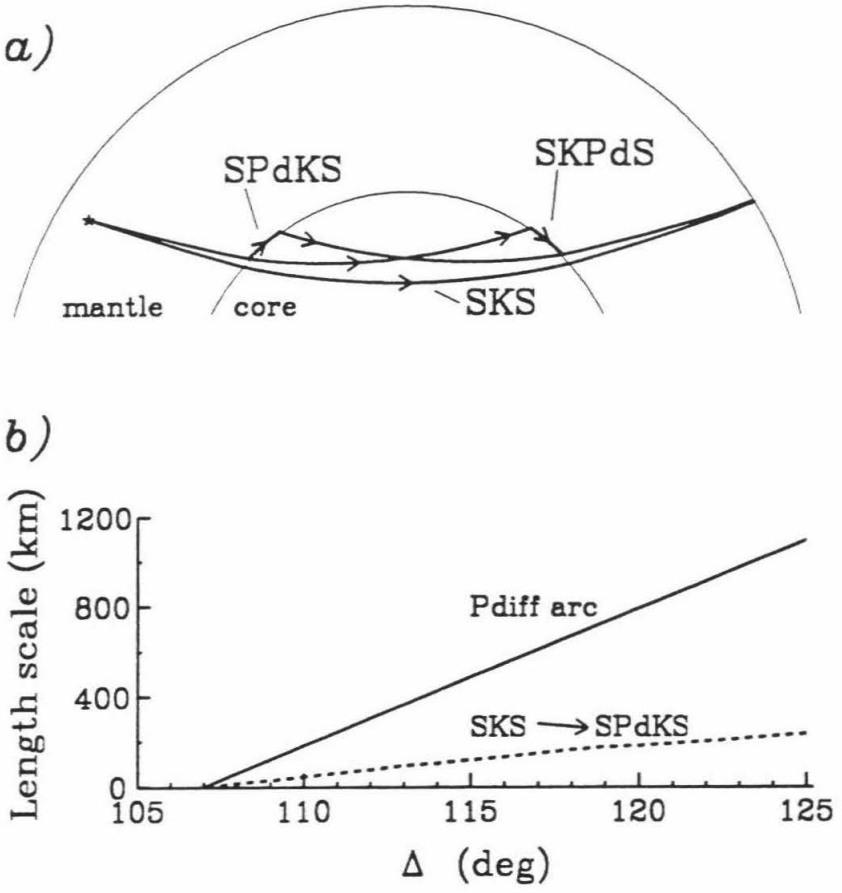

Figure 5.2: (a) Cross-section showing ray paths of SKS and the two end-member SP_dKS paths (of the infinite set of rays comprising SP_dKS, see text). (b) Length of P diffraction arcs (solid line); and distance between S legs of SKS and SP_dKS at base of mantle (dashed line).

synthetics were generated using the reflectivity method [see, for example, Fuchs and Müller, 1971], and the peaks of SKS and SP_dKS are indicated by arrows. The moveout of SP_dKS relative to SKS is easily viewed in the synthetics. The figure shows the extreme closeness of the SKS and SP_dKS paths at the 110^o distance. At the larger distances, SKS and SP_dKS mantle paths are more separated, but still close (Figure 5.2b), and display more divergent outer core paths than at smaller distances.

The purpose of this study is to present data from two source-receiver geometries that display anomalously late SP_dKS times relative to SKS. The main conclusion is that models having relatively low V_P values at the base of the mantle can produce synthetics that agree with the mean of the observations. This implies a strongly negative dV_P/dz gradient for the regions sampled. Affects of V_S structure on SP_dKS-SKS are also discussed.

5.3 Data

Long-period observations (5-15 sec) from deep focus Fiji-Tonga events recorded by North American World Wide Seismographic Stations Network (WWSSN) and Canadian Seismographic Network (CSN) stations, and South American events recorded by European and Eurasian WWSSN stations are ideal to study SP_dKS because of the good station coverage spanned over an appropriate distance range. These records have been optically scanned, digitized and rotated to obtain the SV component of motion. Table 5.1 lists events used in the analysis and Figure 5.4 displays the corresponding path coverage. Plotted are great-circle paths between events (stars) and stations (triangles). Thicker line segments represent the P diffraction zones associated with SP_dKS waves.

Radial component long-period observations for one of the Fiji-Tonga events and

Figure 5.3: Earth cross-section and corresponding long-period radial component reflectivity synthetic is shown for three epicentral distances: 110°, 118°, and 125°. Geometric ray paths for SKS and SP_dKS are shown in the cross-sections, and the separate arrivals are denoted in the synthetics by arrows. The moveout of SP_dKS from SKS with distance is easily viewed in the reflectivity predictions.

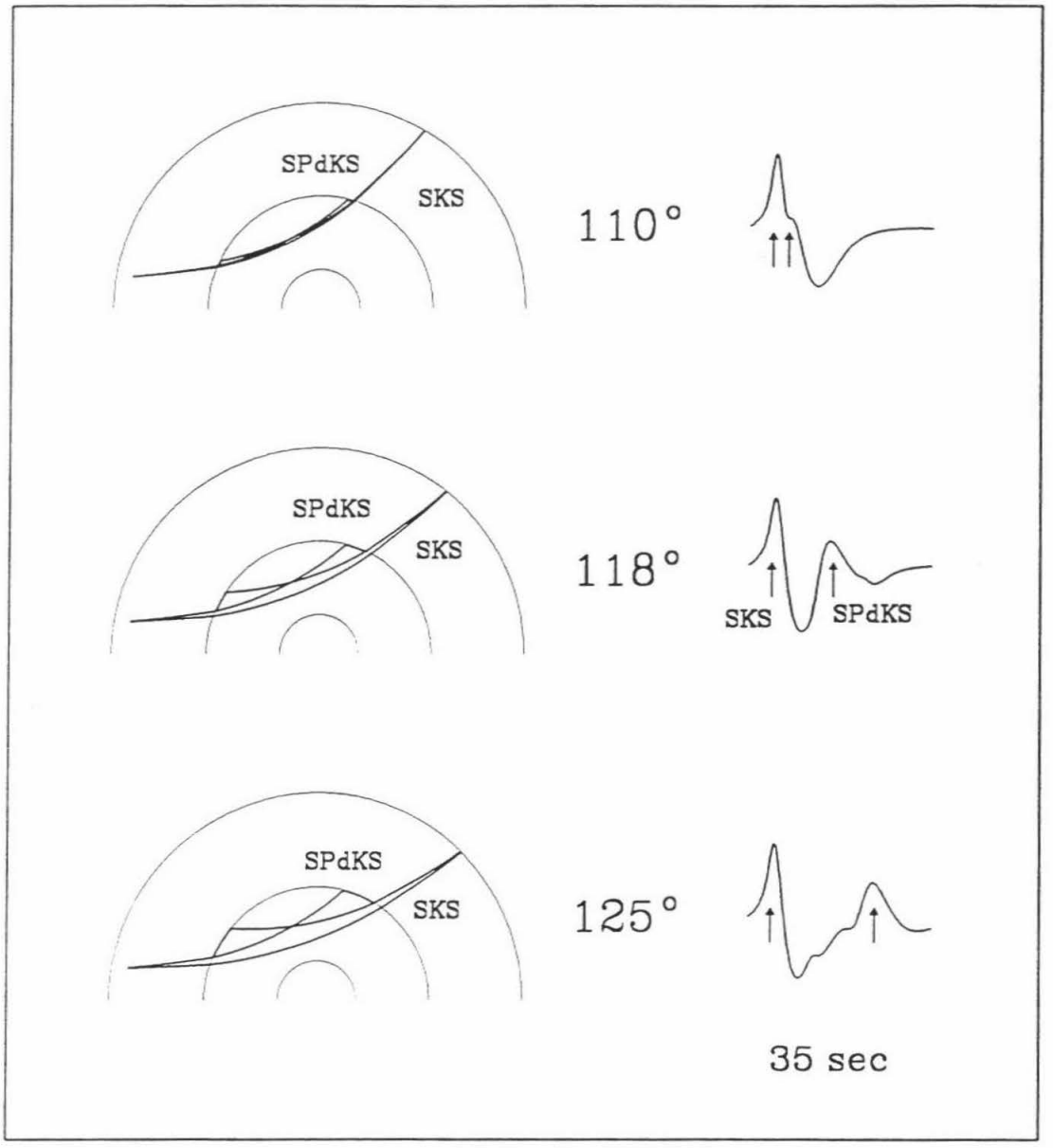
SPdKS
SKS
110°
SPdKS
SKS
118°
SKS
SPdKS
SPdKS
SKS
125°
35 sec

Figure 5.4: Great-circle paths (thin lines) between events (stars) and stations (triangles), for data analyzed from Table 5.1. The thicker line segments represent the P diffraction zones for the SP_dKS phase.

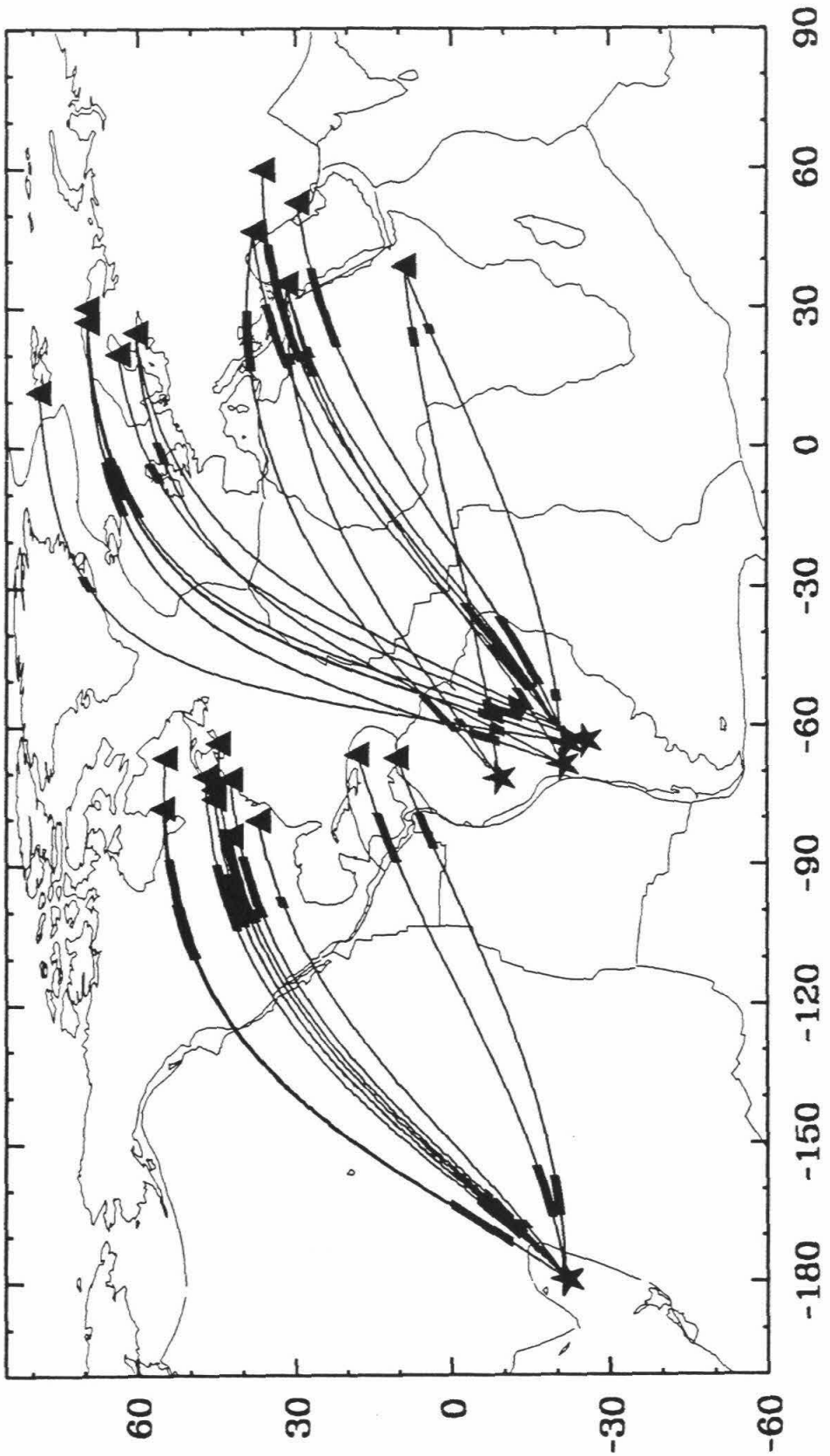
60
30
0
-30
-60
-180
-150
-120
-90
-60
-30
0
30
60
90

Date			Z		
mmddyy	LAT	LON	(km)	M_b	Region
012469	21.87S	179.54W	587	5.9	Fiji-Tonga
062870	21.66S	179.42W	587	5.8	Fiji-Tonga
110365	9.04S	71.32W	587	5.9	Peru-Brazil
082368	21.95S	63.64W	513	5.6	S. Bolivia
102573	21.96S	63.65W	517	6.1	S. Bolivia
122767	21.29S	68.20W	91	6.3	Bolivia
072569	25.49S	63.21W	573	5.6	Argentina

Table 5.1: Event information for $SP_dKS - SKS$ data as reported by ISC.

2 Bolivia events are presented in Figure 5.5. In both columns, amplitudes are normalized to the SKS peak, and all traces have been aligned to the SKS peak (dotted line). Arrows indicate the peak of the SP_dKS arrival. Moveout of SP_dKS behind SKS is easily viewed in the data. Second order features are also present. For example, the records WES (Westin, Massachusetts) and SJG (San Juan, Puerto Rico) in the Tonga column are nearly at the same distance, but differ in azimuth by about 28^o, with SP_dKS at WES arriving almost 2 sec later than that at SJG. Lateral variations in V_P between the two paths can cause such behavior. Records AAM (Ann Arbor, Michigin) of the Tonga event and JER (Jerusalem, Israel) of the 8-23-68 Bolivia event are both near 108.5^o, though only the AAM record shows evidence of SP_dKS. In viewing more AAM and JER records for these source regions, this appears to be a stable pattern. This might be attributed to a high Q path for AAM (the SKS peak is higher frequency than that at JER, see Figure 5.5), resulting in the ability to view the onset of SP_dKS. Complicated SP_dKS arrivals are apparent at stations

TAB (Tabris, Iran) and MSH (Meshed, Iran) for the 8-23-68 Bolivia event. SP_dKS for both records appears as a double arrival. Such a feature may be produced by having different D'' V_P structures on the source and receiver sides of the SP_dKS paths, and is discussed below. Also noteworthy is a slight negative polarity arrival before SP_dKS at HAL (Halifax, Nova Scotia, Canada) for the Tonga event, and SHI (Shiraz, Iran) and MSH for the 8-23-68 Bolivia event. This arrival is the inner core reflected phase $SKiKS$.

5.4 Synthetic Waveform Modeling

As apparent in Figures 5.2 and 5.3, the SP_dKS phase depends strongly on CMB mantle-side V_P at both the source and receiver sides of the path. These effects have been explored in our experiments using a generalized ray code that permits differing V_P mantle structures for the downgoing and upgoing SP_dKS waves. Such tests reveal that the SP_dKS arrival can broaden, becoming longer period and lower amplitude, and even a double arrival, if V_P differs on the two sides of the path. The degree to which V_P differs will determine the separation between the two different SP_dKS arrivals. The technique used to create such synthetics is discussed in Helmberger et al. [1994]. Silver and Bina [1993] discuss the effects of such heterogeneity in relation to $SKKS/SKS$ ratios. In this study, however, we will concentrate on understanding the first-order anomalous features in the data, such as the SP_dKS-SKS differential times and waveshapes. Since most of the data analyzed here has clean, single-peak SP_dKS arrivals, we approach the first-order modeling in the 1-D sense, and leave investigation of 2-D and 3-D structures for future research.

In our modeling experiments, the reflectivity method has been employed to ensure proper handling of all important multiples within the CMB region. In testing different 1-D lower mantle structures, SP_dKS-SKS times were most easily perturbed

Figure 5.5: SV data for a Tonga event recorded in North America (left column) and 2 Bolivia events recorded in Europe and Eurasia (right column). SKS is lined up and amplitudes are normalized. Arrows indicate the SP_dKS arrival, and illustrate the coherent moveout of SP_dKS with respect to SKS.

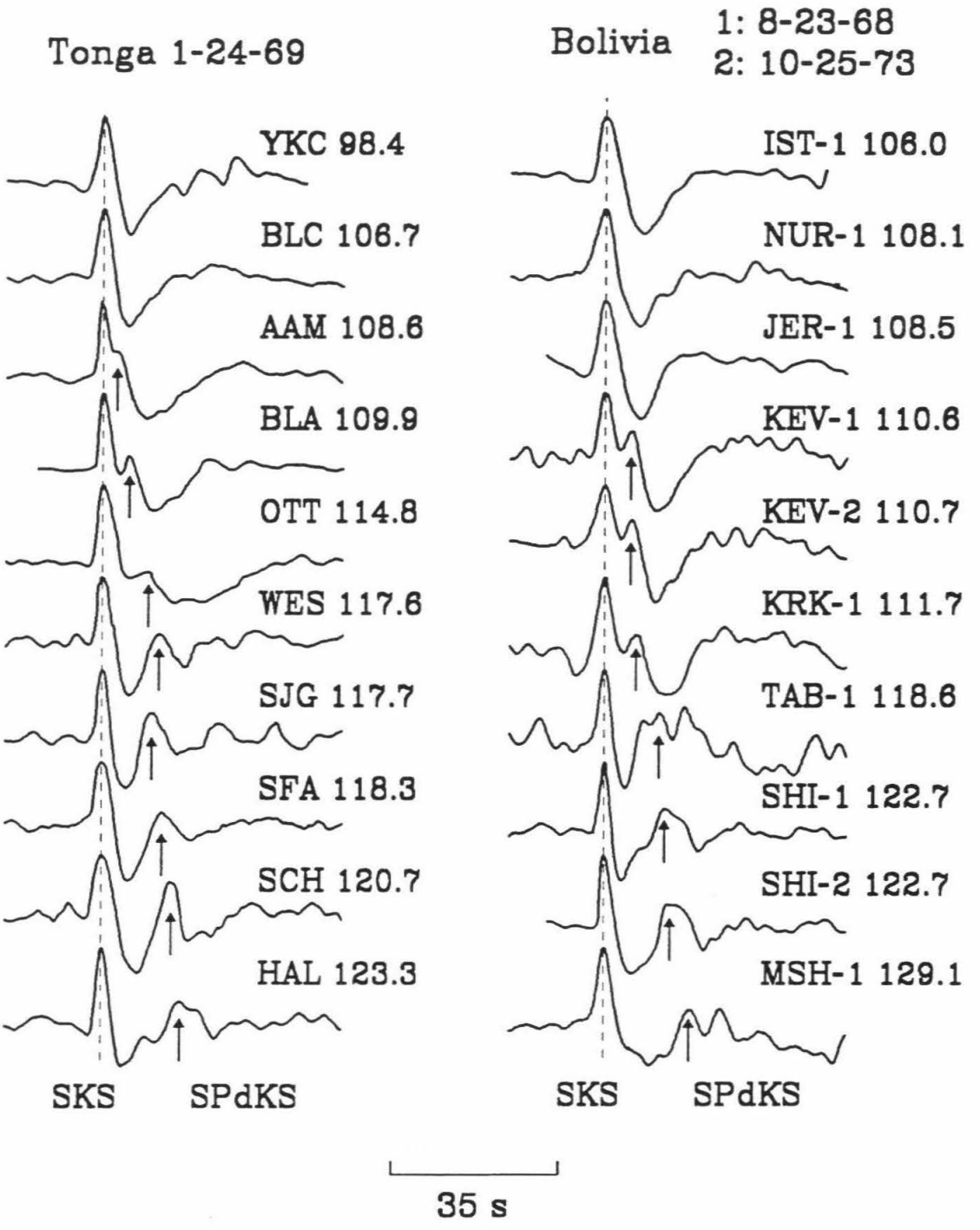
Tonga 1-24-69
YKC 98.4
BLC 106.7
AAM 108.6
BLA 109.9
OTT 114.8
WES 117.6
SJG 117.7
SFA 118.3
SCH 120.7
HAL 123.3
SKS
SPdKS
Bolivia
1: 8-23-68
2: 10-25-73
IST-1 106.0
NUR-1 108.1
JER-1 108.5
KEV-1 110.6
KEV-2 110.7
KRK-1 111.7
TAB-1 118.6
SHI-1 122.7
SHI-2 122.7
MSH-1 129.1
SKS
SPdKS
35 s

by altering the P-wave velocity at the base of the mantle. In this manner, the P_{diff} part of SP_dKS could be independently slowed down to increase SP_dKS-SKS times to compare with the observations. Similar 1-D perturbations in V_S produced little affect on SP_dKS-SKS times due to both SKS and SP_dKS being affected similarly, thus producing no significant difference time anomaly.

The PREM reference model [Dziewonski and Anderson, 1981] is displayed along with two models containing low-velocity zones (LVZ) at the base of D'' in Figure 5.6. Models P-5_50 and P-5_100 contain a 5% reduction in V_P from PREM at the base of the mantle, with an overlying linear gradient connecting to PREM 50 and 100 km, respectively, above the CMB. SV motions of SKS and SP_dKS have been produced for these 3 models and convolved with a long-period WWSSN instrument for comparison to the data. Figure 5.7 displays synthetics for PREM, P-5_50 and P-5_100. The source depth in the synthetics is 560 km. The development of the first visible SP_dKS arrival in the PREM synthetics occurs at a larger distance than in the data (compare with Figure 5.5). The shift in distance to match the SP_dKS-SKS times of the data and the PREM synthetics is 2-3°. The SP_dKS travel time curve of PREM is super-imposed on the P-5_50 and P-5_100 synthetics to illustrate increased SP_dKS-SKS times in both P-5_50 and P-5_100 due to decreased V_P values at the base of the mantle. Model P-5_100 produces the largest SP_dKS-SKS times due to the thicker zone of reduced V_P. The low amplitude but visible $SKiKS$ phase, the SKS phase that reflects off the inner core, is also indicated in the figure. $SKiKS$ interferes with SP_dKS at the larger distances.

Waveform comparisons of synthetic predictions through model P-5_100 to the observations for the Fiji-Tonga event of Figure 5.5 are presented in Figure 5.8. Radial component long-period traces are shown, and the stations and distances are indicated. The SKS-SP_dKS interference is well-predicted by the synthetics. Some travel time anomalies still exist, however, such as at station CAR (Caracas, Venezuela),

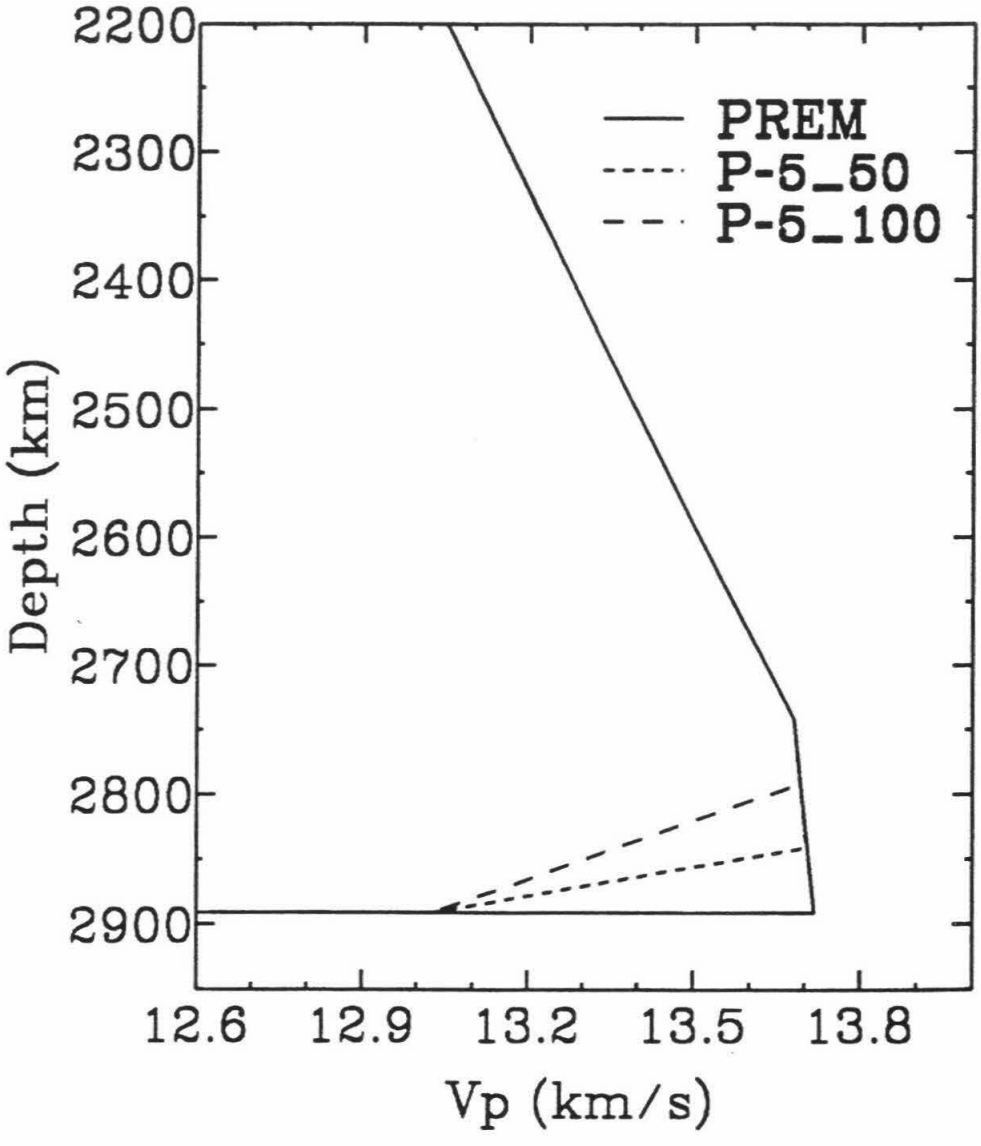

Figure 5.6: V_P profiles for the PREM model and 2 models containing a 5% reduction from PREM at the base of the mantle.

Figure 5.7: Reflectivity synthetics as filtered through a long-period WWSSN instrument of SKS and SP_dKS (and $SKiKS$) for the models of Figure 5.6.

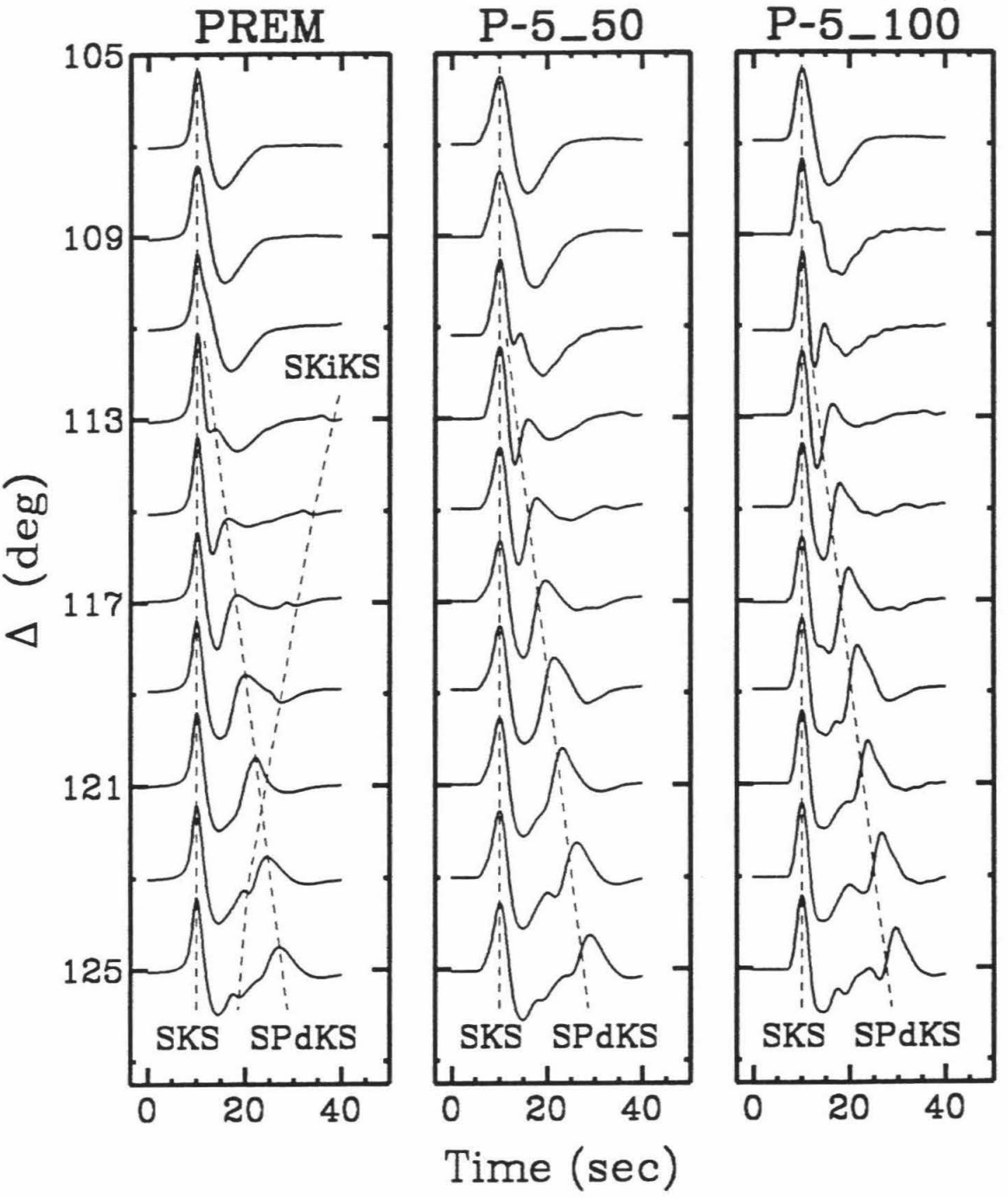
PREM
P-5_50
P-5_100
105
109
113
117
121
125
Δ (deg)
SKiKS
SKS
SPdKS
SKS
SPdKS
SKS
SPdKS
0
20
40
0
20
40
0
20
40
Time (sec)

where the predicted SP_dKS peak arrives before the observation. A summary of the SP_dKS-SKS differential times is presented in the next section.

Models P-5_50 and P-5_100 are meant to illustrate the type of V_P reductions necessary to match the SP_dKS-SKS times and waveforms, but are certainly non-unique. Many models having different LVZ thicknesses and amplitudes were tested, and a small trade-off between thickness and amplitude of the LVZ exists. Nevertheless, if a 1-D modeling approach is pursued with the SP_dKS data, a LVZ in V_P at the base of the mantle of several percent, and as large as 5%, is the most effective way of explaining the observations. However, there exists the problem of lateral variations between the source and receiver sides of the path at the CMB, as well as between the South America and Fiji-Tonga data sets. This will be discussed in the next section.

5.5 Differential Travel Times

As a first effort in understanding the anomalous SP_dKS-SKS times, we have explored 1-D models that contain perturbations to PREM in the lowermost 50-100 km of the mantle. In this approach, there is a trade-off between V_P at the CMB and the thickness of the layer over which the V_P values depart from PREM. However, 1-D synthetic tests varying V_P and V_S lower mantle structure, as well as outer core V_P structure, show that SP_dKS-SKS times are most strongly affected by the mantle V_P value at the CMB interface. The other features investigated only produced second-order effects on the synthetics. The thickness of the low-velocity zone (LVZ) at the base of the mantle necessary to model the data depends on the wavelengths of interest. For the long-period WWSSN data, a LVZ 50 km thick can model the anomalies if V_P is lowered by 6% (to 12.9 km/s). Broadband data will help to resolve this non-uniqueness through investigating frequency dependence of SP_dKS waves.

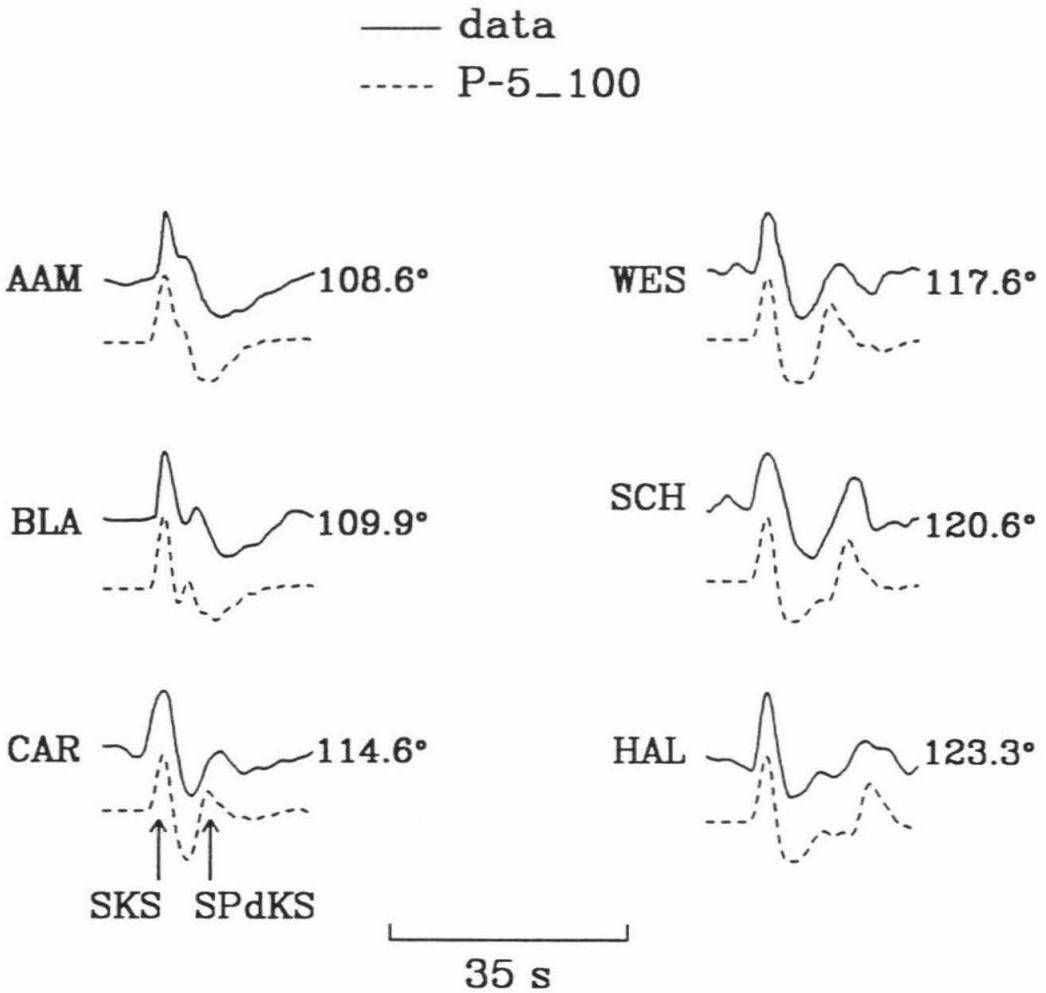

Figure 5.8: Six radial component records from the Fiji-Tonga event of Figure 5.5 (solid traces) plotted with predictions from the P-5_100 model (dotted traces). The first and second pulses are SKS and SP_dKS, respectively.

The differential times (peak to peak) of SP_dKS and SKS are summarized in Figure 5.9. Also included are those of the models in Figure 5.6. The SP_dKS-SKS curves deviate from straight lines due to the interference of SP_dKS with the back swing of the SKS phase. The first-order feature apparent in Figure 5.9 is that PREM under-predicts the SP_dKS-SKS times by 2-3 sec on average. Predictions from model P-5_100 fit the average of the data, with scatter in the data on the order of 1-2 sec. Predictions from model P-5_50 are about 1/2 sec smaller than those of model P-5_100. The two data points near 123° have anomalously small times (records SHI-1,2, Figure 5.5). This implies that the source- and receiver-side P diffraction zones for paths to SHI from South America average to a more PREM-like V_P at the CMB (or faster.) All the other data in the figure, however, require anomalously slow V_P values at the CMB, with large lateral variations in V_P (and probably dV_P/dz) necessary to explain the scatter with such 1-D structures.

5.6 Discussion

Upper mantle anisotropy can cause distortions and splitting in broadband SKS waveforms [see, e.g., Silver and Chan, 1988]. Such effects, however, are not observed for the long-period WWSSN and CSN data, and hence are assumed not to contribute to the scatter seen in Figure 5.9. Also, synthetic tests show that SP_dKS-SKS times and waveforms are insensitive to small perturbations (± 5 km) in CMB depth, or event source depth. The first-order analysis of this paper does not address discontinuity structures at the top of the D″ layer (which only produce second-order effects on SP_dKS). A ±50 km event mislocation along azimuth will contribute ±0.4 sec to the SP_dKS-SKS times. If small scale-length lateral variations in V_S exist at the base of the mantle, then SKS or SP_dKS may be preferentially affected. For 5-15 sec waves traveling at 7.2 km/s, wavelengths are 36-108 km, which is smaller than

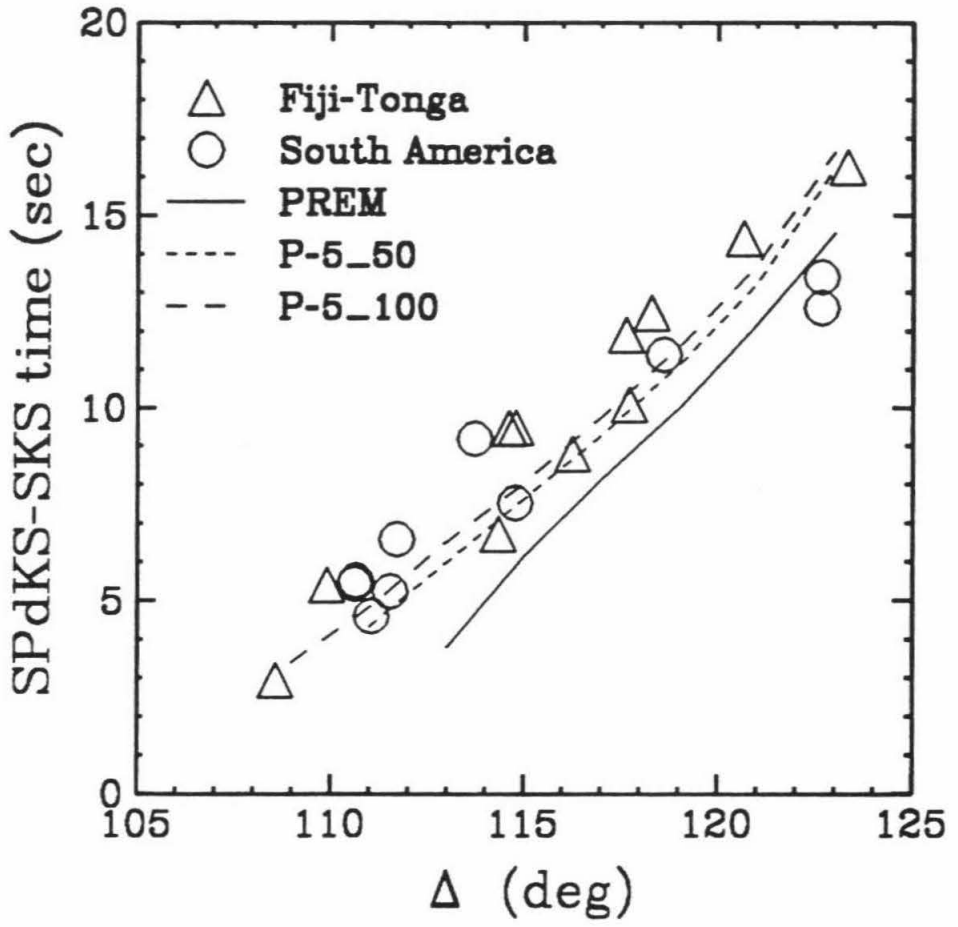

Figure 5.9: Peak to peak differential travel times of $SP_dKS - SKS$ for the data (symbols) and the predictions from the synthetics (lines).

the separation between SKS and SP_dKS for a large part of the distance range in Figure 5.2b (dotted line). A 1% reduction in V_S over a 200 km layer at the base of the mantle traversed only by SP_dKS (and not SKS) will increase the SP_dKS-SKS time by only 0.6 sec, if the same anomaly exists at the core entrance and exit locations. A similar scenario with a 2% reduction in V_S will result in a 1.2 sec increase of the difference time. We are unable to resolve such features, however, since the data are scattered at distances where SKS and SP_dKS paths are separated by less than a wavelength in D'' (109-112°, see Figure 5.9). Other factors, such as laterally varying CMB V_P surely contributes to the scatter.

The degree to which 2-D V_S variations and lateral gradients affect SP_dKS are still undetermined. As seen with the family of core underside reflections $SmKS$ (e.g., SKS, $S2KS$, $S3KS$, ...), strong lateral gradients in V_S can affect raypaths resulting in travel time and waveform perturbations [Garnero and Helmberger, 1994]. For most of the $SmKS$ wavegroup, adjacent mantle paths for the different $SmKS$, e.g., SKS and $SKKS$, are further separated in the lowermost mantle than $SP_dKS - SKS$ separations. For this reason, such lateral gradients are expected to place a smaller role for the $SP_dKS - SKS$ anomalies. Nevertheless, these affects must be considered in future work analyzing these phases. In particular, the Fiji-Tonga dataset traverses a slow lower mantle region on the source-side of the wavepaths [Garnero and Helmberger, 1993; Wysession et al., 1994]. Absolute and differential time anomalies of $SmKS$ waves will provide important information in this regard.

If the anomalously low CMB V_P values needed to model the SP_dKS data are linearly connected to the overlying mantle of the PREM model (as done for models P-5_50 and P-5_100), super-critical velocity gradients and thus departures from adiabaticity result. Better resolving the vertical V_P structure at the base of the mantle is necessary, and can provide important information about the thermal boundary layer at the CMB. Analyzing more data, along with the inclusion of broadband data, is

necessary. Further constraints may be added by folding in information from short- and long-period (as well as broadband) direct P-waves, at distances where the wave starts to diffract around the Earth's core. Unfortunately, past detailed short-period P-wave analyses [e.g., Young and Lay, 1989; and Ruff and Helmberger, 1982] are for different CMB samples than encountered in this study.

Anomalous amplitude ratios of PcP/P have been used to infer a strong negative V_P gradients at the base of the mantle by, for example, Müller et al. [1977] and Niazi and McLaughlin [1987]. These studies, however, while presenting structures qualitatively similar to those tested here, are for different CMB regions than those sampled here. A similar study by Schlittenhardt [1986] argues for low Q in the D" region to explain PcP/P ratios. Schlittenhardt [1986] points out that the low Q necessary to explain his observations prevents the ability to resolve low V_P gradients at the base of the mantle.

In general, past seismological studies of the radial velocity structure in the D$''$ region have resulted in velocity gradients ranging from very negative to slightly positive [for reviews, see Cleary, 1972; and Young and Lay, 1987b]. Reconciling the strongly negative gradient implied from this study with contrasting positive (or slightly negative) gradients of past studies remains a task for future work. Silver and Bina [1993] point out the affect of the sudden drop in SKS amplitudes on $SKKS/SKS$ ratios (at the ScP critical ray parameter) is strongly dependent on mantle-side CMB V_P. For a path geometry similar to ours in the Pacific, they conclude a 2.0-2.5% reduction in CMB V_P is consistent with their observations. SP_dKS data require a larger reduction in V_P, though the agreement in trend for the similar data is encouraging.

Of particular importance is mapping out the lateral variations in SP_dKS-SKS anomalies. Many additional source geometries to those studied here exist with the desired distance range for SP_dKS analysis. Redundancy in wavepath geometries

may ultimately help in reducing the non-uniqueness of attributing SP_dKS-SKS anomalies to the source- or receiver-sides of paths. This may be augmented by observations of SP_dS waves, which are $ScS(SV)$ waves that couple with P_diff at the CMB in the same fashion as SP_dKS [Choy, 1977]. SP_dS waves should be observable as a separate phase moving out later in time behind ScS waves starting at distances near 27^o, which corresponds to the same ray parameter that produces the first detectable SP_dKS arrival. No observations of SP_dS have yet been reported. In a preliminary search for the phase, difficulties such as other seismic arrivals in the predicted time window of SP_dS, precluded its detection. Nonetheless, if SP_dS can be observed at distances in absence of interfering arrivals, it will provide an added constraint to the SP_dKS observations.

5.7 Conclusion

Anomalous differential times between long-period SP_dKS and SKS are presented for two different source-receiver geometries: Fiji-Tonga events recorded in North and South America, and South American events recoreed in Europe and Eurasia. The SP_dKS-SKS times most strongly depend on V_P at the base of the mantle near the SKS core entrance and exit locations. The anomalous times can be fit, on average, by 1-D models containing a 5% reduction in V_P from PREM at the CMB, distributed over 50-100 km. This V_P structure above the CMB is non-unique, having a small trade-off in V_P reduction and thickness of the LVZ. The inclusion of more data (along with broadband data) will help better resolve the structure.

The scatter in the data suggest lateral variations of the low V_P values. V_P structure at the CMB differing on the source- and receiver-sides of SP_dKS paths can result in SP_dKS anomalies as well, whereby SP_dKS becomes a broadened or double arrival. These lateral variations, however, along with the affect of strong

lateral gradients in lowermost mantle V_S structure, are assumed to be second order and are left for future work.

The large reduction in V_P at the base of the mantle results in a strongly negative dV_P/dz gradient. This gradient in turn can be used, along with proposed material properties of the region, to imply a temperature gradient. Unfortunately, the uncertainties due to lateral variations in both P and S structure would make such a calculation premature. While past studies have also suggested strongly negative dV_P/dz gradients (though for different CMB regions than studied here), the thickness and strength of such a LVZ (where present) remains poorly resolved. The principal finding of this study, that a zone of low V_P velocity at the base of the mantle explains SP_dKS-SKS observations, however, is robust.

Chapter 6

Constraining Outermost Core Velocity With $SmKS$ Waves

6.1 Abstract

$SmKS$ waves (m=2,3,4), seismic waves that travel as S-waves in the mantle, P-waves in the core, and reflect (m-1) times on the underside of the core-mantle boundary, are well-suited for constraining outermost core V_P structure. This is due to closeness of the mantle paths and also the shallow depth range these waves travel in the outermost core. High quality optically scanned and digitized World Wide Seismographic Station Network and Canadian network recordings from a deep focus Java Sea event which sample the outer core beneath the northern Pacific, the Arctic, and northwestern North America (spanning 1/8th of the core's surface area), are utilized as an example to show the strength of $SmKS$ waves in resolving outermost core structure. $S3KS - S2KS$ and $S4KS - S3KS$ differential travel times were measured using the cross-correlation method and compared to those from reflectivity synthetics created from core models of past studies. For the event studied, the PREM core model, with possibly a small V_P decrease in the outermost 50 km of the core, provides a good fit to

the data. In addition to the travel times, $SmKS$ (m=2,3,4) waveform analysis rules out models with a strong low-velocity zone at the top of the outer core. Constraints and uncertainties in deriving outer core structure from $SmKS$ are discussed.

6.2 Introduction

Resolving the seismic properties of the Earth's outermost core is integral in gaining an understanding of the dynamics of the overall core-mantle boundary (CMB) region. The family of $SmKS$ waves (m=2,3,4), waves that traverse the mantle as S-waves, converting to P-waves in the core and reflecting (m-1) times at the underside of the CMB, are well-suited to investigate such structure. These waves, in particular the higher multiples, have been described as whispering gallery modes, and have been discussed theoretically by Choy [1977], Kind and Müller [1975], Choy et al. [1980], and Chapman and Orcutt [1985]. In previous outer core studies, SKS times and $SKKS-SKS$ differential times have played a dominant role and $SKKKS-SKKS$ times a more minor role (if any) in deriving an outer core model. (Hereafter, $SKKS$, $SKKKS$, etc., are referred to as $S2KS$, $S3KS$, etc., respectively, and values of m for $SmKS$ are printed as a subscript, e.g., $SmKS_{234}$ indicates m=2,3,4.) Due to 3-D lateral variations in lower mantle V_S structure, great care must be taken when using just SKS and/or $S2KS-SKS$ times to model core structure. Waveforms and difference times of $SmKS_{234}$ waves are ideal for studying the outermost core due to the closer proximity of their mantle paths, and their shallow outer core paths. The advantage of using $SmKS_{234}$ over $SmKS_{12}$ is minimizing possible contamination from unknown mantle heterogeneity, as well as having wavepaths bottoming in the outer core much closer to the CMB.

Figure 6.1 presents typical scale lengths for $SmKS_{1234}$ for the PREM model [Dziewonski and Anderson, 1981] and a 500 km source depth. Figure 6.1a displays

$SmKS_{1234}$ geometric ray paths for 140^o in epicentral distance, a range where such phases are commonly visible; Figure 6.1b gives the distance between adjacent $SmKS$ CMB crossing locations (e.g., $S2KS$ vs. $S3KS$), measured at the CMB on either the source- or receiver-side of the wavepaths; and Figure 6.1c shows the bottoming depths into the core (as measured from the CMB) of the individual $SmKS$ geometric ray paths. CMB distances between $S2KS$ and $S3KS$, and between $S3KS$ and $S4KS$ are relatively small (Figure 6.1b), and their differential times should thus be affected significantly less by 3-D mantle structure than those of SKS and $SKKS$. For example, the distance range for which SKS and $S2KS$ waveforms are both stably observed is $100^o - 125^o$, which have CMB separations of around 700 km. Similar CMB separations for $SmKS_{23}$ and $SmKS_{34}$ are around 300 km and 150 km, respectively, and thus should have waveforms and travel times perturbed less by mantle heterogeneity. This has been corroborated in a study of $SmKS_{123}$ by Souriau and Poupinet [1991], who report that residuals of $S2KS-SKS$ times display strong coherent regional variations, while residual $S3KS - S2KS$ time variations remain small. Figure 6.1c illustrates the usefulness of $SmKS_{234}$ in investigating the outermost core, since these waves, especially $SmKS_{34}$, travel in the outer 100-200 km of the core.

A profile of $SmKS_{1234}$ waveforms produced by the reflectivity method [see, for example, Fuchs and Müller, 1971] for the PREM model, and filtered through a long-period World Wide Seismographic Station Network (WWSSN) instrument are presented in Figure 6.2. The separate $SmKS$ phases are indicated by dotted lines. Also noted is the SP_dKS arrival, the SKS wave that couples with a diffracted P-wave on the source- and receiver-sides of the SKS wavepaths [see Choy, 1977; Kind and Müller, 1975; and Garnero et al. 1993c]. $S2KS$ is largest phase of the $SmKS$ wavetrain for this distance range. SKS is shown to reduce in amplitude and split into two arrivals due to the inner core triplication (SKS_{DF} and SKS_{BC}). In this

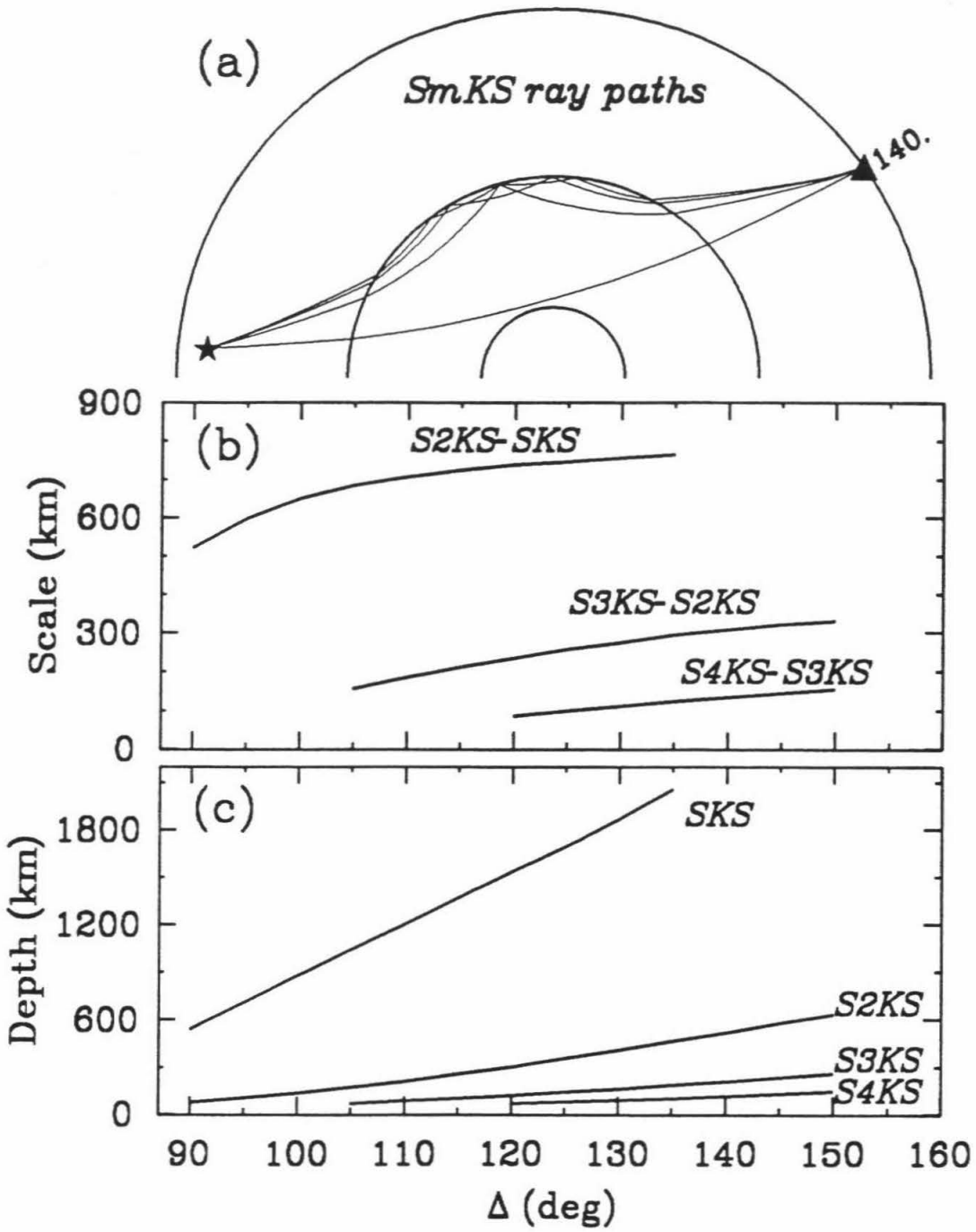

Figure 6.1: Scale lengths for $SmKS$ (m=1,2,3,4): (a) $SmKS$ geometric ray paths for 140°; (b) horizontal distances between adjacent $SmKS$ at the CMB; (c) bottoming depths of $SmKS$ below the CMB.

study we focus our analysis on $SmKS_{234}$, which are all well developed phases at the larger distances. The tail of $S4KS$ is seen to have a pronounced back-swing to the wavelet, this is the development of $S5KS$, which is not explored here.

The purpose of this study is to explore the usefulness of $SmKS_{234}$ in resolving and placing constraints on outermost core V_P structure. A deep focus Java Sea event recorded throughout North America is used as an example to illustrate the power of $SmKS_{234}$ for these purposes. Observed $S3KS - S2KS$ and $S4KS - S3KS$ differential times ($T_{S3KS-S2KS}$ and $T_{S4KS-S3KS}$, respectively) and waveforms are compared to predictions from synthetics generated using outer core models of past studies. For the event studied, the PREM model with a slight reduction in V_P in the outermost 50 km of the core matches the observations well.

6.3 Data and Reflectivity Synthetics

Long-period observations (10-20 sec) from a deep focus Java Sea event (3/24/67, -6.01°S, 112.33°E, depth 606 km) were optically scanned, digitized, and rotated into longitudinal components of motion. The event was well recorded by North American WWSSN and Canadian Seismographic Network (CSN) stations. Figure 6.3 displays the great circle raypaths along with surface projections of the CMB crossing locations of $SmKS_{234}$ for this event. For this source-receiver geometry, the azimuthal wavepath coverage spans roughly 1/8th of the surface area of the Earth's outermost core.

Figure 6.4a shows 21 long-period radial component WWSSN and CSN recordings of the $SmKS_{234}$ wave group for the Java Sea event. All traces have maximum amplitudes normalized to unity, and are lined up on the peak of the $S2KS$ arrival. The dotted lines indicate the arrivals of $S2KS$, $S3KS$, and $S4KS$. Figure 6.4b displays synthetics generated using the reflectivity method for the PREM model,

Figure 6.2: Radial component $SmKS$ reflectivity synthetics as filtered through a long-period WWSSN instrument for the PREM model and a source depth of 500 km. $SmKS$ and SP_dKS arrivals are indicated by dotted lines.

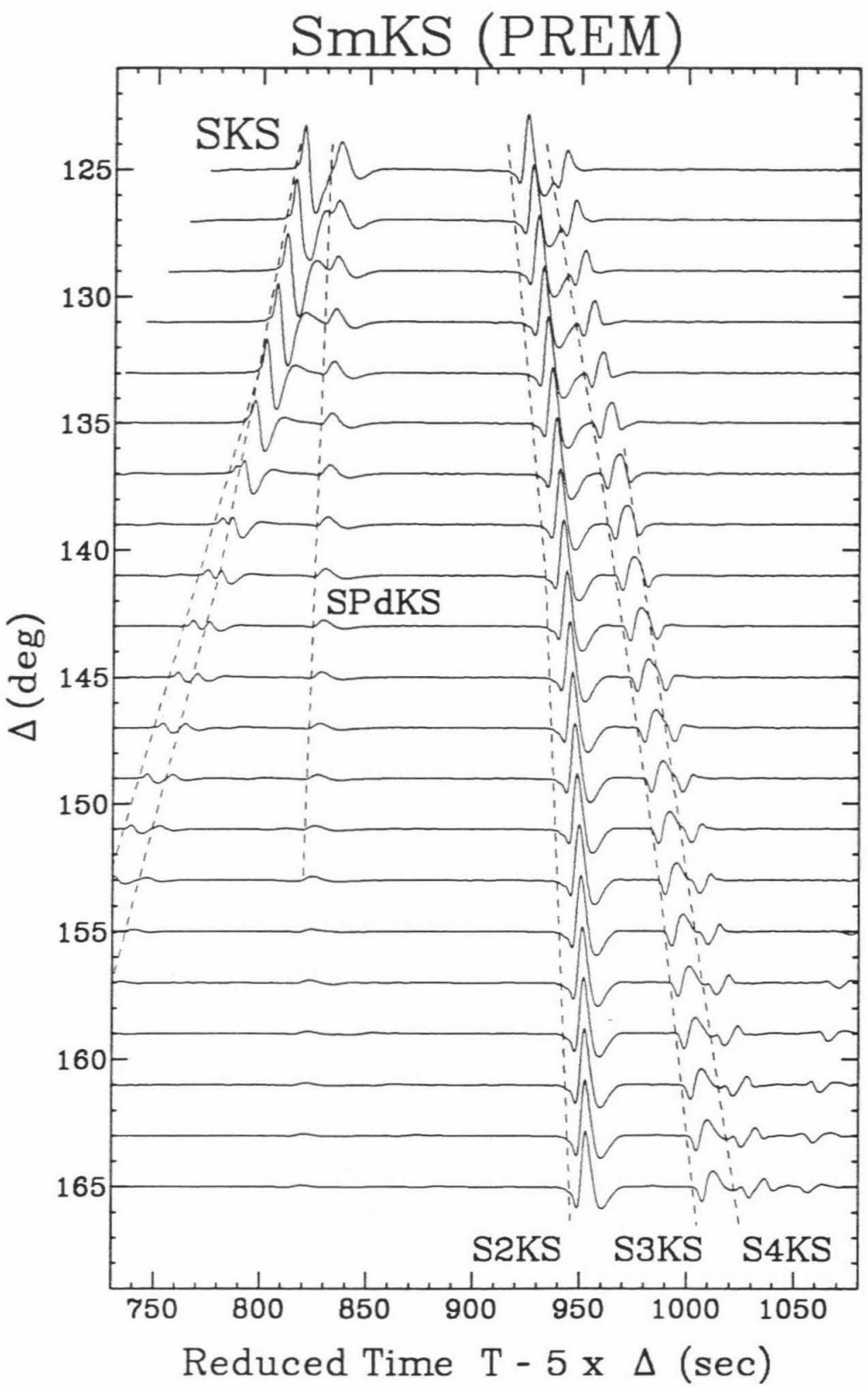
SmKS (PREM)
SKS
SPdKS
S2KS
S3KS
S4KS
125
130
135
140
145
150
155
160
165
Δ (deg)
750
800
850
900
950
1000
1050
Reduced Time T - 5 x Δ (sec)

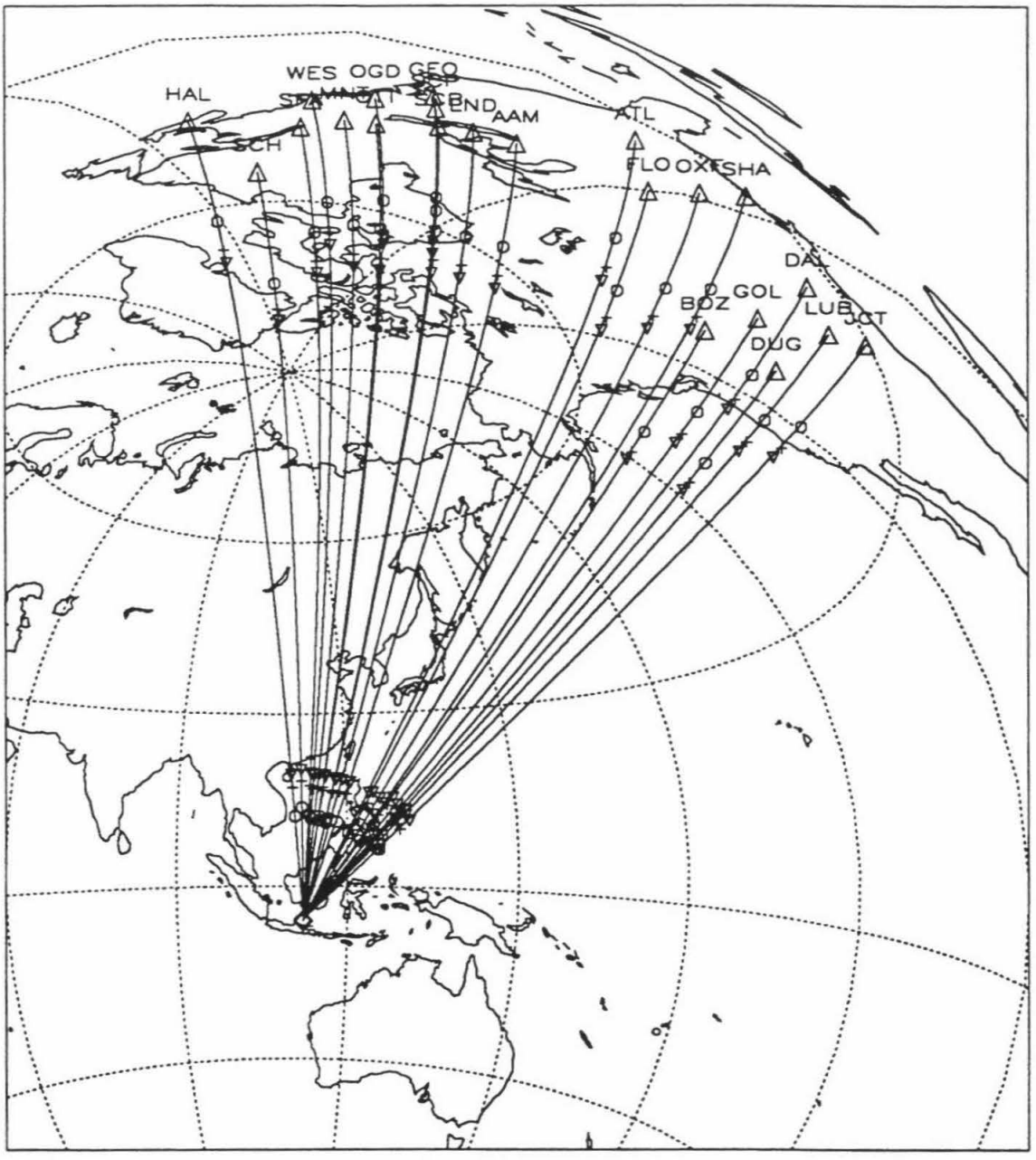

Figure 6.3: Great circle raypaths for the 3/24/67 Java Sea event. Surface projections of the CMB crossing locations of $S2KS$, $S3KS$, and $S4KS$ are shown by circles, crosses, and triangles, respectively. Larger triangles are the WWSSN and CSN stations.

filtered through a long-period WWSSN instrument, for the appropriate source depth and distances of the data. The synthetics were computed using the focal mechanism for the Java event as determined by Fitch and Molnar [1970] to account for any possible radiation pattern effect, though such an effect is expected to be minimal. As seen in data, $SmKS_{23}$ are well-recorded for the whole distance range. $S4KS$, however, is expected to be small until distances greater than 140^o or so. About half of our observations for the Java event at distances greater than 138^o show contributions to the tail of $S3KS$ in the form of $S4KS$, as in the synthetics. Large variabilities in $S4KS$ amplitudes may be due to ray path perturbations caused by small scale lower mantle heterogeneity or CMB topography, and are discussed more detail in Chapter 7.

An important consideration in analyzing $SmKS_{234}$ phases is the $\pi/2$ phase shift (Hilbert transform) that occurs each time a wave reflects at the underside of the CMB [e.g., see Choy and Richards, 1975; and Choy, 1977]. $S2KS$, $S3KS$, and $S4KS$ are phase shifted $\pi/2$, π, and $3\pi/2$, respectively, from SKS. The reflectivity method includes this affect.

6.4 Analysis of Travel Times

To measure the differential times $T_{S3KS-S2KS}$ and $T_{S4KS-S3KS}$, the standard cross-correlation method was used. For $T_{S3KS-S2KS}$ times, $S2KS$ was Hilbert transformed (denoted H($S2KS$)) prior to correlation to be in phase with $S3KS$. Similarly, for $T_{S4KS-S3KS}$ times, $S3KS$ was Hilbert transformed (denoted H($S3KS$)) prior to correlation. Thus $T_{S3KS-S2KS}$ and $T_{S4KS-S3KS}$ times discussed in this paper are in actuality $S3KS$-H($S2KS$) and $S4KS$-H($S3KS$) times, respectively. Times from the correlation procedure were cross-checked by overlaying synthetics with the data. Typical time window lengths of $SmKS_{234}$ phases used in the correlation procedure

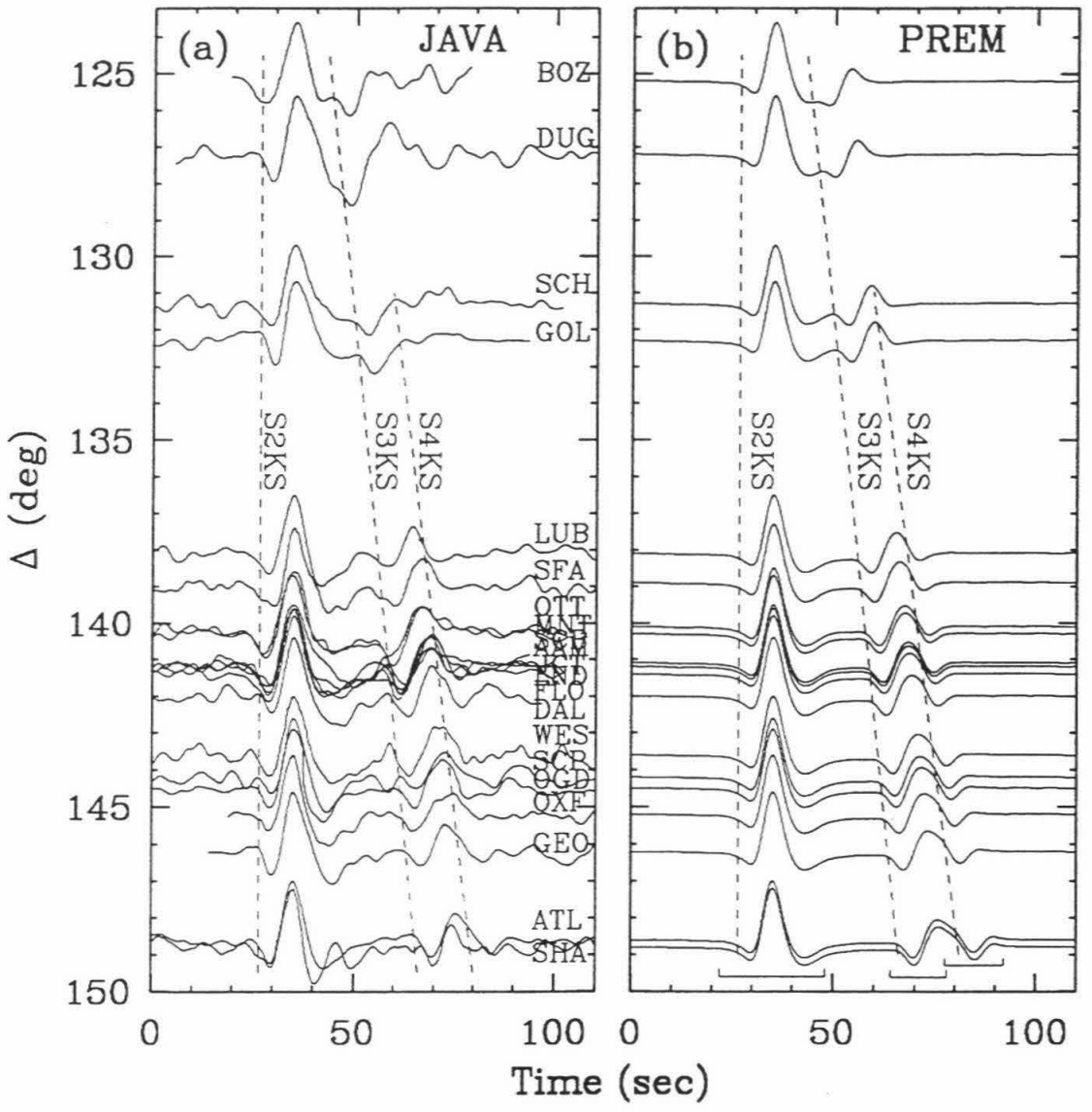

Figure 6.4: (a) Long-period radial component data from the Java Sea event and (b) reflectivity synthetics for PREM. In both profiles, traces are lined up on $S2KS$ peaks, and maximum amplitudes are normalized to unity.

are shown as shaded time windows in Figure 6.5, and also included at the bottom of Figure 6.4b as indicated by the horizontal brackets. The exact same Hilbert transformation, windowing and correlation measuring procedure was used for the data and synthetics.

$SmKS_{234}$ times were also calculated from reflectivity synthetics computed for the following radially symmetric outer core models of past studies: KHR [Hales and Roberts, 1971], KLY [Lay and Young, 1990], KSP [Souriau and Poupinet, 1991], *iasp91* [Kennett and Engdahl, 1991], SP6 [Morelli and Dziewonski, 1993], and KTH [Tanaka and Hamaguchi, 1993a]. Synthetics were also computed for the PREM model having the outermost 50 km of the core decreased to a CMB V_P of 7.94 km/sec (a 1.5% reduction, model KGHJ). Figure 6.6 displays the outermost 400 km of the above core models. Four observations having good signal-to-noise ratio (SNR) near 141^o (from Figure 6.4a) are compared to waveform predictions for the above models (Figure 6.7). All traces are lined up and normalized in amplitude to the $S2KS$ peak. The dotted lines correspond to peaks in $SmKS_{234}$ for PREM to illustrate the different relative arrival times. Data differential times exhibit small scatter, and are very similar to predictions of PREM and KGHJ for this range. Differences between PREM and KGHJ are virtually indistinguishable at this distance, and is pursued in greater detail below. Models KTH, *iasp91* and KLY display $S3KS$ peaks delayed by at least 1 sec from the same peaks for the data, PREM and KGHJ. Models KHR and SP6 have even greater $S3KS$ delays (3 sec), and appear incompatible with our data sample. Model KSP predictions have waveform distortions due to the extreme LVZ just beneath the CMB (Figure 6.6.) Such an LVZ distorts the first pulse of each of $S2KS$ and $S3KS$, and produces waveforms incompatible with our data and synthetics at all ranges.

Residual times of $T_{S3KS-S2KS}$ and $T_{S4KS-S3KS}$ (denoted $\delta T_{S3KS-S2KS}$ and $\delta T_{S4KS-S3KS}$, respectively) are calculated with respect to PREM for the data and

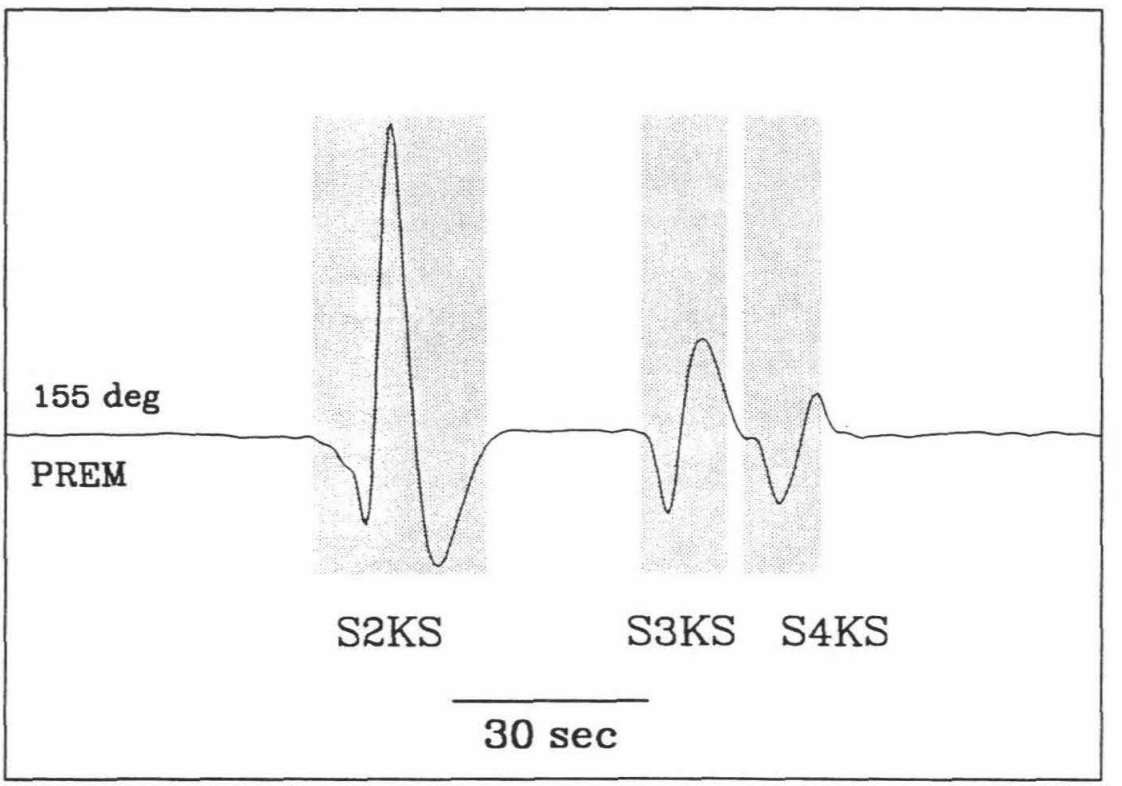

Figure 6.5: Reflectivity synthetic seismogram for the PREM model along with shaded boxes indicating typical time window used in the cross-correlation scheme.

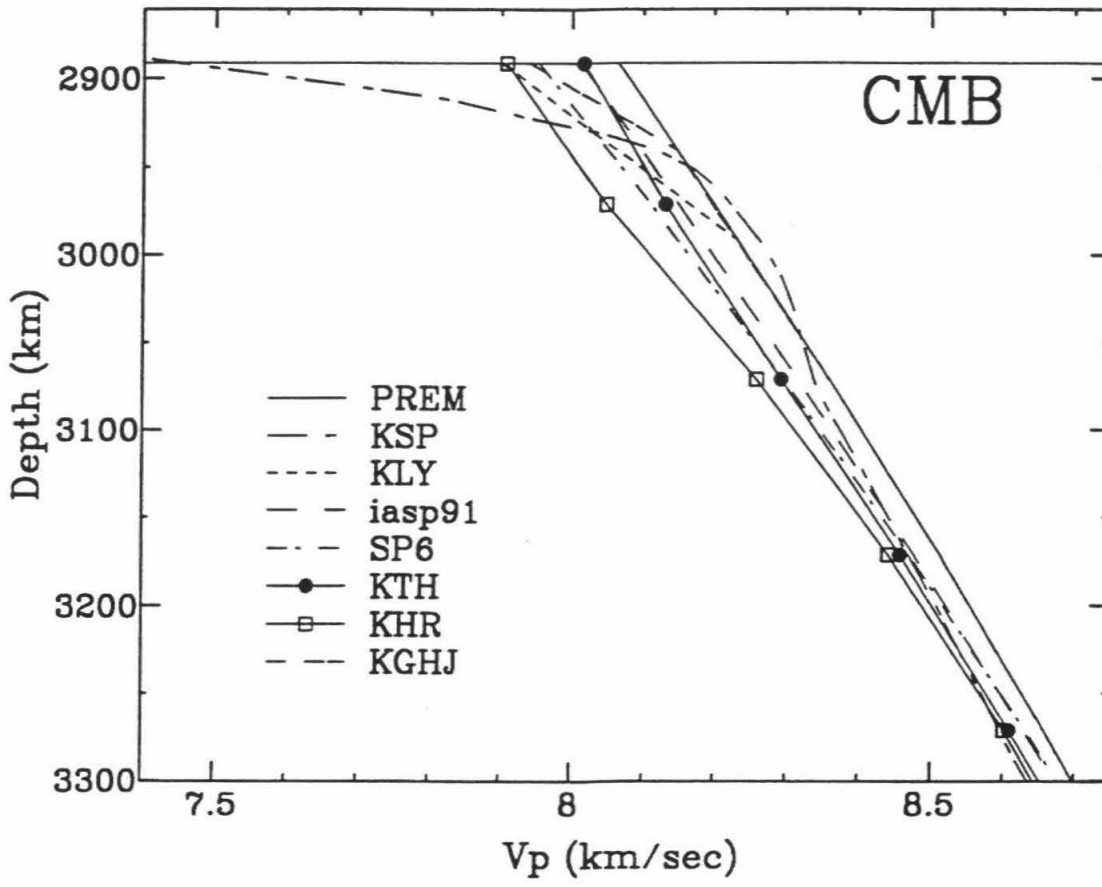

Figure 6.6: V_P profiles of the outermost 400 km of the outer core. (Model names and authors described in text).

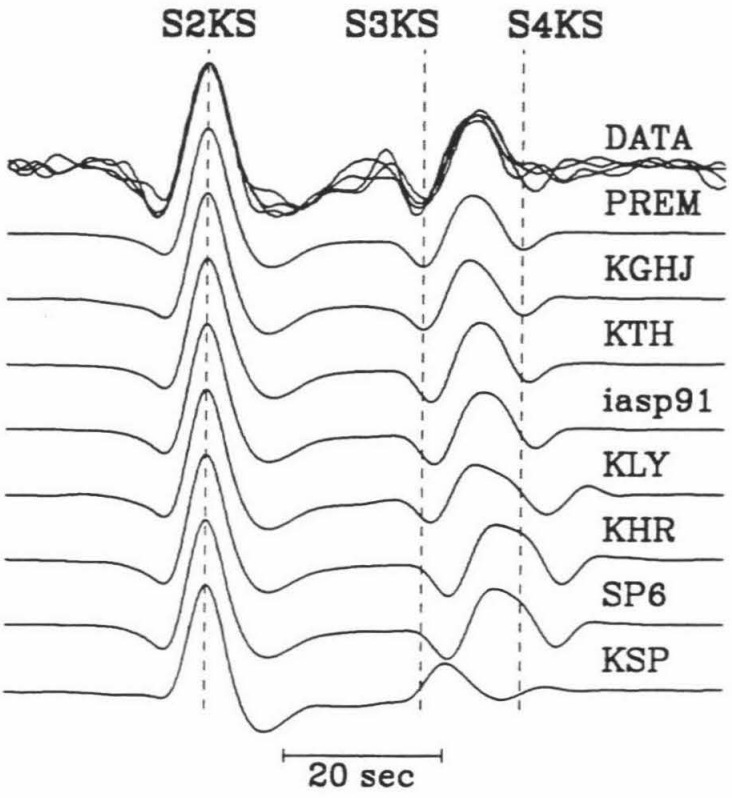

Figure 6.7: Radial component Java Sea event observations (Figure 6.4) and synthetics near 141°. Traces normalized in time and amplitude to $S2KS$ peaks. Dotted lines indicate peaks of $S3KS$ and $S4KS$ from the PREM predictions.

synthetics, and displayed in Figure 6.8. The Java data (circles) have 1 sec error bars to emphasize that some error is expected from the digitization process, as well as from the correlation procedure when the SNR is low. The errors may easily be larger if phase mis-identification occurs, though $SmKS_{234}$ are easily identified in Figure 6.1. Figure 6.8a shows $\delta T_{S3KS-S2KS}$ of the data is scattered about the PREM time (zero line) within ± 1 sec, with the PREM and KGHJ models providing the best fit for this path geometry. Predictions from model KGHJ are nearly identical to PREM, since $S2KS$ and $S3KS$ are not differentially affected by the thin LVZ since they both traverse the top 50 km of the core fairly steeply. Other models tested predict $S2KS$ and $S3KS$ to be more separated than seen in the observations (or PREM). This is due to having V_P values less than PREM in the outermost 100 to 700 km of the core, resulting in higher dV_P/dz values, thus preferentially slowing down $S3KS$ relative to $S2KS$, and $S4KS$ relative to $S3KS$. We were unable to confidently make $T_{S3KS-S2KS}$ and $T_{S4KS-S3KS}$ measurements from model KSP due to $S3KS$ and $S4KS$ waveform distortions (Figure 6.7) caused by the extreme LVZ just beneath the CMB (as discussed above). Such a strong LVZ changes the onset of these waves to appear even further phase shifted, and is incompatible with the Java Sea observations.

Observed $\delta T_{S4KS-S3KS}$ residual times are presented in Figure 6.8b, and scatter at values greater than PREM, averaging near 0.5 sec. We have interpreted this to imply a V_P reduction in the outermost core of PREM to construct model KGHJ, which in turn preferentially slows down $S4KS$ relative to $S3KS$. Model KGHJ also yields $\delta T_{S4KS-S3KS}$ times greater than PREM. It is possible to trade-off such a LVZ with slightly increased V_P values at depths greater than those penetrated by $S4KS$. This would speed up $S3KS$ relative to $S4KS$, thus increasing $\delta T_{S4KS-S3KS}$, and roughly equally speed up $S2KS$ and $S3KS$, therefore not affecting $\delta T_{S3KS-S2KS}$ times. Such trade-offs must be pursued with absolute times (or differential times

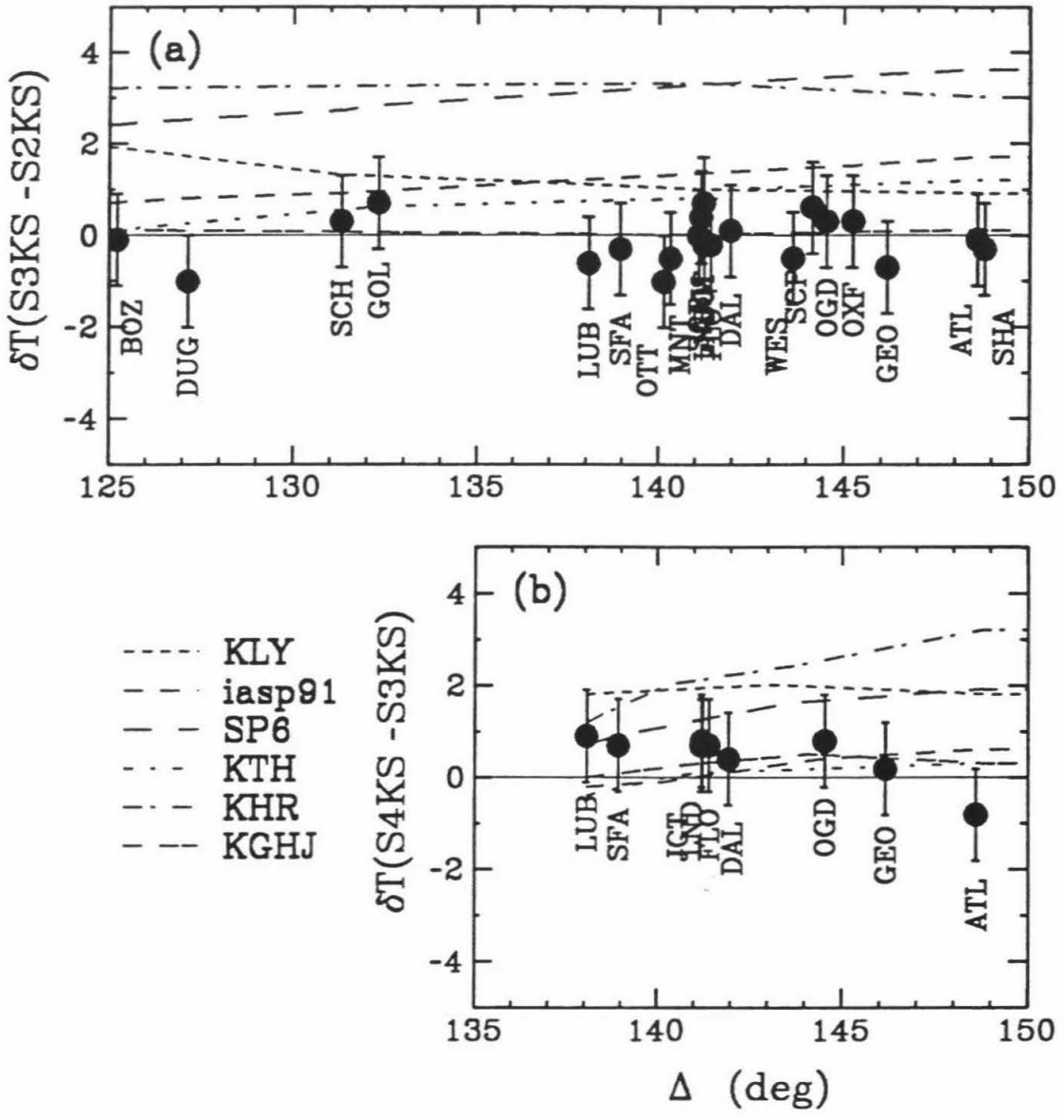

Figure 6.8: (a) $\delta T_{S3KS-S2KS}$ and (b) $\delta T_{S4KS-S3KS}$ differential times (dots) and predictions (lines) with respect to PREM.

out to larger distances, hence deeper penetrating waves), though in this note we arbitrarily pursue a LVZ just beneath the CMB. The next best fitting models to $\delta T_{S3KS-S2KS}$ and $\delta T_{S4KS-S3KS}$ are KTH and *iasp91*, respectively. Slightly faster velocities in these two models for the depth range 3000-3300 km would serve to improve their fit to the Java data by speeding up $S3KS$ more than $S2KS$ and $S4KS$, hence reducing $\delta T_{S3KS-S2KS}$ and increasing $\delta T_{S4KS-S3KS}$ to better agree with the data. $\delta T_{S3KS-S2KS}$ and $\delta T_{S4KS-S3KS}$ residuals for model KLY are larger than the data by 1-1.5 sec, implying the LVZ in KLY is too large to fit the Java data. However, we perturb the PREM model in the same fashion as KLY, that is, to adjust outermost core velocities to fit the observations. Models SP6 and KHR both predict times nearly 3 sec larger than the data for $\delta T_{S3KS-S2KS}$ and 0-2 sec for $\delta T_{S4KS-S3KS}$, which is discussed in the next section.

The predictions of model KGHJ (Figure 6.6) are close to the PREM and data times for $\delta T_{S3KS-S2KS}$ and the data for $\delta T_{S4KS-S3KS}$. The thin LVZ in the outermost 50 km accomplishes this by slowing down $S4KS$ more than $S2KS$ and $S3KS$. This model is by no means unique, but provides an explanation of the data with relatively little perturbation to the PREM model. Our tests find that increasing the thickness of this LVZ layer will also slow down $S3KS$ for the wavelengths we are studying, producing $T_{S3KS-S2KS}$ times larger than the Java data. Also, strongly decreasing the CMB V_P of this layer distorts the front of the $S3KS$ and $S4KS$ waveforms to be incompatible with observations. This emphasizes the importance of cross-checking predicted waveforms with data in the modeling process of outermost core structure using $SmKS$.

6.5 Discussion

An abundance of high-quality $SmKS_{234}$ data are available from the WWSSN archives for deep focus events. Until more broadband data is available for these distance ranges, with a dense sampling throughout the distance range, the WWSSN data will provide the opportunity to map out the details of outermost core structure.

The discrepancy between the observations and predictions for the Java event may be attributed to several different causes. Models KHR and SP6 overpredict the residual times in Figure 6.8. This may be related to the $\pi/2$ phase shift of $S2KS$ not being taken into consideration in the Hales and Roberts [1971] study, which was subsequently used in constructing SP6 [Morelli and Dziewonski, 1993]. This will in turn result in larger values of $T_{S3KS-S2KS}$ when correlating peak to peak times, and thus result in a slower outer core to model these times. Predictions from the other models are closer to the data, but over predict the $\delta T_{S3KS-S2KS}$ times due to pronounced outer core low velocity zones. This may be due to not properly accounting for 3-D mantle heterogeneity when constructing models using $SmKS_{12}$ times. The affects of such heterogeneity on $SmKS_{1234}$ are explored in the following chapter of this thesis [Garnero and Helmberger, 1994]. The raypaths of $SmKS_{234}$ for the Java event (Figure 6.3) traverse V_S perturbations in D'' of $\pm 1\%$, according to the 3-D mantle model SH12_WM13 [Su et al., 1992]. It is proposed that such small mantle anomalies are an explanation of the relatively small scatter seen in the data in Figure 6.8, thus enabling a more confident probe of outermost core structure that is so easily masked by strong mantle heterogeneity.

A different approach of reconciling the predictions of the radially symmetric core models and the Java data is outer core lateral heterogeneity [Souriau and Poupinet, 1990; Kohler and Tanimoto, 1992; and Tanaka and Hamaguchi, 1993b]. The Java data show no distance or azimuthal trend (from the hypocenter) of $SmKS_{234}$ times, though the data are restricted to 1/8th of the globe's outer core. If outer core hetero-

geneity exists, $SmKS_{234}$ phases are ideal to map it out, as well as assess the trade-off between D'' and outer core heterogeneity. Such heterogeneity, however, is in contradiction with dynamical arguments of limits of density and velocity perturbations in the outer core [Stevenson, 1987].

Of geodynamical significance is the issue of outermost core chemical stratification [e.g., Masters, 1979; Lay and Young, 1990; and Tanaka and Hamaguchi, 1993a]. The inhomogeneity index η [Bullen, 1975] is often used to infer departures from chemical homogeneity in the Earth. Adopting this approach implies model KGHJ departs from homogeneity in the outermost 50 km of the core, however, we do not emphasize this due to the non-uniqueness of the model. With more $SmKS_{234}$ data over extended distance ranges (out to 170°), the details of this structure may be better mapped.

6.6 Conclusion

$SmKS_{234}$ waves are well-suited for constraining outermost core V_P structure due to the closeness of the mantle paths and the shallow depth range of paths in the outermost core. $S3KS - S2KS$ and $S4KS - S3KS$ differential times are measured from data and reflectivity synthetics using the cross-correlation method. Records from a deep focus Java Sea event recorded throughout North America are well-modeled with the PREM model, with an improved fit from slightly slower velocities in the outermost 50 km of the core relative to PREM. This model, KGHJ, implies chemical stratification in the outermost 50km of the core, though this result is not stressed due to uncertainties in the model. 1-D models of past studies displaying outer core velocities lower than PREM over extended depth ranges produce $SmKS_{234}$ differential times incompatible with the Java Sea observations. Nearly all of the past studies used SKS times or $S2KS - SKS$ times in model derivations, which can be more significantly affected by lower mantle heterogeneity due to increased wavepath

separations near the CMB in comparison to $SmKS_{234}$. Extreme low-velocity zones in the outermost core distort $SmKS_{234}$ waveforms, producing waveshapes not supported by $SmKS$ data. Outer core heterogeneity is not necessary to explain the Java Sea data presented here. Future studies using this technique may help resolve issues of scale lengths of D$''$ heterogeneity, outer core heterogeneity, and outer core chemical stratification, and is the subject of the next chapter.

Chapter 7

On Seismic Resolution of Lateral Heterogeneity in the Earth's Outermost Core

7.1 Abstract

Issues concerning resolution of seismically determined outermost core properties are presented. Travel time behavior of the commonly used family of $SmKS$ waves, which travel as S in the mantle, P in the core, reflecting (m-1) times at the underside of the core-mantle boundary (CMB), are analyzed over a large distance range ($125^o - 165^o$). Long-period World Wide Seismographic Station Network data are utilized due to the presently unsurpassed $\approx$20 year time span of operation for global station coverage. In regions where lower mantle heterogeneity is predicted small, $SmKS$ observations are well predicted by the PREM reference model, with the addition of a slight reduction in V_P in the top 50 km of the core (1.5%). Such a reduction implies chemical stratification in this 50 km zone, though this model feature is not uniquely resolved. Data having wave paths through areas of known D$''$ heterogeneity ($\pm$2%) exhibit

systematic anomalies in $SmKS$ differential times. Two-dimensional wave propagation experiments demonstrate how large scale lower mantle velocity perturbations can explain long wavelength behavior of such anomalous $SmKS$ times, though heterogeneity on smaller scales may be responsible for the observed scatter about these trends. If lower mantle heterogeneity is not properly accounted for in deriving a core model, misfit of the mantle model maps directly into core structure. The existence of outermost core heterogeneity is difficult to resolve at present due to uncertainties in global lower mantle structure. Resolving a one-dimensional chemically stratified outermost core also remains difficult due to the same uncertainties; and if such stratification exists, it must have a vertical scale length right beneath the CMB of greater than 25 km to be detected by the long-period data. Inclusion of the slowly accruing broadband data should help in this regard. Restricting study to higher multiples of $SmKS$ (m=2,3,4) can help reduce the affect of mantle heterogeneity due to the closeness of the mantle legs of the wavepaths. $SmKS$ waves are ideal in providing additional information on the details of lower mantle heterogeneity.

7.2 Introduction

The structure and dynamics of Earth's outer core plays an increasingly important role in multidisciplinary studies of the region. In particular, whether or not the outermost core contains lateral heterogeneity or chemical stratification will have strong implications on fluid motions and patterns right beneath the core-mantle boundary (CMB) and hence the geomagnetic field, as well as the overall dynamical, chemical and thermo-mechanical behavior of the core-mantle system. As progress is made in theoretical studies of such physical properties [e.g., Fearn and Loper, 1981; Bloxham and Gubbins, 1987; Bloxham, 1990; Jault and Le Mouël, 1991ab; Loper, 1991; and Voorhies, 1994], parallel progress in resolving these phenomena in

the Earth is desired. Presently, in order to detect lateral heterogeneity and chemical stratification in the Earth's outermost core, seismic methods must be employed. However, since the seismic approach is an indirect way of getting at these issues, inherent uncertainties exist. It is the focus of this work to analyze seismic data commonly used for such study, and present the resolution and uncertainties of this data.

The transition from the mantle to the core is sharp, and can sustain multiple under-side reflections of seismic energy [e.g., see Gutengberg, 1959]. The only documented commonly-recorded seismic phases with wavepath turning depths in the topmost half of the outer core are the family of $SmKS$ waves (m=1, 2, 3, etc.) These phases travel as SV waves in the mantle, convert to P waves in the core reflecting (m-1) times at the underside of the CMB, then convert back to SV for the final mantle leg of the path. $SmKS$ are the outermost core's equivalent to upper mantle multi-reflected S waves, S, SS, SSS, etc., and provide a dense sampling of the outer core over an extended distance range ($85^o - 165^o$ and beyond). Commonly notated as SKS, $SKKS$, $SKKKS$, etc., we use the notation SKS, $S2KS$, $S3KS$, etc., to denote the separate phases. A short hand is used to designate specific $SmKS$ by writing the values of m as a subscript; for example, $SmKS_{234}$ indicates $SmKS$ with (m=2,3,4), or $S2KS$, $S3KS$, and $S4KS$, respectively. If no subscript is written then we are referring to any value of m. $SmKS$ waves having ray turning depths near the top of the outer core are possibly the best suited seismic waves for providing information on outermost core heterogeneity, chemical stratification, and general 1-dimensional (1-D) structure, and for this reason have been prolifically used in outer core modeling studies. Figure 7.1 shows a cross-section of the Earth containing raypaths for $SmKS_{234}$ for 3 different distances. $S2KS$, $S3KS$ and $S4KS$ paths are denoted by solid, dashed and bold solid lines, respectively. As the figure illustrates, the outermost few hundred km of the core is well-sampled by $SmKS_{34}$.

In fact, $S4KS$ paths are almost entirely restricted to the core's outermost 100 km (thin white, unshaded region.)

Previous seismic studies investigating 1-D outermost core structure have relied upon SKS times [e.g., Randall, 1970], $SmKS_{12}$ times [e.g., Hales and Roberts, 1971; Schweitzer and Müller, 1986; Lay and Young, 1990; and Tanaka and Hamaguchi, 1993ab], $SmKS_{123}$ times [Souriau and Poupinet, 1991], and $SmKS_{234}$ [Garnero et al., 1993b]. Studies presenting globally averaged 1-D reference Earth models have used a combination of $SmKS_{12}$ times and normal mode periods [e.g., Dziewonski and Anderson, 1981; Kennett and Engdahl, 1991; and Morelli and Dziewonski, 1993]. $SmKS$ has also been used to infer outermost core heterogeneity [e.g. Souriau and Poupinet, 1990; Schweitzer, 1990; Kohler and Tanimoto, 1992; and Tanaka and Hamaguchi, 1993b] and chemical stratification at the top of the core [e.g., Lay and Young, 1990; Tanaka and Hamaguchi, 1993a; and Garnero et al., 1993b]. Chemical and thermal stratification can also be pursued from observations of the periods of normal modes, though resolution at vertical scales smaller than 200 km for this method is difficult [see Masters, 1979, for a thorough treatment of this approach and discussion of uncertainties involved]. Some studies have incorporated modeling lower mantle heterogeneity in explaining anomalous $SmKS_{12}$ times [e.g., Garnero et al., 1988; and Schweitzer, 1990] or removing the affects of previously published aspherical mantle models [e.g., Schweitzer, 1990; and Tanaka and Hamaguchi, 1993abc]. Many of the above studies have utilized differential rather than absolute times of $SmKS$ in effort to minimize the affects of mantle heterogeneity, source mislocation, and receiver structure. How mantle heterogeneity may affect the various $SmKS$ phases is explored in detail in this study.

Of particular relevance in outer core modeling using $SmKS$ are the scale lengths of the distances between wavepaths of adjacent $SmKS$ waves [Garnero et al., 1993b]. $SmKS_{12}$ for the commonly studied distance range ($100^o - 130^o$) have raypaths sepa-

Figure 7.1: Cross-section displaying $SmKS_{234}$ wavepaths for a 500 km deep source at 130^o, 140^o, and 150^o. $S2KS$, $S3KS$ and $S4KS$ paths are denoted by solid, dashed and bold solid lines, respectively. The outermost 100 km of the core is not shaded (white region), and contains most of the $S4KS$ raypaths.

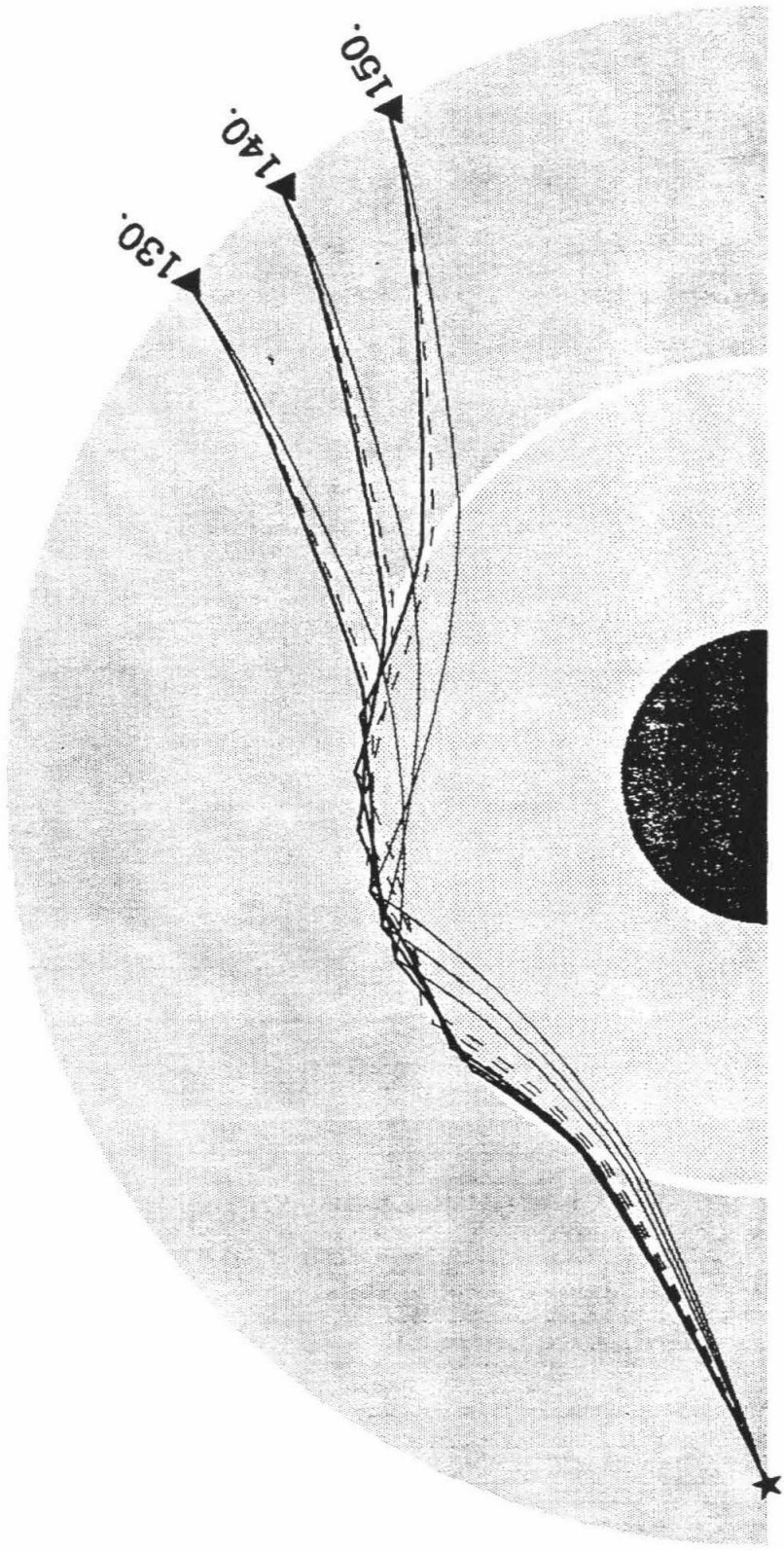
150.
140.
130.

rated by around 700 km at the CMB crossing locations (on the source- or receiver-side of paths). Any mantle heterogeneity having scale lengths of this order or smaller will thus affect such times. While tomographic inversions for global maps of V_S structure typically have minimum lower mantle resolution of scale length on the order of $O(1000)$ km [e.g., Tanimoto, 1990; Su et al., 1992; and Masters et al., 1992], body wave analyses have provided evidence for large changes in lower mantle V_S over shorter scale lengths of order $O(100)$ km [e.g., Lavely et al. 1986; Lay, 1983; Garnero et al., 1988; Weber and Davis, 1990; Gaherty and Lay, 1992; Weber, 1993; and Wysession et al., 1994]. The CMB separation of higher multiple $SmKS$ raypaths is even smaller: around 200-300 km for $SmKS_{23}$ separation, and 100-150 km for $SmKS_{34}$ [Garnero et al., 1993b]. These higher multiples have not been used in past studies for core structure, probably due to the abundance of unanalyzed $SmKS_{12}$ data. Tanaka and Hamaguchi [1993a], however, did analyze $SmKS_{23}$ difference time behavior, but did not include it in their modeling procedure.

In what follows, we present our method of generating 1- and 2-D synthetic seismograms for comparison to data of various regions of the globe. Examples are presented for regions of both relatively strong and weak lower mantle velocity perturbations. Scale lengths of resolution for the data, uncertainties in the model space, and the importance of laterally inhomogeneous raypaths are then discussed.

7.3 Synthetic Seismograms

The reflectivity method [see, for example, Fuchs and Müller, 1971] is used as a 1-D reference technique for computing synthetic seismograms. We also utilize a modified WKBJ technique for computation of 1- and 2-D synthetics. The modified WKBJ method, denoted WKM, is discussed in detail in Helmberger et al. [1994]. Some additional issues relating to WKM generation of large distance $SmKS$ are discussed

below.

As indicated by Chapman and Orcutt [1985], WKBJ seismograms compare well with reflectivity except for regions containing interference of $SmKS$-coupled head waves generated along the CMB. These waves, denoted as SP_dKS, are described by Choy [1977] and pointed out in reflectivity synthetics by Kind and Müller [1975]. Observations of SP_dKS relative to SKS are analyzed by Garnero et al. [1993c].

SP_dKS waves are generated at the ray parameter associated with the critical angle for ScP waves incident on the CMB. This ray parameter corresponds to SKS waves at around 107^o (which is a model dependent distance). Amplitudes of SKS at this ray parameter diminish due to the loss of energy that goes into creating SP_dKS [Silver and Bina, 1993], and at infinite frequency the SKS transmission coefficient goes to zero. $S2KS$, $S3KS$, and $S4KS$ energy at this same ray parameter is affected similarly. The WKBJ method does not properly account for this diffraction effect associated with SP_dKS. It does, however, include the correct CMB transmission coefficients that go to zero at the ScP critical angle. The zero in transmission coefficients generates a truncation arrival in each $SmKS$ arrival, and causes undesirable interference in the $SmKS_{234}$ wave packet. We circumvent this by imposing a "water level" for the transmission coefficients at a ray parameter slightly before the critical angle ray parameter where the transmission coefficient vanishes. This in turn produces synthetics that match extremely well with reflectivity seismograms (Figure 7.2) for the PREM [Dziewonski and Anderson, 1981] model. The profile displayed is for a source depth of 500 km, and responses are filtered through a long-period World-Wide Seismographic Station Network (WWSSN) instrument. For every bounce off the underside of the CMB, $SmKS$ experiences a $\pi/2$ phase shift [a Hilbert transform, see Choy and Richards, 1975; and Choy, 1977] which is included in both techniques. Agreement between WKM and reflectivity at smaller distances than shown in Figure 7.2 is also excellent [Helmberger et al., 1994].

Figure 7.2: Long-period WWSSN WKM (solid) and reflectivity (dotted) synthetics compared for the PREM model. Travel time curves are for WKM traces, which reflectivity traces are plotted above.

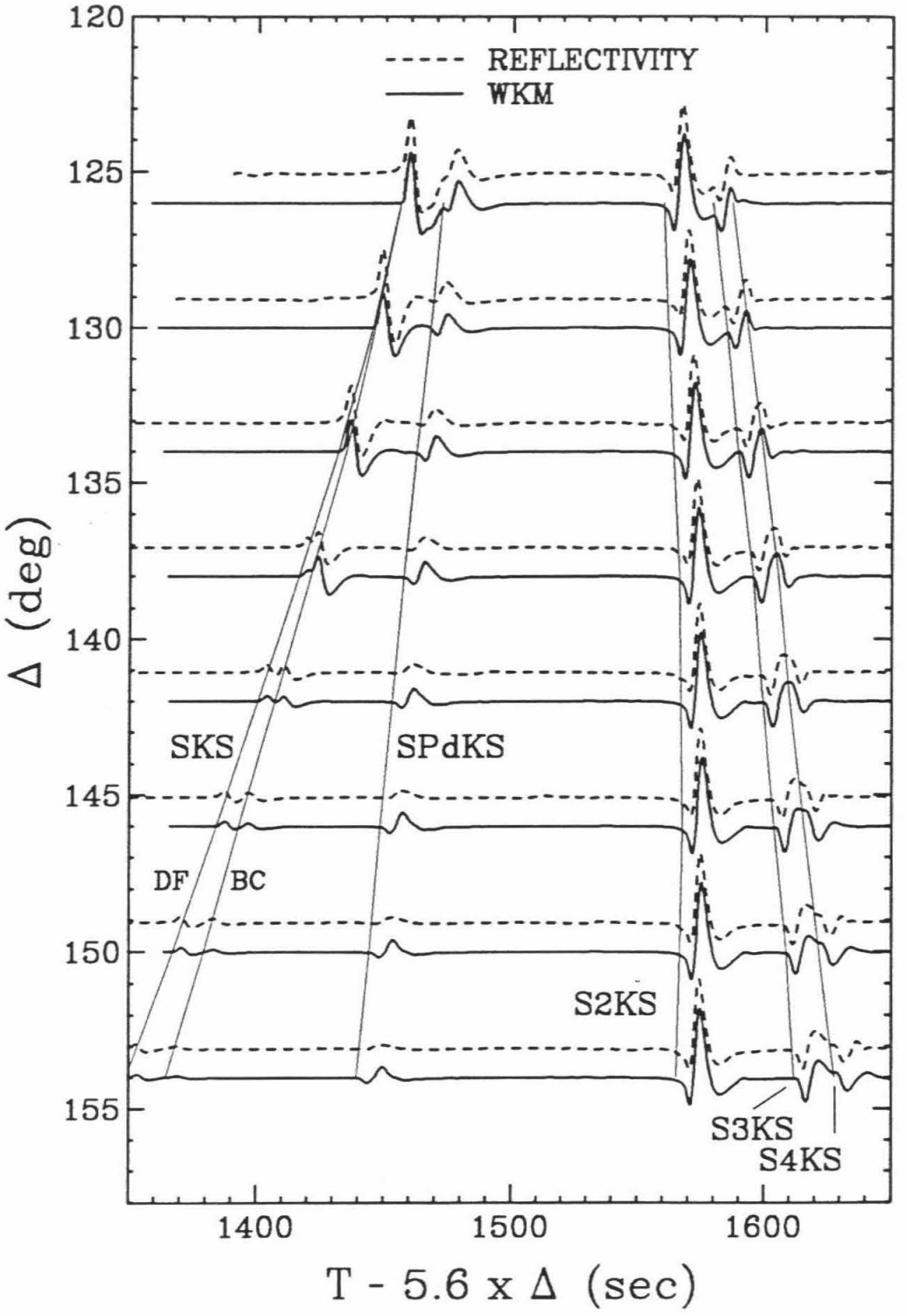
REFLECTIVITY
WKM
120
125
130
135
140
145
150
155
Δ (deg)
SKS
SPdKS
DF
BC
S2KS
S3KS
S4KS
1400
1500
1600
T - 5.6 x Δ (sec)

The water level approximation remains valid since the first arrival energy of $SmKS_{234}$ arrives significantly earlier in time than the energy associated with the critical angle ray parameter. However, this is not the case with SKS, since SKS first arrival energy arrives close in time to SP_dKS. For this reason, we did not modify SKS transmission coefficients, and expect some misfit of the WKM SP_dKS arrival, especially at distances around 110^o, where SP_dKS interferes with the tail of the SKS arrival. Nonetheless, SKS travel time behavior at this distance can still be analyzed, as will be shown shortly.

The WKM method can accommodate 2-D velocity structures containing iso-velocity layers that can vary in thickness in any manner, as long as raypaths do not bottom in laterally varying structure, which is avoided here since the core is kept 1-D in these experiments. Models containing various dipping structures, or low- or high-velocity cosine tapers in D$''$, for example, can thus be explored without the assumption of lateral homogeneity in raypath. This method is applied to $SmKS$ with respect to examples of WWSSN data exhibiting travel time anomalies. The following section presents samples of the data, which is followed by some preliminary modeling experiments.

7.4 Data Set and Travel Times

Due to the long time span of continuous operation, data from WWSSN is utilized. This provides around 2 decades of deep focus events recorded worldwide. $SmKS$ are well-recorded over a large distance range (85^o to beyond 165^o) on the long-period channel with periods of 10-20 s. Only deep focus events are used to minimize any possible slab effects on the waveforms [Vidale, 1987; and Cormier, 1989], source-side complexities and interference from surface reflected phases.

Only $SmKS_{234}$ data are presented here in effort to minimize effects of mantle

heterogeneity, since the difference in their mantle paths is significantly smaller than the difference between SKS and $S2KS$. $S2KS-SKS$ times, $T_{S2KS-SKS}$ (and more so with $S-SKS$ times, T_{S-SKS}), can be significantly affected by mantle structure [Garnero et al., 1988; Schweitzer, 1990; and Garnero and Helmberger, 1993]. For example, deep focus Fiji-Tonga events display $T_{S2KS-SKS}$ times of up to 5 sec greater than that predicted by PREM. This same region was shown to exhibit T_{S-SKS} times up to 10 sec more than PREM predictions; and when correcting these times for various aspherical structures presented in the literature, up to 5 sec anomalies remain for T_{S-SKS} times [Garnero and Helmberger, 1993]. This point is made to emphasize that unmapped mantle structure on many different scale lengths contribute to observed travel time perturbations in $SmKS_{12}$. Schweitzer [1990] emphasized that the smooth long-wavelength aspherical structures could not predict $T_{S2KS-SKS}$ anomalies for the Fiji-Tonga data, and concluded that mantle structure surely contributes to $T_{S2KS-SKS}$ observations. Moving to higher multiple $SmKS$ waves results in: (1) the bottoming depths of raypaths in the outer core being significantly closer to the CMB (Figure 7.1) thus improving coverage in the outermost few hundred km of the core; (2) reducing affects of mantle heterogeneity [Souriau and Poupinet, 1990; and Garnero et al., 1993b]; and (3) enables an extended distance range much beyond limits of $T_{S2KS-SKS}$ (which is limited by SKS dying out before 130°). Thus the effective distance range for studying $SmKS_{234}$ is 125°-165° and beyond.

Figure 7.3 shows a profile of long-period $SmKS_{234}$ for a deep focus Java Sea event recorded at North American WWSSN stations. These records have been optically scanned and digitized on a computer work station, then rotated through the back azimuth to align with the great circle path between station and event to obtain longitudinal and transverse components of motion. $S2KS$ has been aligned in time and normalized to unity, and the dotted lines are $SmKS_{234}$ predictions from PREM. $S2KS$ and $S3KS$ are robust throughout the whole profile, and $S4KS$ is intermit-

tent, and measurable in perhaps only half of the records. Using a cross-correlation technique for difference times, Garnero et al. [1993b] analyzed $S3KS - S2KS$ and $S4KS - S3KS$ difference times ($T_{S3KS-S2KS}$ and $T_{S4KS-S3KS}$, respectively) for this event. The best fitting previously published 1-D structure to the $T_{S3KS-S2KS}$ times was the PREM model, though $T_{S4KS-S3KS}$ observations were slightly larger than the PREM predictions. A 1.5% reduction in V_P in the outermost 50 km of the core produced an improvement in the $T_{S4KS-S3KS}$ predictions without affecting the $T_{S3KS-S2KS}$ times. The Java Sea $SmKS_{234}$ raypaths through D'' traverse V_S perturbations that are predicted to be small [e.g., $\pm 1\%$ in model SH12_WM13, Su et al., 1992], which results in small scatter of the difference times, permitting us to investigate the core structure.

Fiji-Tonga sources recorded in Eurasia and Africa provide an opportunity to study $SmKS_{234}$ out to 165^o because of the station geometry. Figure 7.4 presents great circle raypaths for three deep focus Tonga events. The circles denote the CMB crossing locations of $SmKS_{234}$, and the triangles are WWSSN stations. The digitized and rotated radial component data are displayed in Figure 7.5, and as with Figure 7.3 the $S2KS$ arrivals are aligned in time and normalized in amplitude. The dotted lines depict the observed arrivals of $SmKS_{234}$. Most of the data are cleanly recorded though as we will demonstrate, travel time anomalies exist. $T_{S3KS-S2KS}$ and $T_{S4KS-S3KS}$ times for the data and PREM were measured through the cross-correlation method. For all observations, $S2KS$ was Hilbert transformed to be in phase with $S3KS$, and $S3KS$ was Hilbert transformed to be in phase with $S4KS$, prior to the correlation scheme. The resulting difference times were double checked by overlaying records with synthetics of appropriate distance, source depth, and source time function.

Residual $T_{S3KS-S2KS}$ and $T_{S4KS-S3KS}$ times ($\delta T_{S3KS-S2KS}$ and $\delta T_{S4KS-S3KS}$, respectively, using the convention of observed minus PREM predicted) of the Tonga

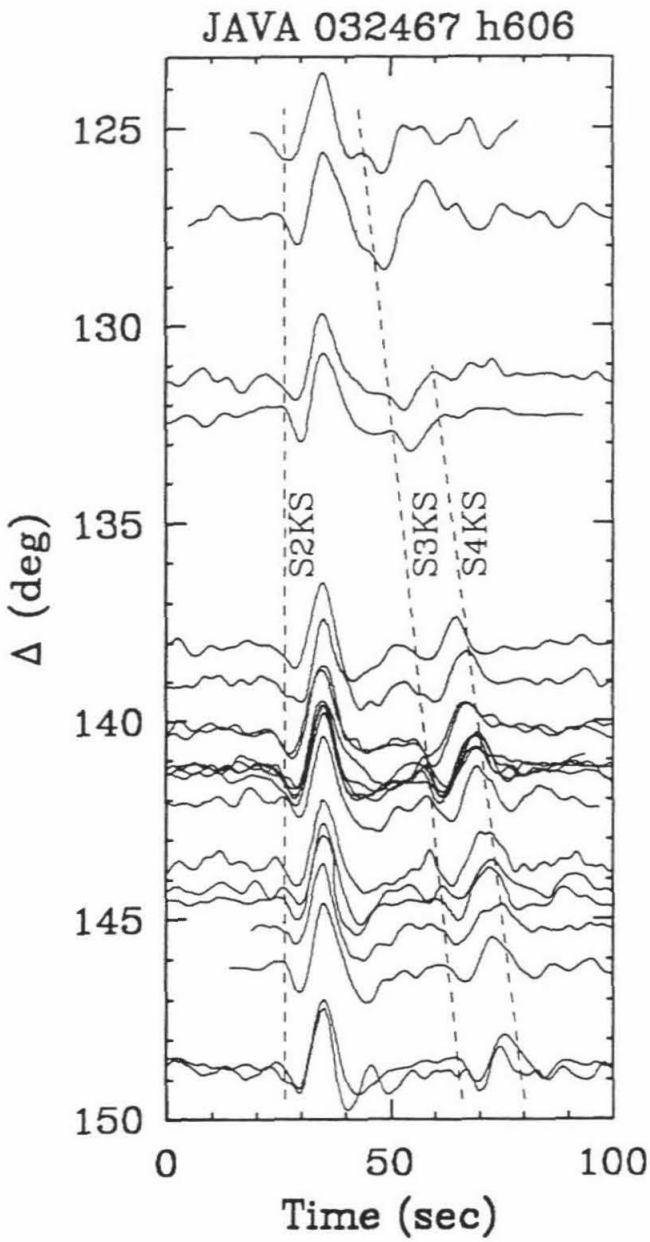

Figure 7.3: LP WWSSN $SmKS_{234}$ observations for a deep focus Java Sea event. Dotted lines correspond to $SmKS_{234}$ times of PREM.

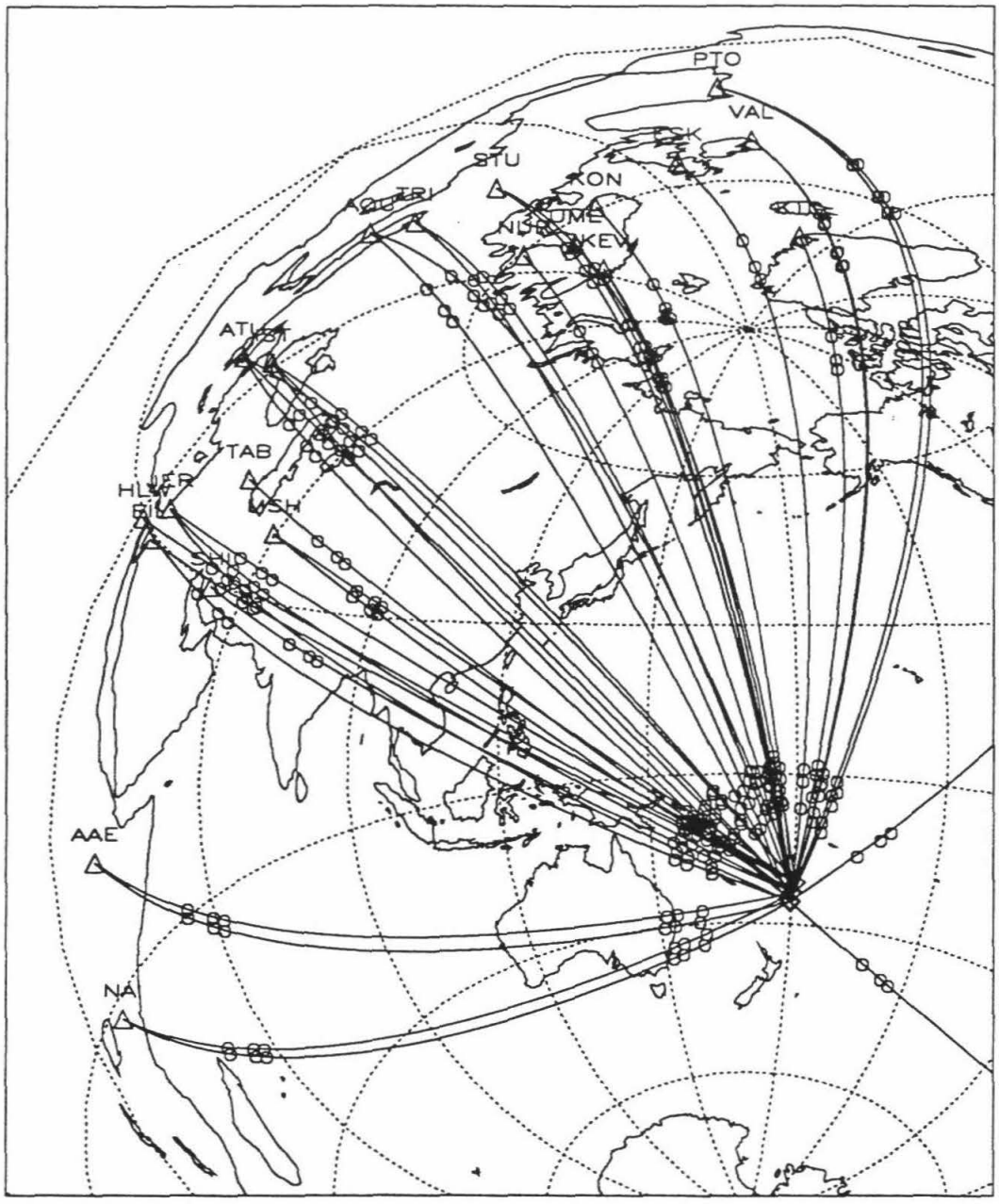

Figure 7.4: Great circle raypaths for 3 Tonga events recorded in Eurasia and Africa. Open-circles denote $SmKS_{234}$ CMB crossing locations projected to the Earth's surface.

Figure 7.5: Long-period WWSSN radial component profiles for 3 deep focus Fiji-Tonga events. Data are aligned on time and amplitude to the $S2KS$ peak. Dotted lines correspond to observed arrival times of $SmKS_{234}$. Event date and source depth are indicated above each panel.

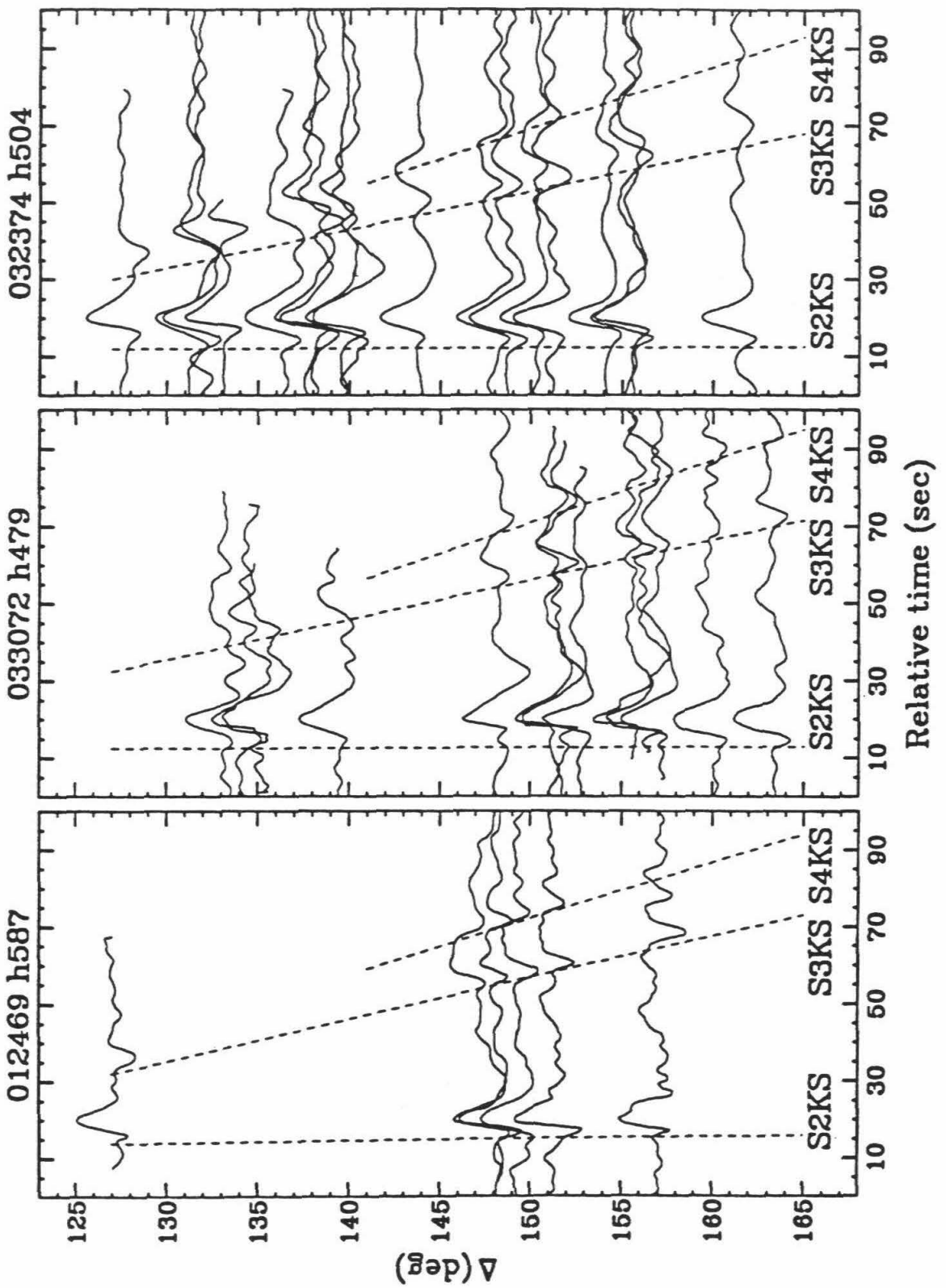
012469 h587
033072 h479
032374 h504
S2KS
S3KS
S4KS
Δ (deg)
Relative time (sec)

events are plotted in Figure 7.6 as a function of epicentral distance and azimuth. A ± 1 sec error bar is included to emphasize that some error may be induced through the digitization procedure, as well as from the correlation procedure when the signal-to-noise ratio (SNR) is low. Phase mis-identification can lead to even larger errors, although $SmKS_{234}$ are generally easily identified, or the records are not included on our analysis. $\delta T_{S3KS-S2KS}$ and $\delta T_{S4KS-S3KS}$ times plotted with distance (Figure 7.6a and 7.6b, respectively) display large scatter, with most observations exhibiting $S3KS - S2KS$ and $S4KS - S3KS$ separations larger than PREM predictions. However, when viewed in terms of source azimuth, the angle between north and the great circle source-receiver path (measured clockwise), some systematics appear (Figure 7.6c and 7.6d). Each datum is plotted at the azimuth to its respective source; the three Tonga sources are located closely enough for this not to induce any errors of significance in viewing all three events on the same plot. For azimuths between 280^o and 350^o, $\delta T_{S3KS-S2KS}$ times are systematically delayed by up to several seconds with respect to PREM (Figure 7.6c). The data outside this azimuth window, though sparse, tapers to values around the PREM prediction (with few exceptions). The long wavelength trend of the $\delta T_{S3KS-S2KS}$ times with azimuth resembles a concave down curve, and is explored below. The set of $\delta T_{S4KS-S3KS}$ times in Figure 7.6 is smaller than that of $\delta T_{S3KS-S2KS}$ times due to the fact that $S4KS$ cannot be reliably measured until almost 140^o in distance. The fewer points in Figure 7.6d make identification of any particular trend difficult. Nonetheless, the $\delta T_{S4KS-S3KS}$ points seem to fall within the scatter and trend of Figure 7.6c.

In analyzing such trends in $SmKS$ times, the inherent trade-off between mantle and core structure is ever present. While we are not currently in a position to resolve this ambiguity, we can investigate affects of mantle structure on $SmKS$ times. Source-side $SmKS_{234}$ lower mantle wavepaths (Figure 7.4) traverse anomalously slow and laterally varying V_S structure, as suggested by both body wave [e.g.,

Figure 7.6: (a) $\delta T_{S3KS-S2KS}$ and (b) $\delta T_{S4KS-S3KS}$ residuals as a function of distance, and (c) $\delta T_{S3KS-S2KS}$ and $\delta T_{S4KS-S3KS}$ residuals plotted against azimuth from source. All residuals are observed minus PREM predictions.

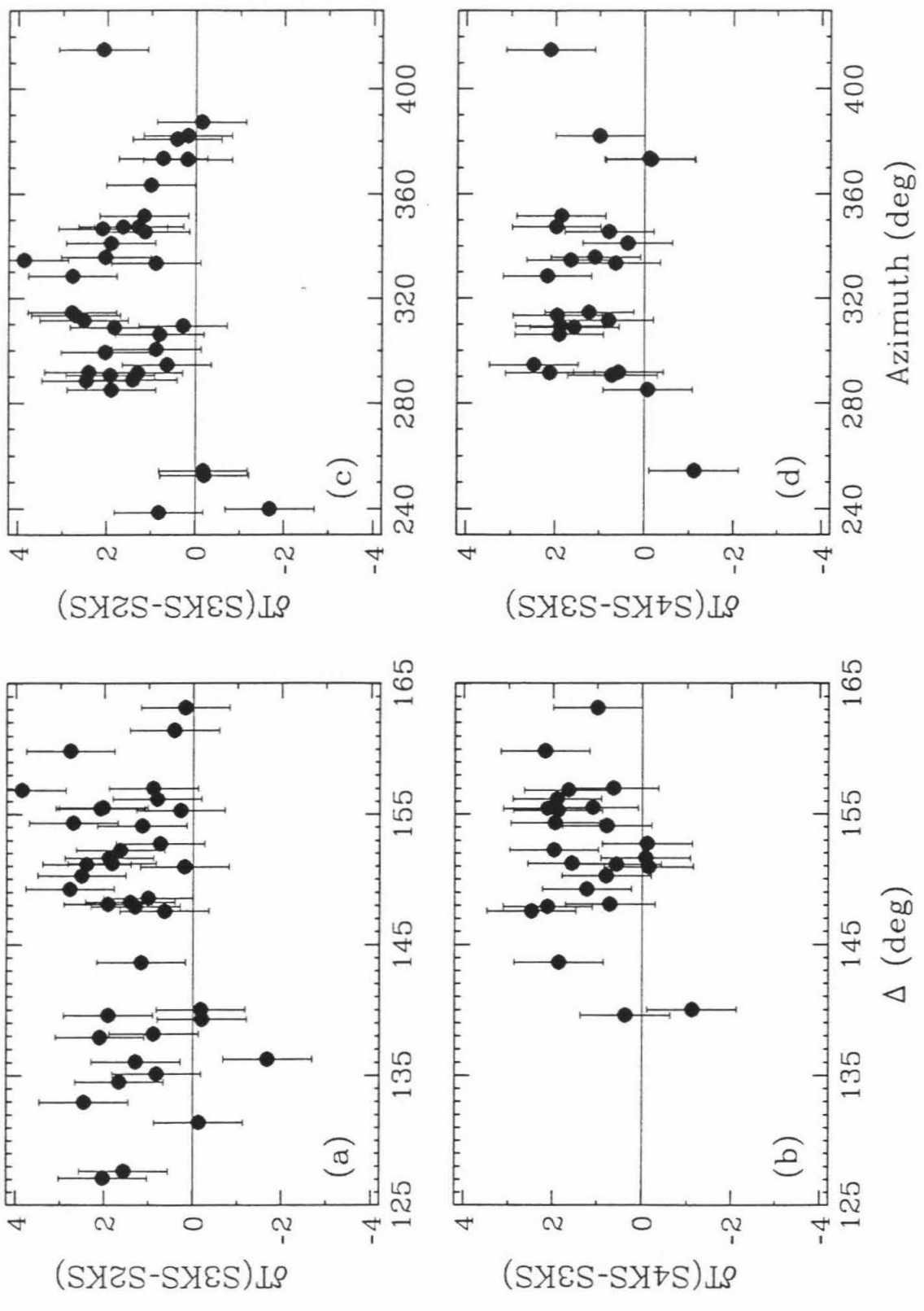
δT(S3KS-S2KS)
δT(S4KS-S3KS)
(a)
(b)
(c)
(d)
Δ (deg)
Azimuth (deg)

Woodward and Masters, 1991; Wysession et al., 1992; and Wysession et al., 1994] and global tomographic inversion studies [e.g., Su et al., 1992, 1994; and Masters et al., 1992]. For the remainder of this paper the aspherical structure of Su et al. [1992], SH12_WM13, is used in discussions of lower mantle V_S lateral variations. This choice is somewhat arbitrary, since other 3-D models will lead to similar conclusions that follow.

The map view of the D'' layer V_S perturbations (δV_S) for SH12_WM13 is presented in Figure 7.7, along with the $S2KS$ (crosses) and $S3KS$ (circles) CMB crossing locations, and the 3 Tonga sources (stars). Dark regions are slower than average V_S regions, light regions are faster than average. Most of the source-side $SmKS$ CMB crossing locations are seen to be in a slow region of D'' . As a first step, δV_S from SH12_WM13 has been extracted for the D'' layer for the corresponding locations of the $S2KS$ and $S3KS$ CMB crossing locations for the Tonga data. The SH12_WM13 δV_S values for both the source and receiver sides of the Tonga wavepaths are displayed in Figure 7.8a with respect to azimuth from source, as defined above. The solid and open crosses designate SH12_WM13 δV_S perturbations at the receiver-side $S2KS$ and $S3KS$ CMB crossing locations, respectively. The solid and open triangles designate δV_S at the source-side $S2KS$ and $S3KS$ CMB crossing locations, respectively. The vertical axis plotting convention is such that negative δV_S values are are plotted above the zero line, which corresponds to slower than average V_S regions; and conversely, values below the zero line correspond to faster than average velocities. As the figure illustrates, receiver-side D'' predictions from SH12_WM13 are roughly within $\pm 1\%$, while source-side perturbations display an azimuthal trend with pronounced slow velocities (more than 2% slower than average) near 300° in azimuth from the Tonga source region.

Figure 7.8b displays the average of the SH12_WM13 source-side δV_S predictions (of Figure 7.8a), along with averaged $\delta T_{S3KS-S2KS}$ time observations of Figure 7.6c.

Figure 7.7: Aspherical structure of D$''$ as depicted by model SH12_WM13, along with $S2KS$ (crosses) and $S3KS$ (circles) CMB crossing locations for the 3 Fiji-Tonga sources (stars). Dark regions depict slower than average and white regions faster than average V_S velocities.

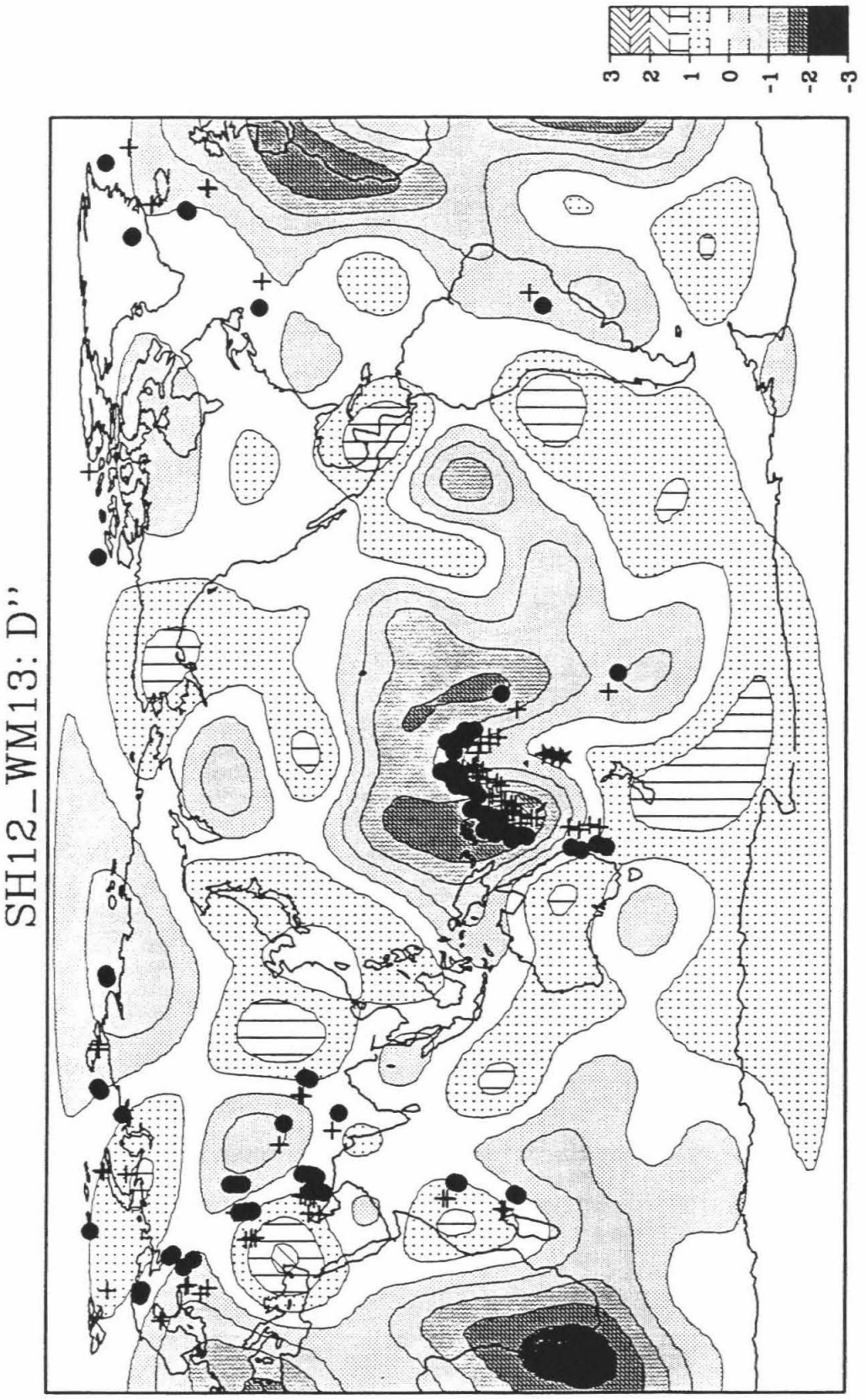
SH12_WM13: D''
3
2
1
0
-1
-2
-3

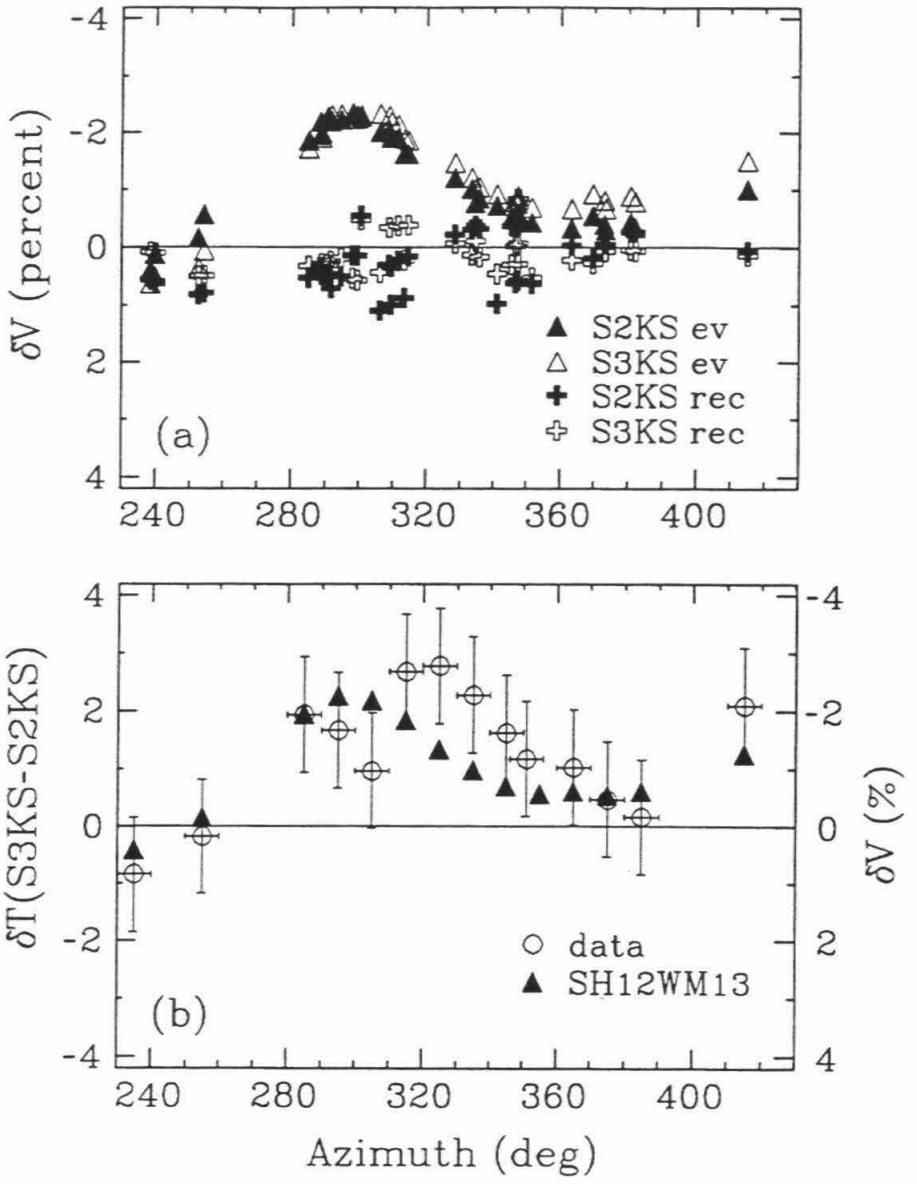

Figure 7.8: (a) SH12_WM13 δV_S values for the D'' region at CMB crossing locations of S2KS (solid symbols) and S3KS (open symbols) for the 3 Fiji-Tonga events. Triangles and crosses correspond to event and receiver sides of the path, respectively. (b) 10° azimuth bin averages of: SH12_WM13 δV_S perturbations for the Tonga source-side $SmKS_{23}$ CMB crossing points (triangles, vertical scale on right) and the observed $\delta T_{S3KS-S2KS}$ residuals (open circles, vertical scale on left).

The $\delta T_{S3KS-S2KS}$ times and δV_S perturbations were averaged in 10^o azimuth bins. The vertical axes for δV_S and $\delta T_{S3KS-S2KS}$ values are on the right and left sides of the figure, respectively. Only the source-side δV_S values are included since the receiver-side values are small on average throughout the azimuth range. Also, the δV_S values for the $S2KS$ and $S3KS$ CMB crossing locations have been averaged in Figure 7.8b. The azimuthal trend of SH12_WM13 δV_S values predict slower than average V_S values in locations where $\delta T_{S3KS-S2KS}$ observations display anomalously large $S3KS - S2KS$ time separations, as well as an azimuthal trend. Figure 7.8b suggests qualitative agreement between SH12_WM13 and the $\delta T_{S3KS-S2KS}$ residuals. This model is used as a starting point in our modeling experiments below, in which we investigate the affects of laterally varying structure on the travel times of $SmKS_{234}$.

7.5 2-D Modeling Experiments

The effects of lower mantle laterally varying structure on synthetics $SmKS$ waveforms are explored in this section. In the 1-D sense, slower than average V_S structure will slow down $S3KS$ more than $S2KS$, since $S3KS$ spends more time in the lower mantle than does the more steeply diving $S2KS$, along with the added affect of the raypaths being perturbed to more deeply penetrating, longer-time paths. This in turn increases $\delta T_{S3KS-S2KS}$, and similarly $\delta T_{S4KS-S3KS}$. However, due to the closeness of the $SmKS_{234}$ raypaths, δT anomalies resulting from 1-D structures displaying lower than average D'' velocities are small and underpredict the observations of Figure 7.6. Correcting $SmKS_{234}$ observations for long-wavelength 3-D structure using laterally homogeneous raypaths of a 1-D reference model will also underpredict the observations, since structure encountered by the separate $SmKS$ phases is negligibly different. If laterally inhomogeneous raypaths are adopted, 3-D

structure will have the added affect on $SmKS_{234}$ times from raypath perturbations, and is explored in what follows. The WKM method enables construction of $SmKS$ waveforms from 2-D structures. Velocity perturbations for this method must be parameterized as a layered structure where layer thicknesses can change laterally across the structure [see Helmberger et al., 1985ab, 1994, for further discussion on the model parameterization and method]. In using this technique, 2-D cross-sections through 3-D structures can be constructed and tested.

The pronounced low-velocity zone (LVZ) on the source-side of the $SmKS$ paths (Figure 7.7) is a 3-D feature, and can be parameterized for WKM input by a series of cross-sections containing various intensities of a LVZ. As a first approximation, only the source-side lower mantle LVZ is parameterized; receiver-side structure is predicted small by SH12_WM13 (roughly within $\pm 1\%$). 2-D cross-sections were constructed using PREM as a starting model, parameterized as a stack of 175 layers from surface to the Earth's center. Thicknesses of layers in the bottom 400 to 900 km of the mantle were then systematically varied to form large scale LVZs. This is accomplished by thickening a given layer to extend to deeper regions, thereby displacing the velocity at a given depth by a slower value. Figure 7.9 displays an example of such a model. The WKM method uses the Earth flattening approximation [e.g., see Müller, 1977], so the model is displayed as a Cartesian stack of layers. Iso-velocity contours are shown depicting the LVZ on the source-side of the path, from end-to-end the anomaly measures about 4500 km. The center of the LVZ contains about a 2% reduction from PREM. First-arrival raypaths for $SmKS_{234}$ for the 2-D structure are shown as solid lines connecting the 500 km deep source (star) and receiver at 150^o (triangle), and those for 1-D PREM are shown as dotted lines. For this particular source-receiver arrangement, the 2-D $SmKS_{234}$ first arrival wavepaths dive more deeply to avoid the source-side lower mantle slow anomaly. These paths are also perturbed due to the effect of dipping velocity interfaces that compose the

cosine taper LVZ. The 2-D paths of $S3KS$ and $S4KS$ are almost superimposed in the lower mantle (source-side), which is a result of the V_S anomaly in the model. Also, due to the source-side anomaly, 2-D receiver-side $S2KS$ and $S3KS$ paths are more separated than those of PREM.

Such perturbations in raypath, as well as those in travel time due to the reduced velocities, combine to yield $SmKS_{234}$ difference time and amplitude anomalies. Comparing WKM $SmKS_{234}$ waveforms for the model shown in Figure 7.9 to those of 1-D PREM predictions illustrates such travel time perturbations. Waveforms calculated from the 2-D model (Figure 7.10, solid traces) exhibit larger $T_{S3KS-S2KS}$ and $T_{S4KS-S3KS}$ separations than those of 1-D PREM (dotted traces). At closer distances (125*supo*), absolute T_{S2KS} times are also affected by the structure. At the larger distances, amplitude ratios between $SmKS_{34}$ and $S2KS$ are reduced in the 2-D predictions.

The predicted $\delta T_{S3KS-S2KS}$ and $\delta T_{S4KS-S3KS}$ travel time residuals (with respect to PREM) for this model are given in Figure 7.11a and 7.11b, respectively, along with the Fiji-Tonga observations as a function of distance. Two curves are plotted with the data and correspond to different lateral placements of the source location with respect to the lower mantle LVZ. The dotted curve corresponds to the placement shown in Figure 7.9, and the dashed curve corresponds to a source located 400 km towards the receiver from this position. The different lateral source placements in turn produce $SmKS_{234}$ raypaths that interact with different parts of the 2-D structure, resulting in different $\delta T_{S3KS-S2KS}$ and $\delta T_{S4KS-S3KS}$ residuals. The dashed curves display $\delta T_{S3KS-S2KS}$ and $\delta T_{S4KS-S3KS}$ anomalies of up to 3 and 2 sec, respectively, and range within the scatter of the observations. In moving the source 400 km closer to the LVZ, $SmKS_{34}$ waves interact more directly with the center of the anomaly than for the original source placement, resulting in the larger predicted anomalies.

Figure 7.9: Earth-flattened 2-D cross-section showing $SmKS_{234}$ first-arrival raypaths for the 2-D structure (solid) and for PREM (dotted). Source (star) is at 500 km depth, and receiver (triangle) is at 150^o. Horizontal lines are iso-velocity lines, and a low velocity zone is depicted on the source-side of paths. The center of the anomaly is a $\approx$2.5% reduction from the PREM model.

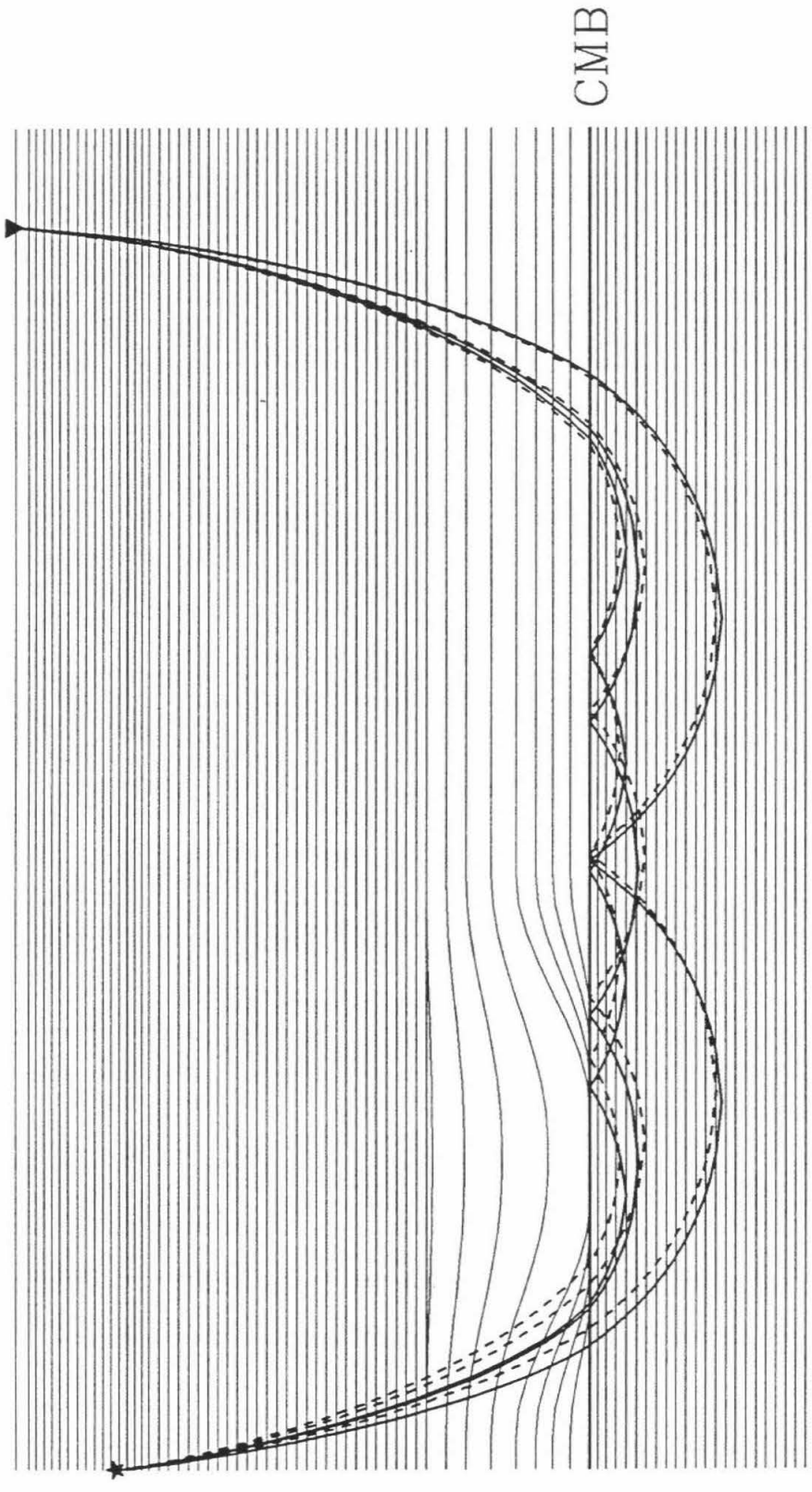
CMB

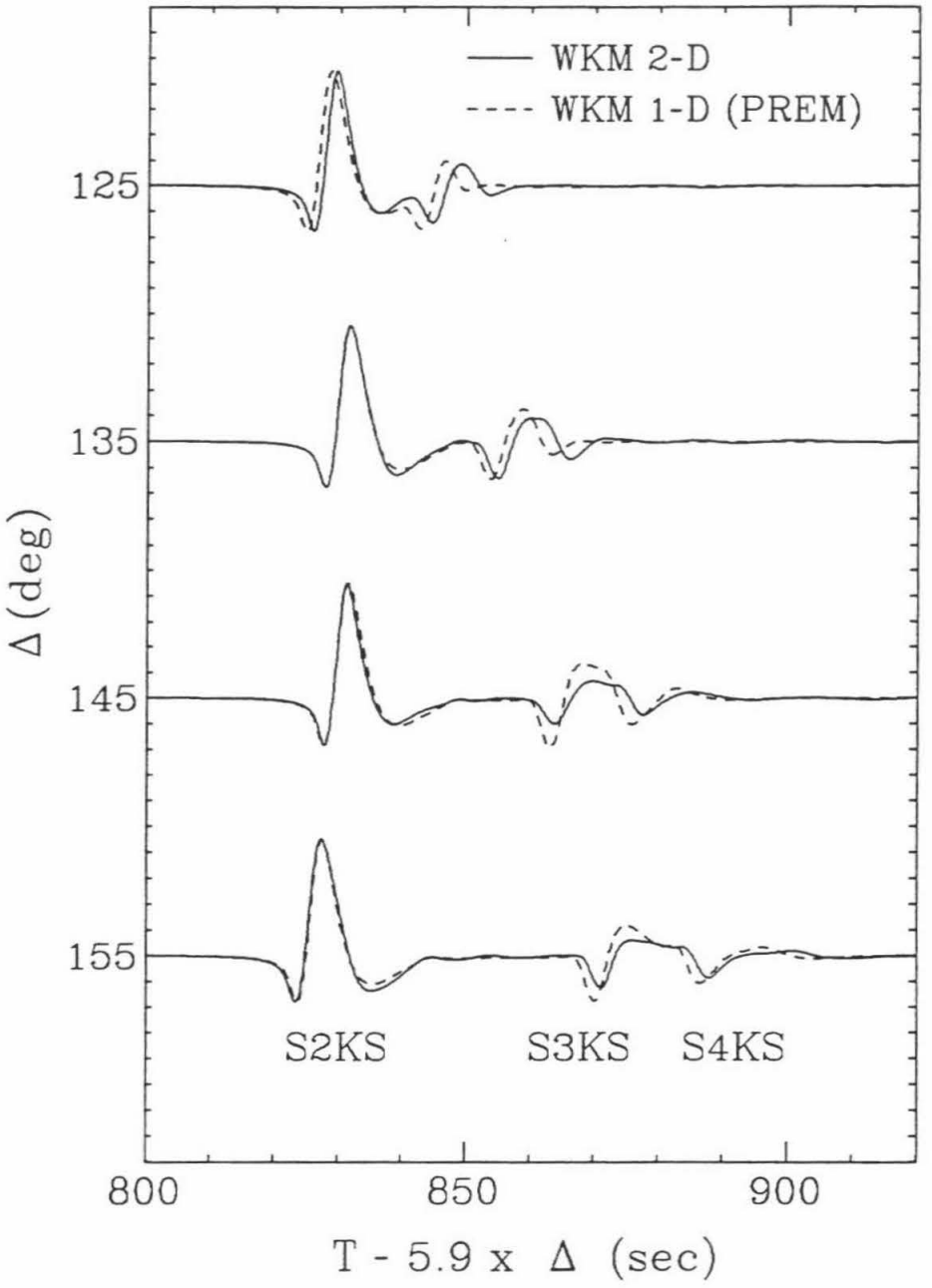

Figure 7.10: WKM $SmKS_{234}$ synthetic waveform comparisons for the 2-D structure of Figure 7.9 (solid) with that of PREM (dotted).

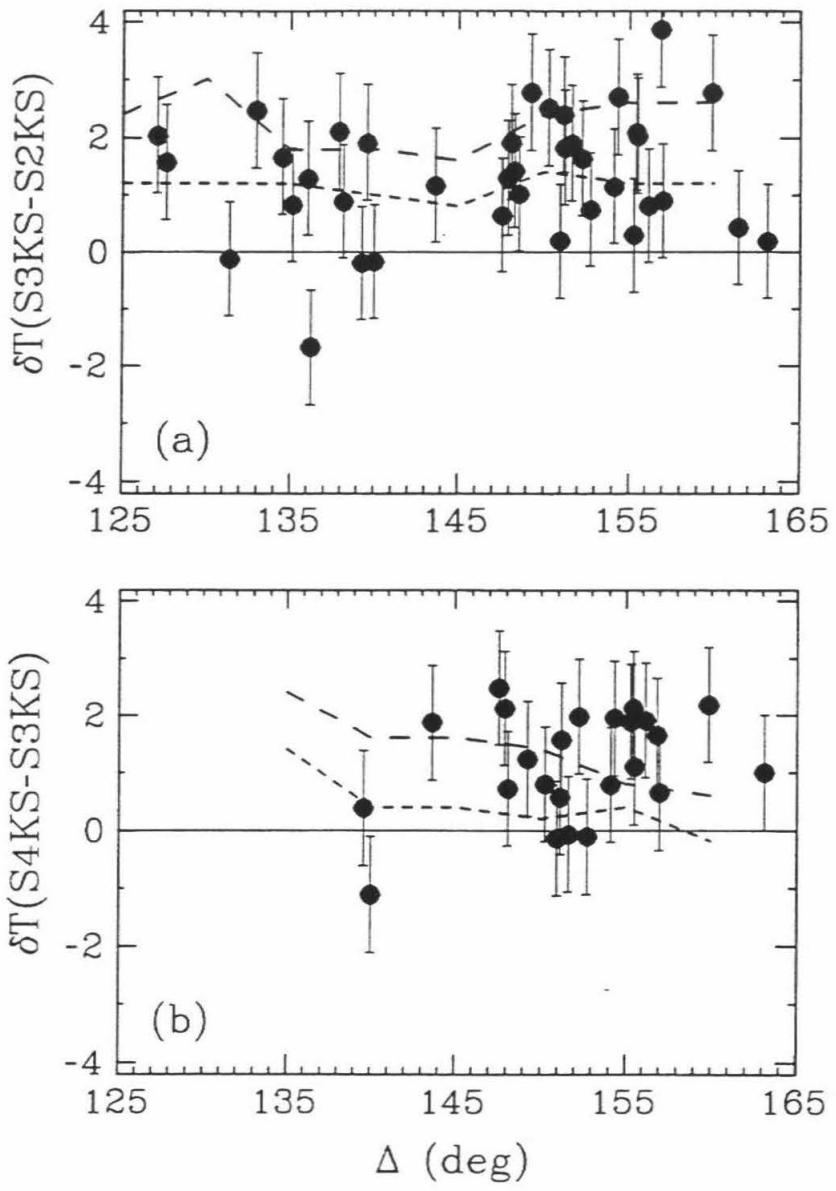

Figure 7.11: (a) $\delta T_{S3KS-S2KS}$ and (b) $\delta T_{S4KS-S3KS}$ observations (solid circles) and predictions for the 2-D structure of Figure 7.9 for source placement at left end of model (dotted line) and 400 km towards the anomaly from left end of model (dashed line).

The model presented in Figure 7.9 contains a LVZ with perturbations from PREM on the order of more than 2%. Reducing the velocities more will have a greater impact on the $SmKS_{234}$ times, causing even larger difference times. Reducing the lateral scale-length of the cosine taper will also produce larger $SmKS_{234}$ difference time anomalies due to increased ray path perturbations. For example, reducing the lateral width of the structure to 2500 km and the vertical extent of the LVZ above the CMB to 500 km, results in $\delta T_{S3KS-S2KS}$ residuals up to 6 sec. This is several seconds larger than observations, thus such large lateral velocity gradients may be too large for the lowermost mantle beneath the Fiji-Tonga sources. Nonetheless, the 2-D wave propagation experiments illustrate the importance of mantle structure in producing travel time anomalies for $SmKS$ waves.

In a detailed analysis of S, ScS, sS, and $sScS$ times, Wysession et al. [1994] report for the same region of study that lateral variations in V_S are of $\pm 3\%$, and in some cases perhaps as large as $\pm 6\%$. They also report lateral wavelengths of low-velocity structure between 1000-2500 km, which are surrounded on three sides by high-velocity anomalies. Our test models contain cosine tapered LVZs and are more simplistic than the structure of Wysession et al. [1994] or SH12_WM13, but are a first step in understanding dependencies of $SmKS$ travel times on mantle structure. A structure such as that presented by Wysession et al. [1994] would produce more varied $\delta T_{S3KS-S2KS}$ and $\delta T_{S4KS-S3KS}$ anomalies than those predicted in Figure 7.11, and whether or not this structure better fits the observations remains for future study. Rather than finding the best fitting lower mantle model to the data, our purpose here has been to show the strong effect lower mantle heterogeneity plays on $SmKS$ times.

7.6 Discussion

$SmKS$ times have been analyzed for source-receiver geometries both containing and in absence of strong lowermost mantle heterogeneity. For a region in absence of such anomalies, $SmKS_{234}$ times are well-predicted by the PREM model, with the additional modification of lowering the outermost 50 km of the core V_P by 1.5% [Garnero et al., 1993b]. This reduction is large enough to imply chemical stratification when using the inhomogeneity index approach of Bullen [1975]. However, uncertainties and non-uniqueness in this structure precludes confidence in such a statement.

2-D wave propagation experiments have demonstrated the importance of the effect of lowermost mantle heterogeneity on $SmKS$ differential times. The combination of laterally varying structure and resulting laterally inhomogeneous raypaths predict $\delta T_{S3KS-S2KS}$ and $\delta T_{S4KS-S3KS}$ residuals on the order of observations. The structures tested were generally long-wavelength; lateral variations on smaller scale lengths [such as that of Wysession et al., 1994] imply even more variability to the $SmKS$ times. In viewing the scatter in Figure 7.6, such variability can be easily accommodated. We have ignored receiver-side lower mantle structure in our 2-D model construction. Any such structure will add complexities to $SmKS$ travel times, and add further uncertainties to solution models. Future $SmKS$ modeling studies must consider mantle structure on both the source- and receiver-sides of the wavepath. If receiver-side anomalies for the Fiji-Tonga data can be demonstrated to contribute minimally to $SmKS$ anomalies, then the azimuthal trend of the data (Figure 7.6c) may ultimately be modeled through construction of various representative 2-D cross-sections using the WKM method or perhaps some 3-D method.

The WKM method is best suited for lower mantle 2-D structures with somewhat longer wavelengths O(1000 km). To assess scale lengths of heterogeneity in the lower mantle using $SmKS$, an alternate method of generating synthetic seismogram waveforms must be sought. Development of the Kirchoff method for this application

would be ideal, and is left for future work.

Complications in the $SmKS$ data due to upper mantle anisotropy, as suggested by Silver and Chan [1988], for example, are not expected to play a role here, since transverse components of the long-period data showed no $SmKS$ energy. Slab effects [Vidale, 1987; and Cormier, 1989] have been assumed minimal, since only deep focus events were studied and $SmKS$ waveforms were not distorted. Such complications, however, cannot be ruled out as a source of some isolated observations containing waveform anomalies.

CMB topography [e.g., Gudmundsson et al., 1986; Creager and Jordan, 1986; Morelli and Dziewonski, 1987; and Doornbos and Hilton, 1988] however, may serve to focus/defocus $SmKS_{234}$ energy, particularly the higher multiples, such as $S4KS$ which displays highly variable amplitudes. How topography affects $SmKS_{234}$ times and waveforms also remains for future work. Synthetic tests will be necessary to assess trade-off of CMB topography with small scale mantle-side heterogeneity that may affect $SmKS$ wavepaths. If outer core heterogeneity can exist in CMB underside "pools" beneath topographic highs, further travel time and waveform perturbations to $S4KS$ may occur, which needs to be explored. It is also uncertain at present how approximating 3-D lowermost mantle structure with 2-D cross-sections may neglect important 3-D focusing/defocusing and off azimuth affects on the $SmKS$ times. Such complexities, if they exist, further emphasize the importance of understanding mantle affects on $SmKS$.

We have not explored D$''$ discontinuity structures here, which have been recently proposed to be a world-wide feature [Nataf and Houard, 1993]. A 1-D D$''$ discontinuity structure does not significantly alter $SmKS_{234}$ times, though any 2-D D$''$ structure [e.g., Garnero et al., 1993a; and Kendall and Shearer, 1994], such as lateral warping or thinning, can significantly affect the difference times [Helmberger et al., 1994]. S-wave scattering as suggested by, for example, Haddon and Buchbinder [1987]

should also complicate $SmKS$ data. Utilizing $SmKS_{234}$ amplitude information in future modeling efforts may help in resolving some of the uncertainties inherent in some of these issues. Source mislocations do not alter results of our analysis, since differential travel times have been studied, which should minimize such affects.

Past studies have presented evidence for lower mantle V_S lateral variations on scale lengths of O(100 km) [e.g., Lay, 1983; Lavely et al. 1986; Garnero et al., 1988; Weber and Davis, 1990; Gaherty and Lay, 1992; Weber, 1993; and Wysession et al., 1994] which are smaller than resolution of present tomographic inversion results O(1000 km). Such variations affect $SmKS$ times and must be considered when correcting $SmKS$ times for mantle structure. Otherwise, unknown mantle heterogeneity maps directly into core structure.

Garnero et al. [1988] and Garnero and Helmberger [1993] have shown how mantle structure can explain anomalous S-SKS and $S2KS - SKS$ times for Fiji-Tonga to north America paths, which traverse a low-velocity lower mantle anomaly beneath the southwest Pacific. Alternately, in analyzing a large data set of S, SKS, and $S2KS$ times, Schweitzer [1990] inverted for small scale laterally varying structure in the lower mantle with and without including the outermost 400 km of the outer core in the inversion. Due to the direct trade-off in mantle and core heterogeneity in $SmKS$, there was not a distinguishable improvement of fit to T_{S-SKS} and $T_{S2KS-SKS}$ time predictions. Fiji-Tonga data recorded in north America, Eurasia, and Africa provide valuable and abundant data for use in $SmKS$ studies. However, anomalous mantle structure must first be mapped out before this data is used to infer variable outermost core properties.

Synthetic tests suggest the long-period data used here cannot well-resolve structure in the outermost 25 km of the core. Broadband $SmKS$ data for regions exhibiting little mantle heterogeneity should help in this regard. Dynamical considerations imply outer core homogeneity [Stevenson, 1987]; if the outer core departs from this

it is of fundamental importance to map this out and explore possible causes. For this reason, better maps of lower mantle heterogeneity on all scales remains necessary. $SmKS$ waves can supplement future inversions, following Schweitzer [1990] by inverting for 3-D mantle structure with and without permitting the outermost core to vary. Raypath inhomogeneity should be considered in such future studies.

$SmKS$ waves can greatly improve wavepath sampling coverage of the lowermost mantle in future tomographic inversions for lower mantle structure. $SmKS$ are commonly recorded for deep focus events. Data from 3 South American events are briefly presented to illustrate the wealth of such data in the WWSSN archives. Figures 7.12 and 7.13 display great circle raypaths and long-period WWSSN radial component waveform observations, respectively. Figure 7.12 shows that the $SmKS_{234}$ CMB crossing locations (circles) occur in a wide variety of regions, and display $\delta T_{S3KS-S2KS}$ time anomalies from -2 to 2 sec (Figure 7.14). The waveforms of Figure 7.13 display $S3KS$ and $S4KS$ amplitude anomalies also. If coupled to data sets of S, ScS, and $S-SKS$ times, better resolution of lower mantle heterogeneity maps can be achieved.

7.7 Conclusions

While outermost core heterogeneity and/or chemical stratification cannot be ruled out at present, our analysis suggests that uncertainties in lower mantle structure preclude confident conclusions concerning these issues when using seismic techniques. Lower mantle structure is shown to systematically affect $SmKS$ behavior. An example of deep focus Fiji-Tonga data is presented whereby $SmKS$ paths traverse lower than average velocities in the lower mantle on the source-side of the paths. A systematic trend in $\delta T_{S3KS-S2KS}$ residual times with respect to azimuth from source is apparent for this data sample. Predictions of δV_S perturbations in the D$''$ layer from

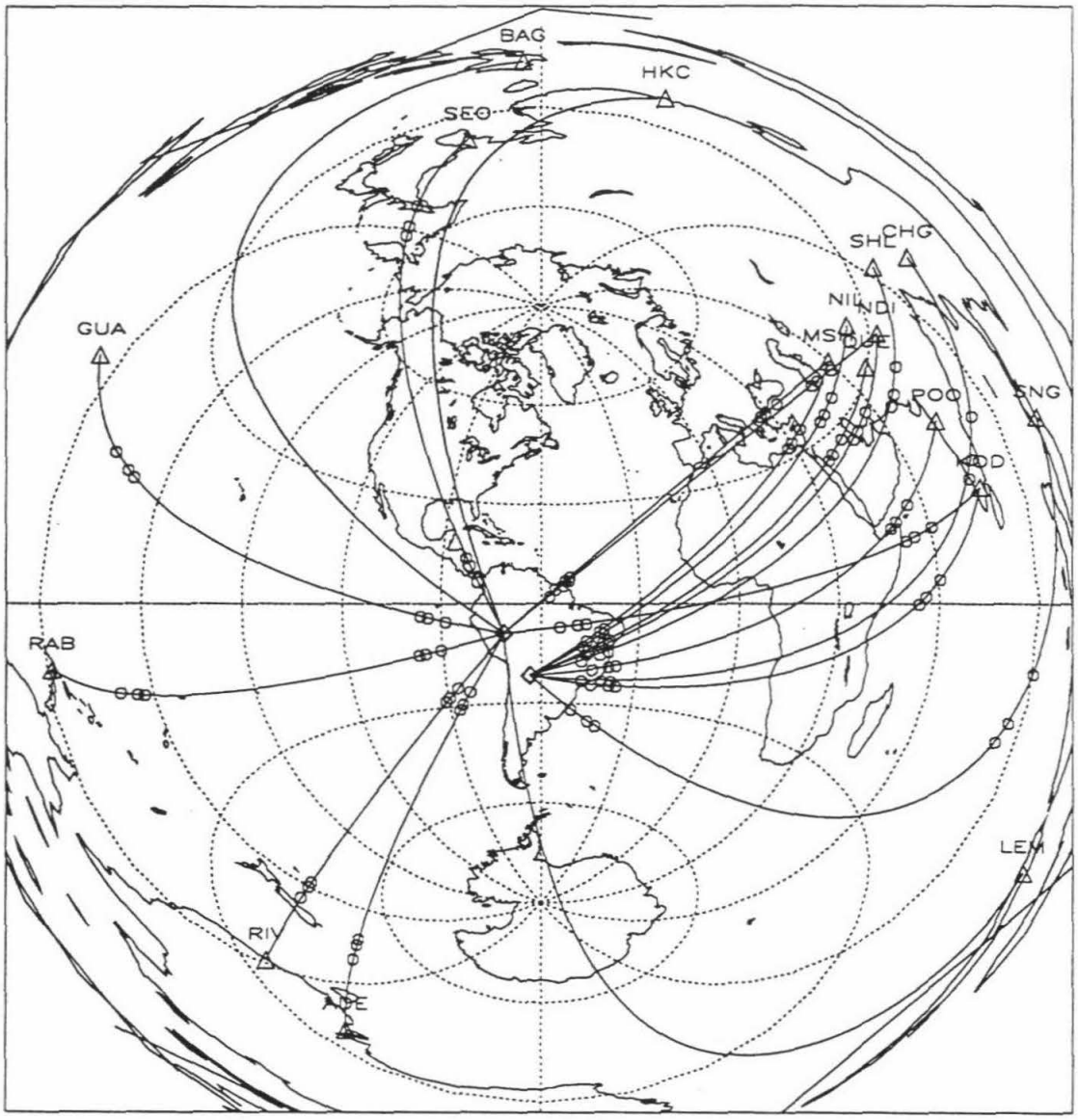

Figure 7.12: Great circle raypaths for 3 South American events recorded in world-wide at WWSSN station. Open-circles denote $SmKS_{234}$ CMB crossing locations projected to the Earth's surface.

Figure 7.13: Long-period WWSSN radial component profiles for 3 deep focus South American events. Dotted lines correspond to observed arrival times of $SmKS_{234}$. Event date and source depth are indicated above each panel.

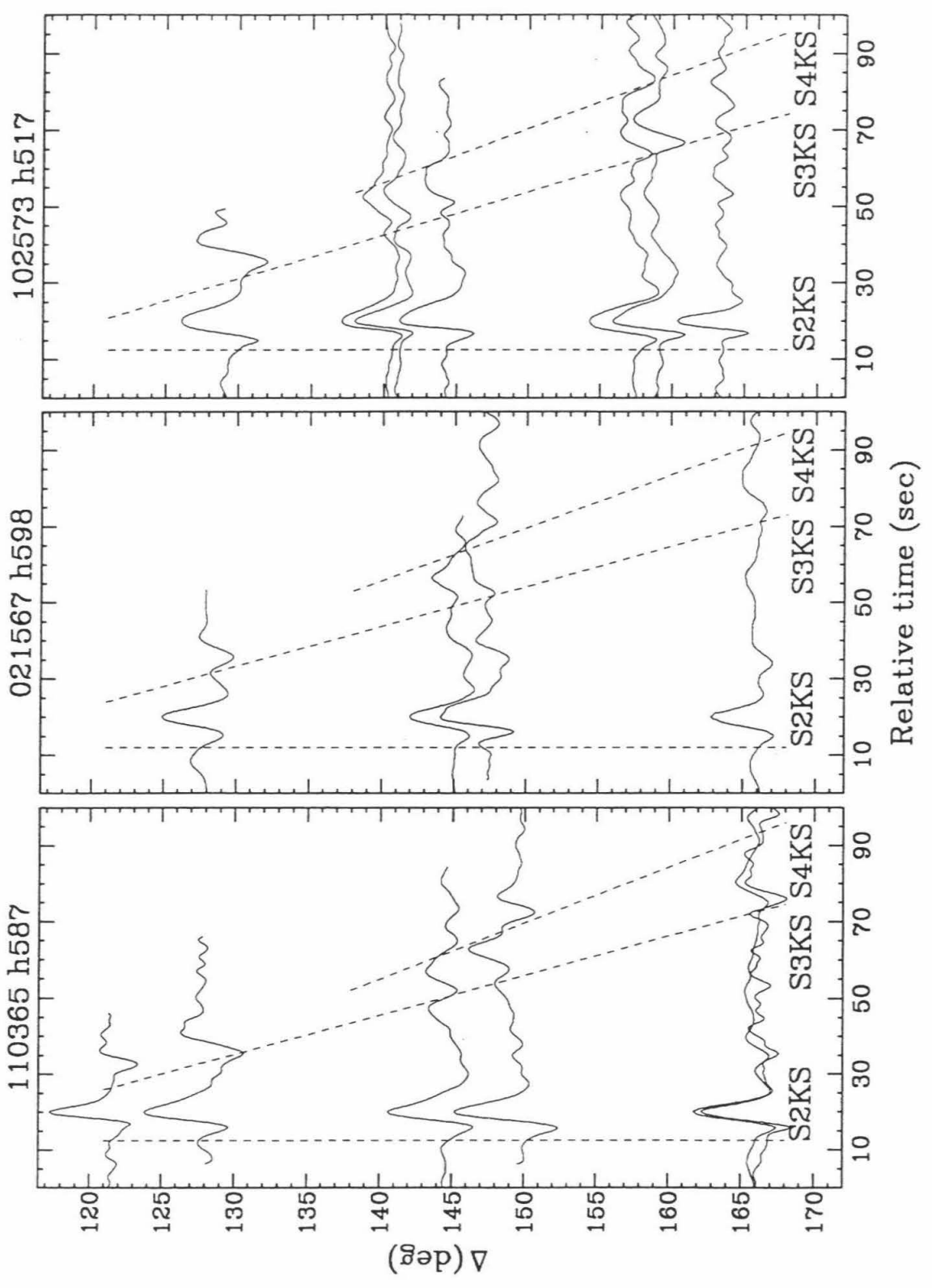
110365 h587
021567 h598
102573 h517
S2KS
S3KS
S4KS
Δ (deg)
Relative time (sec)

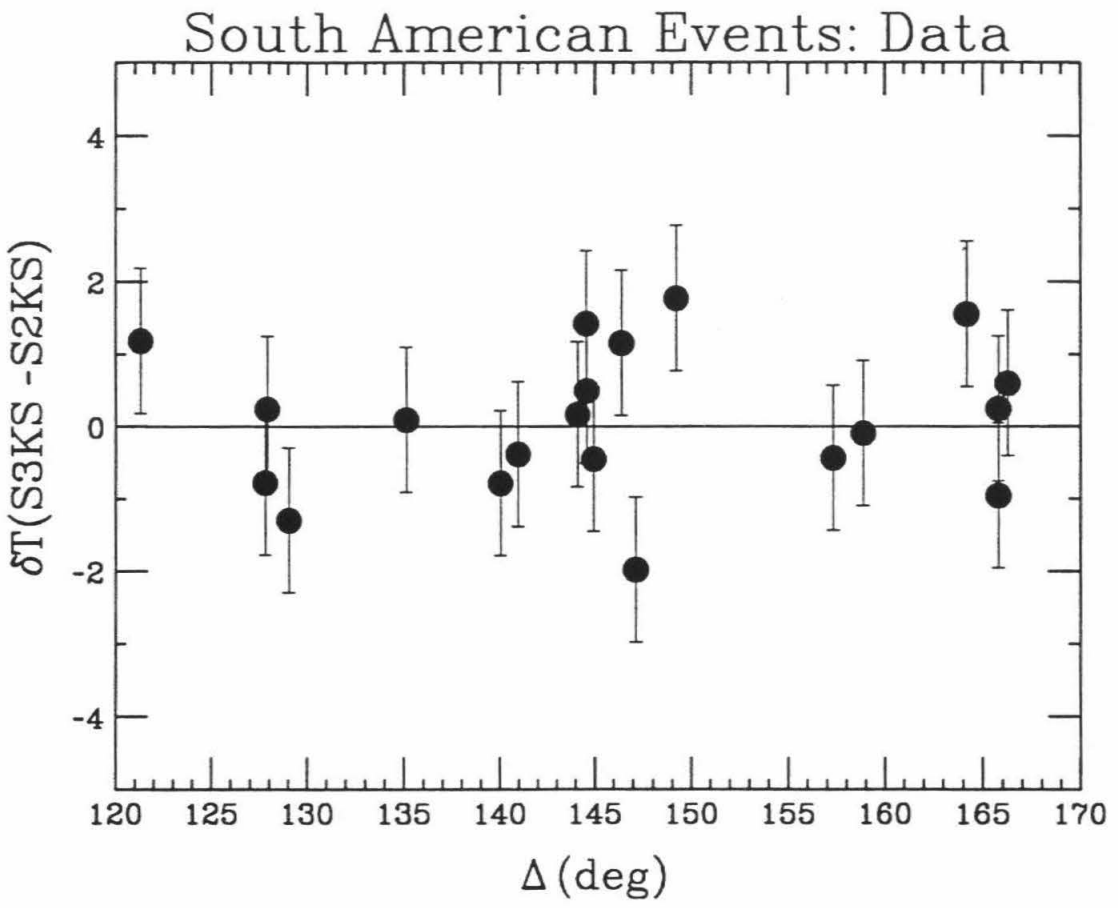

Figure 7.14: $\delta T_{S3KS-S2KS}$ residuals as a function of distance for the 3 South American events of Figures 7.12 and 7.13. All residuals are observed minus PREM predictions.

the 3-D mantle model SH12_WM13 [Su et al., 1992], for the CMB crossing locations of $SmKS$ wavepaths of the Fiji-Tonga data, display a similar azimuthal dependence. Similar azimuthal trends in δV_S perturbations and $SmKS$ difference time anomalies motivates investigating the time anomalies in terms of mantle structure. WKM waveforms are synthesized for 2-D cross-sections simulating slices through 3-D model SH12_WM13. Our tests indicate that such lower mantle structure explains the size of $SmKS$ anomalies observed for the Tonga data. Scatter in the data may indicate heterogeneity at the base of the mantle of many scale lengths, though only the long-wavelength behavior of $SmKS_{234}$ times have been studied here. In the 2-D models tested here, 2-D wave path effects prove important in perturbing $SmKS$ travel times and waveforms.

$SmKS$ data with mantle paths traversing regions with little mantle heterogeneity can be used to study core structure, and suggest that the PREM model with a 1.5% reduction in the outermost core well-predicts observations [Garnero et al., 1993b]. Otherwise, mantle structure must be accurately known in order to make inference on outermost core properties. If future studies indicate that in regions where no lower mantle anomalies exist consistently yield no anomalies in multi-$SmKS$ paths, we will be safe in assuming that the outermost core is 1-D. With this assumption we can then use the full power of multi-$SmKS$ waveform analysis to explore D$''$.

Bibliography

Alexander, S. S., and R. A. Phinney, A study of the core-mantle boundary using P waves diffracted around the Earth's core, *J. Geophys. Res.*, **71**, 5943-5958, 1966.

Anderson, D. L., and R. S. Hart, Q of the Earth, *J. Geophys. Res.*, **83**, 5869-5882, 1978.

Bataille, K., and S. M. Flatte, Inhomogeneities near the core-mantle boundary inferred from short-period scattered PKP waves recorded at the global digital seismograph network, *J. Geophys. Res.*, **93**, 15,057-15,064, 1988.

Bataille, K., R.-S. Wu, and S. M. Flatte, Inhomogeneities near the core-mantle boundary evidenced from scattered waves: a review, *Pageoph,* **132**, 151-173, 1990.

Baumgardt, D. R., Evidence for a P-wave velocity anomaly in D", *Geophys. Res. Lett.*, **16**, 657-660, 1989.

Bloxham, J., On the consequences of strong stable stratification at the top of Earth's core, *Geophys. Res. Lett.*, **17**, 2081-2084, 1990.

Bloxham, J., and D. Gubbins, Thermal core-mantle interactions, *Nature*, **325**, 511-513, 1987.

Bokelmann, G. H. R., and P. G. Silver, The Carribean anomaly: short-wavelength lateral heterogeneity in the lower mantle, *Geophys. Res. Lett.*, **20**, 1131-1134, 1993.

Bolt, B. A., N. Niazi, and M. R. Somerville, Diffracted ScS and the shear velocity at the core boundary, *Geophys. J. R. astr. Soc*, **19**, 299-305, 1970.

Bolt, B. A., and N. Niazi, S velocities in D" from diffracted SH-waves at the core boundary, *Geophys. J. R. astr. Soc*, **79**, 825-834, 1984.

Bullen, K. E., Compressibility-pressure hypothesis and the Earth's interior, *Mon. Not. R. Astron. Soc.*, **5**, 355-368, 1949.

Bullen, K. E., *The Earth's Density*, 420pp., Chapman and Hall, London, 1975.

Chang, A. C., and J. R. Cleary, Precursors to $PKKP$, *Bull. Seism. Soc. Am.*, **68**. 1059-1079, 1978.

Chang, A. C., and J. R. Cleary, Scattered $PKKP$: further evidence for scattering at a rough core-mantle boundary, *Phys. Earth Planet. Inter.*, **24**, 15-29, 1981.

Chapman, C. H., A new method for computing synthetic seismograms, *Geophys. J. R. astr. Soc*, **54**, 481-518, 1978.

Chapman, C. H., and J. A. Orcutt, The computation of body wave synthetic seismograms in laterally homogeneous media, *Rev. Geophys.*, **23**, 105-163, 1985.

Chowdhury D. K., and C. W. Frasier, Observations of PcP and P phases at Lasa at distances from 26° to 40°, *J. Geophys. Res.*, **78**, 6021-6027, 1973.

Choy, G. L., Theoretical seismograms of core phases calculated by frequency-dependent full wave theory, and their interpretation, *Geophys. J. R. astr. Soc*, **51**, 275-312, 1977.

Choy, G. L., and P. G. Richards, Pulse distortion and Hilbert transformation in multiply reflected and refracted body waves, *Bull. Seism. Soc. Am.*, **65**, 55-70, 1975.

Choy, G. L., V. F. Cormier, K. Kind, G. Müller, and P. G. Richards, A comparison of synthetic seismograms of core phases generated by the full wave theory and by the reflectivity method, *Geophys. J. R. astr. Soc*, **61**, 21-39, 1980.

Cleary, J. R., The D" Region, *Phys. Earth Planet. Inter.*, **9**, 13-27, 1974.

Cormier, V. F., Some problems with S, SKS, ScS observations and implications for structure of of the base of the mantle and the outer core, *J. Geophys*, **57**, 14-22, 1985.

Cormier, V. F., Slab diffraction of S waves, *J. Geophys. Res.*, **94**, 3006-3024, 1989.

Creager, K. C., and T. H. Jordan, Slab penetration into the lower mantle, *J. Geophys. Res.*, **89**, 3031-3049, 1984.

Creager, K. C., and T. H. Jordan, Aspherical structure of the core-mantle boundary from PKP travel times, *Geophys. Res. Lett.*, **13**, 1497-1501, 1986.

Davis, J. P. and M. Weber, Lower mantle velocity inhomogeneity observed at GRF array, *Geophys. Res. Lett.*, **17**, 187-190, 1990.

Doornbos, D. J., Seismic wave scattering near caustics: observations of PKKP precursors, *Nature*, **247**, 352-353, 1974.

Doornbos, D. J., On seismic wave scattering by a rough core-mantle boundary, *Geophys. J. R. astr. Soc*, **53**, 643-662, 1978.

Doornbos, D. J., and E. S. Husebye, Array analysis of PKP phases and their precursors, *Phys. Earth Planet. Inter.*, **5**, 387-399, 1972.

Doornbos, D. J., and N. J. Vlaar, Regions of seismic wave scattering in the Earth's mantle and precursors to PKP, *Nature*, **243**, 58-61, 1973.

Doornbos, D. J., and J. C. Mondt, Attenuation of P and S waves diffracted around the core, *Geophys. J. R. astr. Soc*, **57**, 353-379, 1979a.

Doornbos, D. J., and J. C. Mondt, P and S waves diffracted around the core and the velocity structure at the base of the mantle, *Geophys. J. R. astr. Soc*, **57**, 381-395, 1979b.

Doornbos, D. J., S. Spiliopoulos, and F. D. Stacey, Seismological properties of D" and the structure of a thermal boundary layer, *Phys. Earth Planet. Inter.*, **41**, 225-239, 1986.

Doornbos, D. J., and T. Hilton, Models of the core-mantle boundary and the travel times of internally reflected core phases, *J. Geophys. Res.*, **94**, 15741-15751, 1989.

Dziewonski, A. M., Mapping the lower mantle: Determination of lateral heterogeneity in P velocity up to degree and order 6, *Geophys. J. R. astr. Soc*, **89**, 5929-5952, 1984.

Dziewonski, A. and F. Gilbert, The effect of small, aspherical perturbations on travel times and a re-examination of the corrections for ellipticity, *Geophys. J. R. astr. Soc*, **44**, 7-17, 1976.

Dziewonski, A. M., and D. L. Anderson, Preliminary reference Earth model (PREM), *Phys. Earth Planet. Inter.*, **25**, 297-356, 1981.

Dziewonski, A. and J. H. Woodhouse, Global images of the Earth's interior, *Science*, **236**, 37-48, 1987.

Fearn, D. R., and D. E., Loper, Compositional convection and stratification of Earth's core, *Nature*, **289**, 393-394, 1981.

Forte, A. M., A. M. Dziewonski, and R. L. Woodward, Ashperical structure of the mantle, tectonic plate motions, nonhydrostatic geoid, and topography of the core-mantle boundary, in *Dynamics of Earth's Deep Interior and Earth Rotation, Geophys. Monogr. Ser.*, **72**, (eds. J.-L. Le Mouël, et al.), AGU, Washington, D.C., 1993.

Fitch, T. J., and P. Molnar, Focal mechanisms along inclined earthquake zones in the Indonesia-Philippine Region, *J. Geophys. Res.*, **75**, 1431-1444, 1970.

Fuchs, K., and G. Müller, Computation of synthetics seismograms with the reflectivity method and comparison with observations, *Geophys. J. R. astr. Soc*, **23**, 417-433, 1971.

Gaherty, J. B., and T. Lay, Investigation of laterally heterogeneous shear velocity structure in D" beneath Eurasia, *J. Geophys. Res.*, **97**, 417-435, 1992.

Garnero E. J., D. V. Helmberger, and G. Engen, Lateral variations near the core-mantle boundary, *Geophys. Res. Lett.*, **15**, 609-612, 1988.

Garnero E. J., and D. V. Helmberger, Travel times of S and SKS: Implications for 3-D lower mantle structure, *J. Geophys. Res.*, **98**, 8225-8241, 1993.

Garnero, E. J., D. V. Helmberger and S. P., Grand, Preliminary evidence for a lower mantle shear wave velocity discontinuity beneath the central Pacific, *Phys. Earth Planet. Inter.*, **79**, 335-347, 1993a.

Garnero E. J., D. V. Helmberger, and S. P. Grand, Constraining outermost core velocity with SmKS waves, *Geophys. Res. Lett.*, **20**, 2463-2466, 1993b.

Garnero, E. J., S. P. Grand and D. V. Helmberger, Low P-velocity at the base of the mantle, *Geophys. Res. Lett.*, **20**, 1843-1846, 1993c.

Garnero, E. J., and D. V. Helmberger, On seismic resolution of laterally heterogeneity in the Earth's outermost core, *Phys. Earth Planet. Inter.*, (submitted), 1994.

Giardini, D., X.-D. Li, and J. H. Woodhouse, Three-dimensional structure of the Earth from splitting in free oscillations spectra, *Nature*, **325**, 405-411, 1987.

Gourant, F., F. Guyot, J. Peyronneau, and J. P. Poirier, Analytical electron microscope study of high-pressure and high-temperature reactions between silicates and iron alloys; implications for the Earth's core, *J. Geophys. Res.*, **97**, 4477-4487, 1992.

Grand, S. P., Tomographic inversion for shear velocity beneath the North American plate, *J. Geophys. Res.*, **92**, 14065-14090, 1987.

Grand, S. P., Mantle shear structure beneath the Americas and surrounding oceans, *J. Geophys. Res.*, (in press), 1994.

Grand, S. P., and D.V. Helmberger, Uppermantle shear structure beneath Asia from multi-bounce S waves, *Phys. Earth Planet. Inter.*, **41**, 154-169, 1985.

Graves, R. W. and D. V. Helmberger, Upper mantle cross section from Tonga to Newfoundland, *J. Geophys. Res.*, **93**, 4701-4711, 1988.

Gudmundsson, O., R. W. Clayton, and D. L. Anderson, CMB topography inferred from ISC PcP travel times (abstract), *Eos Trans. AGU,* **67**, 1100, 1986.

Gudmundsson, O., Some problems in global tomography: modeling the core-mantle boundary and statistical analysis of travel-time data, Ph.D. Thesis, California Institute of Technology, 1989.

Gutenberg, B., Uber Erdbebenwellen VII A. Boebachtungen an Registrierungen von Fernbeben in Gö und Folgerungen über die Konstitution des Erdkörpers, *Nachr. der Konig, Gesell. der Wiss. zu Göttingen, Math. Phys., K1*, **1**, 1914.

Gutenberg, B., On focal points of *SKS*, *Bull. Seism. Soc. Am.*, **28**, 197-200, 1938.

Gutenberg, B., Earthquake waves reflected at the inside of the core boundary, *J. Geophys. Res.*, **64**, 1503-1508, 1959.

Haddon, R. A. W., and J. R. Cleary, Evidence for scattering of seismic PKP waves near the mantle-core boundary, *Phys. Earth Planet. Inter.*, **8**, 211-234, 1974.

Haddon, R. A. W., and G. G. R. Buchbinder, Wave propagation effects and the Earth's structure in the lower mantle, *Geophys. Res. Lett.*, **13**, 1489-1492, 1986.

Haddon, R. A. W., and G. G. R. Buchbinder, S wave scattering by 3-D heterogeneities at the base of the mantle, *Geophys. Res. Lett.*, **14**, 891-894, 1987.

Hager, B. H., R. W. Clayton, M. A. Richards, R. P. Comer, and A. M. Dziewonski, Lower mantle heterogeneity, dynamic topography, and the geoid, *Nature*, **313**, 541-545, 1985.

Hales, A. L., and J. L. Roberts, The travel times of SKS and S, *Bull. Seism. Soc. Am.*, **60**, 461-489, 1970.

Hales, A. L., and J. L. Roberts, The velocities in the outer core, *Bull. Seism. Soc. Am.*, **61**, 1051-1059, 1971.

Helmberger, D. V., Theory and application of synthetic seismograms, in *Earthquakes: Observation, Theory and Interpretation,* Soc. Italiana di Fisica, pp. 173-222, 1983.

Helmberger, D. V., G. Engen, and S. Grand, Notes on wave propagation in laterally varying structure, *J. Geophys.*, **58**, 82-91, 1985a.

Helmberger, D. V., G. Engen, and S. Grand, Upper-mantle cross-section from California to Greenland, *J. Geophys.*, **58**, 92-100, 1985b.

Helmberger, D. V., L.-S. Zhao, and E. J. Garnero, Construction of synthetics for 2D structures; core phases, *Geophys. J. Int.* (submitted), 1994.

Hide, R., Motions of the earth's core and mantle, and variations of the main geomagnetic field, *Science*, **157**, 55-57, 1967.

Hide, R., and K. Horai, On the topography of the core-mantle interface, *Phys. Earth Planet. Inter.*, **1**, 305-308, 1968.

Hide, R., R. W. Clayton, B. H. Hager, M. A. Spieth, and C. V. Voorhies, Topographic core-mantle coupling and Fluctuations in the Earth's rotation, in *Relating Geophysical Structures and Processes: The Jeffreys Volume Geophysical Monograph*, **76**, 107-120, AGU, Washington, DC, 1993.

Houard, S., and H.-C. Nataf, Further evidence for the 'Lay discontinuity' beneath northern Siberia and the North Atlantic from short-period P-waves recorded in France, *Phys. Earth Planet. Inter.*, **72**, 264-275, 1992.

Houard, S., and H.-C. Nataf, Laterally varying reflector at the top of D" beneath northern Siberia, *Geophys. J. Int.*, **115**, 168-182, 1993.

Jault, D., and J. L. Le Mouël, Exchange of angular momentum between the core and the mantle, *J. Geomag. Geoelectr.*, **43**, 111-129, 1991a.

Jault, D., and J. L. Le Mouël, Physical properties at the top of the core and core surface motions, *Phys. Earth Planet. Inter.*, **68**, 76-84, 1991b.

Jeanloz, R., The nature of the Earth's core, *Ann. Rev. Earth Planet. Sci.*, **18**, 357-386, 1990.

Jeanloz, R., Chemical reactions at the Earth's core-mantle boundary: summary of evidence and geomagnetic implications, in *Relating Geophysical Structures and Processes, The Jeffreys Volume Geophysical Monograph*, **76**, 121-127, 1993.

Jeanloz, R., and F. M. Richter, Convection, composition, and the thermal state of the lower mantle, *J. Geophys. Res.*, **84**, 5497-5504, 1979.

Jeffreys, H., On compressional waves in two superposed layers, *Proceed. Camb. Phys. Soc.*, **23**m 472-481, 1926.

Jeffreys, H. and K. E. Bullens, Seismological Tables, British Association for the Advancement of Science, London, 1948.

Jones, G. M., Thermal interaction of the core and the mantle and long-term behavior of the geomagnetic field, *J. Geophys. Res.*, **82**, 1703-1709, 1977.

Jordan, T. H., P. Puster, G. A. Glatzmaier, P. J. Tackley, Comparisons between seismic Earth structures and mantle flow models based on radial correlation functions, *Science*, **261**, 1427-1431, 1993.

Kanamori, H. Spectrum of P and PcP in relation to the mantle-core boundary and attenuation in the mantle, *J. Geophys. Res.*, **72**, 559-571, 1967.

Kendall, J.-M., and P. M. Shearer, Lateral variations in D" thickness from long-period shear-wave data, *J. Geophys. Res.*(in press), 1994.

Kennett, B.L.N., and E.R. Engdahl, Traveltimes for global earthquake location and phase identification, *Geophys, J. Int.*, **105**, 429-465, 1991.

Kumagai, H., Y. Fukao, N. Suda, and N. Kobayashi, Structure of the D" layer inferred from the Earth's free oscillations, *Phys. Earth Planet. Inter.*, **73**, 38-52, 1992.

Kind, R., and G. Müller, Computations of SV waves in realistic Earth models, *J. Geophys.*, **41**, 149-172, 1975.

Kind, R., and G. Müller, The structure of the outer core from SKS amplitudes and travel times, *Bull. Seism. Soc. Am.*, **67**, 1541-1554, 1977.

Knittle, E., and R. Jeanloz, High-pressure metallization of FeO and implications for the Earth's core, *Geophys. Res. Lett.*, **13**, 1541-1544, 1986.

Knittle, E., and R. Jeanloz, Simulating the core-mantle boundary: An experimental study of high-pressure reactions between silicates and liquid iron, *Geophys. Res. Lett.*, **16**, 609-612, 1989.

Knittle, E., and R. Jeanloz, Earth's core-mantle boundary: Results of experiments at high pressures and temperatures, *Science*, **251**, 1438-1443, 1991.

Kohler, M. D., and T. Tanimoto, One-layer global inversion for the outermost core velocity, *Phys. Earth Planet. Inter.*, **72**, 173-184, 1992.

Krüger, F., M. Weber, F. Scherbaum, and J. Schlittenhardt, Double beam analysis of anomalies in the core-mantle boundary region, *Geophys. Res. Lett.*, **20**, 1475-1478, 1993.

Lavely, E. M., D. W. Forsyth, and P. Friedemann, Scales of heterogeneity near the core-mantle boundary, *Geophys. Res. Lett.*, **13**, 1505-1508, 1986.

Lay, T., Localized velocity anomalies in the lower mantle, *Geophys. J. R. astr. Soc*, **72**, 483-516, 1983.

Lay, T., Evidence of a lower mantle shear velocity discontinuity in S and sS phases, *Geophys. Res. Lett.*, **13**, 1493-1496, 1986.

Lay, T., Structure of the core-mantle transition zone: A chemical and thermal boundary layer, *Eos*, **70**, 49-59, 1990.

Lay, T., and D. V. Helmberger, A lower mantle S-wave triplication and the shear velocity structure of D", *Geophys. J. R. astr. Soc*, **75**, 799-838, 1983a.

Lay, T., and D. V. Helmberger, Body-wave amplitude and travel-time corrections across North America, *Bull. Seism. Soc. Am.*, **73**, 1063-1076, 1983b.

Lay, T., and D. V. Helmberger, The shear-wave gradient at the base of the mantle, *J. Geophys. Res.*, **88**, 8160-8170, 1983c.

Lay, T., and C. J. Young, The stably-stratified outermost core revisited, *Geophys. Res. Lett.*, **17**, 2001-2004, 1990.

Lay, T., and C. J. Young, Analysis of SV waves in the core's penumbra, *Geophys. Res. Lett.*, **18**, 1373-1376, 1991.

Li, X., D. Giardini, and J.H. Woodhouse, Large-scale three-dimensional even-degree structure of the Earth from splitting of long-period normal modes, *J. Geophys. Res.*, **96**, 551-577, 1991.

Loper, D. E., The nature and consequences of thermal interactions twixt core and mantle, *J. Geomag. Geoelectr.*, **43**, 79-91, 1991.

Masters, G., Observational constraints on the chemical and thermal structure of the Earth's deep interior, *Geophys. J. R. astr. Soc*, **57**, 507-534, 1979.

Masters, G., and P. M. Shearer, Summary of seismological constraints on the structure of the Earth's core, *J. Geophys. Res.*, **95**, 21,691-21,695, 1990.

Masters, G., H. Bolton, and P. Shearer, Large-scale 3-dimensional structure of the mantle (abstract), *Eos Trans. AGU.*, **73**, 201, 1992.

Menke, W., Effect of heterogeneities in D" on the decay rate of P_{diff}, *J. Geophys. Res.*, **91**, 1927-1933, 1986a.

Menke, W., Few 2-50 km corrugations on the core-mantle boundary, *Geophys. Res. Lett.*, **13**, 1501-1504, 1986b.

Mitchell, B. J., and D. V. Helmberger, Shear velocity at base of mantle from observations of S and ScS, *J. Geophys. Res.*, **78**, 6009-6020, 1973.

Mondt, J. C., SH waves: theory and observations for epicentral distances greater than 90 degrees, *Phys. Earth Planet. Inter.*, **15**, 46-59, 1977.

Morelli, A., Teleseismic tomography: core-mantle boundary, in *Seismic Tomography: Theory and Practice*, (eds. H. M. Iyer and K. Hirahara), Chapman and Hall, London, 1993.

Morelli, A., and A. M. Dziewonski, Topography of the core-mantle boundary and lateral homogeneity of the liquid core, *Nature*, **325**, 678-683, 1987.

Morelli, A., and A. M. Dziewonski, Body wave traveltimes and a spherically symmetric P- and S-wave velocity model, *Geophys. J. Int.*, **112**, 178-194, 1993.

Mula, A. H., Amplitudes of diffracted long-period P and S waves and the velocities and Q structure at the base of the mantle, *J. Geophys. Res.*, **86**, 4999-5011, 1981.

Mula, A. H., and G. Müller, Ray parameters of diffracted long period P and S waves and the velocities at the base of the mantle, *Pageoph.*, **118**, 1272-1292, 1980.

Müller, G., Earth-flattening approximation for body waves derived from geometric ray theory - improvements, corrections and range of applicability, *J. Geophys.*, **42**, 429-436, 1977.

Müller, G., A. M. Mula, and S. Gregersen, Amplitudes of long-period PcP and the core-mantle boundary, *Phys. Earth Planet. Inter.*, **14**, 30-40, 1977.

Nataf, H.-C., and S. Houard, Seismic discontinuity at the top of D": a world-wide feature?, *Geophys. Res. Lett.*, **20**, 2371-2374, 1993.

Neuberg, J., and J. Wahr, Detailed investigation of a spot on the core-mantle boundary using digital PcP data, *Phys. Earth Planet. Inter.*, **68**, 132-143, 1991.

Niazi, M., and K. L. McLaughlin, Observations of explosion generated PcP spectra at near-normal incidence, *J. Geodynam.*, **8**, 1-16, 1987.

Olham, R. D., Constitution of the interior of the Earth as revealed from earthquakes, *Quart. J. Geol. Soc.*, **62**, 456-475, 1906.

Olson, P., G. Schubert, and C. Anderson, Plume formation in the D'' -layer and the roughness of the core-mantle boundary, *Nature*, **327**, 409-413, 1987.

Olson, P. and C. Kincaid, Experiments on the interaction of thermal convection and compositional layering at the base of the mantle, *J. Geophys. Res.*, **96**, 4347-4354, 1991.

Phinney, R. A., and S. S. Alexander, P wave diffraction theory and the structure of the core-mantle boundary, *J. Geophys. Res.*, **71**, 5959-5975, 1966.

Phinney, R. A., and S. S. Alexander, The effect of a velocity gradient at the base of the mantle on diffracted P waves in the shadow, *J. Geophys. Res.*, **74**, 4967-4971, 1969.

Poupinet, G., A. Souriau, and L. Jenatton, A test on the Earth's core-mantle boundary structure with antipodal data: example of Fiji-Tonga earthquakes recorded in Tamanrasset, Algeria, *Geophys. J. Int.*, **113**, 684-692, 1993.

Pullium, R. J., and P. B. Stark, Bumps on the core-mantle boundary: are they facts or artifacts?, *J. Geophys. Res.*, **98**, 1943-1955, 1993.

Randall, M. J., SKS and seismic velocities in the outer core, *Geophys. J. R. astr. Soc*, **21**, 441-445, 1970.

Rekdal, T., and D. J. Doornbos, The times and amplitudes of core phases for a variable core-mantle boundary layer, *Geophys. J. Int.*, **108**, 546-556, 1992.

Revenaugh, J., and T. H. Jordan, Mantle layering from ScS reverberations 4. The lower mantle and the core-mantle boundary, *J. Geophys. Res.*, **96**, 19,811-19,824, 1991.

Rodgers, A., and J. Wahr, Inference of core-mantle topography from ISC PcP and PKP traveltimes, *Geophys. J. Int.*, **115**, 991-1011, 1993.

Ruff, L. J., and D. V. Helmberger, The structure of the lowermost mantle determined by short-period P-wave amplitudes, *Geophys. J. R. astr. Soc*, **68**, 95-119, 1982.

Sacks, S., Diffracted wave studies of the Earth's core 1. Amplitudes, core size, and rigidity, *J. Geophys. Res.*, **71**, 1173-1181, 1966.

Schlittenhardt, J., Investigation of the velocity- and Q-structure of the lowermost mantle using PcP/P amplitude rations from arrays at distances of $70^o - 84^o$, *J. Geophys.*, **60**, 1-18, 1986.

Schlittenhardt, J., J. Schweitzer, and G. Müller, Evidence against a discontinuity at the top of D", *Geophys. J. R. astr. Soc*, **81**, 295-306, 1985.

Schweitzer, J., Laufzeiten und Amplituden der Phasen SKS und SKKS und die Struktur des äußeren erdkerns, Diploma thesis, 117 pp., Institut für Meteorologie und Geophysik der Johann Wolfgang Goethe-Universität, Frankfurt, Germany, 1984.

Schweitzer, J., Anomalous S-phases and the structure in the lower mantle and at the core-mantle boundary beneath the central Pacific, *TERRA cognita*, **8**, 152, 1988.

Schweitzer, J., Untersuchung zur Geschwindigkeitsstruktur im unteren Erdmantel und im Bereich der Kern-Mantel-Grenze unterhalb des Pazifiks mit Scherwellen, (in German) Phd. thesis, Frankurt Univ., 134 pp., 1990.

Schweitzer, J., and G. Müller, Anomalous difference traveltimes and amplitude ratios of SKS and SKKS from Tonga-Fiji events, *Geophys. Res. Lett.*, **13**, 1529-1532, 1986.

Silver, P., and W. W. Chan, Implications for continental structure and evolution from seismic anisotropy, *Nature*, 355, 34-39, 1988.

Silver, P., and C. R. Bina, An anomaly in the amplitude ratio of SKKS/SKS in the range 100-108^o from portable teleseismic data, *Geophys. Res. Lett.*, **20**, 1135-1138, 1993.

Sipkin, S. A., and T. H. Jordan, Lateral heterogeneity of the upper mantle determined from the travel times of multiple ScS, *J. Geophys. Res.*, **81**, 6307-6320, 1976.

Sipkin, S. A., and T. H. Jordan, Multiple ScS travel times in the western Pacific: Implications for mantle heterogeneity, *J. Geophys. Res.*, **85**, 853-861, 1980.

Sleep, N. H., Gradual entrainment of a chemical layer at the base of the mantle by overlying convection, *Geophys. J. R. astr. Soc*, **95**, 437-447, 1988.

Snoke, J. A., and I. S. Sacks, Seismic modelling of lateral heterogeneity at the base of the mantle, *Geophys. J. R. astr. Soc.*, **86**, 801-814, 1986.

Song, X.-D., and D. V. Helmberger, Velocity structure near the inner core boundary from waveform modeling, *J. Geophys. Res.*, **97**, 6573-6586, 1992.

Souriau, A., and G. Poupinet, A latitudinal pattern in the structure of the outermost liquid core, revealed by the travel times of SKKS-SKS seismic phases, *Geophys. Res. Lett.*, **17**, 2005-2007, 1990.

Souriau, A., and G. Poupinet, A study of the outermost liquid core using differential travel times of the SKS, SKKS, and S3KS phases, *Phys. Earth Planet. Inter.*, **68**, 183-199, 1991.

Stacey, F. D., and D. E. Loper, The thermal boundary-layer interpretation of D″ and its role as a plume source, *Phys. Earth Planet. Inter.*, **33**, 45-55, 1983.

Stark, P. B., and N. W. Hengartner, Reproducing Earth's kernel: uncertainty of the shape of the core-mantle boundary from PKP and PcP travel times, *J. Geophys. Res.*, **98**, 1957-1971, 1993.

Stevenson, D. J., Limits on lateral density and velocity variations in the Earth's outer core, *Geophys. J. R. astr. Soc*, **88**, 311-319, 1987.

Su, W.-J., and A.M. Dziewonski, Predominance of long-wavelength heterogeneity in the mantle, *Nature*, **352**, 121-126, 1991.

Su, W.-J., R.L. Woodward, and A.M. Dziewonski, Joint inversions of travel-time and waveform data for the 3-D models of the Earth up to degree 12 (abstract), *Eos Trans. AGU.*, **73**, 201-202, 1992.

Su, W.-J., R.L. Woodward, and A.M. Dziewonski, Degree 12 model of shear velocity heterogeneity in the mantle, *J. Geophys. Res.*, **99**, 6945-6980, 1994.

Tanaka, S., and H. Hamaguchi, Velocities and chemical stratification in the outermost core, *J. Geomag. Geoelectr.* (in press), 1993a.

Tanaka, S., and H. Hamaguchi, Degree one heterogeneity at the top of the Earth's core, revealed by SmKS travel times, in *Dynamics of Earth's Deep Interior and Earth Rotation, Geophys. Monogr. Ser.*, **72**, (eds. J.-L. Le Mouël, et al.), AGU, Washington, D.C., 127-134, 1993b.

Tanaka, S., and H. Hamaguchi, Travel times and velocities in the outer core based on the global observations of SmKS seismic phases, *Tohoku Geophys. J.* (Sci. Rep. Tohoku Univ., Ser. 5), **34**, 55-87, 1993c.

Tanimoto, T., Long-wavelength S-wave velocity structure throughout the mantle, *Geophys. J. Int.*, **100**, 327-336, 1990.

Vidale, J. E., Waveform effects of a high-velocity, subducted slab, *Geophys. Res. Lett.*, **14**, 542-545, 1987.

Vidale, J. E., and H. M. Benz, A sharp and flat section of the core-mantle boundary, *Nature*, **359**, 627-629, 1992.

Vidale, J. E., and H. M. Benz, Seismological mapping of fine structure near the base of the Earth's mantle, *Nature*, **361**, 529-532, 1993.

Vinnik, L. V., V. Farra, and B. Romanowicz, Observational evidence for diffracted SV in the shadow of the Earth's core, *Geophys. Res. Lett.*, **16**, 519-522, 1989.

Voorhies, C. V., Steady flows at the top of the Earth's core derived from geomagnetic field models, *J. Geophys. Res.*, **91**, 12,444-12,466, 1986.

Voorhies, C. V., Simultaneous solution for the core magnetic field and fluid flow beneath an electrically conducting mantle, *J. Geophys. Res.*, **99**, 6685-6693, 1994.

Weber, M., P- and S-wave reflections from anomalies in the lowermost mantle, *Geophys. J. Int.*, **115**, 183-210, 1993.

Weber, M., and J. P. Davis, Evidence of a laterally inhomogeneous lower mantle structure from P- and S-waves, *Geophys. J. Int.*, **102**, 231-255, 1990.

Weber, M., and M. Kornig, Lower mantle inhomogeneities inferred from PcP precursors, *Geophys. Res. Lett.*, **17**, 1993-1996, 1990.

Weber, M., and M. Kornig, A search for anomalies in the lowermost mantle using seismic bulletins, *Phys. Earth Planet. Inter.*, **73**, 1-28, 1992.

Woodward, R.L., and G. Masters, Lower-mantle structure from ScS-S differential travel times, *Nature*, **352**, 1991.

Wright, C., and J. A. Lyons, Further evidence for radial velocity anomalies in the lower mantle, *Pageoph.*, **119**, 137-162, 1981.

Wright, C., K. J. Muirhead, and A. E. Dixon, The P wave velocity structure near the base of the mantle, *J. Geophys. Res.*, **90**, 623-634, 1985.

Wysession, M. E., E. A. Okal, and C. R. Bina, The structure of the core-mantle boundary from diffracted waves, *J. Geophys. Res.*, **97**, 8749-8764, 1992.

Wysession, M. E., C. R. Bina, and E. A. Okal, Constraints on the temperature and composition of the base of the mantle, in *Dynamics of Earth's Deep Interior and Earth Rotation, Geophys. Monogr. Ser.*, **72**, (eds. J.-L. Le Mouël, et al.), AGU, Washington, D.C., 181-189, 1993.

Wysession, M. E., L. Bartko, and J. Wilson, Investigating the core-mantle boundary using GDSN core-reflected shear waves, *J. Geophys. Res.*(submitted), 1994.

Young, C. J., and T. Lay, Evidence for a shear velocity discontinuity in the lower mantle beneath India and the Indian Ocean, *Phys. Earth Planet. Inter.*, **49**, 37-53, 1987a.

Young, C. J., and T. Lay, The core-mantle boundary, *Ann. Rev. Earth Planet. Sci*, **15**, 25-46, 1987b.

Young, C. J., and T. Lay, The core shadow zone boundary and lateral variations of the P velocity structure of the lowermost mantle, *Phys. Earth Planet. Inter.*, **54**, 64-81, 1989.

Young, C. J., and T. Lay, Multiple phase analysis of the shear velocity structure in the D" region beneath Alaska, *J. Geophys. Res.*, **95**, 17,385-17,402, 1990.

Zhang, J., and T. Lay, Investigation of a lower mantle shear wave triplication using a broadband array, *Geophys. Res. Lett.*, **11**, 620-623, 1984.